UDC 520/524 (082)
UDC 113/119 (082)

YU ISSN 0373-3742

ПУБЛИКАЦИЈЕ АСТРОНОМСКЕ ОПСЕРВАТОРИЈЕ У БЕОГРАДУ
PUBLICATIONS OF THE ASTRONOMICAL OBSERVATORY OF BELGRADE

Св. 82 **No. 82**

VI SERBIAN - BELARUSSIAN SYMPOSIUM ON PHYSICS AND DIAGNOSTICS OF LABORATORY & ASTROPHYSICAL PLASMA

INVITED LECTURES AND CONTRIBUTED PAPERS

Belgrade, Serbia, 22 - 25 August 2006

Edited by Milivoje Ćuk, Milan S. Dimitrijević, Jagoš Purić and Nenad Milovanović

B E L G R A D E
2007

PUBLICATIONS OF THE ASTRONOMICAL OBSERVATORY OF BELGRADE

FOUNDED IN 1947

Published and copyright © by Astronomical Observatory,
Volgina 7, 11160 Belgrade, Serbia

Director of the Astronomical Observatory: Dr Zoran Knežević
Internet address `http://www.aob.bg.ac.yu`

Typesetting: Nenad Milovanović

The publication of this issue is financially supported by the Ministry of Sciences and Environmental Protection of the Republic of Serbia

Number of copies / тираж: 300

Production: Kultura ad, Milutina Milankovića 4, Novi Beograd, Serbia

VI SERBIAN-BELARUSIAN SYMPOSIUM ON PHYSICS AND DIAGNOSTICS OF LABORATORY & ASTROPHYSICAL PLASMA

Belgrade, 22.-25. August 2006

Scientific Organizing Committee

M. Ćuk, Co-chairman (Serbia)
M. S. Dimitrijević, Co-chairman (Serbia)
V. S. Burakov, Co-chairman (Belarus)
A. F. Chernyavski, Co-chairman (Belarus)

V. I. Arkhipenko, Vice-chairman, (Belarus)
S. Đurović, Vice-chairman (Serbia)

L. Č. Popović, Scientific Secretary (Serbia)

V. M. Astashynski (Belarus)
V. S. Gaponenko (Belarus)
V. K. Goncharov (Belarus)
N. Konjević (Serbia)
M. M. Kuraica (Serbia)
O. P. Kuznechik (Belarus)
A. L. Mosse (Belarus)
T. Nenadović (Serbia)
J. Purić (Serbia)
L. V. Simonchik (Belarus)

Local Organizing Committee

M. M. Kuraica, Chairman (Serbia)
N. Cvetanović, Vice-chairman (Serbia)

M. Dačić (Serbia)
I. P. Dojčinovič (Serbia)
N. Milovanović (Serbia)

ACKNOWLEDGMENTS

VI SERBIAN-BELARUSIAN SYMPOSIUM ON PHYSICS
AND DIAGNOSTICS OF LABORATORY & ASTROPHYSICAL PLASMA
was organized by

Faculty of Physics, University of Belgrade
P.O.Box 368, Studentski trg 12-16
11000 Belgrade, Serbia

Center for Science and Technology Development
Obilićev venac 26
11000 Belgrade, Serbia

Astronomical Observatory
Volgina 7, 11160 Belgrade, Serbia

under the auspices and with support of the Ministry of Science and Environmental Protection of the Republic of Serbia

SPONSORS

Studentski centar "Beograd", Univerzitet u Beogradu, Svetozara Markovića 56, Beograd

Visoka škola turističkih studija, Bulevar AVNOJ-a 152a, Beograd

Gradsko Saobraćajno preduzeće "Beograd", Knjeginje Ljubice 29, Beograd

TABLE OF CONTENTS

Invited Lectures

Contributed papers

INVITED LECTURES

VI Serbian-Belarusian Symp. on Phys. and Diagn. of Lab. &
Astrophys. Plasma, Belgrade, Serbia, 22 - 25 August 2006
eds. M. Ćuk, M.S. Dimitrijević, J. Purić, N. Milovanović
Publ. Astron. Obs. Belgrade No. 82 (2007), 11-21 *Invited lecture*

THE CATHODE LAYER CHARACTERISTICS OF THE NORMAL DC ATMOSPHERIC PRESSURE GLOW DISCHARGE

V. I. Arkhipenko, A. A. Kirillov, L. V. Simonchik, S. M. Zgirouski

Institute of Molecular and Atomic Physics, NAS of Belarus,
ave. Nezalezhnastsi 70, 220072 Minsk, Belarus; kirillov@imaph.bas-net.by

Abstract. The normal cathode fall and current density of the atmospheric pressure glow discharges for the different "cathode material – working gas" pairs are determined. The gas temperature in the cathode region was measured in each case. Laws of similarity were used to establish the conformity of obtained data to the corresponding ones for the low pressure glow discharges.

1. INTRODUCTION

There is large increasing interest in Atmospheric Pressure Glow Discharges (APGD) because they can be used for a wide range of technological applications without the need of vacuum systems. Some fundamental properties of the APGD plasmas have been experimentally characterized including discharge dynamics, optical emission, and densities of charged particles and excited species, but the experimental cathode fall parameters of the APGD have not been determined. To a lesser extent the APGD have also been studied numerically. Results of these numerical studies agree favorably with the macroscopic features of the measured discharge current and voltage. Theoretical models offer useful tools to understand atmospheric glow discharges, but precision of model results isn't high due to an imperfect data of elementary processes rates, especially, large uncertainties in the electron yield per ion for practical cathodes. That is why the results of every model calculation need experimental testing.

There are a lot of experimental data relatively the normal cathode fall and current density in the Low Pressure Glow Discharges (LPGD) presented in well-known books [1-4], for example. The dependence of the normal cathode fall of the LPGD on pressure was discovered in [5]. It was established that the cathode fall V_c decreases on 10÷15% at the increase of pressure from 1 Torr to a few tens of Torr in the LPGD in helium and neon with steel cathode. At the same time the change of cathode fall in the neon LPGD with titanium cathode was not observed. As to

atmospheric pressure, there are a few references where the experimental cathode fall parameters of the APGD are presented. The increase of the gas pressure up to the atmospheric one leads to a decrease in the dimensions of the glow discharge region characteristics and to the sharp increase in the heat release in cathode region. Determination of the normal cathode fall and current density of the different APGDs and their testing using laws of similarity are important current research topics and necessary for further optimization of the different APGD applications.

The cathode fall parameters were investigated in details for the self-sustained normal dc APGD in helium with the stainless steel cathode in [6]. The objectives of this work are to determine both the cathode fall and current density in self-sustained normal dc APGDs in other gases, namely, argon, neon, nitrogen, air and carbon dioxide. At the same time the different cathode materials are used as well.

2. EXPERIMENT

The experiments were performed in the installation geometry described in [6]. The electrodes were put in a pressurised chamber. The weakly rounded tungsten anode (6 mm in dia) was used in our experiments. To the contrary, the different material planar water-cooled cathodes were used. A working gas (helium, argon, neon, nitrogen, air and carbon dioxide) at a flow of 2 litre/min at atmospheric pressure was provided through the discharge chamber. The glow discharge was ignited by contacting anode and cathode and then by moving away one of each other. The interelectrode gap was about 2 mm.

Table 1. Current regions of the self-sustained normal dc APGD burning (Ampere)

Gas / Cath. material	He	Ne	Ar	N_2	Air	CO_2
Copper	0.02 – 8	0.02 – 1.6	0.01 – 2	0.06 – 1.1	0.1 – 0.4	0.02 – 0.1
Stainless steel	0.02 – 6.5	0.02 – 1	0.01– 0.3	0.08 – 0.6	0.1 – 0.4	0.02 – 0.1
Titanium	0.08 – 1	0.03 – 0.6	0.03 – 0.1	0.02 – 0.1		
Duralumin	0.01 – 0.2	0.01 – 0.1				

The discharge was fed by controlled dc power supplies with output voltage up to 600 V and 1200 V. The ballast resistance in the anode circuit was changed from ~75 Ω up to 2.5 kΩ. The voltage applied to electrodes and the discharge current were measured by means of a digital dc voltmeter (CH300, instrumental error 0.1%) and an amperemeter (M1104, instrumental error 0.2%), correspondingly. In table 1 the current ranges for different pairs of the gases and cathode materials where the APGD was observed in given experiments are presented.

The photo of the APGD at discharge current of 1 A in helium is presented in fig. 1. One can see, the structure of the glow discharge is as follows: a thin (less than 1 mm thick) disc of glow emission resides above the cathode surface, whereas the glowing column is adjacent to anode.

Fig. 1. Photo of the APGD in helium.

There is the Faraday dark space between these glow regions. The anode surface is covered with a glowing layer. The positive column is constricted to a diameter about 3–5 mm.

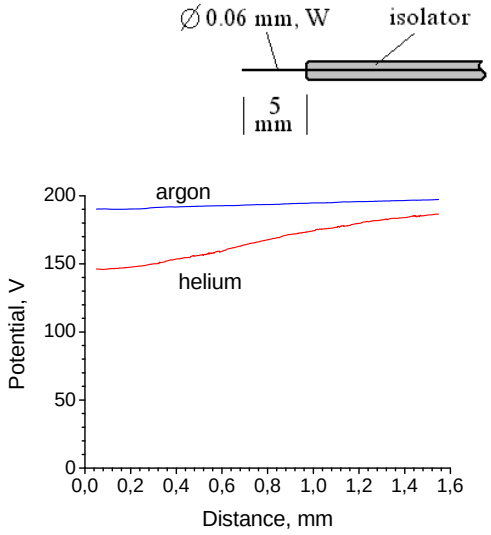

Fig. 2. Axial profiles of potential in the APGD in helium and argon at discharge current of 0.5 A.

The electric probe technique was used for the cathode fall measurements. The cathode fall voltage V_c was measured with the help of a tungsten probe 60 μm in diameter (see an upper picture insert in fig. 2).

The length of the uninsulated wire was 5 mm. The probe was put into discharge from one side and it was parallel to the cathode surface. The probe could move along the discharge axes by a stepper motor and by a microscrew in perpendicular direction.

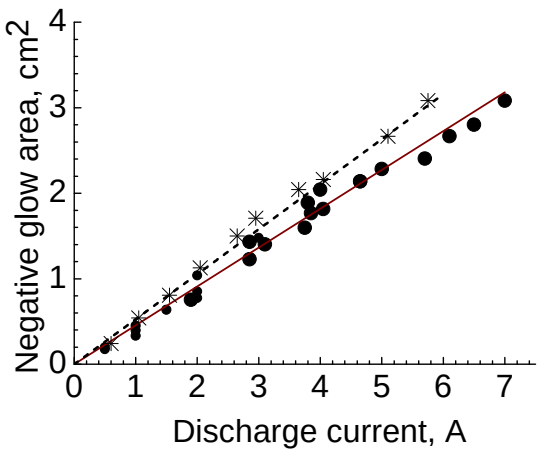

Fig. 3. Dependence of the area of the negative glow *S* on discharge current for the APGD in helium: closed circles – copper cathode, snowflakes – stainless steel cathode.

The probe potential V_p was measured by a digital voltmeter CH300 (input resistance is 10 MΩ) and determined by two ways. In most cases it was measured with respect to the grounded cathode. We supposed that $V_c \approx V_p$ at the instant just before the probe touched (or just after it detached) of the cathode. Axial profiles of potential in the APGD in helium and argon at discharge current of 0.5 A are presented in fig.2 for example.

In the cases when the probe setting into cathode region brought to the discharge instability the other way was used to determine the cathode fall. In this case the probe potential V_p was measured with respect to anode. At the same time the interelectrode voltage V_{ac} was determined. The cathode fall is $V_c \approx V_{ac} - V_p$ at the small interelectrode gaps in ranges of 0.2 – 0.5 mm.

The current density was defined as the ratio of discharge current *I* to the area of negative glow *S*. In fig. 3 dependences of negative glow area *S* on discharge current for the APGD in helium with the copper and stainless steel cathodes are presented. The linearity of the dependence of negative glow area on discharge current indicates that current density is constant, as in the case of a normal glow discharge. According to the figure 3 current densities are 2.3 A/cm^2 and 1.8 A/cm^2 for copper and stainless steel cathodes correspondingly. It is necessary to note that the water-cooling of cathode was applied at discharge currents more than 0.5 A to provide normal current density. The measurements were mainly fulfilled at the

discharge current of 0.2 A. But we always carried out the experiments at the range of discharge current lower and higher of this value to make sure that it is a normal mode of the APGD.

As it is known, current density in cathode fall depends strongly on the gas temperature in this volume even at discharge current of the order of 1 mA. More definitely, it depends on a gas density. Therefore, knowledge of the gas temperature is necessary for every measurement of current density to use the laws of similarity. The method of the relative rotational line intensity of molecular gases was used for the gas temperature determination [7-9]. The band (0,1)(λ = 427.81 nm) from the first negative system of molecular nitrogen ion $N_2^+(B^2\Sigma_u^+)$ served as a working band. When this band wasn't observed (for example in case of argon or neon) we used (0, 0) (λ = 308 nm) OH band to determine the gas temperature.

3. RESULTS

The normal cathode falls V_c for the LPGD and APGD are given in table 2. Cathode falls we measured in the APGDs for various "cathode material – working gas" pairs are shown in thick print lines. The pressure value of 740 Torr is typical atmospheric pressure for Minsk (Belarus) where experiments were fulfilled.

Table 2. The normal cathode falls in the APGDs

Gas / Cathode material	He		Ne		Ar		N_2	
	p, Torr	V_c, V	*p*, Torr	V_c, V	*p*, Torr	V_c, V	*p*, Torr	V_c, V
Copper	1	177 [1]	1	220 [1]	1	130 [1,3]	1	208 [1]
		204 [5]		200 [3]				
				148 [5]				
	740	**145±5**	**740**	**145±5**	**740**	**190±5**	**740**	**202±5**
Iron	1	150 [1,3]	1	150 [1,3]	1	165 [1,3]	1	215 [1]
	20	131 [5]	40	129 [5]				
Steel	**740**	**140±5**	**740**	**145±5**	**740**	**185±5**	**740**	**195±10**
Titanium	1	115 [1,3]	1	114 [1,3]	1	99 [1,3]		
			40	113 [5]	15	99 [5]		
	740	**142±5**	**740**	**155±5**	**740**	**150±5**	**740**	**380±10**
Aluminum	1	140 [1,3]	1	120 [1,3]	1	100 [1,3]		
	3.5	<173 [10]						
Duralumin	**740**	**110±5**	**740**	**125±5**				

As one can see in table 2, the normal cathode falls of the APGDs are differing from ones for the LPGDs in sufficient bulk of cases. The increase or decrease of the normal APGD cathode falls at the transition from low pressure to atmospheric one depends on the "cathode material – working gas" pairs.

The cathode fall values obtained by us for the APGD with the stainless steel cathode in helium, neon and nitrogen do not practically differ from ones in discharges at 1 Torr. The cathode falls V_c in the APGDs with the copper and stainless steel cathodes in helium and neon are significant less than in the corresponding LPGDs. At the same time the cathode fall in the nitrogen APGD with the same cathodes does not change. The significant growth of the cathode fall voltage with pressure increase takes place for both the cooper and titanium cathodes in the argon APGD.

There are simple seeming explanations of observed differences, namely, the differences in both the cathode surface preparation and the gas composition in low and atmospheric pressure experiments. At low pressure the cathode cleaning by the high-current glow discharge was used when the sputtering of cathode material takes place. But the APGD itself is the high current glow discharge and the sputtering takes place in it. We used in the experiments the gases containing the impurities less than 0.02%. At the same time, our experiments [14] showed that the addition of the admixture of other gases into working gas less than 0.1% doesn't have effect on the electrical parameters of the APGD. Therefore, probably, the differences of the cathode fall values at low and atmospheric pressure are due to pressure effect.

Current densities in the cathode region of both the LPGD and APGD are presented in tables 3 and 4. Ibidem the corresponding temperatures in cathode region of the APGDs are given as well. According to references the temperature in cathode region of the LPGD at pressure 1 Torr is 290 K, i.e. it is a room temperature.

Table 3. The normal current density of the glow discharge. Rare gases

Gas / Cath. material	He			Ne			Ar		
	LPGD	APGD		LPGD	APGD		LPGD	APGD	
	j, μA/cm^2	j, A/cm^2	T_g, K	j, μA/cm^2	j, A/cm^2	T_g, K	j, μA/cm^2	j, A/cm^2	T_g, K
Copper		**2.3 ± 0.2**	**720**		**2.3 ± 0.2**	**650**	40 /5/	**3.8 ± 1.5**	**980**
Iron	2.2 [1,3]			6 [1,3]			160 [1] 100 [11]		
Stainless steel		**1.8 ± 0.2**	**650**		**1.2 ± 0.2**	**740**		2.5 ± 0.4[13] **2.3 ± 0.4**	550 **950**
Titanium		**1.0± 0.1**	**600**		**0.8 ± 0.1**	**690**		**1.0 ± 0.2**	**910**
Aluminum Duralumin	<15 [10]	**1.4±0.1**	**615**		**1.1±0.1**	**615**	110± 20 [12]		

Table 4. The normal current density of the glow discharge. Molecular gases

Gas / Cath. material	N_2			Air			CO_2		
	LPGD	APGD		LPGD	APGD		LPGD	APGD	
	j, μA/cm^2	j, A/cm^2	T_g, K	j, μA/cm^2	j, A/cm^2	T_g, K	j, μA/cm^2	j, A/cm^2	T_g, K
Copper		**8.0 ± 0.5**	**2700**	240 [1]	**11 ± 1**	**3000**		**11.5 ± 1**	**2800**
Iron Stainless steel	400 [1,3]	**5.0 ± 0.5**	**2100**		**6 ±1**	**2400**			

Current density in the LPGD with various "cathode material – working gas" pairs changes on two orders of magnitude. For the LPGD with stainless steel cathode, for example, current density is 2.2 μA/cm^2 in helium discharge and 400 μA/cm^2 for nitrogen one. In case of the APGD the current density changes only on order of magnitude, namely, from ~ 1 A/cm^2 up to ~ 10 A/cm^2. Current density in both the LPGD and APGD is high in the molecular gas discharges in comparison with ones in rare gases. However the difference between the APGD current densities for various "cathode material – working gas" pairs is less than in case of the LPGD. It can be explained by a strong gas heating in discharges with high current density. Gas temperature at the end of cathode region in rare gas APGD does not exceed 1000 K. At the same time the gas temperature is in the range of 2000÷3000 K in the molecular gas APGD.

4. LAWS OF SIMILARITY

Gas discharge parameters at different gas densities are connected by laws of similarity [1]

$$V=V_l,\quad d = d_l \frac{p_l T}{p T_l},\quad j = j_l \left(\frac{p T_l}{p_l T} \right)^2, \tag{1}$$

which are correct when a number of limitations on discharge ionization mechanisms are fulfilled. Here d – cathode fall thickness. Parameters with subscript l correspond to the low pressure discharge. But laws of similarity (1) can not be used immediately for the comparison of the LPGD and APGD parameters due to gas temperature change in the APGD cathode layer. It takes place due to significant volumetric heat release. In this case it is necessary to use the one-dimension models of cathode fall region taking into account a volumetric heat release [15, 16]. These models, essentially, are a summarizing of similarity principle on a gas with inhomogeneous density.

The model of [15] is based on the following assumptions: (i) gas heating in the cathode fall is caused by collisions between the positive ions and neutral gas atoms; (ii) both the electric field and the ion current density decrease linearly with distance from the cathode; (iii) gas thermal conductivity is proportional to gas

temperature, $\lambda(T) = \alpha T$. In this model, the heat conduction equation for the gas in the cathode fall has the form

$$T\frac{d^2T}{dx^2} + \left(\frac{dT}{dx}\right)^2 + \frac{E_{\max} j}{\alpha}\left(1 - \frac{x}{d}\right)^2 = 0, \tag{2}$$

where j is current density, $E_{\max}$ is electric field near the cathode surface, and d is the cathode fall thickness.

Then according to [15], the cathode fall region, which is nonuniform in temperature, is replaced by a sheath with a uniform average temperature <T>, and the electric parameters of the cathode fall are determined by using laws of similarity for a normal glow discharge (1). Expression for gas temperature within a cathode layer obtained in [15] is approximate. It is correct in asymptotic approximation of very high heat release. Exact solution of equation (2) has a following form [6]:

$$T = T_c\sqrt{1 + q(1 - \xi^4)}\ , \tag{3}$$

where $\xi = 1 - x/d$. Then

$$\langle T\rangle = T_c\left[\frac{1}{3} + \frac{\sqrt{2}}{3}\ \sqrt{1+q}\ \sqrt[4]{1+\frac{1}{q}}\ F(\varphi, \frac{1}{\sqrt{2}})\right]\ . \tag{4}$$

Here $F(\varphi, k)$ is the elliptic integral of the first kind and

$$\varphi = \arcsin\frac{\sqrt{2}}{\sqrt{1+\sqrt{1+(1/q)}}}\ , \tag{5}$$

where the dimensionless parameter

$$q = \frac{V_c jd}{3\lambda_c T_c} \tag{6}$$

is the heat release power in the cathode fall normalized to the heat flux with a gradient near the cathode surface of $2T_c/d$. Here, V_c is the cathode fall voltage and λ_c is the gas thermal conductivity at the temperature T_c. The exact solution of the heat conduction equation [6] was used at calculations according to model [15] (model ESS).

In [16] (model BS), an attempt was made to calculate the parameters of the cathode fall with allowance for a nonuniform temperature distribution in it. According to [16], the local characteristics of the cathode fall at atmospheric pressure can be expressed in the form

$$dx = \delta(x)\frac{p_l T(x)}{p T_l}dx_l\ ,\ \ E(x) = \varepsilon(x)\frac{pT_l}{p_l T(x)}E_l(x_l)\ , \tag{7}$$

where $\delta(x)$ and $\varepsilon(x)$ are the corrections related to the deviation of the current density j from the normal local value $j_n(x)$ determined from the scaling law. To calculate the corrections $\delta(x)$ and $\varepsilon(x)$, we used formulas

$$\frac{j}{j_n(x)} = \frac{1}{\delta(x)(1+\ln\delta(x))^2}\ , \qquad \varepsilon(x) = \frac{1}{1+\ln\delta(x)}\ . \tag{8}$$

The temperature profile in the cathode fall is calculated from the heat conduction equation

$$\frac{d}{dx}\left(\lambda(T)\frac{dT}{dx}\right) + Ej_T = 0\ , \tag{9}$$

where j_T is the fraction of the current density that causes gas heating. For a normal glow discharge, the current density j is believed to correspond to the minimum of the cathode fall voltage. So, it is necessary to find such solution of a boundary problem of the heat conduction equation added by algebraic relation, which minimizes of the cathode potential of cathode layer. In [16], in contrast to [15], it was the electron current also contributes to the cathode fall along with the ion current.

5. DISCUSSION

Let's compare the parameters of cathode fall region using the one-dimension models [15, 16] of this region. According to model [15] the cathode fall does not depend on gas pressure. At the same time the cathode fall determined by model [16] increases while pressure is increasing. The stronger temperature inhomogeneity in cathode layer is the more this increase is. However even in case of the molecular gases the difference of cathode fall values in glow discharges at atmospheric and low pressures does not exceed a few Volts. Therefore, the significant differences of cathode fall values at low and atmospheric pressure marked above (see table 2) can not be explained in frames of models [15, 16].

Experimental and calculated according to models [15, 16] values of both the current density in cathode region and gas temperature in negative glow are presented in tables 5 and 6. The cathode fall region parameters corresponding to pressure of 1 Torr [1] were used in these calculations.

Table 5. Experimental and calculated parameters of the cathode fall. Rare gases

Gas-cath. material	He-Fe		Ne-Fe		Ar-Fe	
	j, A/cm^2	T, K	j, A/cm^2	T, K	j, A/cm^2	T, K
Experiment	1.8±0.2	650	1.2±0.2	740	2.5±0.4	950
Model ESS	0.47	470	1.0	540	6.5	1230
Model BS	0.48	465	1,1	520	7.4	1240

Table 6. Experimental and calculated parameters of the cathode fall. Molecular gases

Gas-cath. material	N_2-Fe		Air-Cu	
	j, A/cm^2	T, K	j, A/cm^2	T, K
Experiment	5.0±0,5	2100	11.0±1.0	3000
Model ESS	8.7	1730	7,7	1400
Model BS	6.9	2280	6,2	1850

The calculated current density for steel-helium pair is less than experimental one in 4 times. Calculated gas temperature is below as well. The opposite situation is in the APGD in argon when the calculated current density value exceeds the experimental one in a few time, and calculated temperature is significantly high than experimental one. A good agreement between the calculated and experimental values takes place for discharges in neon and nitrogen. Probably, the observed differences between the calculated and experimental data are significative above all about changes in the elementary process balance in the discharge plasma at the transition from low pressure to atmospheric one.

In [6] a comprehensive investigation of the APGD in helium with stainless steel cathode was fulfilled. Besides a cathode fall, current density and gas temperature the cathode fall thickness and heat flux to the cathode were determined as well. A good agreement between experimental and calculated values including a heat flux to the cathode was observed. However it was necessary to use the increased value of current density (in 6 times) and the increased cathode fall thickness (in 2 times) in comparison with classical LPGD parameters at these calculations. Experimental determination of the three main parameters of the cathode fall region (V, j and d) allows, probably, to calculate more exactly a heat mode of discharge operation in cases of other gases. The last is very important for a number of applications.

6. CONCLUSIONS

The normal cathode fall and current density of the atmospheric pressure glow discharges for the different “cathode material – working gas” pairs were determined. The gas temperature in the cathode region was determined in each case. The laws of similarity were used to establish the conformity of obtained data to the corresponding ones for the LPGDs.

The calculated current density for steel-helium pair is less than experimental one in 5 times. The opposite situation is in the APGD in argon when the calculated current density value exceeds the experimental one on the order of magnitude. A good agreement between the calculated and experimental values takes place for discharges in neon and nitrogen. Probably, the observed differences between the calculated and experimental data are significative above all about changes in the elementary process balance in the discharge plasma at the transition from low pressure to atmospheric one.

REFERENCES

1. A. Engel and M. Steenbeck, Electrishe Entladungen. Ihre Physik und Technik. Berlin (1934)
2. G. Francis, Handbuch der Physik. Ed. by S. Flugge (Springer-Verlag, Berlin), **22**, 53 (1956)
3. V.L. Granovskiy, Electrical current in gas. Steady current. Moscow (1971)
4. Yu. P. Raizer,. Gas Discharge Physics. Moscow (1987)
5. P.N. Chistjakov, Physical electronics, **3**, 3 (1966)
6. V.I. Arkhipenko, S.M. Zgirovski, A.A. Kirillov and L.V. Simonchik, Plasma Phys. Rep., **28**, 858 (2002)
7. V.N. Ochkin, S. Yu. Savinov, N.N. Sobolev, Trudy PhIAN, **157,** 6 (1985)
8. V.I. Arkhipenko, S.M. Zgirouski, A.A. Kirillov, L.V. Simonchik, 21st SPIG, 685 (2002)
9. C.O. Laux, R.J. Gessman, C.H. Kruger, F. Roux, F. Michaud, S.P. Davis, JQSRT, **68,** 473 (2001)
10. E.A. Den Hartog, D.A. Doughty, J.E. Lawler, Phys. Rev. A, **38 (**1988) 2471.
11. A.V. Phelps, Plasma Sour. Sc. Technol., **10** (2001) 329.
12. V.A. Lisovskiy, S.D. Yakovin, Rus. Letter J. Tech. Phys., **26,** 88-94 (2000)
13. T. Farouk, B. Farouk, D. Staack, A. Gutsol, A. Fridman, Plasma Sour. Sc. Technol., **15**, 676 (2006)
14. V.I. Arkhipenko, S.M. Zgirouski, A.A. Kirillov, L.V. Simonchik, Plasma Sources Sci. Technol., **14**, 757 (2005)
15. A. Engel, B. Seeliger and M.Z. Steenbesk, Phys., **85,** 144 (1933)
16. G.A. Baranov, S.A. Smirnov, Zh. Tekh. Fiz., **69,** 49 (1999)

VI Serbian-Belarusian Symp. on Phys. and Diagn. of Lab. &
Astrophys. Plasma, Belgrade, Serbia, 22 - 25 August 2006
eds. M. Ćuk, M.S. Dimitrijević, J. Purić, N. Milovanović
Publ. Astron. Obs. Belgrade No. 82 (2007), 23-33 *Invited lecture*

STUDIES AND CHARACTERIZATION OF QUASI-STATIONARY COMPRESSION PLASMA FLOWS GENERATED BY GAS-DISCHARGE AND EROSIVE PLASMA ACCELERATORS

V. M. Astashynski[1], S. I. Ananin[1], V. V. Askerko[1],
E. A. Kostyukevich[1], A. M. Kuzmitski[1], A. A. Mishchuk[1],
M. M. Kuraica[2,3], I. P. Dojčinović[2,3], J. Purić[2,3]

[1]Institute of Molecular and Atomic Physics, National Academy of Sciences of Belarus,Nezalezhnastsi Ave. 70, 220072 Minsk, Belarus
e-mail: ast@imaph.bas-net.by
[2]Faculty of Physics, University of Belgrade,
P.O. Box 368, 11001 Belgrade, Serbia
[3]Center for Science and Technology Development,
Obilicev Venac 26, Belgrade, Serbia
e-mail: ivbi@ff.bg.ac.yu

Abstract. The results of investigations on compression plasma flows generated by gas-discharge magnetoplasma compressors and erosive plasmadynamic systems are presented. Electron temperature and plasma concentration in such quasi-stationary plasma accelerators (plasma guns) both were measured with spatio-temporal resolution. The characterization of quasi-stationary plasma flows was conducted using the dynamic coefficients specifically introduced. These coefficients were calculated based on the temporal evolution of the electron density and temperature in plasma obtained in these experiments.

1. INTRODUCTION

One of the major scientific and practical problems in plasma physics is development of methods for obtaining high-energy directional dense plasma streams including compression plasma streams, and controlling their parameters. Such plasma streams open up essentially new opportunities for fundamental research into dynamics of plasma formations in electromagnetic fields of the complex configuration. In addition, they are of interest owing to application of such plasma

flows in various technological processes (processing and hardening of surfaces, deposition of coatings, etc.).

Earlier we investigated physical processes in gas-discharge quasi-stationary plasmadynamic systems operating at different input energy (for example, magnetoplasma compressor (MPC) with storage energy up to 30 kJ and quasi-stationary high-current plasma accelerator (QHPA) such as P-50M), capable to generate compression plasma flows (CPFs) [1-4]. Such accelerators are placed in the vacuum chambers as their operations demand working gases to be fed into the discharge devices. Besides, for the first time we have received compression erosive plasma flows, generated by specially designed erosive plasmadynamic systems operating in the air at atmospheric pressure [5]. Only a material of an inner electrode determines the composition of compression erosive plasma flows.

In the present paper, the results of spectroscopic investigations of both the gas-discharge MPC of compact geometry, and the erosive plasmadynamic systems are presented. These investigations made it possible to calculate dynamic coefficients suggested in [4-5] that show a degree of "stationarity" of the basic thermodynamic parameters of compression flows in studied plasmas accelerators.

2. EXPERIMENTAL SETUP

The gas-discharge compression plasma flows were obtained using a MPC of compact geometry powered with a capacitive storage (C_0 = 1200 μF) operating at initial voltages, U_0, from 3 up to 5 kV [6-9]. The MPC discharge device (Fig. 1) with an outer electrode 5 cm in diameter and 12 cm in length is mounted in a vacuum chamber measuring 30 x 30 x 150 cm. The discharge device of MPC-CG employing hydrogen as plasma-forming substance operates with pulse system of gas feed.

The discharge duration in the MPC is up to 100 μs and the peak value of discharge current, depending on initial parameters of discharges, ranges from 70 to 120 kA (Fig. 2).

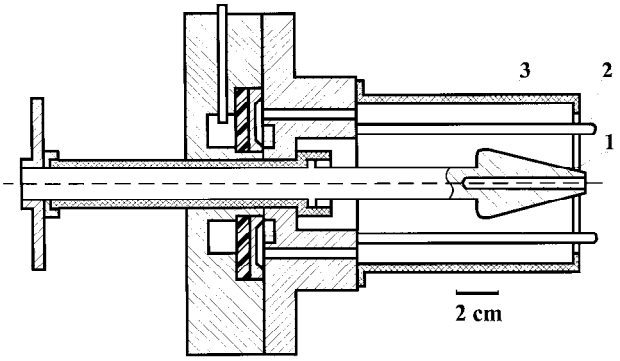

Fig. 1. Scheme of MPC discharge device: 1 - cathode, 2 - anode rods, 3 - cover.

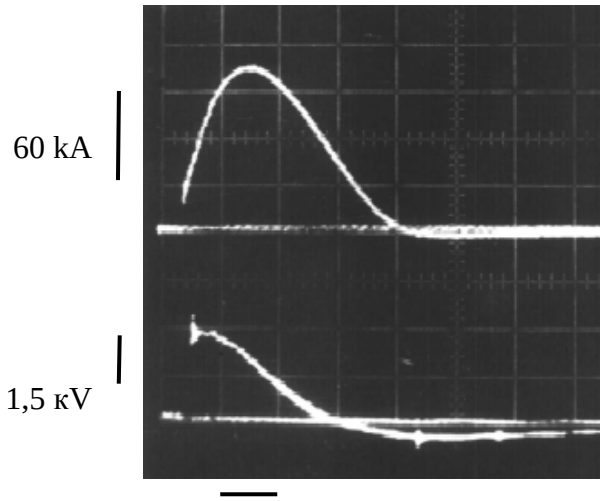

Fig. 2. Oscillogram of the discharge current and voltage in MPC-CG. Bar size is 25 μs.

Under these conditions, a CPF 6-10 cm long and 0.7-1 cm in diameter forms at the outlet of the MPC discharge device (Fig. 3). The CPF retains stability for about 80 μs; thereafter it starts diverging in a half-angle of 5 to 15°. The plasma velocity in compression flow varies in the range of $(4–8)\cdot10^6$ cm/s, depending on the MPC initial parameters.

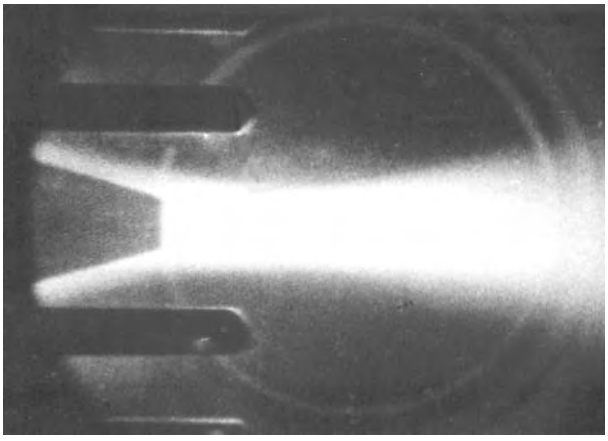

Fig. 3. Photograph of CPF: exposure time 2 μs.

The schematic of the discharge device of the erosive system intended to generate CPFs in ambient air is shown in Fig. 4 [5]. The outer electrode of the discharge device is sectionalized (made of a set of rods). The energy storage (W_0 ~ 15 kJ, C_0 = 1500 μF) is sectionalized as well, each section of the capacitor bank being connected to an inner electrode and to one of rods (sections) of an outer electrode. Thus, the whole battery is involved in the formation of the plasma flow from the inner electrode, whereas only one section of the battery is involved in the formation of a plasma jet from each of the rods of the outer electrode. Such a discharge system generates four current-carrying plasma jets (1 per each of 4 rods comprising the outer electrode), and the stable main compression erosive plasma stream from the inner electrode (Fig. 5).

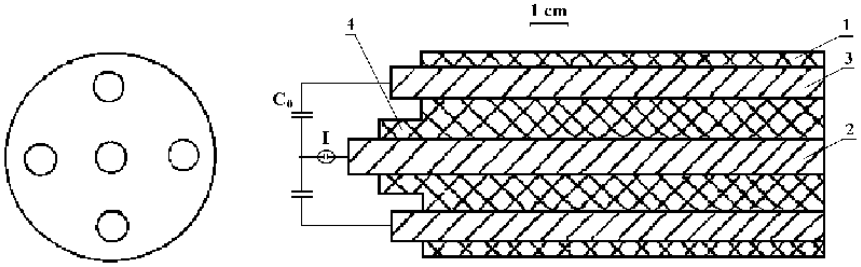

Fig. 4. Diagram of the discharge device of the erosive system: 1 - insulator-body, 2 - inner electrode, 3 - roads of outer electrode; I - ignitron, C_0 - energy storage.

The main compression plasma stream and the outer plasma jets are compressed due to the interaction of their currents with azimuth self-magnetic field. Since currents in the compression stream and in the outer jets flow in the opposite directions, the electrodynamic interaction between them causes these jets to repulse from a compression stream due to which the erosion products of the outer electrode do not get in the main stream. In addition, by the same reason the resulting magnetic field maximum of currents of the plasmadynamic system should be located in an area between the compression stream and the outer plasma jets, which not only influences positively the flow macro stability, but also results in the effect of magnetic self-isolation of a separating dielectric of the discharge system.

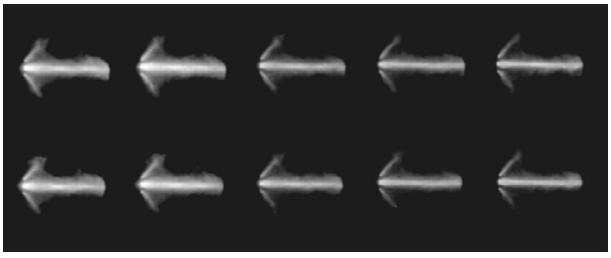

Fig. 5. Photograph of compression erosive plasma flow.

Formation of the erosive compression plasma stream comes to an end ~ 25 μs from the beginning of the discharge current. From this time, the compression stream of 1-2 cm in diameter and ~ 15 cm long becomes macro stabile, and a material of the inner electrode governs its composition, as spectroscopic studies show. High stability of the erosive plasma stream along with its small divergence, as well as rather great the flow length/diameter ratio indicate the compressive character of the plasma flux. Shown in Fig. 6 are typical oscilloscope traces of the discharge current and voltage in the erosive system.

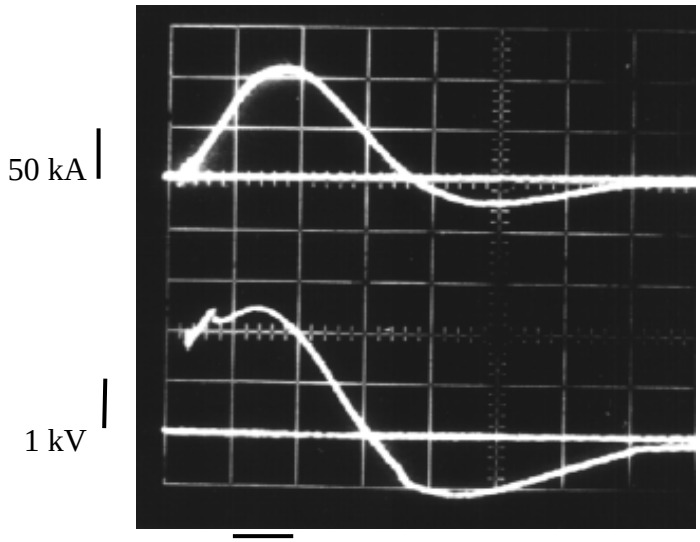

Fig. 6. Oscillogram of the discharge current and voltage in the erosive system at U_0 = 5 kV. Bar size is 25 μs.

3. STUDIES OF GAS-DISCHARGE MPC

Spectroscopic studies of the compression plasma flow in MPC of compact geometry were carried out with the use of a spectrograph ISP-30 combined with spectrochronograph SP-452. The image of the cross section of a compression flow 3 cm apart from an edge of the inner electrode was projected at the spectrograph slit. The plasma emission spectra in 300-700 nm wavelength ranges show continuous radiation, lines of atomic hydrogen and the most intense (resonant) lines of atoms of elements comprising a material of electrodes. When decreasing a mass flow of working gas, the line intensities of the electrodes material, as well as the number of lines is increasing.

The electron concentration N_e in the compression plasma flow was determined via the line H_β broadening caused by the linear Stark effect. The N_e definition relative error in the method under experimental conditions achieves 30%

due to the presence of continuous radiation. The temporal dependence of electron concentration in the CPF is shown in Fig. 7. It should be noted that the N_e values shown in Fig. 7 are averaged along the line of sight, as well as over the exposure time, defined by the spectrochronograph shutter (~ 10 μs).

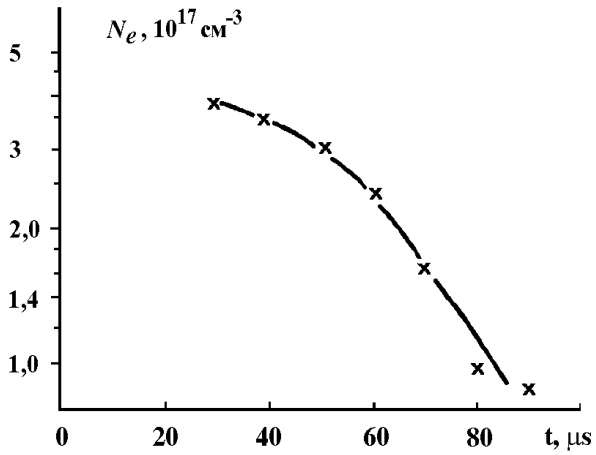

Fig. 7. Temporal dependence of electron concentration in the CPF of MPC.

Electron temperature T_e in the plasma flow was determined from the relative intensities of H_β and H_γ lines only for a time interval from 35 to 40 μs. At the 10 g/sec mass flow rate of hydrogen and the peak discharge current of 80 κA, the electron temperature in a compression flow 3 cm apart from an edge of the cathode makes $(25\text{-}30)\cdot 10^3$ K.

4. THE STUDIES OF EROSIVE PLASMADYNAMIC SYSTEM

Spectroscopic examinations of compression erosive plasma flows were carried out with the aid of a VFU-1 high-speed camera operating in a mode of a cinespectrograph due to a spectral attachment based on a diffraction grating. Frames of emission spectrum of erosive plasma flows are shown in Fig 8a.

The electron concentration in the plasma flow was determined by method based on broadening of spectral lines of the copper caused by quadratic Stark effect. Chosen for this purpose was the autoionisation copper line Cu I with λ = 458,7 nanometers since it has a high value of lower level, and its self-absorption is low. Lines selected for processing featured clearly observable asymmetrical contours which can only be attributed to Stark broadening alone (neither Doppler, nor natural broadening result in contour asymmetry). Doppler broadening of CuI line (458,7) at $T = 15\cdot 10^3$ K was as small as 0,05 A^0, while the instrumental one - 1 A^0 (the value of instrumental broadening was accepted equal to the half-width of the narrowest line in a stepwise spectrum of iron), so they were taken into consideration by a simple

subtraction of their values from a half-width of a line specified. Due to the presence of continuum and a considerable value of the natural broadening of the autoionization Cu line caused by the spreading of the autoionization level, the relative error in definition of the electron concentration is great enough and makes ~ 50 %. The temporal dependence of electron concentration N_e of a compression erosive plasma flow in a cross-section ~9 cm apart from the edge of the discharge device is shown in Fig. 8b.

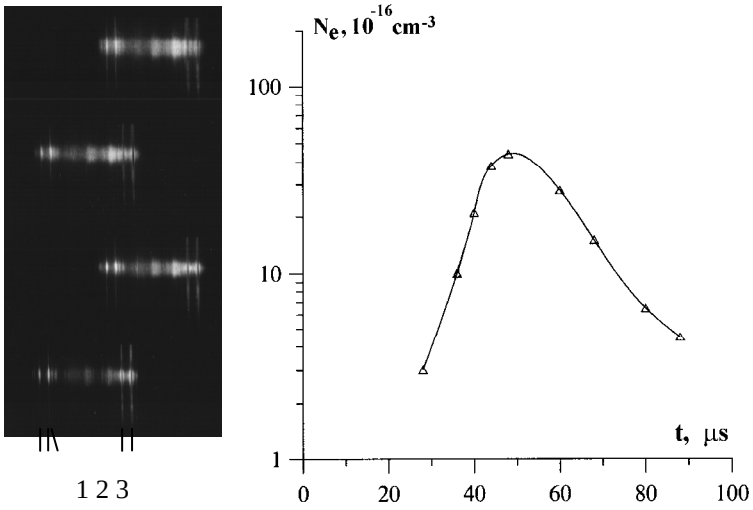

Fig. 8. Frames of emission spectrum of erosive plasma flows (left): 1 - line Cu II 456 nm, 2 - line Cu I 459 nm, 3 - line Cu I 465 nm, 4 - line Cu I 515 nm, 5 - line Cu I 522 nm. Temporal dependence of electron concentration (right).

Spectroscopic investigations have shown that the compression erosive plasma flow demonstrates large opacities. Under these conditions, a reliable method of determination of plasma temperature is the method of photoelectric recording of radiation [5]. Using this method it was possible to determine the spectral density of energy emission (SDEE) of radiation b_λ of a compression flow and its spectral absorption constants α_λ.

Knowing b_λ and α_λ, from Kirchhoff law and Plank formulas for a black body one may to find the true plasma temperature:

$$T = \frac{hc}{\lambda k \cdot ln(\frac{2hc^2\alpha_\lambda}{\lambda^5 b_\lambda})}.$$

Experiments on recording plasma radiation of a compression erosive flow and definition of its spectral absorption constants were carried out as shows a drawing in fig. 9. Radiation was recorded by calibrated photodiodes FD-5G combined with sets

of optical filters, which were cutting out spectral ranges of 465 - 555 and 745 - 1120 nm.

The self-exposure to radiation of plasma was provided with the flat mirror 4 mounted behind a beam-splitting plate 3. Plasma radiation of a compression flow was selected with two rectangular diaphragms the size 1×10 cm, inserted in each measuring channel. One of photodiodes (7) recorded a radiation flow (Φ_s) of explored source, whereas the second one (8) – a radiation of the source plus the radiation that was reflected from a mirror and passed through plasma (total flow Φ_Σ). Photodiodes were placed at equal distances (~ 1,5 m) from the emitting source. Such an arrangement of photodiodes, taking into account linear dimensions of the source, made it possible to consider it point source.

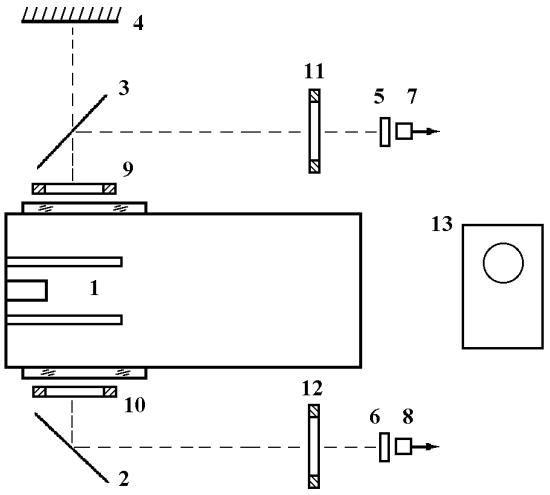

Fig. 9. Block diagram of experiments on recording plasma radiation: 1 - discharge device; 2,3 - beam-splitting plate; 4 - flat mirror; 5,6 - optical filters; 7,8 - photodiode; 9-12 - diaphragm; 13 - oscillograph.

In experiment conditions, radiation flow through plasma is:

$$\Phi_{trans} = I_s \Omega_{reff} (1-\rho_3)^2 \rho_4 (1-\alpha_\lambda) = \Phi_s \frac{\Omega_{ref}}{\Omega_s} (1-\rho_3)^2 \rho_4 (1-\alpha_\lambda),$$

where I_s - radiant intensity of the source; α_λ - a spectral absorption constant of plasma; Ω_{ref} - a spatial angle in which the photodiode 8 records the emission reflected from the mirror 4; Ω_s - a spatial angle in which the photodiode 7 records the emission of the source; ρ_3 - reflectivity of a beam-splitting plate 3, and ρ_4 - reflectivity of the mirror 4.

Let's write down the expression for the total emission flow recorded by the photodiode 8:

$$\Phi_{\Sigma} = \Phi_s + \Phi_{trans} = \Phi_s[1 + \frac{\Omega_{ref}}{\Omega_s}(1-\rho_3)^2 \rho_4 (1-\alpha_\lambda)],$$

from which it is easy to find α_λ:

$$\alpha_\lambda = 1 - \frac{\Omega_{reff}}{\Omega_s}(\frac{\Phi_{\Sigma}}{\Phi_s} - 1)\frac{1}{(1-\rho_3)^2 \rho_4}.$$

Shown in Fig. 10 are the time variations of spectral absorption constants α_λ, for spectral intervals of 465-555 and 745-1120 nm.

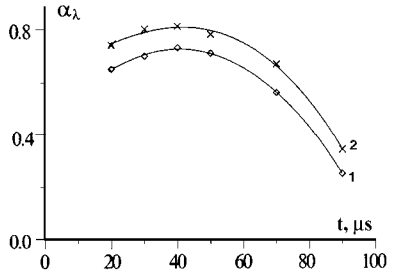

Fig. 10. Time variations of spectral absorption constants α_λ, at U_0 = 5 kV for spectral intervals: 1) 465-555 nm; 2) 745-1120 nm

As already noted, to calculate plasma temperature it is necessary to know also spectral density of energy emission b_λ of a compression flow. It can be calculated, if one knows spectral density of radiant energy E_λ of a plasma flow which is determined by integration on time of a signal from the photodiode recording radiant power P_λ.. For this purpose, the mirror in Fig. 9 was removed, and in front of photodiodes, the optical filters that were cutting out different spectral ranges were placed.

Values of plasma temperature in both of these spectral intervals within the limits of experimental error were identical, which proves the reliability of results obtained. Time dependence of plasma temperature of a compression erosive flow is shown in Fig. 11.

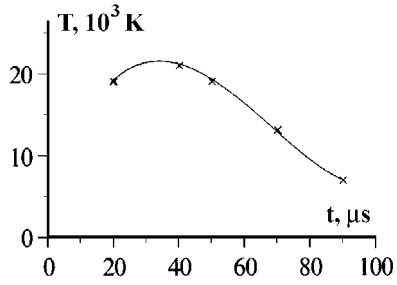

Fig. 11. Time dependence of plasma temperature of a compression erosive flow at U_0 = 5 kV.

5. DISCUSSION

To gain an idea of how the behaviour of the basic thermodynamic parameters, N_e and T_{pl}, corresponds with a discharge current (i.e. to estimate a degree of "stationarities" of these parameters), let us calculate for them the dynamic coefficients $\eta(t)$, suggested in [4,5]. For the electron concentration of $\eta_N(t) = N_e(t)/I_d(t)$, and for temperature – $\eta_T(t) = T_{n\lambda}(t) / I_d(t)$.

Calculated data $\eta_N(t)$ for a compression flow generated by discharge MPC-CG, are shown in Fig. 12. As may be seen, $\eta_N(t)$ at a steady-state stage of a compression flow (from ~ 30 μs) is essentially invariable. This means that the electron concentration tracks a discharge current, i.e. the compression plasma flow is quasi-stationary.

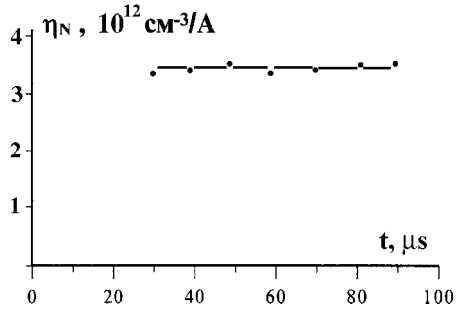

Fig. 12. η for compression plasma flow of MPC-CG.

Results of calculations $\eta(t)$ for erosive plasmadynamic system are shown in Fig. 13. One can see that for the most part of a quasi-stationary stage of discharge $\eta_N(t)$ and $\eta_T(t)$ are practically constant, i.e. N_e and T_{pl} for this time interval "follow" a discharge current. At the beginning of discharge $\eta_N(t)$ decreases, i.e. N_e rises more slowly, than I_d, which may be associated with a delay in ejecting the working substance (erosion of electrodes) relative to a discharge current.

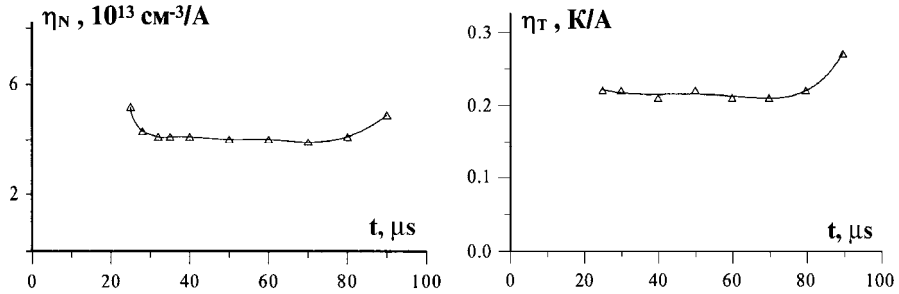

Fig. 13. η for erosive plasmadynamic system: η_N (left); η_T (right).

Comparatively small increase in both η_N *(t)* and η_T *(t)* at the end of the discharge which implies that velocity and temperature of plasma at this time decay more slowly than a discharge current, may be explained by certain inertia of process of a plasma flow collapse (relative to a discharge current).
Thus, as the studies show, a compression plasma flow at a stage of the steady existence is quasi-stationary (i.e. its key parameters "follow" a discharge current) both in the gas-discharge MPC-CG and in erosive plasmadynamic system.

REFERENCES

1. V.M. Astashinskii and E.A. Kostyukevich, Sov. J. Plasma Phys. (*Engl. transl.*), **7,** 282 (1981)
2. V.M. Astashinskii, G.I. Bakanovich, and L.Ya. Min'ko, Sov. J. Plasma Phys. (*Engl. transl*.), **10,** 609 (1984)
3. V.M. Astashinskii, A.A. Man'kovskii, L.Ya. Min'ko et al., Sov. J. Plasma Phys. *(Engl. transl.),* **18,** 47 (1992)
4. S.I. Ananin, V.M. Astashinskii, E.A. Kostyukevich, et al., Plasma Physics Reports, **24,** 936 (1998)
5. V.M. Astashinskii, Journal of Applied Spectroscopy, **67**, 312-319 (2000)
6. V.M. Astashinsky, E.A.Kostyukevich, A.M. Kuz'mitsky and L.Ya. Min'ko, SPIE Proceedings, **1121**, 650 (1990)
7. V.M. Astashinskii, G.I. Bakanovich, A.M. Kuz'mitskii et al., Journal of Engineering Physics and Thermophysics, **62,** 281 (1992)
8. I.P. Dojčinović, M.P. Gemišić, B.M. Obradović M.M. Kuraica, V.M. Astashinskii, J. Puric., Journal of Applied Spectroscopy, **68**, 824 (2001)
9. J. Purić, I.P. Dojčinović, V.M. Astashynski, M.M. Kuraica and B.M. Obradović, Plasma Sources Science and Technology, **13,** 74 (2004)

VI Serbian-Belarusian Symp. on Phys. and Diagn. of Lab. &
Astrophys. Plasma, Belgrade, Serbia, 22 - 25 August 2006
eds. M. Ćuk, M.S. Dimitrijević, J. Purić, N. Milovanović
Publ. Astron. Obs. Belgrade No. 82 (2007), 35 *Invited lecture*

SELECTION OF SOLID PROPELLANT FOR LASER PLASMA ENGINE

N. A. Bosak[1], A. N. Chumakov[1], Yu. A. Stankevich[2]

[1]*Institute of Molecular and Atomic Physics of National Academy of Sciences of Belarus*
220072, Minsk, Belarus, e-mail: bosak@imaph.bas-net.by
[2]*Heat and Mass Transfer Institute of National Academy of Sciences of Belarus*

Abstract. Possibility of jet thrust creation at laser action on absorbing condensed mediums was revealed many years ago (G.A. Askaryan, 1962, A. Kantrowitz, 1972). But only now the idea of laser propulsion has chance of using for control of micro- and nano-satellites movement. Such satellite needs obtaining the strictly verified impulses for its orbits correction. One of the promising directions of solving this problem is creation of laser-plasma engine of ablative type with solid-state working substance (solid propellant). The important characteristic of laser engine is its working resource which depends on used solid propellant. This report is devoted to optimal selection of solid propellant based on experimental determination of specific mass-removal of various materials irradiated by pulsed laser in vacuum.

Dependences of specific mass removal on laser radiation power density were studied by experimental and numerical methods. The experimental results were obtained for number of metals (Al, Bi, brass), for graphite and composites (glass fibre and carbon fibre plastics, sol-gel glass SiO_2 containing 40 % of graphite particles) irradiated in vacuum (P_0 = $2 \cdot 10^{-2}$ mm Hg) by Nd:YAG laser (1064 nm wavelength, ~20 ns and ~200 μs pulse duration, irradiance in the range of $1 - 2 \cdot 10^4$ MW/cm^2). The simulation results, which were obtained for Al and graphite samples, are compared to the experimental ones, for the range of power density $30 - 10^4$ MW/cm^2. It was found out that experimental dependences of specific mass removal on laser radiation power density are characterized by areas with dominance evaporative or explosive mechanism of target destruction. Obtained results showed mainly evaporative regime of graphite and brass destruction for laser irradiances 30-600 MW/cm^2 that comes with specific mass removal ensuring necessary resource for created laser plasma microengine.

VI Serbian-Belarusian Symp. on Phys. and Diagn. of Lab. &
Astrophys. Plasma, Belgrade, Serbia, 22 - 25 August 2006
eds. M. Ćuk, M.S. Dimitrijević, J. Purić, N. Milovanović
Publ. Astron. Obs. Belgrade No. 82 (2007), 37-43 *Invited lecture*

SPACE-TIME-RESOLVED OPTICAL EMISSION SPECTROSCOPY OF LASER ABLATION PLASMA FOR MICROANALYSIS OF UNIQUE SOLID SAMPLES

V. Burakov[1], E. Dovnar-Zapolskaya[2], V. Kiris[1],
E. Klyachkovskaya[1], N. Kozhukh[3], S. Raikov[1]

[1]*Institute of Molecular and Atomic Physics, 220072 Minsk, Belarus*
[2]*Institute of Arts, Ethnography and Folklore, 220072 Minsk, Belarus*
[3]*National Art Museum of Republic of Belarus, 220030 Minsk, Belarus*

Abstract. Space-, time- and spectrally resolved optical diagnostics of laser ablation plasma has provided the opportunity to realize absolute (calibration-free) analyses of solid or powder materials. This variant of optical emission spectroscopy of pulsed plasma allows the matrix effects to be overcome, yielding precise and accurate quantitative results on elemental composition of materials without use of calibration curves, certified reference materials, and internal standards. Such analysis is very close to the nondestructive mode with minimum possible ablated mass that is very important in many applications especially for unique museum exhibits and jeweler samples.

1. INTRODUCTION

Laser ablation (LA) of solid samples is a well-established analytical technique, which combines sampling and atomization in one step. Therefore, direct and express spectrochemical analysis without any sample preparation is possible. During the last decade, the necessity of applications of the LA optical emission spectroscopy technique to the "truly real life" problems (industrial, environmental, medical, archaeological, art, etc.) has extremely increased in number and in variety. Recently any variant of spectrochemical analysis of solid materials required obligatory calibration of a spectrometer with the help of the certificated reference materials (CRM). The nomenclature of solid CRM is limited mainly by the most widely used metals and alloys, some samples of ceramic materials, glasses etc. This circumstance is the main limitation of wide introduction of direct analysis of solid materials, for example laser-induced breakdown spectroscopy (LIBS) and LA-ICP, in routine practice. Moreover, even the small differences in matrixes and surface properties of analyzed materials as compared with the reference samples as well as

the possible variations in ablation laser energy must be thoroughly taken into account. Therefore, during the last decade different approaches have been undertaken to overcome or at least to discriminate the above mentioned problems in the most widely spread LA based analytical technique, namely LIBS. The realization of the main goal of the last time attempts to make LIBS really quantitative is based on the development of calibration-free algorithm of LIBS, which is in turn based on the perfection of optical diagnostics of pulsed plasma. In general, last achievements in instrumentation and data processing in optical emission spectroscopy of pulsed ablation plasma allows the matrix effects to be overcome, yielding precise and accurate quantitative results on elemental composition of materials without use of calibration curves, CRM, and internal standards [1-6]. LA is at present the only source of atomic spectra that allows realizing by detailed optical diagnostics of plasma the unique possibility of absolute (calibration-free) elemental analysis of solid materials. Starting from 1999 the really calibration-free technique is now developing in instrumentation and algorithms by research teams from Italy and Belarus and last time from Australia and USA, and is utilizing mainly for analyses of as much as possible variety of solid metallic and dielectric materials to optimize the analytical procedures and to examine once again the proposed technique.

In this work further development of calibration-free LIBS and its approbation for microanalyses of a material of unique solid samples on an example of determination of component concentrations of the bronze and gold alloys, flint glasses, fragments of jeweller ornaments of an archaeological origin, and pigments from easel paintings have been carried out.

2. THEORETICAL BACKGROUND

In general, with the LTE assumption, after determination of the plasma temperature (possible by different ways), the concentration of species of one of the element of interest in plasma can be obtained from the measurement of just one experimental emission line. When the concentration of atomic species of a given element is known, it is possible to determine the concentrations of the other ionization stages by making use the Saha-Boltzmann equation. Such procedure is commonly employed in plasma spectroscopy.

The basic assumptions concerning the state of the laser ablation plasma are as follows. (i) The plasma composition is representative of the actual target material composition prior to the ablation (stoichiometric ablation). This assumption is fulfilled in laser ablation conditions typical for the spectrochemical analysis, when the power density on the target exceeds 1 GW/cm^2. (ii) In the actual temporal and spatial observation window the plasma is locally in thermodynamic equilibrium. Theoretically, thermal plasmas at electron number densities higher than 10^{23} m^{-3} are considered to be in LTE. (iii) For the optical emission spectrometry the plasma is optically thin (no self-absorption). This assumption is usually well verified for non-resonant lines emitted in comparatively small plasma volume. Although the self-

absorption can be modeled and compensated, the safest approach in these cases is just to ignore the self-absorbed lines for the purpose of rapid quantitative analysis.

According to the classical equation for intensity of a spectral line, we have the following relation:

$$\bar{I}_j^{ki}/(A_{ki}g_k/U_j^a)=(FC_j)\exp(-E_k/T), \quad (1)$$

where $\bar{I}_j^{ki}$ is the line integral intensity corresponding to the transition between two levels k and i for the j element; A_{ki} is the transition probability; g_k and E_k are the k level degeneracy and energy; U_j^a is the partition function of the j atom; F is an experimental parameter that takes into account the optical efficiency of the collection system as well as some plasma parameters; C_j is the concentration of the emitting atomic species; T is the plasma temperature. With the help of the relation (1) first of all the value FC_j is determined for the atomic species of each element present in the sample taking into account LTE in the analytical volume of a plasma. Temperature is measured as a rule by conventional method from Boltzmann plots. On received values FC_j their sum is calculated with the account of ionic component in relation to which concentration of each of elements in an analyzed sample is determined:

$$\sum_j \{FC_j+b(U_j^i/U_j^a)\exp[-(V_j-\Delta V_j)/T](FC_j)\}=FM, \quad (2)$$

where $b=6.06\cdot10^{21}T^{3/2}/N_e$; T (eV), N_e (cm^{-3}) is the electron concentration; U_j^i is the partition function of the j ion; V_j and ΔV_j are the ionization potential and its decrease in plasma; M is the total concentration of atomic and ionic components in plasma. Electron concentration is usually measured with the help of Saha equation. For the j element (j=1) we can write:

$$\{FC_1+b(U_1^i/U_1^a)\exp[-(V_1-\Delta V_1)/T](FC_1)\}/FM=C_1^a+C_1^i. \quad (3)$$

The total concentration of atomic and ionic components is:

$$\sum_j (C_j^a+C_j^i)=1-\varepsilon, \quad (4)$$

where ε is the total concentration of all elements in the sample which are not detected experimentally by the spectrometer used (as a rule trace and microelements with concentrations below the detection limit).

3. EXPERIMENTAL

The LIBS instrumentation employed in our work is at present quite standard and maximum suitable for routine practice and relies on the use of multichannel detection for recording the space-, time-, and spectrally resolved emission, produced by focusing laser pulse on the surface of a sample under analysis (Fig. 1).

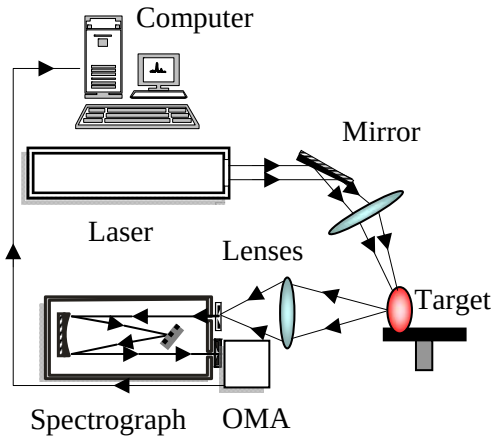

Fig. 1. Experimental set-up for LIBS.

The fundamental (1.06 μm) or the second harmonic (0.53 μm) of a nanosecond Q-switched Nd:YAG laser (LOTIS) with a pulse duration of 5-6 ns is employed in the LIBS measurements. The laser beam is focused on the sample surface by means of a 50 mm focal length plano-convex quartz lens, and a single- or multipulse measurements are performed. A sample-holding positioner can be used to maintain the ablation plume with controllable distance of the probing zone from the target surface and to preselect the irradiated surface zone. Laser pulse energy values range from 5 to 300 mJ with a spot diameter on the sample of approximately 30–100 μm. The light emitted from the plasma plume is collected with a plano-convex quartz lens with a 63 mm focal length into the compact spectrograph (SOLAR) equipped with appropriate diffraction gratings for high and medium spectral resolution measurements at a narrow or wide spectral range, respectively. The maximum spectral resolution, about 1 pm, can be obtained if necessary with the help of the echelle grating with double dispersion. The spectrum is recorded with the help of an optical multichannel analyzer (ORMINS) with a linear CCD detector (TOSHIBA).

4. RESULTS AND DISCUSSION

Detailed structural characterization and identification of key chemical constituents can uncover important information on historical and artistic significance of artworks. A major concern when an analysis is to be performed on valuable objects, such as museum exhibits is the preservation of its integrity and aesthetic value.

In general, the LA process can be divided schematically into two main stages: (i) evaporation of the solid target and formation of the laser plasma; (ii)

expansion of the ablated material into a background gas. Depending on the laser characteristics, LA of solids involves processes of heating, melting, vaporization, ejection of atoms, ions, molecules, clusters and larger solid and liquid particles, shock waves, plasma initiation and plasma expansion, ablation plume expansion in the afterglow.

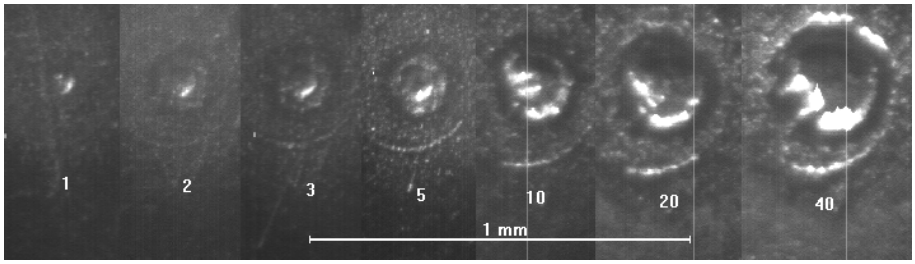

Fig. 2. Typical craters formed on a surface of a bronze sample at various number of laser shots.

Laser-induced plasma characterization will be very helpful for determining the optimal conditions of LIBS, and intensive experimental diagnostics must be in progress to get a more accurate knowledge of all the physical and chemical processes involved in the phenomenon. In this context some preliminary experiments have been carried out with the aim of optimization of laser ablation procedure. They mainly include bidimensial imaging with the help of the CCD matrix of the geometrical shape and size of: (i) the crater formed in the target material (Fig. 2) and (ii) the radiating ablation plume (Fig. 3).

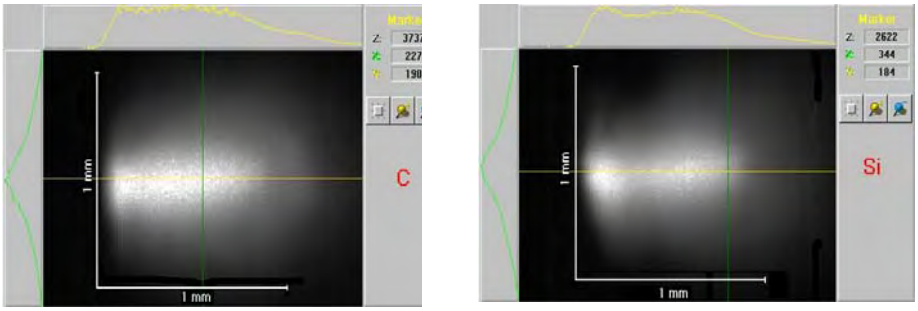

Fig. 3. Typical images of laser ablation plume near a carbon and silicon targets.

LIBS analysis is very close to the nondestructive mode with minimum possible ablated mass that is very important in many applications especially for unique museum exhibits and jeweler samples. Material consumption in a typical

single pulse experiment is minimal (estimated around 10^{-8} -10^{-7} g for a typical crater formed). Thus, LIBS can be regarded as a nearly nondestructive technique. The spatial resolution achieved by LIBS across a surface is nearly microscopic. In addition, the technique has the capability of providing depth-profiling information.

One of the demonstrations of opportunities of the calibration-free variant of the LIBS technique has been experimentally realized for the analysis of a material of gold alloys to determine a caratage of tested samples (see the Table 1 below). Rather good conformity of the results of the calibration-free measurements of concentrations of gold in the analyzed materials to the certified data has been demonstrated. The maximum deviation is about 4% that is conventional for the analysis with the help of LA. The similar results have been also obtained for the bronze, brass and glass samples.

Table 1.

Sample	Caratage of Gold Alloys	
	Measured data	Reference data
1	359	375
2	581	583
3	588	585
4	797	831
5	903	899
6	916	900
7	990	998
8	1000	1000

Table 2.

Calibration-Free Analyses of Bracelets	
Matrix:	
$[PbO/SiO_2/CaO]+[Al_2O_3/Mn_2O_3/MgO/Na_2O/K_2O]$	
Major components:	
Sample I	Sample II
PbO – 43 %	PbO – 53 %
SiO_2 – 39 %	SiO_2 – 25 %
CaO – 11 %	CaO – 11 %
Minor components:	
I	II
Cu_2O – 1.5 %	CuO – 2 %
Mn_2O_3 – 3.0 %	Mn_2O_3 – 1.5 %

As the typical archaeological objects for the calibration-free LIBS research, fragments of bracelets (presumably with a glass basis) from the National Museum of the History and Culture of Belarus have been chosen (see the Table 2 below). These samples were found in the compact places at excavations of: (i) the Minsk Fortress and (ii) the Polotsk Fortress. Polotsk is the oldest known town in territory of Belarus. The time period of the archeological layers, in which the given fragments of bracelets were found, is dated by the 11-13th centuries. Chemical composition of the glass matrixes and the components responsible for specific coloring of samples were determined taking into account recorded emission spectra and the data obtained by several researchers mainly with the help of conventional chemical analyses for the similar glass samples found in different regions of the world.

Besides, the calibration-free LIBS technique has been applied for the microanalysis of pigment materials from the different sections of the well-known easel paintings “Landscape of Pool with an Obelisk and Ruins of an Aqueduct” and “Garden of Borghese Villa in Rome” of the famous French artist Hubert Robert (1733-1808). These old paintings from the National Art Museum of Republic of Belarus require thorough investigations of the pigments for confirmation of their originality taking into account the rich biography of the paintings. Obtained quantitative data on elemental composition of the selected pigment microsamples from all paint layers including the ground layer alongside with art and historical examinations have formed the base for the exact identification of the originality of the tested paintings.

ACKNOWLEDGEMENTS

The authors appreciate the support provided by the Ministry of Culture of Republic of Belarus, Management of the State Research Program “Photonics” and Belarusian Republic Foundation for Fundamental Research which enabled this work to be undertaken. The authors are grateful to Professor N. Konjević for helpful discussions.

REFERENCES

1. A. Ciucci, M. Corsi, V. Palleschi, S. Rastelli, A. Salvetti, E. Tognoni. Appl. Spectrosc., **53**, 960-964 (1999)
2. M. Corsi, V. Palleschi, A. Salvetti, E. Tognoni. Res. Adv. in Appl. Spectrosc., **1**, 41-47 (2000)
3. M. Corsi, G. Cristoforetti, V. Palleschi, A. Salvetti, E. Tognoni. Eur. Phys. J., **D13**, 373-377 (2001)
4. V.S. Burakov, V.V. Kiris, P.A. Naumenkov, S.N. Raikov. J. of Appl. Spectrosc., **71**, 676-682 (2004)
5. M.V. Belkov, V.S. Burakov, V.V. Kiris, N.M. Kozhukh, S.N. Raikov. J. of Appl. Spectrosc., **72**, 352-357 (2005)
6. P. Yaroshchyk, D. Body, R.J.S. Morrison, B.L. Chadwick. Spectrochim. Acta, **B61**, 200–209 (2006)

VI Serbian-Belarusian Symp. on Phys. and Diagn. of Lab. &
Astrophys. Plasma, Belgrade, Serbia, 22 - 25 August 2006
eds. M. Ćuk, M.S. Dimitrijević, J. Purić, N. Milovanović
Publ. Astron. Obs. Belgrade No. 82 (2007), 45-55 *Invited lecture*

THE LASER METHOD OF METAL NANOPARTICLE FORMATION WITH THE HELP OF SPATIAL SEPARATION

A. M. Chaplanov[1], V. K. Goncharov[2], K. V. Kozadaev[2],
M. I. Markevich[1], M. V. Puzyrou[2]

[1] *Institute of Electronics BAS, 22 Logoiskii trakt; 220090, Minsk, Belarus,*
e-mail: markevich@inel.bas-nen.by
[2]*A.N.Sevchenko Scientific-Research Institute of Applied Physical Problems*
of Belarussian State University, 7 Kurchatov Str., 220064, Minsk, Belarus,
e-mail: kozadaeff@mail.ru

Abstract. The water nickel nanoparticle suspension was formed by the method of laser erosion using the spatial separation. Nickel nanoparticles diameter and their concentration in water medium were measured with an employment of the laser probing method. The analysis of obtained nanosize particles suspension was carried out by the atomic-power spectroscopy and electron spectroscopy.

1. INTRODUCTION

The nanotechnologies have a wide distribution at the present time. These technologies deal with formation and implementation of the matter particles with nanometer sizes [1]. The physical and chemical matter properties at that range of sizes differ both from single atoms, ions and from massive solids. This fact allows to weaken or to strengthen the known metal properties and to create absolutely new metal or contain-metal materials with unusual and inaccessible before properties. The application of nanoparticles is of great interest of such spheres as medicine, electronics, chemical industry, optics etc.

At the present work, the new method of water nanoparticle suspensions formation is offered. The formation method is based on the penetration of the metallic target erosion products in water medium during the laser action on metallic target.

2. METHODS OF THE METAL NANOPARTICLE SUSPENSION GETTING

Nowadays several methods of nanoparticle suspensions formation are known: electrical discharge in liquids and laser erosion in liquids.

The metal electrodes (Ni, W, steel) placed in liquid medium (water, ethanol) are used for the metal nanoparticle suspension production by the electrical discharge method. The electrodes destroy and great amount of micro- and nanoparticles form during the electric discharge (ark [2] or spark [3]). They consist of every possible sorts and kinds of chemical compounds of electrode and liquid medium materials. The applying of spark discharge [3] provides more effective electrode material entry to discharge zone in compare with ark discharge. The employment of alternating current discharge is governed by the necessity to have uniform erosion of both electrodes. The WC nanoparticles with the diameter from 2.5 to 35 nm were obtained [3]. The possibility of metal (Ag, Au, Ti, Cu and their alloys) nanoparticle production by the laser erosion is under recognition at the work [4]. It was showed that during laser erosion of metal target placed in liquid medium the significant quantity of nanosize objects (with dimensions of 10-100 nm) is formed. The second harmonic of Nd:YAG laser (λ=532 nm) or irradiation of copper vapor laser (λ=510nm) were applied for the laser acting.

Both of these methods possess significant disadvantage: the chemical purity of obtained suspensions seems to be very questionable. The chemical composition of given nanosize objects includes all chemical spectrum (and every possible sorts and kinds of their combinations) both the target (electrode) material and liquid medium substance as the processes of particle formation pass in liquid medium

3. THE SPATIAL AND TIME DISTRIBUTIONS OF THE DROP-LIQUID PHASE OF METAL EROSION LASER JET (WHEN ACTING WITH RECTILINEAR QUASI-STATIONARY LASER PULSE)

The erosion laser jet forms by the action of the moderate laser irradiation intensity (10^5 -10^6 W/cm^2) on the metallic target surface. It consists of a vapor, plasma and drop-liquid phase particles. The particles move to laser jet formed by two mechanisms: the bulk vapor [5,6] (small particles (10-100 nm)) at the beginning of laser action and hydrodynamic mechanism [7,8] (1-100 μm) to the end of the laser action. A highly disperse liquid-drop phase with a plasma moves perpendicularly to the surface target when the depth of crater less than its diameter. More large particles move in the form of cone under small angle to the target surface over border effects on a crater, forming so-called dynamic crown. Since the highlight with laser or plasma irradiation is absent at that moment, the particles are invisible to experimenters. To investigate the dynamic of those particles it's advisable to use the irradiation of subsidiary laser. That probing irradiation must satisfy the next basic requirements: the irradiation wavelength must correspond to

the spectral sensitivity of recording equipment and duration of the laser pulse must be significantly less than duration of the typical dynamic processes in erosion laser jet (10^{-6} s).

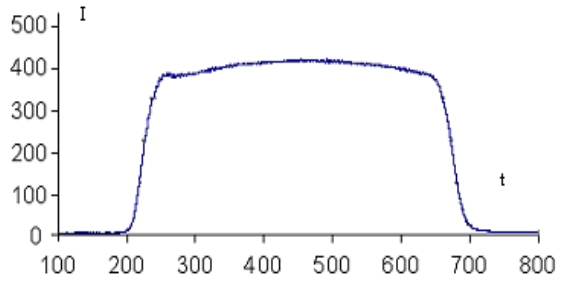

Fig. 1. The time shape of rectilinear quasi-stationary laser pulse.

At present work, the erosion laser jets are investigated. They was obtained during the action of rectilinear laser irradiation pulse (of Nd: glass laser) on surface of metal target made from aluminum alloy D16T. The pulse had duration 500 μs (see fig.1). Diameter of irradiated spot on target surface was equal up to 10 mm, Nd laser irradiation power density at the irradiated spot - $1.4 \cdot 10^6$ W/ cm^2. The crater depth after the laser acting was ~ 0.3 mm.

At the fig.2 were shown frames observed by implementation of highlighting mono-pulse (duration ~50 ns) of ruby laser. As reference of the time (0 s) the beginning of Nd laser irradiation recession (rectilinear pulse) was accepted.

As it is shown at fig. 2 liquid drops formed due to hydrodynamic mechanism appear only when some time passing after the beginning of acting laser irradiation recession. Moreover, as it can be seen from frame-by-frame photography the laser jet enlarges. It's necessary to note that target erosion products (drop-liquid phase) fly under not great angle to target surface. In such way, they form cone-shaped three-dimensional figure and the cone-opening angle (~ 155º) is unchangeable with the time passing. It proves the fact that during all registration time the shape of solid crater borders and it (crater) depth are unchangeable too. This is means that all liquid layer of metal forced by the recoil momentum of acting laser irradiation recession, start to move from the centre of crater to its borders and run out. The run out angle depends on deepness of the crater and form of its borders.

To define the dynamic of liquid phase from the erosive crater (with commensurable diameter and depth) the focusing of acting laser irradiation was changed (reduced). So far the spot with diameter 5 mm was irradiated by the same laser on the target surface. At that case Nd laser irradiation power density at the irradiated spot reached up to $1.7 \cdot 10^7$ W/ cm^2. The crater depth after the laser acting was ~ 0.6 mm.

At such levels of laser pulse power density the intensity of vaporization is significantly higher than in case of acting laser irradiation focusing in spot with diameter of 10 mm. Due to this fact the erosion crater has the greater deepness with

the passing of time. Therefore, liquid drops formed by the hydrodynamic mechanism must start flying under the greater angle to the target surface.

The results of this experiment are given at the fig. 3. As it can be seen from the fig. 3,a at the moment of the beginning of acting Nd laser irradiation recession the “large” particles not appear yet. But passing some time (see fig. 3,b) it can be seen that in the erosion laser jet the liquid drops start to penetrate. In which connection the angle between the direction of their dispersion and target surface is greater than at the previous experiment. That says about the greater influence of the solid crater borders at liquid drops trajectory at present experiment.

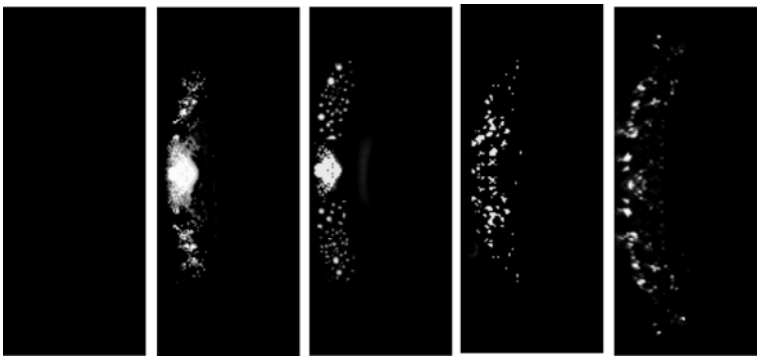

Fig. 2. The frame of drop-liquid phase erosion laser jet (diameter of irradiated spot 10 mm) passing time interval Δt after the beginning of acting laser irradiation recession: a) Δt= 0 μs, b) Δt= 170 μs, c) Δt=260 μs, d) Δt=350 μs, e) Δt=450 μs.

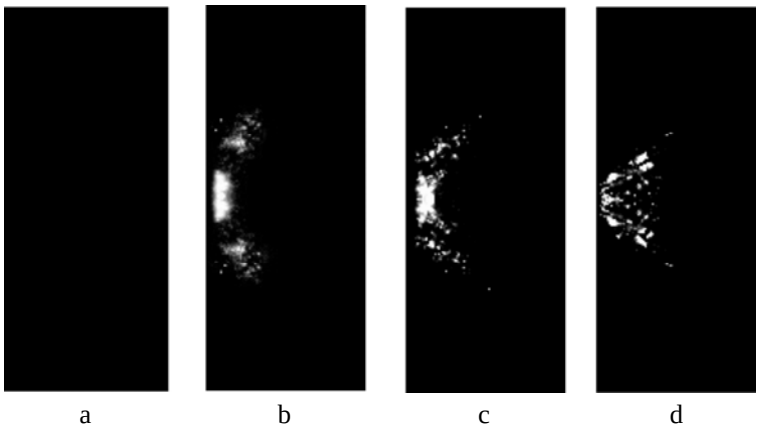

Fig. 3. The frame of drop-liquid phase erosion laser jet (diameter of irradiated spot 5 mm) passing time interval Δt after the beginning of acting laser irradiation recession: a) Δt= 0 μs, b) Δt= 30 μs, c) Δt=250 μs, d) Δt=450 μs.

During the action of laser pulse with bell-shaped form (when the fronts of laser intensivity increasing and decreasing are commensureable to pulse duration) at the matal liquid drops formed due to hydrodynamic mechanism penetrate into laser jet significately earlie (even at the time of laser pulse intensivity resession). This fact is determined by the distinctions in process of condenced phase formation. In this case drop-liqiud phase forms both due to bulk vapore mechanism and due to hydrodynamic mechanism, which are passing simultaneously [9]. At this work, it was established that the time and spatial distribution of erosion laser jet drop-liquid phase had the common features for the wider circrle of metals.

4. FORMATION THE WATER NANOPARTICLE SUSPENSIONS

Therefore, the “small” and “big” particles possess the different directions of dispersion. This effect allows to separate particles spatially by a diaphragm placing (see fig.4). Thus, small particles mainly move in the cavity with water after diaphragm. This is the objects of the present work.

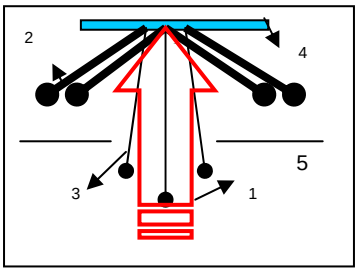

Fig. 4. Scheme of the laser erosion mechanism. 1) Acting laser irradiation, 2) The particles formed by hydrodynamic mechanism, 3) The particles formed by the bulk vapor mechanism, 4) Sample, 5) Mask.

The installation base [10] on Nd-glass laser with λ=1.06 μm produce semi-stationary high power pulses with duration ~ 1.2 ms, energy 1 kJ and focusing diameter 10 mm. The water suspension of nanoparticles was produced by the multi action of the laser irradiation on nickel target.

5. THE CONTROL OF METAL NANOPARTICLES CHARACTERISTICS IN WATER SUSPENSIONS

In water medium particle characteristics was controled with the emplamentation of laser probing method [11]. This method was optimized for the probing of nanoobjects in pan fulled with water.

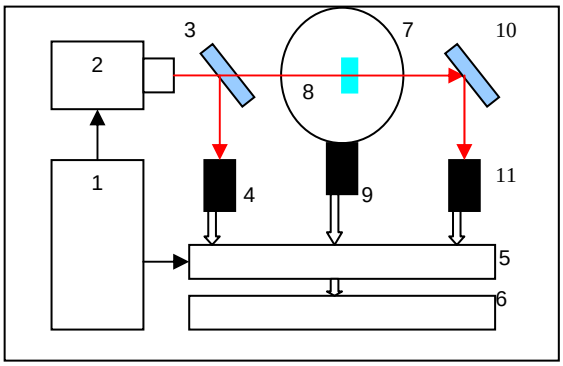

Fig. 5. The scheme of experimental equipment for the laser probing. 1 - System of synchronization, 2 - Ruby laser, 3, 10 - Beam splitter, 4, 9, 11 - Photo detectors, 5 - ADC, 6 - Computer, 7 - Integrating sphere, 8 - Sample

The main point of this method (at the present work) is following – see fig. 5. At the investigated sample 8 placed in the centre of integrating sphere 7 the probing laser irradiation is act. Scattered by the sample irradiation distributes uniformly all along the inside suffused surface of sphere. To define the intensivity of scattered irradiation the photo detector 9 is placed into one of sphere apertures. Two athers photodectors 4,11 registrate the intensivity of probing irradiation and the intensivity of passing throu the sample irradiation correspondinly. The absorbed (by the sample) part of probing irradiation can be determined from the balance of energy.

Therefore, for the spherical particles with size that significantly less than the probing irradiation wavelength ($d << \lambda$) there is known following equation [11]:

$$\frac{Q_{рас}}{Q_{пог}} = \frac{\pi^3}{9}\left(\frac{d}{\lambda}\right)^3 \frac{(n^2 - \chi^2 - 1)^2 + 4n^2\chi^2}{n\chi}, \quad (1)$$

Taking into account $n = \frac{n_{part}}{n_{med}}$ and $\chi = \frac{\chi_{part}}{n_{med}}$, where d - effective particle diameter; n_{part} - index of medium refraction; $m_{part} = n_{part} - i \cdot \chi_{part}$ - complex index of refraction of particle material; Q_{scat} and Q_{abs} - efficiencies of scattering and absorption (rates of scattering cross-section and absorption cross-section to square of transverse section of particle); λ – probing laser irradiation wavelength.

On condition that we have single scattering approximation, (average free path of scattered photon is more than probing sample size) it's known the following equation: $\frac{K_{scat}}{K_{abs}} = \frac{Q_{scat}}{Q_{abs}}$. The effective particle diameter can be determed (using formula (1)) by the comparison of experimentally measured $\frac{K_{scat}}{K_{abs}}$ with the theoretically calculated $\frac{Q_{scat}}{Q_{abs}}$,

Formula for the particle concentration definition can be observed by the following way. The cross-section of irradiation extinction at the one particle is $S_{ext}^1 = Q_{ext} \pi \cdot r^2$ [12]. In probing sample volume the quantity of particles is $N_V = NSl$. Then cross-section of the extinction on all particles in probing volume is $S_{ext} = S_{ext}^1 N_V = Q_{ext} \pi \cdot r^2 NSl$. On condition that we have single scattering approximation, the rate of extinction cross-section (on the particles in probing volume) to transverse section of the probing beam is equal to relative extinction coefficient $K_{ext} = K_{scat} + K_{abs}$, i.e. $\frac{S_{ext}}{S} = K_{ext} = K_{scat} + K_{abs} = Q_{ext} \pi \cdot r^2 Nl$. Then we can determed the concentration

$$N = \frac{K_{\text{scat}} + K_{abs}}{\pi r^2 Q_{ext} l} \qquad (2)$$

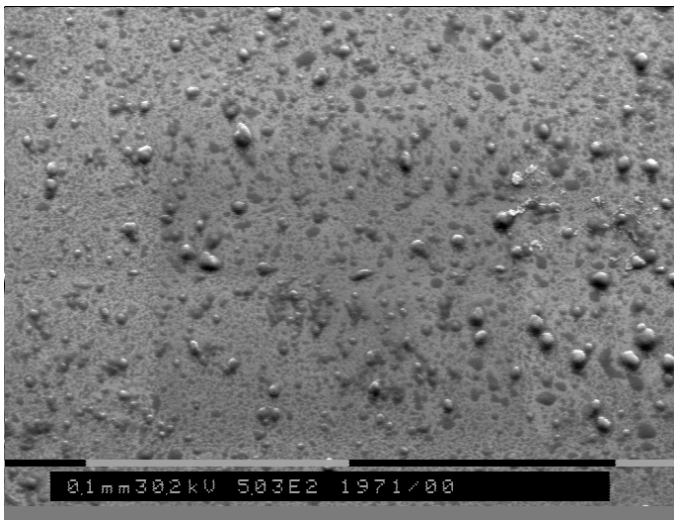
0,1mm30,2kV 5,03E2 1971/00

a

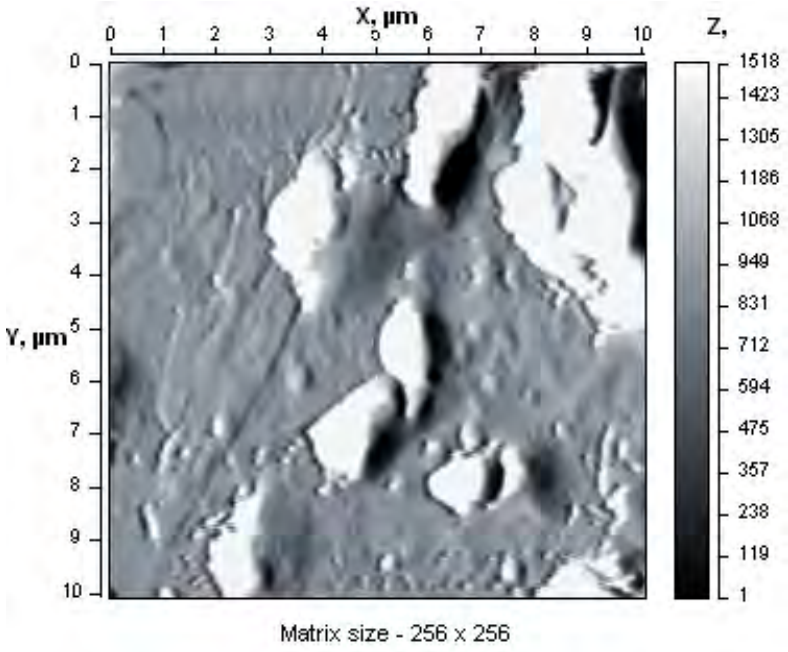
X, µm
0 1 2 3 4 5 6 7 8 9 10
Y, µm
0 1 2 3 4 5 6 7 8 9 10
Z,
1518
1423
1305
1186
1068
949
831
712
594
475
357
238
119
1
Matrix size - 256 x 256

b

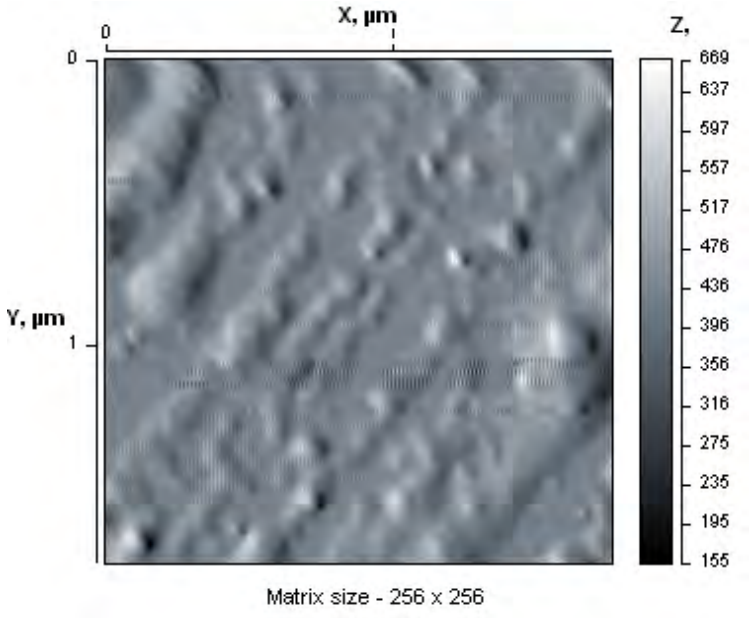

c

Fig 3. Relief surface image of substrate with nickel nanoparticles: a – obtained without diaphragm (electron microscope); b – obtained without diaphragm (image of atomic-power microscope); c – obtained with diaphragm (image of atomic-power microscope).

Consequently, by experimentally measuring K_{scat}, K_{abs} (rates of scattering by the sample irradiation and absorbed irradiation to intensity of probing laser irradiation), l (interacting length of probing laser irradiation with investigated sample) and theoretically calculating Q_{ext} (the method of calculation Q_{ext} is given in proper way at [12]) it's possible to determine average particle concentration in transparent optical medium using formula (2).

At the present work analysis of two examples was made. The first one – water suspension of nickel particles, obtained with an employment of a diaphragm (small particles was in water). The second one – water suspension has nickel particles, obtained without this procedure (i.e. small and large particles flow move in water).

It has been determined parameters by the method laser probing of the sample obtained using diaphragm: the average particles diameter 85 nm, average particles number concentration 1.2×10^{9} cm^{-3}. The probing of the sample obtained without diaphragm shows that the large particles ~ 1 µm are in a water suspense.

The comparative analysis of suspense's (by the atomic-power and electronic microscopy) was made to prove the results, obtained with laser probe method. The water samples were evaporated and drifted on substrate.

Relief surface image of substrate with nickel nanoparticles, obtained without diaphragm is given in Fig.3a. This image was taken with an employment of the electron microscope. Average particles size at the image is 3-5 μm. This fact is in agreement with data obtained with an employment the probing laser method. However we can see at this image that there are a lot of submicron particles with the relatively large particles. They are in the resolution limit of the electron microscope. Submicron particles of this sample have been found with an employment of the atomic-power microscope (Fig.3b). At this image we can clear see the relatively large particles ~2-4 μm and small particles ~40-70 nm.

The investigating results of the particles obtained with an employment of diaphragm are given in Fig.3c. This image has been made with an employment of the atomic-power microscopy. The nickel particles were prepared similar previous case. Even the primary relief surface investigation of the substrate shows a significant reduction of the large particles quantity. Image analysis (Fig.3c) shows that effective particles diameter is 80 nm with dispersion 40% .

Effective particles diameter measured by the laser probe method is in agreement with results obtained with an employment of atomic-power microscopy.

5. CONCLUSION

Thus it's possible to produce nanosize nickel particles with effective diameter ~70-80 nm and their suspense's using mechanism of the metal laser erosion. The main advantage of given method is independence the process of nanoparticles suspense production on the type of penetrating medium and its physical-chemical properties. So it's possible to produce metallic suspense's of nanoparticles in different mediums apart from corrosive mediums to material nanoparticles.

REFERENCES

1. П.А. Витязь. Наноструктурные материалы – 2004. Беларусь – Россия. Минск, 7 (2004)
2. N. Parkansky, B. Alterkop, R.L. Boxman, S. Goldsmith, Z. Barkay, Y. Lereah. Powder Technology. **150**, (2005)
3. В.С. Бураков, Н.А. Савастенко, П.Я. Мисаков, Н.В. Тарасенко. Труды ИМАФ НАНБ, 435-437. (2005)
4. А.В. Симакин, В.В. Воронов, Г.А. Шафеев. Труды института общей физики им. Прохорова, **60**, 83-107 (2004)
5. Б.М.Жиряков, Н.Н.Рыкалин, А.А.Углов, А.К.Фанибо. Журнал технической физики. **41**, 1037 (1971)
6. В.К.Гончаров, В.И.Карабань, В.А.Остромецкий. Квантовая электроника, **13,** 1235 (1986)
7. П.И.Угляков. ЖЭТФ, **52**, 820 (1967)
8. О.И.Путренко. А.А.Янковский. ЖПС, **15**, 596, (1971)
9. В.И. Насонов. ЖПС, **73**, 210-219 (2006)

10. А.П.Бык, В.К.Гончаров, В.В.Захожий, В.И.Карабань, В.И.Кваченок, В.Н.Колесников, В.В.Ревинский, А.Ф.Чернявский, В.Н.Баринов. Москва , 1986, **38** (Препринт / Физ. ин-т АН СССР).
11. В.К. Гончаров, К.В. Козадаев, М.И. Куницкий, М.В. Пузырев ИФЖ . **78**, № 6, 122-125 (2005)
12. К. Борен, Д. М. Кафмен Поглощение и рассеяние света малыми частицами.: Мир, 1986.

VI Serbian-Belarusian Symp. on Phys. and Diagn. of Lab. &
Astrophys. Plasma, Belgrade, Serbia, 22 - 25 August 2006
eds. M. Ćuk, M.S. Dimitrijević, J. Purić, N. Milovanović
Publ. Astron. Obs. Belgrade No. 82 (2007), 57-58 *Invited lecture*

EFFECTIVE REGIMES OF LASER PLASMA FORMATION FOR FILMS DEPOSITIONS AND SPECTROCHEMICAL ANALYSIS OF MATERIALS

A. N. Chumakov[1], N. A. Bosak[1], A. M. Kuzmitsky[1], A. M. Petrenko[1], V. V. Shkurko[1], M. Sambuu[2]

[1]*Institute of Molecular and Atomic Physics of National Academy of Sciences of Belarus*
220072, Minsk, Belarus, e-mail: chumakov@imaph.bas-net.by
[2]*Belarussian State University*

Abstract. The action of intensive laser radiation on absorbing condensed mediums results in formation of laser plasma which is widely used both for deposition of thin films in vacuum, and for spectrochemical analysis of materials. The method of pulsed laser deposition in vacuum provides obteining of high velocities of condensation up to 10^4–10^8 nm/s with good enough reproducibility of chemical composition of irradiated material in deposited films. However, efficiency of such deposition essentially depends on repetition rate of laser pulses. With increase of repetition rate of laser pulses the conditions of laser plasma formation and its subsequent gasdynamic motion are being modified, that results in change of spatially-temporal distribution of plasma parameters and conditions of films deposition. In present work, the capabilities of effective formation of laser plasma are explored at multi-pulsed high-frequency ($f \leq 50$ kHz) laser action on materials and features of pulsed laser deposition of films and coatings on various substrates in vacuum, including in the presence of external electrical field, are investigated.

It was established on the basis of complex experimental researches and numerical calculations of pulse-periodic laser action on metals and carbon materials that the interaction of individual plasma formations initiate changes of conditions for plasma deposition on a substrate only for repetition rates of laser pulses more than 10–20 kHz in vacuum and 1–5 kHz in atmospheric air. Diamond-like and conductive carbon films on various substrates are obtained experimentally at irradiation of graphite by pulsed solid-state laser generating on 1060 nm wavelength with repetition rates of laser pulses up to 20 kHz. Multiple growth of carbon films deposition velocity is found out for intensities of external electrical field exceeding 3 kV/cm. The dependence of structure and electrical conductivity of deposited coatings on the direction and intensity of external electrical field is established. This

result can find application for deposition diamond-like and conductive carbon films. The new possibilities for development of LIBS technique for material analysis are revealed using double pulse laser action at two wavelengths of laser radiation.

VI Serbian-Belarusian Symp. on Phys. and Diagn. of Lab. &
Astrophys. Plasma, Belgrade, Serbia, 22 - 25 August 2006
eds. M. Ćuk, M.S. Dimitrijević, J. Purić, N. Milovanović
Publ. Astron. Obs. Belgrade No. 82 (2007), 59 *Invited lecture*

CONNECTION OF RADIO-INTERFEROMETRIC WITH OPTICAL OBSERVATIONS AND CREATION OF A NEW REFERENCE FRAME FOR POSITION DETERMINATION OF CELESTIAL OBJECTS

Miodrag Dačić

Astronomical Observatory, Volgina 7, 11160 Begrade, Serbia
e-mail: mdacic@aob.bg.ac.yu

Abstract. It is undispensable, for observations of stars and other objects for the needs of astrophysical investigations, to know their positions as much precisely as possible. The development of long base radio-interferometry enabled the connection of radio-interferometric and optical observations, and consequently, the connection of reference frame for extra galactic radio sources, which positions are practically unchanged for a number of decades. In such a way, a new reference frame of high accuracy is obtained, where coordinates of observed objects are given.

VI Serbian-Belarusian Symp. on Phys. and Diagn. of Lab. &
Astrophys. Plasma, Belgrade, Serbia, 22 - 25 August 2006
eds. M. Ćuk, M.S. Dimitrijević, J. Purić, N. Milovanović
Publ. Astron. Obs. Belgrade No. 82 (2007), 61-70 *Invited lecture*

COLLISIONS WITH CHARGED PARTICLES AND SPECTRAL LINE SHAPES IN ASTROPHYSICAL PLASMAS – RESEARCH ON BELGRADE ASTRONOMICAL OBSERVATORY 2002-2005

Milan S. Dimitrijević

Astronomical Observatory, Volgina 7, 11160 Belgrade, Serbia

Abstract Activities on the project "Influence of collisional processes on the astrophysical plasma spectra", supported by the Ministry of Science and Environment protection of Serbia from 1st January 2002 up to 31st December 2005 are reviewed, and selected bibliography of the project participants, including other scientific results, is presented.

1. INTRODUCTION

The project “Influence of collisions with charged particles on astrophysical plasma spectral line shapes” was financialy supported by Ministry of Science and Environment protection of Republic of Serbia under the contract number GA-1195, starting with 2002 up to 2005. The contract 146001 for the project under the same name is signed also for the 2006-2010 period. The objective of this contribution is to present the results obtained up to now. Since our main scientific activity was realized through this project, our aim is to inform Belarussian colleagues on our achievments and directions of future activities in order to stimulate the development of Serbian – Belarussian collaboration within this research field.

2. RESEARCH ON THE INFLUENCE OF COLLISIONAL PROCESSES ON THE ASTROPHYSICAL PLASMA SPECTRA ON BELGRADE ASTRONOMICAL OBSERVATORY

Investigations made within the frame of the Project concern plasma in astrophysics, laboratory and technology and the corresponding modelling, determination and research of atomic and molecular processes, optical properties and spectra, with a particular accent on the role of collisional processes. The

particular attention has been paid to the investigation of spectral line profiles, broadened by collisions with charged particles (Stark effect). Such investigations are of interest for the diagnostics and modelling of stellar plasma, plasma in laboratory and technological plasma.

Semiclasical perturbation and Modified semiempirical methods were used, tested and investigated. Stark broadening parameters, line width and shift, were determined for a large number of spectral lines of Ag I, Ar I, Cd I, Ga I, Ge I, Kr I, Ne I, F II, In II, Ne II, Ti II, Be III, Cd III, Co III, Cu III, F III, S III, Si III, Zn III, and Si IV. The results obtained were applied for the investigation of the influence of Stark broadening of spectral lines in stellar atmospheres.

Particularly was investigated the role of Stark broadening at chemically peculiar A type (Ap) stars, as for example Stark broadening of the neutral chromium spectral lines in the spectrum of chromium rich star Beta CrB and of neutral silicon spectral lines in the roAp 10 Aql star atmosphere. Ab initio calculations of Stark broadening parameters of Ne V spectral lines, observed by cosmical Rendgen telescope "Chandra" was made by using the SUPERSTRUCTURE code and the semiclassical perturbation Stark broadening theory. The Modified semiempirical theory was adapted to use more accurate collision strengths from literature, instead of semiempirical Gaunt factor. The adapted theory was applied and tested on ionized oxygen spectral lines.

The large optical flare was observed on AT Microscopii, and modelled using PHOENIX code for the modelling of stellar atmospheres.

The influence of the (n - n') mixing in Rydberg H*(n) atom - H(1s) collisions in Solar atmosphere was investigated, as well as the influence of symmetrical chemi-ionization and chemi-recombination processes in low temperature atmospheric layers of helium rich DB white dwarfs. Moreover, the influence of these processes on hydrogen Rydberg energy level populations in atmospheres of M type red dwarfs, was investigated with PHOENIX code.

Transition probabilities for Kr II, Ne II, Kr III were also investigated. The influence of Stark broadening of Cd II spectral laser lines, on the hollow cathode discharge laser working mode was considered.

The influence of the radiation pressure on micron-size individual dust grains was experimentally investigated, as well as rotation and alignment of the analogs of interstellar dust grains.

By modelling with PHOENIX, lithium in GJ117 atmosphere was considered.

One of the objectives of the Project is development of database BELDATA. Participants of the Project published 43 papers in leading international journals, from which 29 are part of the Project and 14 are connected with other research fields. In total, Project participants published 261 bibliographic items, and 156 are related to the Project while 107 are not.

3. COLLABORATION AND ORGANIZATION OF CONFERENCES

Participants of the project collaborate with colleagues in Bulgaria, Russia, France, Greece, Ukraine, Tunisia, Spain, Hungary, United Kingdom, Germany, Holland and USA.

In order to stimulate collaboration, and professional discussion of results obtained, particular efforts were made in organization of conferences. Participants of the Project have not only take part in organization of 17 scientific conferences as members of Scientific Committees, but five of them organized directly, giving in such a way their contribution to the development of scientific collaboration. Conferences organized by the participants of the Project are: **1.** DEVELOPMENT OF ASTRONOMY AMONG SERBS II, Belgrade 5-7. IV **2002; 2.** IV SERBIAN CONFERENCE ON SPECTRAL LINE SHAPES, Arandjelovac, 10-15. X 2003**; 3.** IV SERBIAN-BULGARIAN ASTRONOMICAL CONFERENCE, Belgrade, 21-24. IV 2004**; 4.** DEVELOPMENT OF ASTRONOMY AMONG SERBS III, Belgrade 25-28. IV 2004**. 5.** 5th SERBIAN CONFERENCE ON SPECTRAL LINE SHAPES IN ASTROPHYSICS, Vršac 6 - 10 June 2005**.**

4. PARTICIPANTS

From 2002 to 2004, 10 researchers were working on this project, and in 2005 seven, all from Belgrade Astronomical Observatory. The coordinator of the project during all period (1st January 2002 - 31st December 2005) was M. S. Dimitrijević, and the participants are: Edi Bon (not in 2005), Miodrag Dačić, Milan S. Dimitrijević, Darko Jevremović, Predrag Jovanović (not in 2005), Nenad Milovanović, Luka Č. Popović, Zoran Simić, Dragana Tankosić, and Zorica Cvetković (not in 2005).

During four years, ten participants were engaged for 227 research months, i.e. 18.9 years. The average age was around 40 years (or year of birth 1963.5).

5. CONCLUSION

Review of our activities during the 2002-2005 period and the corresponding bibliography of the project participants, is an illustration of our results and and might be helpful and inspirative for ideas on the collaboration development with our colleagues. In order to show all our interests and demonstrate possibilities for possible collaboration, all bibliographic items in international journals, and not only references related to the project, are included.

APPENDIX

With an asterisk are denoted papers which are not a part of the considered project.

1. PAPERS IN THE LEADING INTERNATIONAL JOURNALS

1. M. S. Dimitrijević, S. Sahal-Bréchot: STARK BROADENING OF In II SPECTRAL LINES, Physica Scripta **65**, (2002), 83-95.
2. S. Djeniže, V. Milosavljević, M. S. Dimitrijević: STARK SHIFTS AND TRANSITION PROBABILITIES IN THE Ne II SPECTRUM, Astron. Astrophys. **382**, (2002), 359-367.
3. M. S. Dimitrijević, Lj. Skuljan, S. Djeniže: STARK BROADENING OF THE Ar I SPECTRAL LINES 763.51, 738.39 AND 696.54 nm, Physica Scripta **66**, (2002), 77-81.
4. *M. S. Dimitrijević: MILUTIN MILANKOVIĆ (1879-1958) AND HIS CONTRIBUTION TO EUROPEAN ASTRONOMY, Astronomische Nachrichten **323**, (2002), 570-573.
5. S. Djeniže, M. S. Dimitrijević, A. Srećković, S. Bukvić: STARK SHIFTS AND TRANSITION PROBABILITIES IN Si III AND Si IV SPECTRA, Astron. Astrophys. **396**, (2002), 331-336.
6. D. Garcia-Alvarez, D. Jevremović, J. G. Doyle, C. J. Butler, OBSERVATIONS AND MODELLING OF A LARGE OPTICAL FLARE ON AT MICROSCOPII, Astronomy and Astrophys ics **383**, (2002), 548-557.
7. *L. Č. Popović, E. G. Mediavilla, A. Kubičela, P. Jovanović: BALMER LINES EMISSION REGION IN NGC 3516: KINEMATICAL AND PHYSICAL PROPERTIES, Astronomy and Astrophysics **390**, (2002), 473-480.
8. *E. Bon, M. M. Ćirković, I. Milosavljević: A NEW PROPOSITION FOR REDATING THE MITHRAIC TAUROCTONY SCENE, Astronomische Nachrichten **323**, (2002), 579-580.
9. *C. Abajas, E. Mediasvilla, L. Č. Popović, A. Oscoz: THE INFLUENCE OF GRAVITATIONAL MICROLENSING ON THE BROAD EMISSION LINES OF QUASARS, Astrophysical Journal **576**, (2002), 640-652.
10. D. Tankosić, L. Č. Popović, M. S. Dimitrijević: THE ELECTRON-IMPACT BROADENING PARAMETERS FOR Co III SPECTRAL LINES, Astron. Astrophys. **399**, (2003), 795-797.
11. M. S. Dimitrijević, M. Dačić, Z. Cvetković, S. Sahal-Bréchot: STARK BROADENING OF MULTICHARGED IONS OF ASTROPHYSICAL INTEREST. XXIII Be III, Astron. Astrophys. **400,** (2003), 791-793.
12. A. Srećković, M. S. Dimitrijević, S. Djeniže, S. Bukvić: STARK BROADENING PARAMETERS IN THE S III SPECTRUM, Astron. Astrophys. **400,** (2003), 1155-1159.

13.A. A. Mihajlov, D. Jevremović, P. Hauschildt, M. S. Dimitrijević, Lj. M. Ignjatović, F. Alard: INFLUENCE OF CHEMI-IONIZATION AND CHEMI-RECOMBINATION PROCESSES ON THE POPULATION OF HYDROGEN RYDBERG STATES IN ATMOSPHERES OF LATE TYPE DWARFS, Astron. Astrophys. **403**, (2003), 787-791.
14.M. S. Dimitrijević, T. Ryabchikova, L. Č. Popović, D. Shulyak, V. Tsymbal: ON THE INFLUENCE OF STARK BROADENING ON Si I LINES IN STELLAR ATMOSPHERES, Astron. Astrophys. **404**, (2003), 1099-1106.
15.A. A. Mihajlov, Lj. M. Ignjatović, M. S. Dimitrijević, Z. Djurić: SYMMETRICAL CHEMI-IONIZATION AND CHEMI-RECOMBINATION PROCESSES IN LOW-TEMPERATURE LAYERS OF HELIUM-RICH DB WHITE DWARF ATMOSPHERES, Astrophys. J. Suppl. Series **147**, (2003), 369-377.
16.V. Milosavljević, S. Djeniže, M. S. Dimitrijević: EXPERIMENTAL AND CALCULATED STARK WIDTHS WITHIN THE Kr I SPECTRUM, Phys. Rev. E **68**, (2003), 016402-1-8.
17.M. S. Dimitrijević, P. Jovanović, Z. Simić: STARK BROADENING OF NEUTRAL GERMANIUM SPECTRAL LINES, Astron. Astrophys. **410**, (2003), 735-739.
18.M. S. Dimitrijević, S. Sahal-Bréchot: STARK BROADENING OF Ag I SPECTRAL LINES, Atomic Data and Nuclear Data Tables **85**, (2003), 269-290.
19.S. Djeniže, V. Milosavljević, M. S. Dimitrijević: TRANSITION PROBABILITIES IN Kr II AND Kr III SPECTRA, European Physical Journal D **27**, (2003), 209-213.
20.*L. Č. Popović, E.G. Mediavilla, P. Jovanović, J. A. Muñoz: THE INFLUENCE OF MICROLENSING ON THE SHAPE OF THE AGN FE K LINE, Astronomy and Astrophysics **398**, (2003), 975-982.
21.*L. Č. Popović: 2003, BALMER LINES AS DIAGNOSTICS OF PHYSICAL CONDITIONS IN ACTIVE GALACTIC NUCLEI BROAD EMISSION LINE REGIONS, Astrophysical Journal 599, (2003), 140-146.
22.*L. Č. Popović, E. Mediavilla, E. Bon, N. Stanić, A. Kubičela: THE LINE EMISSION REGION IN III ZW 2: KINEMATICS AND VARIABILITY, Astrophysical Journal **599**, (2003), 185-192.
23.N. Milovanović, M. S. Dimitrijević, L. Č. Popović, Z. Simić,: IMPORTANCE OF COLLISIONS WITH CHARGED PARTICLES FOR STELLAR UV LINE SHAPES: Cd III, Astronomy and Astrophysics **417**, (2004), 375-380.
24.M. M. Abbas, P. D. Craven, J. F. Spann, W. K. Witherow, E. A. West, D. L. Gallagher, M. L. Adrian, G. J. Fishman, D. Tankosić, A. LeClair, R. Sheldon, R., E. D. Thomas: RADIATION PRESSURE MEASUREMENTS ON MICRON-SIZE INDIVIDUAL DUST GRAINS, Journal of Geophysical Research: Space Physics, **108**, (2003) SSH 2-1.
25.N. Milovanović, M. S. Dimitrijević, L. Č. Popović, Z. Simić,: IMPORTANCE OF COLLISIONS WITH CHARGED PARTICLES FOR STELLAR UV LINE SHAPES: Cd III, Astronomy and Astrophysics **417**, (2004), 375-380.
26.M. S. Dimitrijević, M. Dačić, Z. Cvetković, Z. Simić: STARK BROADENING OF Ga I SPECTRAL LINES, Astronomy and Astrophysics **425**, (2004), 1147-1152.

27.A. Srećković, S. Bukvić, S. Djeniže, M. S. Dimitrijević: STARK BROADENING PARAMETERS IN SINGLY AND DOUBLY IONIZED FLUORINE SPECTRA, Astronomy and Astrophysics **420**, (2004), 769-774.
28.V. Milosavljević, S. Djeniže, M. S. Dimitrijević: ELECTRON AND ION CONTRIBUTIONS TO THE Ne I SPECTRAL LINE BROADENING, Journal of Physics B: Atomic, Molecular and Optical Physics **37**, (2004), 2713-2724.
29.L. Csillag, M. S. Dimitrijević: ON THE STARK BROADENING OF THE 537.8 nm AND 441.6 nm Cd^+ LINES EXCITED IN A HOLLOW CATHODE LASER DISCHARGE, Applied Physics B: Lasers and Optics **78**, (2004), 221-223.
30.N. Ben Nessib, M. S. Dimitrijević, S. Sahal-Bréchot: STARK BROADENING OF THE FOUR TIME IONIZED SILICON SPECTRAL LINES, Astronomy and Astrophysics **423**, (2004), 397-400.
31.M. M. Abbas, P. D. Craven, J. F. Spann, D. Tankosić, A. Le Clair, D. L. Gallagher, E. A. West, J. C. Weingartner, W. K. Witherow, A. G. G. M. Tielens: LABORATORY EXPERIMENTS ON ROTATION AND ALIGNMENT OF THE ANALOGS OF INTERSTELLAR DUST GRAINS BY RADIATION, Astrophysical Journal **614**, (2004), 781-795.
32.*D. Olević, Z. Cvetković: ORBITS OF 10 INTERFEROMETRIC BINARY SYSTEMS CALCULATED BY USING THE IMPROVED KOVAL'SKIJ METHOD, Astronomy and Astrophysics **415**, (2004), 259-264.
33.*F. Zakharov, L. Č. Popović, P. Jovanović: ON THE CONTRIBUTION OF MICROLENSING TO X-RAY VARIABILITY OF HIGH-REDSHIFTED QSOS, Astronomy and Astrophysics **420**, (2004) 881-888.
34.*L. Christensen, S. F. Sanchez, K. Jahnke, T. Becker, L. Wisotzki, A. Kelz, L. Č. Popović, M. M. Roth: INTEGRAL FIELD SPECTROSCOPY OF EXTENDED Ly EMISSION FROM THE DLA GALAXY IN Q 2233+31, Astronomy and Astrophysics **417**, (2004) 487-497
35.*L. Č. Popović, E. Mediavilla, E. Bon, D. Ilić: CONTRIBUTION OF THE DISK EMISSION TO THE BROAD EMISSION LINES IN AGNS: TWO-COMPONENT MODEL, Astronomy and Astrophysics **423**, (2004) 909-918.
36.*L. Č. Popović, E. G. Mediavilla, E. Bon, D. Ilić, G. Richter: H II EMISSION LINE REGION IN LEDA 212995, A SMALL NEIGHBORING GALAXY OF Mrk 1040, Astronomische Nachrichten **325**, (2004) 376-379.
37.M. S. Dimitrijević, T. Ryabchikova, L. Č. Popović, D. Shulyak, S. Kan: ON THE INFLUENCE OF STARK BROADENING ON Cr I LINES IN STELLAR ATMOSPHERES, Astronomy and Astrophysics **435**, (2005), 1191-1198
38.W. F. Mahmoudi, N. Ben Nessib, M. S. Dimitrijević: MODIFIED SEMIEMPIRICAL ELECTRON WIDTH CALCULATIONS OF SINGLY-IONIZED OXYGEN SPECTRAL LINES, Astronomy and Astrophysics **434**, (2005), 773-778.
39.A. A. Mihajlov, Lj. Ignjatović, M. S. Dimitrijević: PROCESSES OF (n - n')-MIXING IN COLLISIONS OF RYDBERG H*(n) ATOMS WITH H(1s) IN THE SOLAR ATMOSPHERE Astronomy and Astrophysics **437**, (2005), 1023-1027.

40.Z. Simić, M. S. Dimitrijević, N. Milovanović, S. Sahal-Bréchot: STARK BROADENING OF Cd I SPECTRAL LINES, Astronomy and Astrophysics **441**, (2005), 391-393.
41.D. J. Christian, M. Mathioudakis, D. Jevremović, P. H. Hauschildt, E. Baron: ^{6}Li IN THE ATMOSPHERE OF GJ 117, Astrophysical Journal **632**, (2005), L127-L130.
42.*D. Olević, Z. Cvetković: ORBITS OF SIX BINARY STARS, Revista Mexicana de Astronomia y Astrofisica, **41**, (2005), 17-24.
43.*L. Č. Popović, G. Chartas: THE INFLUENCE OF GRAVITATIONAL LENSING ON THE SPECTRA OF LENSED QUASI-STELLAR OBJECTS, Monthly Notices of the Royal Astronomical Society **357,** (2005), 135-144.

2. PAPERS IN THE INTERNATIONAL JOURNALS

1.*M. S. Dimitrijević, E. Theodossiou: THE CALENDAR OF THE GREEK OR-TODOX CHURCH, Astron. Astrophys. Transactions **21**, (2002), 145-147.
2. M. С. Димитриевич: ШТАРКОВСКОЕ УШИРЕНИЕ СПЕКТРАЛЬНЫХ ЛИНИЙ Ne II И Ne III, Ж. Прикл. Спектроск. **70**, (2003), 439-443.
3 M. S. Dimitrijević: STARK BROADENING IN ASTROPHYSICS (APPLICATIONS OF BELGRADE SCHOOL RESULTS AND COLLABORATION WITH FORMER SOVIET REPUBLICS), Astronomy and Astrophysics Transactions **22**, (2003), 389-412.
4. A. A. Mihajlov, D. Jevremović, Lj. M. Ignjatović, P. Hauschildt, M. S. Dimitrijević: THE INFLUENCE OF CHEMICAL IONIZATION AND CHEMICAL RECOMBINATION PROCESSES ON THE PLASMA PARAMETERS IN LOW-TEMPERATURE LAYERS OF STELLAR ATMOSPHERES, Astronomy and Astrophysics Transactions **22**, (2003), 513-517.
5. M. S. Dimitrijević: STARK BROADENING OF Ne II AND Ne III SPECTRAL LINES, Journal of Applied Spectroscopy **70**, (2003), 493-497.
6. V. Milosavljević, M. S. Dimitrijević, S. Djeniže: MEASURED AND CALCULATED STARK BROADENING PARAMETERS FOR SEVERAL Ar I SPECTRAL LINES, High Temperature Material Processes **7**, (2003), 525-533.
7. M. S. Dimitrijević, S. Sahal-Bréchot: STARK BROADENING OF SPECTRAL LINE SHAPES (ON THE FRENCH-SERBIAN COLLABORATION), High Temperature Material Processes, An International Journal, **7**, (2003), 313-318.
8.*L. Č. Popović, P. Jovanović, E. G. Mediavilla, J. A. Muñoz: Influence OF MICROLENSING ON THE ACTIVE GALACTIC NUCLEUS Fe Kα LINE, Astron. Astrophys. Trans. **22**, (2003), 719-725.
9. Z. Simić, M. S. Dimitrijević, L. Č. Popović, M. Dačić: STARK BROADENING OF F III LINES IN LABORATORY AND STELLAR PLASMA, Ж. Прикл. Спектроск. **72**, (2005), 412-415.
10.Z. Simić, M. S. Dimitrijević, L. Č. Popović, M. Dačić: STARK BROADENING OF F III LINES IN LABORATORY AND STELLAR PLASMA, Journal of Applied Spectroscopy **72**, (2005), 443-446.

11.*E. Danezis, E. Theodossiou, I. Gonidakis, M. S. Dimitrijević: „UN-TANGIBLE WORLD“ AND MODERN PHYSICS European Journal for Science and Theology **1** (2005), 29-35.
12.M. Christova, M. S. Dimitrijević, S. Sahal-Bréchot: STARK BROADENING OF Ar I SPECTRAL LINES EMITTED IN SURFACE WAVE SUSTAINED DISCHARGES, Memorie della Societa Astronomica Italiana Supplementi **7**, (2005), 238-241.
13.B. Zmerli, N. Ben Nessib, M. S. Dimitrijević: TEMPERATURE DEPENDENCE OF NON HYDROGENIC ATOM-LINES STARK WIDTHS, Memorie della Societa Astronomica Italiana Supplementi **7**, (2005), 242-243.
14.E. Danezis, D. Nikolaidis, E. Lyratzi, L. Č. Popović, M. S. Dimitrijević, E. Theodossiou, A. Antoniou: A NEW MODELING APPROACH FOR DACs AND SACs REGIONS IN THE ATMOSPHERES OF HOT EMISSION STARS, Memorie della Societa Astronomica Italiana Supplementi **7**, (2005), 107-113.
15.H. Elabidi, N. Ben Nessib, M. S. Dimitrijević: ELECTRON IMPACT BROADENING OF MULTICHARGED NEON SPECTRAL LINES, Memorie della Societa Astronomica Italiana Supplementi **7**, (2005), 213-216.
16.E. Lyratzi, E. Danezis, D. Nikolaidis, L. Č. Popović, M. S. Dimitrijević, E. Theodossiou, A. Antoniou: A NEW APPROACH FOR THE STRUCTURE OF H ̇ REGIONS IN 120 Be-TYPE STARS, Memorie della Societa Astronomica Italiana Supplementi **7**, (2005), 114-121.
17.M. S. Dimitrijević, T. Ryabchikova, L. Č. Popović, D. Shulyak, S. Kan: ON THE INFLUENCE OF STARK BROADENING OF Cr I LINES IN THE Cr-RICH Ap STAR CrB ATMOSPHERE, Memorie della Societa Astronomica Italiana Supplementi **7**, (2005), 126-127.
18.A. A. Mihajlov, Lj. Ignjatović, M. S. Dimitrijević: PROCESSES OF ATOM – ATOM (n - n') - MIXING INFLUENCE ON HYDROGEN ATOM RYDBERG STATES POPULATIONS IN STELLAR ATMOSPHERES, Memorie della Societa Astronomica Italiana Supplementi **7**, (2005), 151-157.
19.W. F. Mahmoudi, N. Ben Nessib, M. S. Dimitrijević, S. Sahal-Bréchot: CONTRIBUTION TO THE SEMI – CLASSICAL AND MODIFIED SEMI – EMPIRICAL IMPACT STARK BROADENING CALCULATIONS OF SINGLY IONIZED CARBON AND OXYGEN SPECTRAL LINES, Memorie della Societa Astronomica Italiana Supplementi **7**, (2005), 217-220.
20.Z. Simić, L. Č. Popović, M. S. Dimitrijević, M. D. Dačić: STARK BROADENING PARAMETERS FOR Cu III AND Zn III SPECTRAL LINES, Memorie della Societa Astronomica Italiana Supplementi **7**, (2005), 236-237.
21.N. Milovanović: THE STARK BROADENING EFFECT IN HOT STAR ATMOSPHERES: Ti II, Memorie della Societa Astronomica Italiana Supplementi **7**, (2005), 132-135.
22.Z. Simić: INFLUENCE OF IMPACTS WITH CHARGED PARTICLES ON Cd I AND F III SPECTRAL LINES IN STELLAR PLASMA, Memorie della Societa Astronomica Italiana Supplementi **7**, (2005), 122-125.

23.M. A. Jarzembski, D. V. Tankosić: DISCHARGE OF NEGATIVELY CHARGED MICROMETER SIZE PARTICLES IN AN ELECTRODYNAMIC BALANCE DUE TO RADIOACTIVITY, Journal of Aerosol Science **36**, (2005) 1023-1035.
24.*P. Jovanović: MICROLENSING EFFECT ON Fe Kα LINE AND X-RAY CONTINUUM IN THE CASE OF THREE GRAVITATIONALLY LENSED QUASARS: MG J0414+0534, QSO 2237+0305 AND H1413+117, Memorie della Societa Astronomica Italiana Supplement **7**, (2005) 56-59.
25.*C. Abajas, E. Mediavilla, J. A. Muñoz, L. Č. Popović: GRAVITATIONAL MICROLENSING EFFECTS ON THE BROAD EMISSION LINES OF QUASARS, Memorie della Societa Astronomica Italiana Supplement **7,** (2005), 48-55.
26.*I. Chilingarian, Ph. Prugniel, L. Č. Popović: THE HISTORY AND DYNAMICS OF THE STELLAR POPULATION IN THE CENTRAL KPC OF ACTIVE GALAXIES, Memorie della Societa Astronomica Italiana Supplement **7**, (2005), 42-43.
27.*D. Ilić, E. Bon, L. Č. Popović: KINEMATICS OF THE BLR AND NLR IN AGN Mrk 817, Memorie della Societa Astronomica Italiana Supplement **7**, (2005) 30-33.
28.*E. Bon: THE DISK CONTRIBUTION TO THE SHAPE OF THE BALMER BROAD EMISSION LINES IN AGNs, Memorie della Societa Astronomica Italiana Supplement **7**, (2005) 34-37.
29.*D. Ilić, L. Č. Popović, V. Borka: THE UV SPECTRAL PROPERTIES OF RADIO LOUD AND RADIO QUIET QSOs: THE RATIO OF NV/Lyα AND CIV1550/Lyα, Memorie della Societa Astronomica Italiana **7,** (2005), 51-52.
30.*L. Č. Popović: CONNECTION BETWEEN THE X-RAY, UV AND OPTICAL EMISSION LINE REGIONS OF AGN, Memorie della Societa Astronomica Italiana **7**, (2005) 43-46.

3. INVITED LECTURES AT INTERNATIONAL CONFERENCES PUBLISHED IN BOOKS OF INTERNATIONAL PUBLISHERS

1. M. S. Dimitrijević, L. Č. Popović, N. Milovanović, S. Simić, Z. Simić, P. Jovanović: APPLICATIONS OF THE MODIFIED SEMIEMPIRICAL METHOD FOR STELLAR PLASMA INVESTIGATIONS, 21th Summer School and International Symposium on the Physics of Ionized Gases, 21th SPIG, The Physics of ionized Gases, Invited Lectures, Topical Invited Lectures and Progress Reports, eds. N. Bibić, T. Grozdanov, M. K. Radović, M. S. Jovanović, Vinča Institute of Nuclear Sciences, Belgrade (2003), 413-424.
2.L. Č. Popović, M. S. Dimitrijević, E. Mediavilla, E. Danezis, E. Lyratzi, E. Bon, D. Ilić, P. Jovanović, E. Theodossiou, M. Dačić: SOME SPECTROSCOPIC METHODS FOR ASTROPHYSICAL PLASMA RESEARCH, in: "The Physics of Ionized Gases", 22nd Summer School and International Symposium on the Physics of Ionized Gases, Invited Lerctures, Topical Invited Lectures and Progress Reports,

eds. Lj. Hadžievski, T. Grozdanov, N. Bibić, American Institute of Physics Conference Proceedings **740**, (2004), 497-508.

3. *S. Simić, L. Č. Popović: SPECTRAL DEPENDENCE OF THE GRB LIGHT CURVE PULSE, in: "The Physics of Ionized Gases", 22nd Summer School and International Symposium on the Physics of Ionized Gases, Invited Lerctures, Topical Invited Lectures and Progress Reports, eds. Lj. Hadžievski, T. Grozdanov, N. Bibić, American Institute of Physics Conference Proceedings **740**, (2004).
4. *L. Č. Popović: PHYSICAL AND KINEMATICAL PROPERTIES IN CENTRAL PART OF ACTIVE GALAXIES: FROM NARROW TO BROAD EMISSION LINES, Proceedings of the 17th International Conference on Spectral Line Shapes, June 21-25, 2004 – Paris, France, ed. E. Dalimier, Editions FRONTIER GROUP – 2004, 257-264

4. INVITED LECTURES AT INTERNATIONAL CONFERENCES

1. M. S. Dimitrijević: SOLAR PLASMA AND STARK BROADENING INVESTIGATIONS, Proceedings of the Regional meeting on Solar physics: Solar researches in the South-Eastern European countries: Present and perspectives, 24-28 April 2001, Bucharest, Romania, Observations Solaires (2002), 133-137.
2. M. S. Dimitrijević, L. Č. Popović, M. Dačić, Z. Cvetković: APPROXIMATE METHODS FOR STARK BROADENING CALCULATIONS FOR ASTROPHYSICALLY IMPORTANT SPECTRAL LINES, Proc. 3rd Bulgarian-Serbian Astronomical Meeting, May 13-15, 2002, Gjolechitsa, Bulgaria, eds. G. Ivanov, M. S. Dimitrijević, P. Jovanović, Publ. Astron. Obs. Belgrade **73**, 13-26.
3. L. Č. Popović, P. Jovanović, E. Bon, M. S. Dimitrijević: GRAVITATIONAL MICROLENSES IN ACTIVE GALACTIC NUCLEI, Proc. 3rd Bulgarian-Serbian Astronomical Meeting, May 13-15, 2002, Gjolechitsa, Bulgaria, eds. G. Ivanov, M. S. Dimitrijević, P. Jovanović, Publ. Astron. Obs. Belgrade **73**, 49-65.
4. M. S. Dimitrijević, L. Csillag: 2004, ON THE STARK BROADENING OF THE Kr II 469.4 nm, Ar II 476.5 nm AND Ar II 480.6 nm LINES, Proceedings of the V symposium of Belarus, Serbia and Montenegro on Physics and Diagnostics of Laboratory and Astrophysical Plasmas (PDP-V'2004), September 20-23, Minsk, eds. V. S. Burakov, A. F. Chernyavskii, National Academy of Sciences of Belarus, Institute of Molecular and Atomic Physics, Minsk 2004, 40-43.
5. M. S. Dimitrijević: 2005, FULLERENES AND ASTRONOMY, Proceedings of the IV Serbian-Bulgarian Astronomical Conference, Belgrade 21-24 April 2004, eds. M. S. Dimitrijević, V. Golev, L. Č. Popović, M. Tsvetkov, Publications of the Astronomical Society "Ruđer Bošković", **5,** 51-58.

5. THESES

1. Zoran Simić: 2004, УТИЦАЈ СУДАРА СА НАЕЛЕКТРИСАНИМ ЧЕСТИЦАМА НА СПЕКТРАЛНЕ ЛИНИЈЕ Cd I И F III У ЗВЕЗДАНОЈ ПЛАЗМИ (Influence of collisions with charged particles on Cd I and F III spectral lines in stellar plasma), MSc Thesis, Faculty of Mathematics, Belgrade.

VI Serbian-Belarusian Symp. on Phys. and Diagn. of Lab. &
Astrophys. Plasma, Belgrade, Serbia, 22 - 25 August 2006
eds. M. Ćuk, M.S. Dimitrijević, J. Purić, N. Milovanović
Publ. Astron. Obs. Belgrade No. 82 (2007), 71-82 *Invited lecture*

SILICON SINGLE CRYSTAL SURFACE MODIFICATION BY COMPRESSION PLASMA FLOW ACTION

I. P. Dojčinović[1,2], M. M. Kuraica[1,2], J. Purić[1,2]

[1]Faculty of Physics, University of Belgrade,
POB 368, 11001 Belgrade, Serbia
[2]Center for Science and Technology Development,
Obilićev venac 26, 11000 Belgrade, Serbia
e-mail: ivbi@ff.bg.ac.yu

Abstract. Modification of silicon single crystal surface by the action of nitrogen quasistationary compression plasma flow (CPF) generated by magnetoplasma compressor is studied. It was found that during single pulse surface treatment regular fracture features are obtained on the Si (100) surface in the target central part. Some of these regular structures can become free from the underlying bulk, formed as blocks ejected from the surface. Also, oriented silicon periodic structures are produced in the target periphery part. These surface phenomena are results of specific conditions during CPF interaction with silicon surface. High plasma flow energy density, large dynamic pressure, thermodynamic parameters gradients and induced magnetic field on treated surface cause rapid heating and melting of surface layer, as well as surface fracturing, long existence of molten layer and fast cooling and recrystalisation.

1. INTRODUCTION

High-power pulsed energy streams interaction with material surfaces results in surface modification, as well as the material removing from surface in the form of vapor, liquid droplets, or solid flakes due to evaporation, sputtering, ablation, exfoliation etc.

During surface treatment rapid melting and resolidification of surface layer is occured. High temperatures and consequent thermal stresses, as well as mechanically strained surface during treatment, result in significant deformation and

fracture of the layer, induced defects, cracking and exfoliation of the coating. Also, cracks being characteristic of a molten material which is resolidified very quickly.

Material surface modification by pulsed energy beams such as pulsed laser, ion beams and plasma flows are of great importance, especially for grating-like patterns formation, i.e. wave-like periodic structures. The interplay between sputtering and surface diffusion smoothing processes is responsible for the creation of ripple structures, i.e. wave-like surface morphologies, when the direction of the ion beam is tilted to the surface normal [1,2]. On non-metal surfaces, including silicon, at normal incidence ripples are not observed [2]. Laser induced periodic surface structures (LIPSS) due to the incident laser light, have a period which coresponds to laser wavelenght [3]. Laser induced periodic structures with period which is much higher than laser wavelenght are described as laser induced capillary waves [3,4]. In the case of plasma surface interaction, the formation of periodical structures was not observed so far. In several types of plasma sources [5-7] rapid melting and solidification have occurred, but wave-like structures have not been yet observed.

Surface and interface properties are very important for semiconductor devices and their engineering applications. Supersonic compression plasma flow (CPF) is using for silicon single crystal surface modification. In central part of treated silicon surface regular fracture features are obtained. It was found that some of these structures as blocks can be ejected from the surface. In the periphery part of silicon samples surface highly oriented periodic cylindrical shaped structures are obtained. Surface cleavage and exfoliation phenomena, as well as ripple structures formation, as the results of specific conditions during CPF interaction on silicon surface are, also, observed and studied.

2. EXPERIMENTAL SETUP

Si (100) surface of single crystal were treated with quasistationary compression plasma flow produced by magnetoplasma compressor (MPC). MPC is a plasma source firstly designed, developed and investigated by group led by Prof. Morozov. This quasistationary plasma accelerator (plasma gun) is described elsewhere [8-12], therefore only a few details are given here for the sake of completeness.

The MPC consists of the specially designed electrode system [8]. Conically shaped cathode of MPC defines the profile of acceleration channel. Using nitrogen as working gas at 500 Pa pressures and 800 μF, 4 kV capacitor bank, the obtained current maximum was up to 100 kA and time duration up to 150 μs with current half period ~70 μs. In the MPC inter electrode region the plasma is accelerated due to the Ampere force. The plasma flow is compressed due to interaction between longitudinal current component and intrinsic azimuth magnetic field (pinch effect) [8]. The stable CPF is formed 20 μs after the beginning of the discharge. During a quasistationary phase the plasma flow parameters are slowly changing in time within certain volume. It is a consequence of an ion-drift acceleration of magnetized plasma realized using the specially shaped accelerating channel [13]. Namely, the

continual ionization processes take part in working gas introduced in interelectrode region. The plasma is steadily accelerated and permanently compressed. Time development of CPF was observed using IMACON 790 high speed camera operating in streak mode, using parallel positioned slit along CPF axis. In Fig. 1 discrete plasma structures of CPF, seen as light and dark regions, are observed. These structures occur with ~5 MHz frequencies.

The advantages of MPC, as compared to other types of plasma accelerators, are high stability of generated CPF, size (CPF up to 6 cm in length and 1 cm in diameter), and high plasma parameters (electron density ~10^{17} cm^{-3} and temperature up to 3 eV), as well as the CPF time duration (quasistationary stable phase is 40-50 μs) and large flow velocity (40 km/s in nitrogen) sufficient for material surface modification. Beside that, the operation in the ion current transfer mode [13] with the minimization of the electrodes erosion represents an additional and very important advantage of the quasistationary plasma accelerators in comparison with the classical ones. The electrodes surfaces are protected of the erosion due to the magnetic field self-shielding. Magnetic flux conservation is a particular characteristic of CPF. During the action of CPF on a sample surface, due to CPF deceleration and frozen-in magnetic field, current loops (vortices) are formed.

For the studies of CPF interaction with silicon surfaces, commercial one-side polished n-type silicon wafers (100 orientation) 300 μm thick and 10 mm in diameter were used. The samples were glued to the cylindrical brass holder of the same diameter with conductive carbon paste, and mounted perpendicularly in front of the MPC cathode at the distance of 5 cm. Silicon samples are exposed to a single plasma pulse. A target surface is parallel to the direction of gravitation force and perpendicular to the plasma flow velocity. Therefore, the gravitation force has no influence on the surface wave's formation. To investigate the morphology of treated silicon surface, optical microscopy (OM), scanning electron microscopy (SEM) and atomic force microscopy (AFM) were used.

3. RESULTS

OM and SEM micrographs of a treated Si (100) surfaces are given in Fig. 2 and Fig. 3, respectively. In central part of the treated surfaces two sets of fracture lines intersecting at 90º form a grid that divides the surface into rectangular blocks (Fig. 2). Some of the blocks are ejected from the surface, and large holes at the surface emerged. In this case development of subsurface fracture, parallel to the surface, is occured. A typical hole is shown in Fig. 2. At the bottom of arisen holes very small ripple structures are observed.

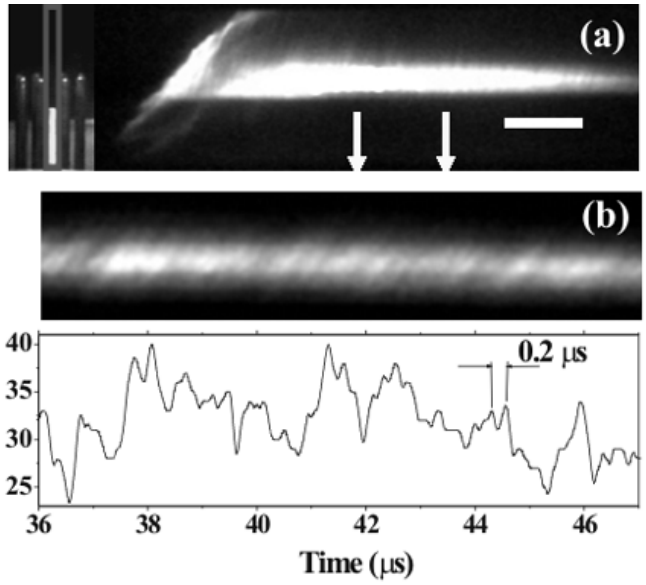

Fig. 1. The compression plasma flow intrinsic oscillations: a) Time and space development of CPF from the cathode onwards. Bar size is 10 μs. b) Enlarged time period indicated by arrows with its light intensity variation represented versus time.

Surface fracture and periodic cylindrical structures obtained by plasma pulse treatment of the Si (100) sample surface are shown in Fig. 3. Periodic silicon structures are obtained on the periphery part of the target surface. Wavelengths (hill-to-hill distances) of highly oriented periodical silicon structures are in the range from 100 nm up to 5 μm [14-18]. The lengths of these structures are in the range from 50 μm up to one millimeter (Fig. 2). Typical wavelength is about 2-3 μm and length 200 μm. The AFM micrographs were used for the periodical structures surface investigation (Fig. 4). Structures are smooth, homogenous and sinusoidally shaped with an amplitude (half hill-to-valley distance) of about 0.2-0.3 μm [17]. It is worth to emphasize that this structures are obtained by single plasma pulse treatment of the Si sample surface. The regular silicon surface structures can be obtained on the area region up to several square millimeters. They are covering up to 50 % of the whole surface. SEM micrographs of the obtained parallely oriented periodic structures on Si (100) surface are shown in Figs. 5-7.

These periodical structures are not dependent on the crystal orientation. Similar structures were obtained, also, using hydrogen and argon plasma flow interaction with silicon samples. The shapes of obtained structures were not dependent on the working gas [15]. Also, after plasma flow exposure, the sample was treated by HF acid and has been concluded that the obtained cylindrical structures are made of pure silicon [14].

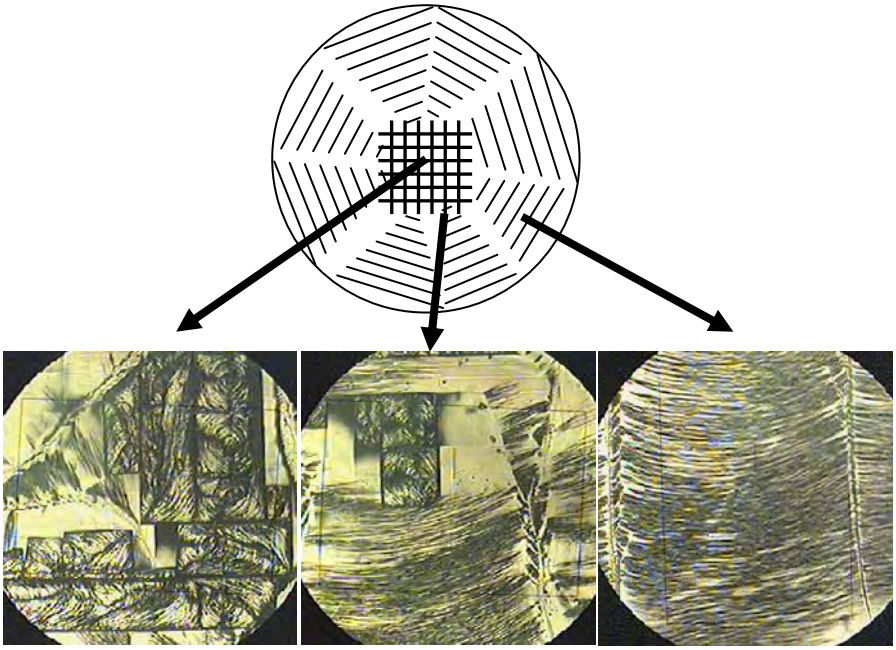

Fig. 2. Schematic diagram and optical microscopy micrographs of CPF treated Si (100) surface. Micrographs size are 1×1 mm^2.

4. DISCUSSION

The formation of observed surface features may be explained by energetic action of CPF on the surface (absorbed energy 10-15 J per pulse, flow power density ~$1 \cdot 10^5$ W/cm^2 [16]). The interaction of CPF with silicon sample surface causes the evaporation of a thin surface layer and formation of a shock-compressed plasma layer (SCPL) [14]. Formation of this cloud of dense target plasma results in the shielding of a processed surface from a direct action of a CPF and surface protection from further excessive evaporation. A thickness of this plasma plume is about 1 cm. Using the high speed camera, time of interaction was estimated to be 40-50 μs [14]. It may be taken that molten layer exists on the target surface during the interaction. By analyzing the cross section of treated silicon sample, thickness of near-surface molten layer is estimated at 6-10 μm.

Energetic action of CPF causes the fast heating and melting of the surface layer and the presence of high dynamic pressure of CPF of the order of several atmospheres [16]. Namely, CPF kinetic energy thermalization causes the heating of target surface and high gradient of thermodynamic parameters is occurred. Target surface is heated by convective and radiative heating. Beside that, deceleration of the CPF results in the formation of current loops (vortices), due to freezing of

magnetic field into plasma, and magnetic field 1-10 mT is induced at the surface [16].

Formation of regular fracture features (Figs. 2,3) can be explained by considerable fraction of the absorbed plasma flow energy trapped into fractures rather than converted to heat energy [19,20]. Single crystal silicon is well known as a typical anisotropic material and it is very brittle at room temperature [21]. Low adhesion between blocks and silicon bulk, and eventual ejection of blocks from the CPF treated surface, can be explained by development of subsurface fracture, parallel to the surface. Cracking between the block and the bulk is growing due to local energy absorption.

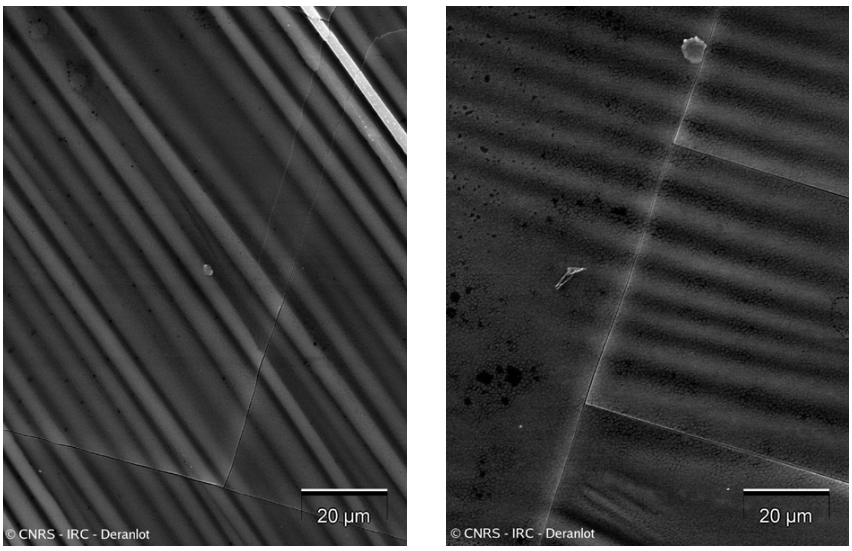

Fig. 3. SEM micrographs of silicon surface obtained after single pulse treatment by CPF.

An aim of this paper is to compare periodical structures obtained on CPF treated silicon surface with wave-like periodical structures obtained by laser, ion beam and plasma flow silicon surface treatment.

Laser induced periodic surface structures (LIPSS), theoretically and experimentally observed elsewhere [3], corresponds to a non-uniform energy input into the sample, modulated by the interference between the incident wave and an induced surface wave. Targets are made of intrinsic and extrinsic semiconductors, metals and dielectrics. At normally incident laser beam, periodical surface structures are perpendicular to the laser beam polarization and have a period which corresponds to laser wavelength. In some case, the structures have a period which is much higher than laser wavelength. These structures are described as laser-induced capillary waves [4].

Ripple structures on silicon surface, created by ion bombardment [1], are based on the interplay between the sputtering and surface diffusion smoothing

processes. The sputtering yield depends on the local surface curvature. This dependency leads to a surface instability (negative surface tension) where the erosion velocity in depressions is greater than on mounds of the surface. On the other hand, surface diffusion tends to smooth the surface topography. The interplay between these two effects is responsible for the creation of cones, dots and holes on surfaces at normal ion incidence, and especially for ripple and wave-like surface morphologies, when the direction of the ion beam is tilted to the surface normal (off-normal incidence) [1,2]. In case of grazing-incidence sputtering geometries ($\theta \geq 70^{o}$) orientation of the surface structures is forced to be parallel to the ion beam orientation. For angles smaller then the critical incident angle, structures become perpendicular to the ion beam orientation. In non-metal substrates, including silicon, at normal incidence ripples are not observed [2]. The ripples can be created by bombardment at normal ion incidence in the case of some metals (Ag, Cu) due to anisotropic surface diffusion [2].

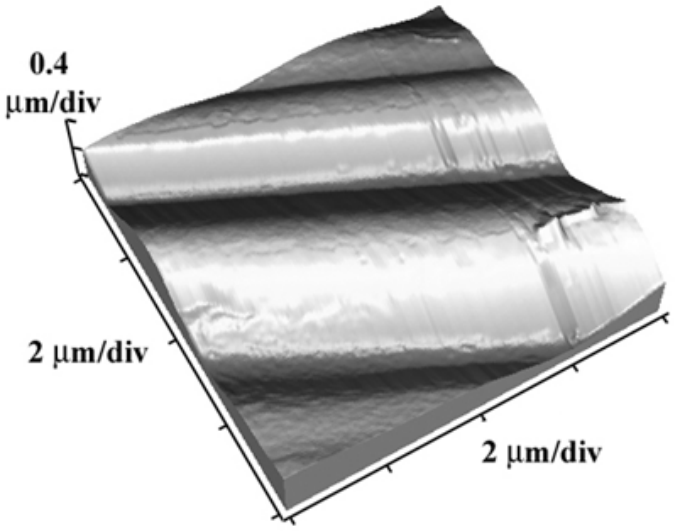

Fig. 4. AFM micrograph of CPF treated Si (100) surface.

In the case of plasma surface interaction experiments, the periodical silicon surface structure formation has not been observed so far, although the time of interaction varied up to 10 μs, and delivered plasma energy density was of the order of 10 J/cm^2, which is comparable to our experimental conditions. Using several types of plasma sources such as coaxial plasma gun [5], pulsed plasma beam [6] and thermal plasma jet [7], rapid melting and resolidification have occurred, but wave-like structures have not been observed.

However, in our experiment we have obtained silicon periodical surface structures. This can be attributed to specific property of compression plasma flow. The energy density delivered to the surface is about 10 J/cm^2 and surface is

completely and uniformly melted. Due to the fast cooling of the melted surface layer, which is usually occurring in this kind of experiment, the surface structures formed during melt phase are freezing (quenched) at a particular moment during a process of the melt resolidification [15,17]. Therefore, the basic effects of the CPF action on solid target are surface melting, formation of different surface patterns and their freezing during fast cooling (quenching effect). This process may be compared with laser surface interaction. Three main similarities of CPF used here and laser beams of high fluences are: i) silicon surface uniform melting; ii) perturbation action on melted surface layer; and, iii) quenching of the produced surface wave structures. In the laser surface interaction at high fluences, the periodical structures results from freezing of capillary waves which are generated on the uniformly melted surface. In this case laser induced plasma plume adiabatically spreads in a direction normal to the treated surface which induces a very strong recoil impulse directed into the treated target [3,4]. Laser induced capillary waves are smooth and sinusoidally shaped structures [3] similar to those obtained by CPF treatment in this experiment.

If free surface of a liquid is put out of balance, waves are formed along the surface under the influence of gravitational pull and surface tension [22]. If the direction of gravitation force is such that it can not contribute to the creation of surface waves, the waves formed at the liquid surface are capillary waves. The dispersion of such capillary waves is given as [22]:

$$\omega^2 = \frac{\gamma}{\rho} k^3 \tag{1}$$

Here, γ is the surface tension, ρ is the density of the liquid, ω is the frequency and k is wave number of the capillary waves. When waves are driven by a periodical force applied on the free liquid surface their frequency has to be close to the frequency of the applied force. In the case of periodical radiation pressure of laser light to the liquid surface, the capillary waves with arbitrary waveform were generated by modulating the laser output [23]. This approach has been used for study of CPF induced capillary waves experimentally observed here. Namely, CPF treatment of the melted silicon surface is periodical perturbation due to CPF intrinsic oscillations.

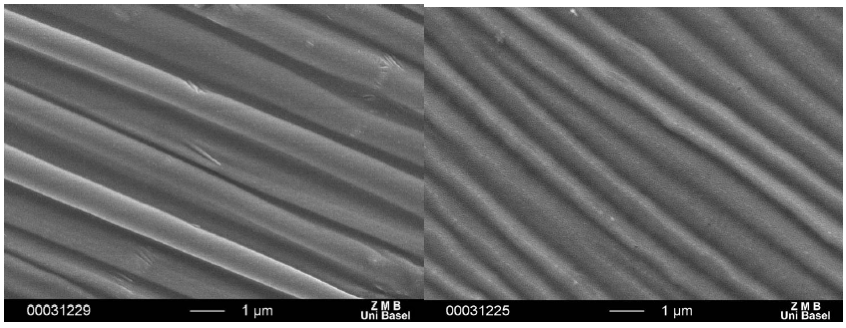

Fig. 5. SEM micrographs of highly oriented periodical structures on treated silicon surface.

On the completely molten silicon surface, in the presence of high dynamic pressure of CPF, perturbation occurs [16]. The obtained periodical cylindrical structures on the surface are liquid structures frozen during fast cooling and recrystallization (quenching effect).

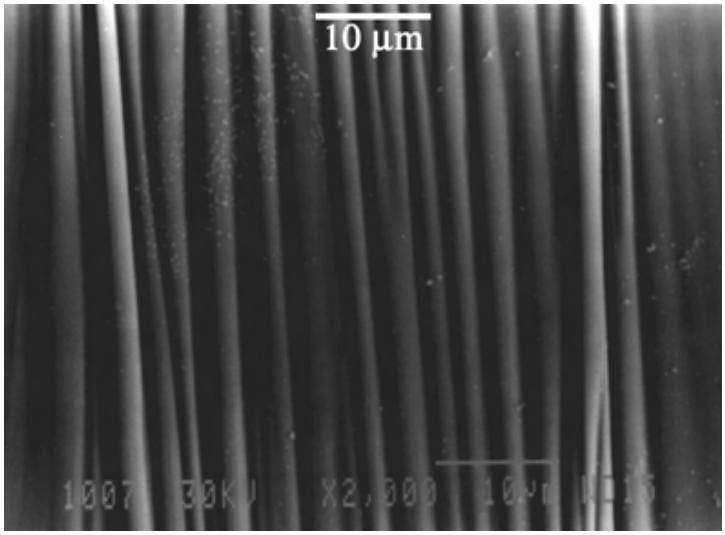

Fig. 6. SEM micrograph of CPF treated silicon surface.

Supposing that the periodical cylindrical structures are frozen surface capillary waves quenched at a particular moment during a process of the melt resolidification, main wave parameters can be estimated using dispersion equation. Taking $\gamma \sim 0.75$ N/m and $\rho \sim 2.5$ g/cm^3 for molten silicon [ref. 24 and references therein], with typical ex situ measured wavelength of periodical structures equal to ~4 μm (Figs. 2-7), calculated capillary wave frequency is found to be ~5 MHz. This value corresponds to the in situ measured frequency of discrete plasma structures, i.e. frequency of perturbation of ~5 MHz (Fig. 1). About 200 plasma pulses delivered to treated silicon surface during 40 μs of plasma flow quasistationary phase. This is a clear indication that the CPF interaction with molten silicon surface can be regarded as a periodical driven force of the induced surface capillary waves.

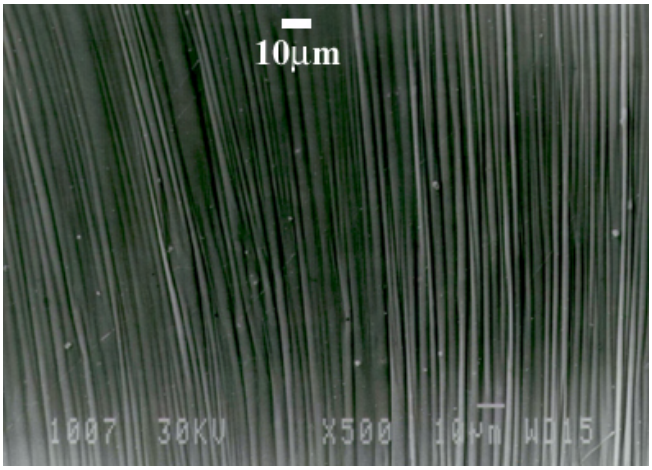

Fig. 7. Silicon surface cylindrical structures obtained by single plasma pulse treatment of the Si (100) sample.

The surfaces of periodical structures are found to be smooth, homogenous and sinusoidally shaped (Fig. 4), as would be expected from frozen capillary waves [3]. Besides the freezing of capillary waves, a rapid solidification can also produce serious cracking problems due to differential stresses. An example of the surface regular fracture together with frozen capillary waves, obtained by single plasma pulse treatment of the Si (100) sample surface, is shown in Fig. 3. During cooling and unloading of treated surface, the residual stresses created in the subsurface region can produce surface fracturing [21]. From Fig. 3 one can conclude that crackings occurre after solidification of periodic cylindrical structures and may be explained with the emerging of residual stresses. Recrystallization occurred under conditions of high dynamic pressure of CPF, high thermodynamic parameters gradients, and induced magnetic field.

5. CONCLUSION

Periodical wave-like patterns, as well as regular fracture features and exfoliations, are observed on silicon single crystal surface treated by CPF. Surface modification is performed by fast heating of the surface in the presence of high dynamic pressure, thermodynamic parameters gradients and induced magnetic field from the CPF. Periodical wave-like structures are induced by the plasma flow action on periphery part of the target and then quenched from the molten state during fast cooling and resolidification. Typical dimensions of parallel cylindrical structures are 2-3 μm in diameter and about 200 μm in length. The regular silicon surface structures can be obtained on the larger area, up to several square millimeters. These structures may be related to plasma induced capillary waves phenomena. The estimated frequency of the capillary waves is found to be in a good agreement as

compared to the frequency of the observed CPF plasma structures. During surface treatment and fast cooling phase, differential stresses in surface layer occurred. As the results of all of these processes rectangular regular fracture features are obtained on the Si (100) surface. Some of these blocks are ejected from the surface.

ACKNOWLEDGEMENT

The authors are grateful to Dr M. Smiljanić and Dr M. Matić from Institute HTM-CMTM in Belgrade for supplying Si substrate and Dr V. Rakić from Faculty of Physical Chemistry and D. Randjelović from Institute HTM-CMTM for the SEM and AFM analyses.

REFERENCES

1. S. Habenicht, K.P. Lieb, J. Koch and A.D. Wieck, Phys. Rev. B, **65**, 115327 (2002)
2. U. Valbusa, C. Boragno and F.B. de Mongeot, J. Phys.: Condens. Matter, **14**, 8153 (2002)
3. J.F. Young, J.E. Sipe and H.M. van Driel, Phys. Rev. B, **30**, 2001 (1984)
4. V.N. Tokarev and V.I. Konov, J. Appl. Phys., **76**, 800 (1994)
5. B. Liu, C. Liu, D. Cheng, R. He, and S. Z. Yang, Thin Solid Films, **390**, 149 (2001)
6. J. Piekoszewski, Z. Werner, J. Langner, and M. Janik-Czachor, Surf. Coat. Technol, **93**, 258 (1997)
7. H. Kaku, S. Higashi, H. Taniguchi, H. Murakami and S. Miyazaki, Appl. Surf. Sci., **244**, 8 (2005)
8. J. Purić, I.P. Dojčinović, V.M. Astashynski, M.M. Kuraica and B.M. Obradović, Plasma Sources Sci. Technol., **13**, 74 (2004)
9. I.P. Dojcinovic, M.R. Gemisic, B.M. Obradovic, M.M. Kuraica, V.M. Astashinskii and J. Puric, J. Appl. Spectroscopy, **68**, 824 (2001)
10. S.I. Ananin, V.M. Astashinskii, G.I. Bakanovich, E.A. Kostyukevich, A.M. Kuzmitski, A.A. Man'kovskii, L.Ya. Min'ko and A.I. Morozov, Sov. J. Plasma Phys., **16**, 102 (1990)
11. M.M. Kuraica, I.P. Dojčinović, M. Nikolić, B.M. Obradović and J. Purić, Czech. J Phys., **56**, 291 (2006)
12. I.P. Dojčinović, M.M. Kuraica, B.M. Obradović, N. Cvetanović and J. Purić, Plasma Sources Sci. Technol., **16**, 72 (2007)
13. A.I. Morozov, Sov. J. Plasma Phys., **16**, 69 (1990)
14. J. Purić, V.M. Astashynski, I.P. Dojčinović and M.M. Kuraica, Vacuum, **73**, 561 (2004)
15. I.P. Dojčinović, M.M. Kuraica and J. Purić, Vacuum, **80**, 1381 (2006)
16. V.V. Uglov, V.M. Anishchik, V.V. Astashynski, V.M. Astashynski, S.I. Ananin, V.V. Askerko, E.A. Kostyukevich, A.M. Kuz'mitski, N.T. Kvasov and A.L. Danilyuk, Surf. Coat. Technol., **158-159**, 273 (2002)

17. I.P. Dojčinović, M.M. Kuraica, B.M. Obradović and J. Purić, Appl. Phys. Lett., **89**, 071501 (2006)
18. I.P. Dojčinović, M.M. Kuraica, B.M. Obradović and J. Purić, Czech. J Phys., **56**, 205 (2006)
19. A. Rosenfeld, D. Ashkenasi, H. Varel, M. Wahmer, and E.E.B. Campbell, Appl. Surf. Sci., **127-129**, 76 (1998)
20. R.L. Webb, L.C. Jensen, S.C. Langford and J.T. Dickinson, J. Appl. Phys., **74**, 2323 (1993)
21. J.A. Hauch, D. Holland, M.P. Marder and H.L. Swinney, Phys. Rev Lett., **82**, 3823 (1999)
22. L.D. Landau and E.M. Lifshitz, Gidrodinamika (in Russian), Nauka, Moskva, 1988
23. K. Sakai, K. Tachibana, S. Mitani and K. Takagi, J. Colloid Interface Sci. **264**, 446 (2003)
24. W.K. Rhim and K. Ohsaka, J. Cryst. Growth, **208**, (2000) 313 (2000)

VI Serbian-Belarusian Symp. on Phys. and Diagn. of Lab. &
Astrophys. Plasma, Belgrade, Serbia, 22 - 25 August 2006
eds. M. Ćuk, M.S. Dimitrijević, J. Purić, N. Milovanović
Publ. Astron. Obs. Belgrade No. 82 (2007), 83-100 *Invited lecture*

EMISSION SPECTRA OF LASER-INDUCED PLASMAS AT THE ELEMENTAL ANALYSIS OF SOLIDS: MEASUREMENT AND MODELING RESULTS

E. Ershov-Pavlov[1], K. Catsalap[1], V. Rozantsev[1],
Yu. Stankevich[2], K. Stepanov[2]

[1]*Institute of Molecular and Atomic Physics, Minsk, Belarus*
[2]*Heat and Mass Transfer Institute, Minsk, Belarus*

Abstract. Results are presented of measurements and numerical modeling of emission spectra of laser plasma plumes arising on surfaces of metal samples at their elemental analysis by the laser-induced breakdown spectroscopy (LIBS) technique. The plasma plumes have been considered, which are induced by single and double laser pulses of the nanosecond range duration.

The modeling of the plume plasma parameters consists of a solution of the thermal, hydro-dynamics and optical problems accounting for the laser beam action on a solid surface. The numerical code allows investigating the dynamics of two-dimensional erosion plumes supposing their axial symmetry. Resulting space and time distributions of parameters in the laser-induced plasmas are used to evaluate the plumes emission spectra supposing a side-on observation case.

The simulation results, which have been obtained for an Al-sample, are compared to the experimental ones, measured at the conditions of common LIBS applications: a Q-switched Nd:YAG laser generating pulses of 15 ns duration and 50 mJ energy at 1064 nm wavelength, which provided ~ $0.85 \cdot 10^9$ W/cm^2 maximum irradiance of the sample surface.

The comparative study is realized for the measured and simulated spectra of the plasma plumes induced at single- and double-pulse excitation modes, which allows examining reasons of the observed efficiency increase of the LIBS elemental analysis at the double-pulse excitation mode.

1. INTRODUCTION

The laser-induced breakdown spectroscopy (LIBS) is nowadays considered to be one of the most promising techniques of the elemental analysis of different types of materials including solids, liquids and gases (see, e.g., [1-3]). The main feature of the LIBS consists of the sample material ablation and excitation till plasma state by powerful pulse laser radiation. It results in the technique unique properties allowing to combine sampling and excitation in a single step and to make rapid in situ and, if necessary, distant analysis with no or minimum sample preparation. Additionally, by due focusing the laser beam one can control position and dimension of the laser erosion spot, as well as the ablation rate, which gives other advantages of the LIBS such as an opportunity of surface mapping and in-depth profiling of the sample elemental composition [4].

Unfortunately, common LIBS techniques have rather moderate sensitivity and measurement precision in comparison with the most developed spectroscopy techniques such as atomic absorption spectrometry (AAS) and inductively coupled plasma - atomic emission spectrometry (ICP-AES) [3], and efforts are being made to increase LIBS analytical efficiency. Among other ways, double-pulse laser excitation technique has been proposed, where the laser erosion plasma is produced by two laser pulses following each other with a certain delay compared to the plasma decay time. The double-pulse (DP) technique use and development as applied to the elemental analysis of solids in air began in 1980's [5-8]. Now a growing interest to the technique can be observed by publications, where different ways of the double-pulse technique realization are considered (see, e.g., [9-19]). Among them, one can find collinear [9-14] and orthogonal (pre-ablation [15-17] and reheating [18, 19]) schemes of the laser pulses (beams) action on samples of different compositions at various laser pulse parameters: energy, duration, wavelength, etc. All schemes give more or less apparent intensity increase of atomic and especially ionic lines in emission spectra of the DP laser plume as compared to one of a single pulse of the same total energy in the common single-pulse (SP) mode.

In spite of the technique active investigation, up to now there is no clear and complete understanding of the processes and mechanisms providing the observed phenomena of the line intensity increase. It is only clear, that the laser beams acting on a sample at the double-pulse mode produce a plasma volume having conditions (density, range and space-time distribution of the plasma parameters), which are more favorable for the emission of the lines under consideration [11, 12, 20, 21]. Further experiments including measurements of the laser plasma parameters with high time and space resolution will provide data for the problem solution. Together with the experiments, numerical modeling of the laser plumes would help much in the problem deeper understanding. One can find some interesting results concerning the laser plume simulation [22-25], but up to now there is actually no model providing an adequate account for the plume formation and expansion, as well as for the plume emission spectra. More, no models have been reported for the double-pulse laser plasma.

Here some results are presented of measurements and numerical simulation of line emission spectra of the laser plumes arising at both single- and double-pulse modes on Al-sample irradiated by a Q-switched Nd:YAG laser beam at the collinear illumination scheme. For this, data on distribution and evolution of plasma parameters in the laser plumes have been obtained first using a part of the numerical code reported earlier [21]. Resulting space and time distributions of the laser-induced plasma parameters have been used to evaluate the emission spectra of the plasma volumes at chosen time intervals supposing a side-on observation. The results have been compared to the experimental spectra measured in the conditions similar as close as possible to those considered at the simulation. The laser generated pulses of 15 ns duration and 50 mJ energy at 1064 nm, which provided ~ $0.8 \cdot 10^9$ W/cm^2 maximum irradiance of the sample surface. The aim of the work consists of comparative analysis of the simulation and measurement data on the laser plume formation, space-time behavior and resulting spectral emission of the plume at both action modes. The analysis results must help to clear up a difference in formation of the laser plumes arising at SP and DP modes, as well as of their emission spectra to finally understand reasons of the spectral line intensity increase at the double-pulse mode.

2. MODELING

The numerical code developed consists of two parts. The first one serves to evaluate the laser plumes formation, i.e. to find parameters of the laser-induced plasma, their instantaneous space distributions and the distributions evolution in time. The second one allows evaluating spectral emission of the laser plumes at a given distribution of the parameters along the observation line by solving the radiation transfer problem.

Laser plume formation modeling. The model considers a range of moderate (10^5-10^{10} W/cm^2) laser irradiation of a solid sample surface. The modeling of the plume plasma parameters supposes a self-consistent solution of the thermal, hydrodynamics and optical problems at the laser beam action on solids. The thermal problem accounts for the processes of heating, melting and evaporation of the samples. Dynamics of the solid samples heating and evaporation is described by a non-stationary heat transfer equation taking into account a dependence on temperature of the thermodynamic characteristics of the sample material

$$\frac{\partial(\rho_{sol} c_p T)}{\partial t} + \mathrm{div}\,\vec{W} = 0; \qquad \vec{W} = -\chi(T)\cdot \mathrm{grad}T. \tag{1}$$

at the boundary conditions

$$W_z(r, z=0, t) = (1-R)q(r, z=0, t) - \rho_{sol} V_{sub} \Delta H,$$
$$V_{sub} = \frac{\rho_{vap}(T_s)\sqrt{\gamma k T_s / m}}{\rho_{sol}}. \tag{2}$$

where ρ_{sol} and ρ_{vap} are density of the sample and vapor, respectively, c_p –is specific heat, W and χ are heat flux and heat conduction coefficient, respectively, at temperature T, q is laser beam irradiance, ΔH is evaporation specific enthalpy, V_{sub} is evaporation rate, γ is adiabatic index, R is a reflection coefficient of the laser radiation at the sample surface.

Gas-dynamics part of the code determines an expansion of the erosion products into the surrounding atmosphere, absorption of the laser radiation by the plume, as well as the resulting plasma evolution after the laser pulse is over. The dynamics of the laser plume expansion is accounted for by a system of the equations of mass, pulse and energy conservation, to which equations are added determining intensity of the laser emission incident to the sample surface and reflected from it:

$$\begin{aligned}
&\frac{\partial \rho}{\partial t} + \mathrm{div}\left(\rho \vec{V}\right) = 0 \\
&\frac{\partial \rho u}{\partial t} + \mathrm{div}\left(\rho u \vec{V}\right) + \frac{\partial P}{\partial z} = 0 \\
&\frac{\partial \rho v}{\partial t} + \mathrm{div}\left(\rho v \vec{V}\right) + \frac{\partial P}{\partial r} = 0 \\
&\frac{\partial \rho E}{\partial t} + \mathrm{div}\left((\rho E + P)\vec{V}\right) + \frac{\partial q_+}{\partial z} - \frac{\partial q_-}{\partial z} = 0
\end{aligned} \tag{3}$$

Here u and v are, respectively, axial and radial components of the velocity vector $\vec{V}$, P is pressure, $E = \varepsilon + \vec{V}^2/2$ is total specific energy of the plasma with internal energy ε. The laser emission intensity directed to the surface q_- and reflected from it q_+ is determined by the expressions

$$q_-(r,z,t) = q(r,\infty,t)\cdot \exp\left(-\int_z^{\infty} \kappa_L dz'\right),$$

$$q_+(r,z,t) = R(T_s)\cdot q_-(r,0,t)\cdot \exp\left(-\int_0^{z} \kappa_L dz'\right), \tag{4}$$

where κ_L is the plasma absorption coefficient at the laser wavelength, and $R(T_s)$ is mentioned above the reflection coefficient of the laser radiation at the sample surface generally depending on temperature.

Boundary conditions taken into account at the problem solution can be written as follows:

$$\rho(r \le r_{spot}) = \rho_{vap}(T_s);\quad P(r \le r_{spot}) = P_{vap}(T_s);\quad u(r \le r_{spot}) = \sqrt{\gamma k T_s / m};\quad \varepsilon(r \le r_{spot}) = \varepsilon(T_s). \tag{5}$$

The above system of equations is solved taken into account data of state equations and of absorption coefficient of the plasma under consideration, which are

pre-calculated supposing the plasma is in the local thermodynamic equilibrium and taken in a tabulated form:

$$T = T(\rho, \varepsilon); \quad P = P(\rho, \varepsilon); \quad N_e = N_e(\rho, \varepsilon); \quad \kappa_L = \kappa_L(T, \rho) \qquad (6)$$

The plasma absorption coefficient at the laser emission frequency is calculated taking into account main mechanisms of the absorption in the plasma (bremsstrahlung, photoionization and selective absorption). Thermal radiation transfer in the laser plume, as well as a difference in thermo-dynamical and optical properties of the erosion products and of ambient air are not taken into account at the calculations.

The code allows evaluating the dynamics of two-dimensional erosion plumes supposing their axial symmetry accounted for by *r*- and *z*-coordinates. A distribution of the power density across the laser spot on a sample surface is set to be Gaussian and to depend only on the radial coordinate *r*. The laser beam is supposed to have a cylindrical form and to fall normally on the sample surface. A dependence of the laser power density on time can be fitted to real experimental data. The calculation results are 2D distributions of the erosion plasma temperature, density and pressure depending on time after the laser beam incidence. More detail on the modeling code can be found in [26].

Line spectra modeling of the laser plume. Space-time characteristics of the laser erosion plasma, which are obtained at the plasma formation modeling discussed above, serve as initial data for the emission spectra simulation. From the data, one finds distributions $T(x), \rho(x)$ of the plasma temperature and density along an observation line x and a time moment chosen. For every point of the distributions at given $T(x), \rho(x)$, one determines the plasma elemental composition

$$\rho = m_H \sum_k \beta_k A_k \sum_{i=1}^{Z_k+1} N_{ki}, \qquad (7)$$

where ρ is plasma density in g/cm^3, $m_H = 1.66 \cdot 10^{-24}$ g is mass of hydrogen atom, k designates different chemical elements in the plasma. Every element has β_k volume ratio, A_k atomic number and N_{ki} (cm^{-3}) number density of atoms and ions (N_{k1} for neutral, N_{k2} for the first ion, etc.).

Further, the plasma ionization composition and population density of excited states are found using equations of the ionization equilibrium for every element in the sample [27]:

$$\frac{N_{i+1}N_e}{N_i} = 2\left(\frac{2\pi mkT}{h^2}\right)^{3/2}\frac{U_{i+1}}{U_i}\exp[-(J_i - \Delta J_i)/kT], \tag{8}$$

Partition functions of atoms and ions are calculated according to Planck − Larkin approximation:

$$U_i = \sum_j g_{ij}\exp\left(-E_{ij}/kT\right)W_{ij}, \qquad W_{ij} = 1-\left(1+\frac{J_i - E_{ij}}{kT}\right)\exp\left(\frac{E_{ij}-J_i}{kT}\right). \tag{9}$$

Here U_i is partition function of ions of the i-th ionization degree, g_{ij} and E_{ij} are their statistical weight and energy of the j-th level, respectively, W_{ij} is Planck − Larkin factor.

The ionization potential lowering ΔJ_i due to Coulomb interaction of particles can be written as follows:

$$\Delta J_i = kT\ln\frac{(1+\gamma/2)\left[1+(z_i+1)^2\gamma/2\right]}{\left(1+z_i^2\gamma/2\right)}, \tag{10}$$

where z_i is charge of ion (i=1 for neutral atom), γ is determined as a positive route of the equation

$$\gamma^2 = \left(\frac{e^2}{kT}\right)^3 4\pi\sum_i \frac{n_i z_i^2}{1+z_i^2\gamma/2}, \tag{11}$$

and for weakly non-ideal plasma it coincides with the common non-ideality parameter.

For the calculation of the particles partition functions, a database is incorporated in the program on energy levels and statistical weights of atoms and ions of different chemical elements.

Further in the program, spectral emission j_λ and absorption κ_λ coefficients are calculated for chosen lines in radiation spectra of the laser plumes under consideration

$$j_\lambda = A_{mn}\frac{hc}{\lambda_0}N_m\phi(\lambda) = \kappa_\lambda 4\pi I_{\lambda P}.$$

$$\kappa_\lambda = \frac{\pi e^2\lambda_0^2}{mc^2}f_{nm}N_n\left[1-\exp\left(-\frac{hc}{\lambda_0 kT}\right)\right]\phi(\lambda), \tag{12}$$

where A_{mn} and f_{nm} are, respectively, transition probability and oscillator strength for the line optical transition, $I_{\lambda P}$ is spectral intensity of the black body radiation, $\phi(\lambda)$ is spectral profile of the plasma emission coefficient within the line. Stark broadening is considered in the program as the main mechanism forming line profiles in the laser plume emission spectra. In this case, emission coefficients for the lines have Lorentzian profiles and can be accounted for by the expression [28]

$$\phi(\lambda) = (\gamma_e / \pi)[\gamma_e^2 + (\lambda - \lambda_0 - \delta_e)^2]^{-1}, \tag{13}$$

where γ_e and δ_e are half-width and shift, respectively, of the profile. These profile parameters are taken proportional to the electron density

$$\gamma_e = w(T) \cdot N_e \cdot 10^{-16}, \qquad \delta_e = d(T) \cdot N_e \cdot 10^{-16}. \tag{14}$$

The proportionality coefficients $w(T)$ and $d(T)$ are known as Stark broadening parameters for the width and shift, respectively. At this approximation, no possible influence of ion micro-fields is taken into account.

Spectral line intensity in the laser plume emission is determined by numerical solution of the radiation transfer equation [29]

$$I_\lambda(\tau) = I_\lambda(0)\exp(-\tau) + \int_0^\tau I_{\lambda P}(\tau')\exp(\tau' - \tau)d\tau',$$

$$\tau = \int_y^{r_0} \kappa_\lambda(y')dy', \tag{15}$$

where r_0 is the plume radial border at a given time moment. The equation solution procedure and spectral line intensity evaluation is performed similar to [30].

The numerical solution of (15) is reduced to a recursion relation for the intensities of the radiation at the neighboring space points [31]. The plasma parameters (ionization state, spectral emission, absorption coefficient and their profiles for the selected line) are calculated at chosen discrete points on the observation line taken into account the temperature profile obtained at the plasma plume formation modeling. Parameters of the optical transitions resulting in the emission of chosen spectral lines, including the lines Stark broadening parameters, transition probabilities and statistical weights of the energy levels, are taken from [28, 32].

3. EXPERIMENTAL

Experimental measurements have been performed using a Laser Spectrochemical Analyzer (LSA) [20]. A general view of LSA and its schematic diagram are shown in Fig. 1. LSA is composed of a

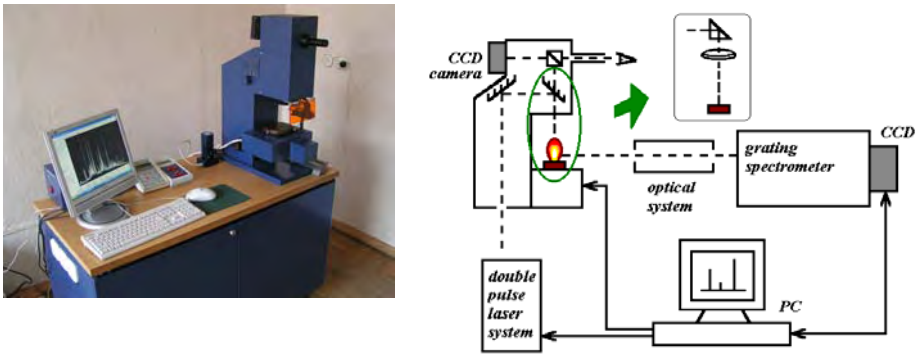

a b

Fig. 1. Laser spectrochemical analyzer: (a) general view and (b) schematic diagram.

Q-switched Nd:YAG double pulse laser, an optical unit consisting of microscope, imaging CCD-camera and PC-controlled sample table, a spectrometer with a CCD-arrays recording system. The laser works at wavelength of 1064 nm. The laser pulses duration and frequency can be controlled in the intervals of 10-20 ns and 1-15 Hz, respectively. The pulses energy is also variable and can be set as high as 100 mJ. The laser can work both in the single- and double-pulse modes at the collinear scheme of the laser beams action on a sample. A time delay between the pulses can be regulated from 0 to 140 μs. The laser action zone is imaged at the PC monitor and can be positioned on a sample with 0.01 mm accuracy. LSA is equipped with a 1-meter grating spectrometer for recording the spectral emission of the laser plumes. Wavelength working interval and spectral resolution of the spectrometer are 200 – 800 nm and 20000, respectively. An optical system serves to deliver the plasma plume emission to the spectrometer entrance slit. LSA operates at a PC control. The PC software allows recording and treatment the plume emission spectra and the erosion crater images, as well as plotting calibration graphs and evaluating elemental compositions of samples.

4. RESULTS AND DISCUSSION

A study has been performed of formation and space-time evolution of laser ablation plumes on aluminum sample in atmospheric pressure air at single- and double-pulse excitation modes. The plume emission spectra have been recorded in the spectral interval of 250-400 nm at 0.74 nm/mm dispersion and 0.015 nm spectral resolution using LSA equipped with PGS-2 spectrograph and TCD1205 CCD array. A side-on observation has been chosen for the measurements. The optical axis has been directed along the sample surface at a chosen distance *z* from it. The plumes have been imaged 3:1 by lenses onto an intermediate slit (diaphragm). The slit edges are perpendicular to the plume axis discriminating a part of the plume of 1 mm height. The second optical system after the diaphragm collected total emission of the "disk" to the spectrograph entrance slit. Displacing the diaphragm along the plume axis, one could record the plume emission at different distances *z* from the surface. The measurements spatial resolution was estimated to be 0.1 and 0.5 mm along the axial and radial directions, respectively.

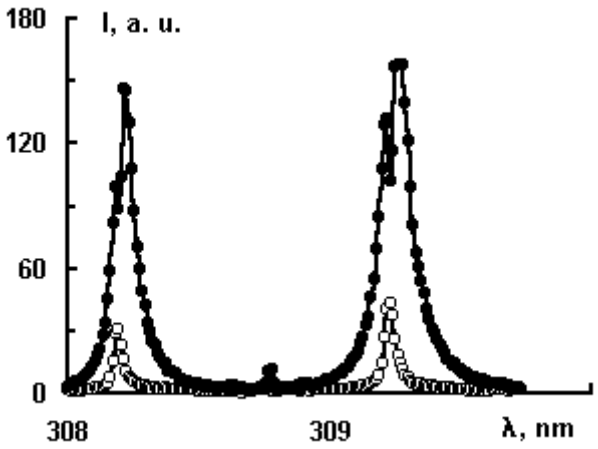

Fig. 2. Emission spectra of the laser-induced Al plasma at SP (open circles) and DP (solid circles) modes recorded 1 mm above the sample surface (one can see atomic lines Al I 308.2 and Al I 309.3 nm).

The measurements have been performed at the action on Al sample polished surface of the laser pulses of 0.05 J energy and 15 ns (FWHM) duration with a "tail" up to 75 ns. The laser beam was focused 5 mm below the surface. For one single-pulse shot, it resulted in 820 MW/cm^2 maximum irradiation of the sample surface at a near-Gaussian spatial distribution with 0.54 mm characteristic radius. At the spectra recording, the sample was irradiated with a series of single or double pulses at 10 Hz frequency. Total emission of laser plumes from 80 single pulses and

40 double pulses at SP and DP modes, respectively, was recorded to increase the signal level keeping equal energy at both modes. The signal measurements were performed with no time resolution. The sample was not moved during the spectra recording. A time delay of 5 μs was realized between the first and the second pulses at the DP mode. The delay was shown to give the most pronounced effect of the DP mode at the conditions under consideration [20]. The intensity increase at DP mode for this work conditions is demonstrated by Fig. 2, where recorded at the both modes spectra of the laser plume emission in a spectral region of Al I atomic lines are presented.

The numerical modeling has been performed at the same conditions as the measurements. The reflection coefficient of the sample R=0.9 has been taken and accepted to be constant. At the simulation of the laser plume formation at DP mode, conditions and plasma parameters of the first laser pulse plume formed to the moment equal to a given time delay between the pulses have been taken as initial ones for the space-time characteristics calculation of the laser plume induced by the second laser pulse. For the rest, the calculation procedure has been performed analogous to the SP plume simulation.

According to the modeling results for the SP mode, the evaporation begins at 8 ns, at 15 ns the plasma occurs, at 30 ns the ablation plume shields the sample preventing material erosion. Further, the laser radiation is totally absorbed by the ablation plume, and a wave of absorption propagates towards the laser beam in the light detonation regime. When the laser pulse is over, the wave of absorption is at 0.5 mm distance from the sample surface, and the plume expansion still has a “one-dimensional” character. Radial inhomogeneity of the laser plume is determined by the distribution of the power density over the erosion spot.

The main difference of the second pulse action at DP mode is existence of a sheet of strongly absorbing plasma near the sample surface. The plasma optical density is around $5 \cdot 10^{-3}$ to the moment of the second pulse action. The density reaches 1 already in 20 ns and 3 in 22 ns after the second pulse begins. The latter value is characteristic for the main time interval of the laser pulse action. The optical density slow decrease begins only in 60 ns from the pulse beginning. Thus according to the calculation, the sample surface is actually shielded from the laser radiation. The radiation strong absorption by plasma results in an increase of the plume dimension in both radial and axial directions. One can observe the increase in Fig. 3, where axial distributions of plasma temperature and density in a laser pulse at SP and in the second pulse at DP modes are shown for different moments from the due pulse action.

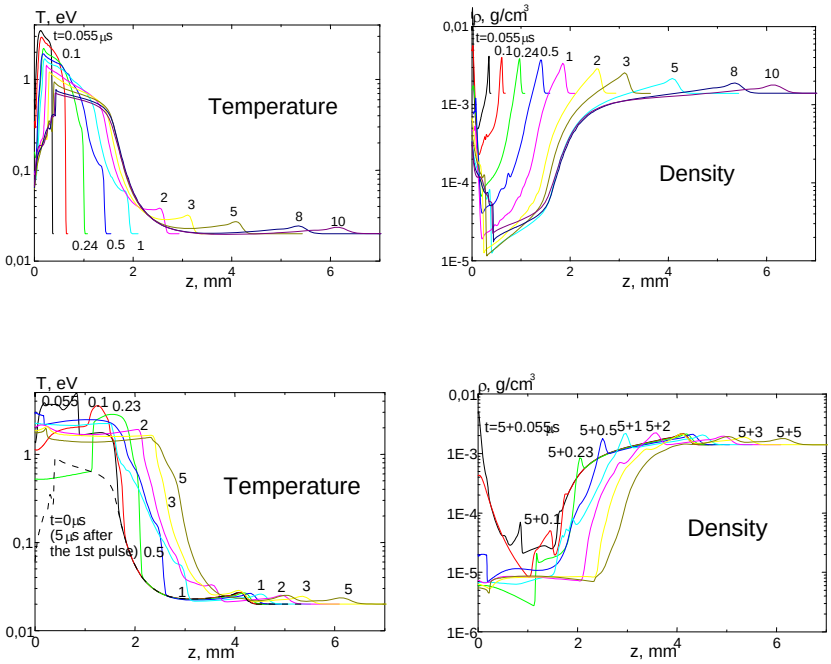

Fig. 3. Axial distribution of plasma temperature and density in the laser plumes at SP (up) and DP (down) modes at different time intervals from the laser pulse action (shown in micro-seconds).

Time evolution of radial distributions of plasma temperature and density in the SP and DP laser plumes is demonstrated by Fig. 4, where the distributions at z=1 mm for different time intervals from the laser pulse action (the second one for the DP mode) are shown. Comparing to the SP plume, higher temperature (20-30 kK, instead of 5-10 kK) and lower density are characteristic for central parts of the DP laser plume. Also the DP plume has complex non-monotonous temperature profiles, contrary to those at the SP mode having one central maximum and nearly parabolic shape. For the first 1-2 μs, pressure is higher in the SP plume, but further it is close to the ambient (atmospheric) one in the both modes.

The radial distributions have been used for the calculations of "side-on recorded" intensity of the spectral line chosen. They have been mostly limited with the temperature of 3000 K. At lower temperature, density of exited atoms is too low and their emission can be neglected. Also, Al vapor condensation begins in this temperature region. Spectral line intensities for all time moments considered have been integrated to obtain the value corresponding to the experimental one measured without any resolution in time.

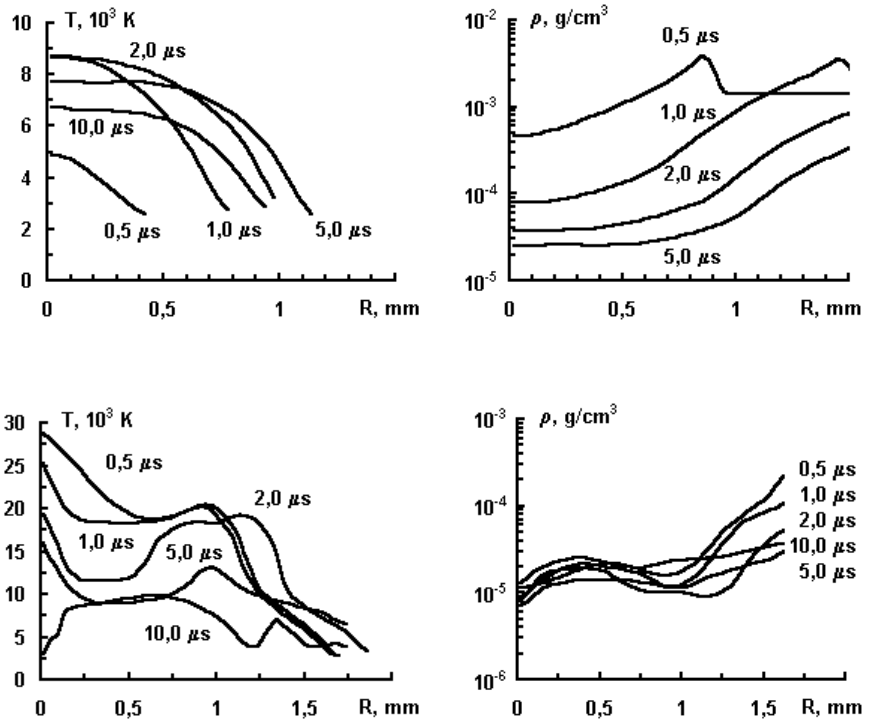

Fig. 4. Radial profiles of temperature (left) and density (right) in the laser plumes at the SP (up) and DP (down) modes for a distance z=1 mm from the sample surface at different time intervals from the laser pulse action (shown in micro-seconds).

An example of the results is presented in Fig. 5, where measured and numerically simulated spectral profiles are presented for integrated in time intensity of Al II line at λ=281.6 nm in emission of the laser plumes at the SP and DP modes at z=1 mm. As far as no absolute calibration has been performed of the experimental data, they were reduced to the absolute scale of the values obtained at the simulation by equalization maxima of the measured and calculated DP line profiles. It is seen that the ion line SP intensity is close to a detection limit and the DP intensity is more than 10 times higher. One can observe a fair agreement of the measured and simulated DP line profiles.

Generally, it is observed that the intensity increase in DP spectra compared to SP ones depends on excitation energy of the lines under consideration. It increases with the excitation energy and it is much stronger for ion than for atomic lines (see, e.g., [20, 33, 34]). This difference is more pronounced for the integrated

in time emission intensity of laser plumes. The observation is confirmed also by the data of our measurements exposed in figures 2 and 5.

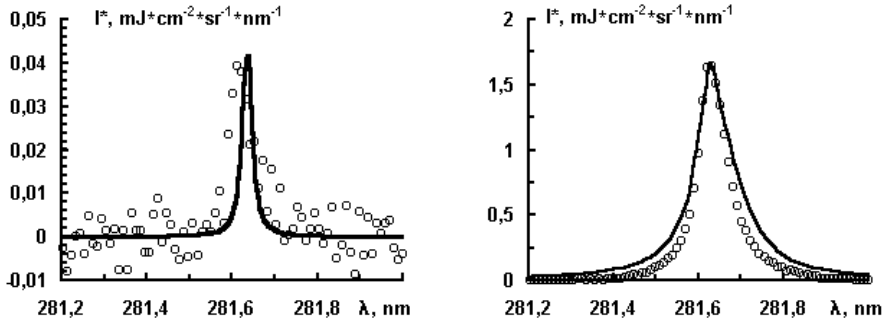

Fig. 5. Measured (points) and simulated (lines) profiles of Al II 281.6 nm line in the laser plume emission at SP (left) and DP (right) modes for a side on observation at z=1 mm from the sample surface.

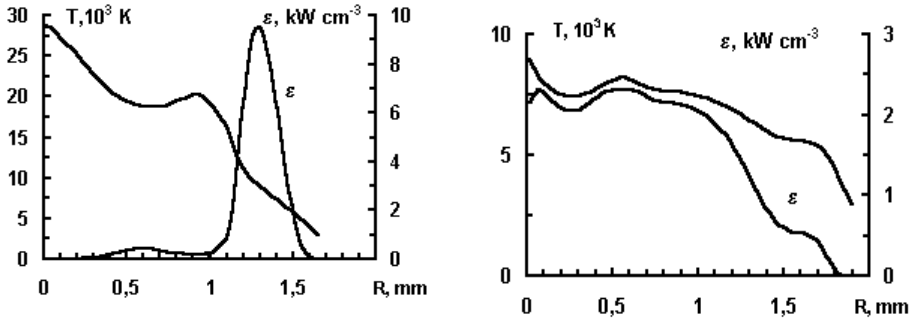

Fig. 6. Radial distribution of plasma temperature and emission coefficient for atomic Al I 308.2 nm line in the DP laser plume and z=1 mm at 0.5 (left) and 15 (right) μs from the second pulse action.

Our numerical simulation data allow better understanding reasons of the intensity increase at DP mode and its dependence on excitation energy of spectral lines. In Fig. 6, radial distributions are shown of plasma temperature and emission coefficient for atomic Al I 308.2 nm line in the DP laser plume at 0.5 and 15 μs from the second pulse action. One can see from the figure that at initial time

moments the atomic line intensity in the laser plume emission spectrum is provided by a narrow space zone at the plume periphery, where the line emission coefficient is high. It is due to a relatively low (around 8000 K) “normal temperature” [35] of the line and to a rather steep temperature radial gradient. In this case, the DP line intensity can be not very different from the intensity at the SP mode, where the plasma temperature does not prevail “normal” one (see Fig. 4). On the contrary, later when the plasma temperature decreases, a zone of the line effective emission occupies nearly all plasma plume volume on the observation line, and the line intensity can noticeably grow up in comparison with the SP mode. The intensity increase will depend on the effective volume dimension. For ion lines the effective emission volume at the DP mode will be much larger from the beginning of the plume expansion. Additionally, the ion emission coefficient will rise strongly over the plume volume due to the elevated “normal temperature”, which in most zones is much higher than the DP plasma temperature resulting in the steep coefficient dependence on temperature.

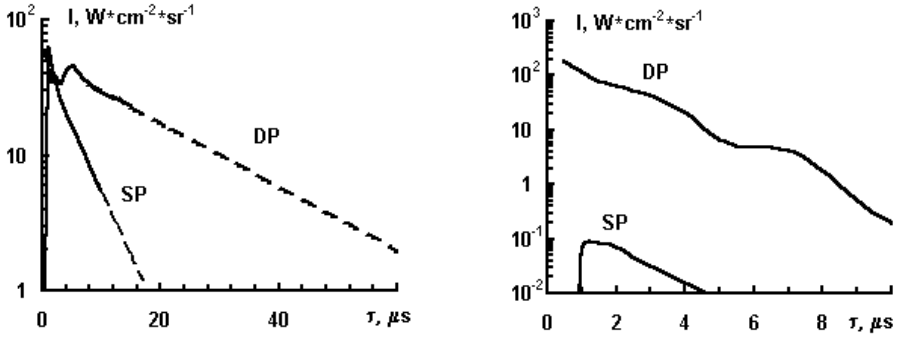

Fig. 7. Total intensity of atomic Al I 308.2 nm (left) and ionic Al II 281.6 nm (right) spectral lines in the SP and DP laser plume emission at z=1 mm depending on time from the laser pulse action. Dashed line shows the data extrapolation.

A behavior in time of the lines intensity in emission spectra of the plumes can be analyzed using Fig. 7, where total intensity of atomic Al I 308.2 nm and ionic Al II 281.6 nm spectral lines in the SP and DP laser plume emission is presented depending on time from the laser pulse action. It is seen from the figure that the DP intensity increase of the atomic line depends on time from the laser pulse action, and for small time intervals one can found no efficiency increase of the DP mode. Possibly, it can explain controversial evaluations of the DP mode influence on atomic line intensity, which can be observed in some papers.

Generally, one can see that for the DP laser plume higher plasma temperature, the plume volume and duration are characteristic. All the factors play certain roles in the observed increase of line intensity in DP plume emission spectra. The factors influence on atomic and ionic lines can be different depending on a temperature interval realized. In our case, the DP intensity amplification of atomic

lines is mainly due to an increase of the effective emission volume dimension and duration. As for the DP intensity of ionic lines, its growth is provided more by the temperature (emission coefficient) increase.

The numerical simulation results on the line intensity in the total emission spectra of SP and DP plumes have been compared to our experimental data. According to the measurement mode, total intensity of atomic Al I 308.2 nm and ionic Al II 281.6 nm lines in emission spectra of the plumes observed at different distances z from the sample surface have been calculated. For every z, the intensity has been integrated over all life time of the plumes. The emission intensity of both pulses at the DP mode has been summed and doubled SP intensity has been taken to compare to each other and to analogous measured values. The measured intensity has been reduced to the calculated intensity scale supposing the intensity values of the SP emission obtained at the simulation and measurements at z=0.5 mm are equal. The results obtained are shown in Fig. 8.

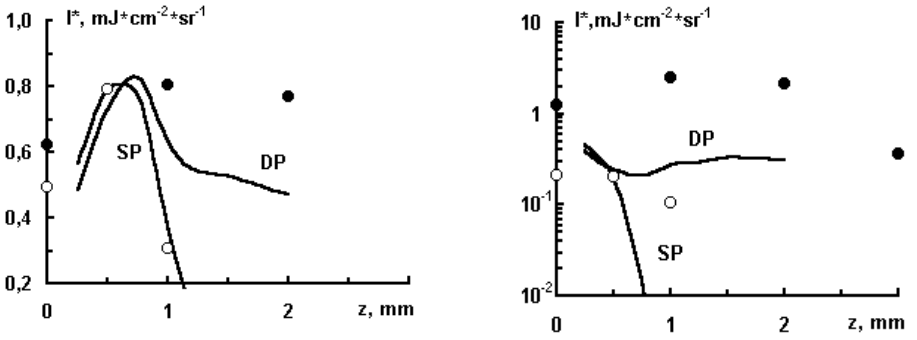

Fig. 8. Integrated in time intensity of atomic Al I 308.2 nm (left) and ionic Al II 281.6 nm (right) lines in emission spectra of the laser plume depending on distance z from the sample surface: lines present the modeling results, points show the measurements data for the SP (open circles) and DP (solid circles) modes.

From the figure it follows that the DP plumes are larger than SP ones and the DP intensity gain depends on a distance z from the sample of the side-on observation line. The gain increases with the distance from the sample. One can state a rather fair agreement of the experiment and simulation data at the SP mode, especially for the atomic line. (Note, the measured values at z=0 can be distorted by the sample border shielding). Generally, experimentally observed plumes are larger than the simulated ones. Partly it can be explained by the radiation energy transfer in the plumes, which is not taken into account in the modeling code. Also, laser erosion of the sample can be higher, than it is given by the model, where constant reflection coefficient is used for both laser plumes in the DP mode.

5. CONCLUSION

Numerical simulation and measurements have been performed of the intensity of atomic and ionic lines in emission spectra at a side-on observation of erosion plasma induced by pulses of a Q-switched Nd:YAG laser on Al sample in single and double pulse excitation modes for typical LIBS conditions. The spectra have been obtained by a numerical solution of the radiation transfer equation for radial distributions of the erosion plasma parameters, taken from the laser plume numerical modeling. The modeling consists of a solution the thermal, hydro-dynamics and optical problems accounting for the laser beam action on a solid surface. The numerical code allows a simulation of the dynamics of two-dimensional erosion plumes supposing their axial symmetry.

A qualitative correlation of the calculated and measured data is observed. The comparison seems to show an important role of the radiation transfer processes in the laser plume formation. The DP plasma expansion lasts longer and it occupies larger volume with non-monotonous temperature distributions. Also, an increase of the laser plasma temperature is observed at the DP mode.

These changes result in the observed increase of line intensity in the DP plume emission spectra. The intensity gain is due to the emitting plasma temperature and volume increase. A role of the factors is different for atomic and ionic lines. In our case, when the DP plasma temperature overcome “normal temperature” for atomic lines, their emission is formed mainly in the plume periphery, and the main reason for their intensity increase is mainly the plasma volume and duration increase. The ionic line intensity increases mainly due to higher plasma temperature (emission coefficient). Note, sometimes one finds no increase in DP plasma temperature measured by relative intensity of atomic lines. It can be shown that such measurement for the considered inhomogeneous laser plasma must give rather a temperature value close to “normal temperatures” of the atomic line used [36].

Further, it is supposed to consider more factors influencing sample erosion, especially at the DP mode and to develop the numerical code including calculations of the energy transfer by the laser plume own radiation with a detailed account of its angular and spectral characteristics.

REFERENCES

1. L.J. Radziemski, Spectrochim. Acta, Part B **57**, 1109-1113 (2002).
2. N. Omenetto, J. Anal. At. Spectrom. **13**, 385-399 (1998).
3. J.D. Winefordner, I.B. Gornushkin, T. Correll et al., J. Anal. At. Spectrom. **19**, 1061-1083 (2004).
4. J.M. Vadillo, J.J. Laserna, Spectrochim. Acta, Part B **59**, 147-161 (2004).
5. V.A. Rozantsev, Proc, Rep. Sci. Sem. Atom. Spectr. Analys. Minsk, 12-14 (1978).
6. V.A. Rozantsev, V.A. Kononov, VII Rep. Conf. Young Sci. on Phys. Abstracts, Mogiliov, 123 (1982).
7. S.M. Pershin, Quantum Electronics, **16**, 325-330 (1982).

8. K. Takaharu, S. Hiroya, S. Koichi, M. Katsusuke, Japanese Patent, JP62-85847 (1987).
9. V.A. Rozantsev, A.D. Shirokanov, A.A. Yankovsky, Zhurn. Prikl. Spektrosk. (Rus) **59**, 431-434 (1993).
10. L. St-Onge, V. Detalle, M. Sabsabi, Spectrochim. Acta, Part B **57**, 121-135 (2002).
11. R. Noll, R. Sattman, V. Sturm, S. Winkelmann, J. Anal. At. Spectrom. **19**, 419-428 (2004).
12. M. Corsi, G. Cristoforetti, M. Giuffrida, M. Hidalgo, S. Legnaioli, V. Palleschi, A. Salvetti, E. Tognoni, C. Vallebona, Spectrochim. Acta, Part B **59**, 723-735 (2004).
13. J.A. Aguilera, C. Aragon, Spectrochim. Acta, Part B **59**, 1861-1876 (2004).
14. X. Mao, X. Zeng, S.-B. Wen, R.E. Russo, Spectrochim. Acta, Part B **60**, 960-967 (2005).
15. D.N. Stratis, K.L. Eland, S.M. Angel, Appl. Spectrosc. **55**, 1297-1303 (2001).
16. C. Gautier, P. Fichet, D. Menut, J.-L. Lacour, D. L'Hermit, J. Dubessy, Spectrochim. Acta, Part B **60**, 265-276 (2005).
17. G. Cristoforetti, S. Legnaioli, L. Pardini, V. Palleschi, A. Salvetti, E. Tognoni, Spectrochim. Acta, Part B **61**, 340-350 (2006).
18. J. Uebbing, J. Brust, W. Sdorra, F. Leis, K. Niemax, Appl. Spectrosc**. 45**, 1419-1423 (1991).
19. C. Gautier, P. Fichet, D. Menut, J.-L. Lacour, D. L'Hermit, J. Dubessy, Spectrochim. Acta, Part B **59,** 975-986 (2004).
20. E. Ershov-Pavlov, M. Petukh, V. Rozantsev, 2nd Euro-Mediter. Symp. on LIBS (Book of abstracts), Hersonissos, Crete, Greece, 12 (2003).
21. E. Ershov-Pavlov, Yu. Stankevich, and K. Stepanov, 3rd Euro-Mediter. Symp. on LIBS (EMSLIBS 2005), Aachen, Germany CD, 4-6_AB10063 (2005).
22. I.B. Gornushkin, C.L. Stevenson, B.W. Smith, N. Omenetto, J.D. Winefordner, Spectrochim. Acta, Part B **56,** 1769-1785 (2001).
23. V.I. Mazhukin, V.V. Nossov, G. Flamant, I. Smurov, J. Quant. Spectr. Rad. Transf. **73**, 451–460 (2002).
24. A. Bogaerts, Z. Chen, R. Gijbels, A. Vertes, Spectrochim. Acta, Part B **58,** 1867-1893 (2003).
25. M. Capitelli, A. Casavola, G. Colonna, A. De Giacomo, Spectrochim. Acta, Part B **59**, 271-289 (2004).
26. G.S. Romanov, A.S. Smetannikov, Y.A. Stankevich, L.K. Stanchits, K.L. Stepanov, V Minsk Int. Heat & Mass Transfer Forum. Minsk, Proc. on CD, No 2.43 (2004).
27. G.S. Romanov, Yu.A. Stankevich, L.K. Stanchits, K.L. Stepanov, Int. J. Heat and Mass Transfer **38**, 545-556 (1995).
28. H.R. Griem, Spectral Line Broadening by Plasmas, N.-Y., London, Acad. Press, 1974.
29. E. A. Ershov-Pavlov and K. L. Stepanov, J. Appl. Spectrosc. **68**, 350–358 (2001).
30. E. A. Ershov-Pavlov, K.Yu. Katsalap, K. L. Stepanov, J. Appl. Spectrosc. **72**, 434–442 (2005).

31. E. A. Ershov-Pavlov, V. E. Okunev, Yu. A. Stankevich, L. K. Stanchits, K. L. Stepanov, Publ. Obs. Astron. Belgrade **66**, 19–33 (1999).
32. http://www.nist.gov
33. M.P. Petukh, V.A. Rozantsev, A.D. Shirokanov, A.A. Yankovsky, Zhurn. Prikl. Spektrosk. (Rus) **67**, 798-801 (2000).
34. C. Gautier, P. Fichet, D. Menut, J.-L. Lacour, D. L'Hermit, J. Dubessy, Spectrochim. Acta, Part B **60**, 792-804 (2005).
35. J.Richter, in Plasma Diagnostics, W. Lochte-Holtgreven ed., Amsterdam (1968).
36. E.A. Ershov-Pavlov, K.L. Stepanov, Proc. 15th Int. Symp. Plasma Chem. (ISPC-15), Orleans. 3 1057-1062 (2001).

VI Serbian-Belarusian Symp. on Phys. and Diagn. of Lab. &
Astrophys. Plasma, Belgrade, Serbia, 22 - 25 August 2006
eds. M. Ćuk, M.S. Dimitrijević, J. Purić, N. Milovanović
Publ. Astron. Obs. Belgrade No. 82 (2007), 101-116 *Invited lecture*

DYNAMICS OF WEAKLY RELATIVISTIC ELECTROMAGNETIC SOLITONS IN LASER PLASMAS

Lj. Hadžievski[1], A. Mančić[2], M. M. Škorić[3]

[1]*Vinča Institute of Nuclear Sciences,*
P. O. Box 522, 11001 Belgrade, Serbia
[2]*Department of Physics, Faculty of Sciences and Mathematics,*
University of Niš, P. O. B. 224, 18001 Niš, Serbia
[3]*National Institute for Fusion Science, Toki, 509-5292, Japan*

Abstract. Dynamical features of one-dimensional electromagnetic solitons formed in a relativistic interaction of a linearly polarized laser light with underdense cold plasma are investigated. The relativistic Lorentz force in an intense laser light pushes electrons into longitudinal motion generating coupled longitudinal-transverse waves. In a weakly relativistic approximation these modes are well described by the generalized nonlinear Schrödinger type of equation, with two extra nonlocal terms. Here, an original analytical solution for a *moving* EM soliton is derived in an implicit form. For an isolated soliton, our analysis shows that the motion down-shifts the soliton eigen-frequency and decreases its amplitude. The effect of the soliton velocity on the stability, is analytically predicted and checked numerically. Results show an enhanced stability in comparison with the standing soliton case. Rich dynamics with examples of (un)stable soliton propagation and breathers creation and formation of unstable structures of cusp type is exposed numerically. The soliton stability is a base for the understanding a complex soliton-pair interaction; which critically depends on solitons amplitude, velocity and a mutual phase relation. Simulations of two interacting EM solitons show a critical dependence on the solitons amplitude, velocity and mutual phase; resulting in either elastic collisions or a break up of the soliton pair.

1. INTRODUCTION

The propagation of intense laser radiation into plasmas has attracted considerable attention in the past. Recently, the interest for this problem is renewed mainly due to two prospective applications: development of the fast ignition concept

in inertial fusion and x-ray lasers. Currently, available laser intensity is as high as $10^{21}\mathrm{W/cm}^2$ at a focus, with tendency to reach soon $10^{23}\mathrm{W/cm}^2$. These intensities are well above the regime where, in the laser plasma interactions, the electrons are forced into motion with relativistic velocities. This strongly affects the dynamics of the laser pulse propagation and with combination of the nonlinear effects induces a large number of nonlinear relativistic phenomena. One of the most interesting phenomena is creation of the relativistic electromagnetic (EM) solitons. Relativistic EM solitons are localized EM structures self-trapped by a locally modified plasma refractive index due to the relativistic electron mass increase and the electron density drop in the ponderomotive force of an intense laser light. These solitons, generated behind the front of the laser pulse are composed of nonlinear, spatially localized low-frequency EM fields with a group velocity close to zero. A large part of the laser pulse energy can be trapped inside these relativistic solitons, creating a significant channel for laser beam energy conversion. This is a known problem in plasma physics which has been studied widely in the past [1-8] but it has recently attracted fresh attention. The relativistic EM solitons in an idealized case of circular polarization were extensively investigated, analytically within the one-dimensional (1D) fully relativistic hydrodynamics model and by PIC (particle-in-cell) simulations [1, 9]. Recently, relativistic EM solitons in electron-ion plasmas have been studied in detail, analytically [9-14], numerically by fluid simulations [15] and by multi-dimensional PIC simulations [7,16-20]. On the other hand, a physically more realistic, but also a more complex case of relativistic EM solitons with a linear polarization, was studied in a weak amplitude limit by some of these authors [20, 21]. Generally taken, the research on solitons has been receiving much attention because of their fundamental importance in nonlinear science [4], as well as being considered to be the essential component of plasma turbulence [13].

In this paper, we treat a case of a linearly polarized intense laser light. In laser-plasma interactions, relativistic Lorentz force sets electrons into motion, generating coupled longitudinal-transverse wave modes. These modes in the framework of one-dimensional weakly relativistic cold plasma approximation can be well described by a single dynamical equation of the generalized nonlinear Schrödinger type[21], with two extra nonlocal (derivative) terms. A new analytical solution for the one-dimensional *moving* EM soliton case is calculated in the implicit form and verified numerically. The soliton existence and its stability properties depending on the soliton velocity and self-frequency shift are studied in detail, by using analytically calculated conserved quantities: photon number (P) and Hamiltonian (H). The results are compared to the standing (non-moving) relativistic EM solitons case [21]. Finally, numerical simulations of the model equation were performed to check the analytical results and study soliton dynamics influenced by small perturbations. A good agreement with our analytical results is found. The results of the soliton stability analysis are base for the understanding a complex soliton-pair interaction, which critically depends on solitons amplitude, velocity and a mutual phase relation. Simulations of two interacting EM solitons show a critical dependence on the solitons amplitude, velocity and mutual phase; resulting in either elastic collisions or a break up of the soliton pair.

2. DYNAMICAL EQUATIONS

We consider a long intense laser pulse propagating through cold collisionless plasma with fixed ions and start with writing the fully relativistic one-dimensional model. The nonlinear EM wave equation, continuity equation and electron momentum equation, in the Coulomb gauge, read:

$$\left(\frac{\partial^2}{\partial t^2} - c^2\frac{\partial^2}{\partial x^2}\right)a = -\frac{\omega_p^2}{n_0}\frac{n}{\gamma}a \tag{1}$$

$$\frac{\partial n}{\partial t} + \frac{\partial}{\partial x}\left(\frac{np}{m\gamma}\right) = 0 \tag{2}$$

$$\frac{\partial p}{\partial t} = -eE_{\|} - mc^2\frac{\partial \gamma}{\partial x} \tag{3}$$

where $a = eA/mc^2$ is normalized vector potential in the *y* direction, *n* is the electron density, *p* is the electron momentum in the *x* direction, $\gamma = (1 + a^2 + p^2/m^2c^2)^{1/2}$, $E_{\|}$ is the longitudinal electric field, n_0 is the unperturbed electron density, and $\omega_p = (4\pi e^2 n_0/m)^{1/2}$ is the background electron plasma frequency.

In a weakly relativistic limit for $|a| << 1$ and $|\delta n| << 1$, introducing the normalized perturbed electron density $\delta n = (n - n_0)/n_0$ and dimensionless variables $x \to (c\omega_p^{-1})x$ and $t \to (\omega_p^{-1})t$, the wave equation for the vector potential envelope *A* ($a \sim A \cdot e^{-it} + cc$) is obtained, as (details are given in Ref. 21):

$$i\frac{\partial A}{\partial t} + \frac{1}{2}A_{xx} + \frac{3}{16}|A|^2 A - \frac{1}{8}(|A|^2)_{xx}A + \frac{1}{48}(A^2)_{xx}A^* = 0 \tag{4}$$

Equation (4) has a form of a generalized nonlinear Schrödinger (GNLS) equation with two extra nonlocal (derivative) nonlinear terms. We can readily derive three conserved quantities: photon number *P* and Hamiltonian *H* and momentum *M*:

$$P = \int |A|^2\, dx,$$

$$H = \frac{1}{2}\int\left\{|A_x|^2 - \frac{3}{16}|A|^4 - \frac{1}{8}[(|A|^2)_x]^2 + \frac{1}{12}|A|^2|A_x|^2\right\}dx \tag{5}$$

$$M = i\int\left(A \cdot A_x^* - A^* \cdot A_x\right)dx$$

We look for a localized stationary solution of (4), in a form of a moving soliton:

$$A = \rho(u)\exp[i\theta(u) + i\lambda^2 t] \tag{6}$$

where, $u = x - vt$, and v is the soliton velocity. Introducing the ansatz (6) in the equation (4), we obtain two equations for the soliton phase and amplitude, respectively:

$$\theta_{uu}\rho(1+\frac{1}{12}\rho^2) + \theta_u\rho_u(2+\frac{1}{3}\rho^2) - 2v\rho_u = 0 \tag{7a}$$

$$\rho_{uu} - \frac{\frac{5}{12}\rho}{1-\frac{5}{12}\rho^2}\rho_u{}^2 = \frac{\left(\frac{\theta_u{}^2}{6} - \frac{3}{8}\right)\rho^3 + \left(2\lambda^2 - 2v\theta_u + \theta_u{}^2\right)\rho}{\left(1-\frac{5}{12}\rho^2\right)} \tag{7b}$$

Under vanishing (localized) boundary conditions $\rho(u), \rho(u)_u, \rho(u)_{uu} \to 0$ for $u \to \pm\infty$, the first integration of (7a) approximately gives $\theta_u(u) = v$, while the first integration of (7b) gives:

$$(\rho_u)^2 = \frac{2\lambda^2 - v^2 - \left(\frac{3}{16} - \frac{v^2}{12}\right)\rho^2}{1-\frac{5}{12}\rho^2}\rho^2 \tag{8}$$

Additional integration of (8) yields a moving soliton solution in an implicit form

$$\pm u = \frac{1}{2\sqrt{2\lambda^2 - v^2}} \ln \frac{\sqrt{1-\frac{\rho^2}{\rho_0^2}} + \sqrt{1-\frac{5}{12}\rho^2}}{\left|\sqrt{1-\frac{\rho^2}{\rho_0^2}} - \sqrt{1-\frac{5}{12}\rho^2}\right|} - \frac{1}{\sqrt{\frac{9}{20}-\frac{v^2}{5}}} \ln \frac{\sqrt{1-\frac{5}{12}\rho^2} + \sqrt{\frac{5}{12}\rho_0^2 - \frac{5}{12}\rho^2}}{\sqrt{\left|1-\frac{5}{12}\rho_0^2\right|}} \quad (9)$$

where ${\rho_0}^2 = \frac{2\lambda^2 - v^2}{3/16 - v^2/12}$ is the maximum amplitude of the linearly polarized moving EM soliton with the self-frequency $\Lambda = \lambda^2 - v^2$. For a zero soliton velocity, $v = 0$, the above solution readily coincides with the standing soliton result of the GNLS equation (4), given by some of these authors [21]. The equation (9) imposes the constraint on the maximum possible soliton amplitude, as $\rho_c < \sqrt{12/5} \approx 1.55$. For $\rho_0 << 1.55$ the soliton profile (9) is the secant hyperbolic, alike the soliton solution of the standard cubic NLS equation. When ρ_0 increases and approaches the value of $\rho_c \approx 1.55$, the original NLS soliton profile steepens and transits toward the pointed, cusp type of a profile.

In order to check the validity of the analytical solution (9), the stationary equations (7a,b) are numerically solved with the vanishing boundary conditions $\rho(u), \rho(u)_u, \rho(u)_{uu} \to 0$ when $u \to \pm\infty$. Numerical results are in a good agreement with the analytical solution for the amplitude (9) and phase $\theta(u)$ (Fig. 1). The only noticeable difference is in the phase $\theta(u)$ (analytical approximation).

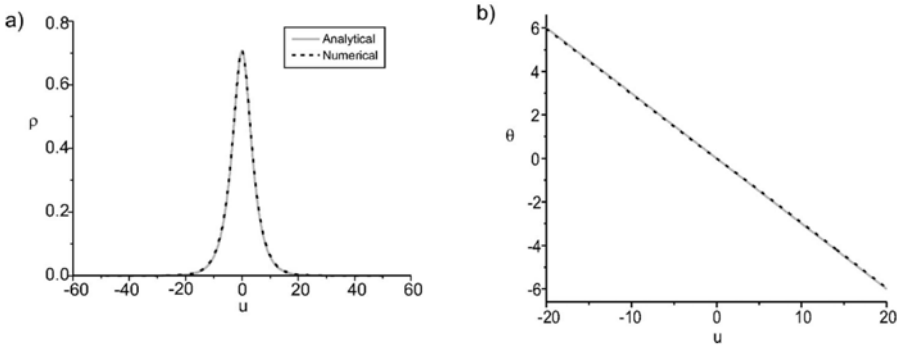

Fig. 1. Example of the EM soliton amplitude profile (a) and phase (b) calculated analytically and numerically for v=0.4 and λ=0.3.

The photon number $P(\lambda, v)$ for the soliton (9), can be calculated explicitly, as:

$$P_0(\lambda, v) = \frac{1}{\sqrt{3/16 - v^2/12}} \left[\rho_0 + \sqrt{\frac{3}{5}} \left(1 - 5\rho_0^2/12\right) \ln \frac{1 + \rho_0 \sqrt{5/12}}{\left|1 - \rho_0 \sqrt{5/12}\right|} \right] \quad (10)$$

When the soliton velocity is zero, expression (10) agrees with the standing soliton solution, obtained earlier [21].

Furthermore, with the ansatz (6), explicit contribution of the velocity dependent - "kinetic" terms in the Hamiltonian (5) is singled out, by:

$$H = \int \left[\left(1 - \frac{5}{12}\rho^2\right)\rho_u + \frac{v^2\rho^2}{\rho_u} - \left(\frac{3}{16} - \frac{v^2}{12}\right)\frac{\rho^4}{\rho_u} \right] d\rho \quad (11)$$

Substitution of (9) into (11) enables us, after rather cumbersome integration, to obtain the explicit analytical expression for the Hamiltonian in a form:

$$H_0 = \frac{3}{200}\frac{40\lambda^2 - 64v^2 + 9}{\sqrt{2\lambda^2 - v^2}}\left(1 - \frac{12}{5{\rho_0}^2}\right)\left(\frac{5{\rho_0}^2}{12}\right)^{3/2} \ln\frac{1+\sqrt{\frac{12}{5{\rho_0}^2}}}{\left|1-\sqrt{\frac{12}{5{\rho_0}^2}}\right|}$$

$$+\frac{\sqrt{2\lambda^2 - v^2}}{4}\left(\frac{12}{5} + \frac{3v^2 - 2\lambda^2}{\frac{3}{16} - \frac{v^2}{12}}\right) \tag{12}$$

3. STABILITY ANALYSIS

In order to check the stability of the moving soliton, we use the renown Vakhitov-Kolokolov stability criterion [2], according to which, solitons are stable with respect to longitudinal perturbations, if:

$$\frac{dP_o}{d\lambda^2} > 0, \tag{13}$$

where, P_0 is the soliton photon number defined by (5). The function $P_0(\lambda)$, given by the expression (10), is shown in Fig. 2, for several values of soliton velocity.

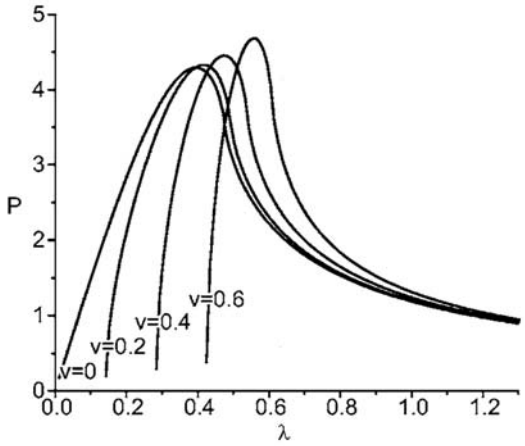

Fig. 2. Photon number $P_0(\lambda)$ shown for different soliton velocities.

According to the condition (13), moving EM solitons turn out to be stable in the region $\lambda < \lambda_s$, where the instability threshold, λ_s corresponds to the maximum value of P_0 for a given velocity (Fig. 2). Therefore, we can conclude that small amplitude linearly polarized moving solitons within the weakly relativistic model are stable. The increase of the soliton velocity shifts the instability threshold λ_s toward larger values leading to the enhanced stability in comparison to the standing soliton case.

The stability criterion for solitons can be alternatively formulated in terms of Hamiltonian and photon number interrelation, following the analysis given in Ref. 22. According to Ref. 22, the concavity of the *H-P* curves is related to the stability of the solitons: concave downwards implies stability, while concave upwards corresponds to instability. This is illustrated in Fig. 3, where *H-P* curves for different soliton velocities are plotted. There are two branches for each soliton velocity: the upper, unstable and the lower, stable branch. The turning point (maximum value of *P*) on each *H-P* curve coincides with the maximum value of P_0 on $P_0(\lambda)$ diagram (Fig.2) for corresponding soliton velocity and produces the same instability threshold values λ_s. The numerically calculated curves $P_0(\lambda)$ and $H_0(P_0)$ are in a good agreement with the analytical results.

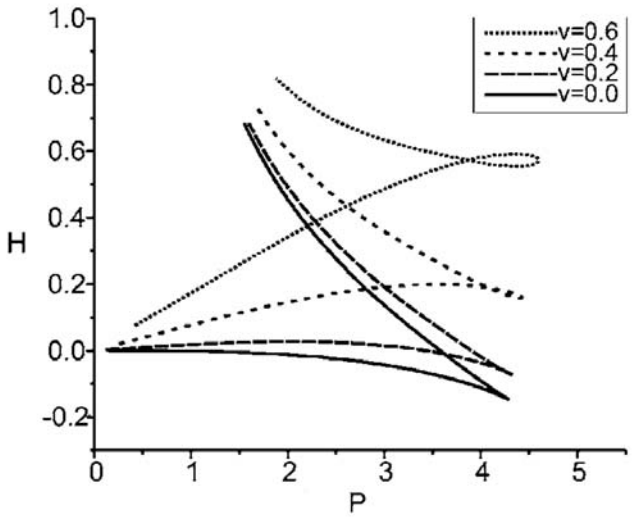

Fig. 3. Hamiltonian versus photon number for different soliton velocities. The lower branches are stable.

Considering the Vakhitov-Kolokolov stability criterion and the constraints on parameters λ, v in the analytical soliton solution (9), we can further expose different regions of the soliton existence and stability. The limits on the parameters λ, v:

$$1 - 5\rho(\lambda, v)^2 / 12 > 0, \;\; 2\lambda^2 - v^2 > 0 \tag{14}$$

together with the soliton stability condition $dP / d\lambda^2 > 0$, define the regions of the soliton existence and stability in (λ, v) space. These regions are shown in Fig. 4.

Above the curve (*a*) no analytical soliton solution exists. However, numerically we can find the stationary soliton solution. Discrepancy in numerical and analytical results in this region is attributed to small initial differences in the phase $\theta(u)$ between the approximate analytical and numerical solutions. Below the curve (c), there are no localized solutions, neither analytical nor numerical. The area of the soliton existence is separated by curve (b). Above the curve (b) is the region where $dP_0 / d\lambda^2 < 0$, resulting in the existence of the unstable solitons. The stable soliton solutions are possible just between curves (b) and (c), where the stability condition $dP_0 / d\lambda^2 > 0$, is satisfied.

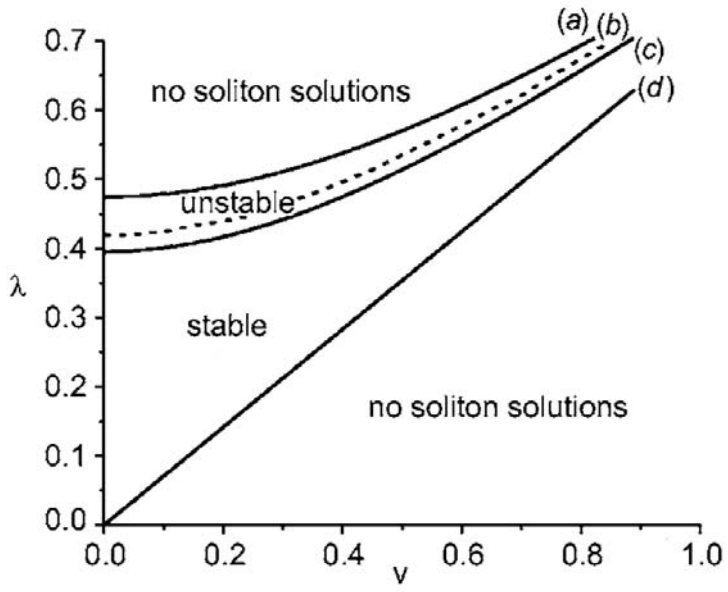

Fig. 4. Soliton existence and stability in different regions of (λ, v) parameter space. Curve (a) 1-5ρ(λ,v)2/12=0, curve (b) dP/dλ2=0 and curve (c) 2λ2-v2=0.

4. SIMULATION RESULTS

In order to check analytical results and our predictions concerning the moving relativistic EM soliton properties and the velocity effect on its existence and stability, we have performed a set of direct numerical simulations of the nonlinear model GNLS equation (4). The split-step Fourier method [23], originally developed for the NLS equation, is implemented in our numerical algorithm.

Numerical results prove that initially launched moving solitons (9), with parameters inside the stability region, bordered with the curves (b) and (c) in Fig. 4., remain stable. The initially unstable solitons with parameters in the region bordered with curves (a) and (b) in Fig. 4. exhibit a slow oscillatory relaxation toward the corresponding stable solitons with the same photon number.

The analytically predicted influence of the soliton velocity on its stability properties is verified numerically. We performed a set of simulations with the initial condition in a form of solitons with fixed value of λ and several values for the soliton velocity v. An example of these simulations is illustrated in Fig. 5. The standing soliton (v=0), with amplitude A_0=1.56, outside the stability region ($\lambda = 0.5$) relaxes toward corresponding stable soliton with the same photon number [Fig. 5(a)]. The moving soliton with the same λ but with the soliton velocity (v=0.3) slightly below the stability threshold exhibits a long-lived oscillations around the corresponding stable soliton state [Fig. 5(b)]. Further increase of the soliton velocity (v=0.7) turns the soliton inside the soliton stability region and the soliton propagation becomes stable [Fig 5(c)]. In this way we have confirmed our analytical prediction that the increasing soliton velocity shifts the instability threshold λ_s toward larger values and acts as a stabilizing factor.

For stable solitons being initially perturbed with the perturbations ε in a form of $\rho_p = \rho_0(1+\varepsilon)$, internal oscillation modes are excited and solitons exhibit long lived oscillating behavior of the breather type. If the initial perturbation of the stable moving soliton grows, the frequency of the excited oscillations increases and amplitude excursion from the initial value grows. A further increase of the perturbation level leads to a further deviation from the stable state and eventually to a rapid aperiodic growth of the amplitude. In this stage, this process is very similar to the initial stage of the collapse phenomenon [4]. However, the amplitude growth is accompanied by a continuous change of the soliton profile toward a highly pointed structure of a cusp type. This process continues up to the point when the amplitude reaches the critical value $\rho_c \approx 1.55$, creating a highly unstable cusp structure. Creation of this structure coincides with a break up of the spectral numerical scheme (conservation loss for H and P) and it was not possible to follow the dynamic behaviour further. This is illustrated in Fig. 6, where the evolution of the initially launched moving (v=0.4) soliton with the photon number $P<P_{max}=P_0(\lambda_s\approx 4.45$, inside the stability region, for different level of the perturbations is followed.

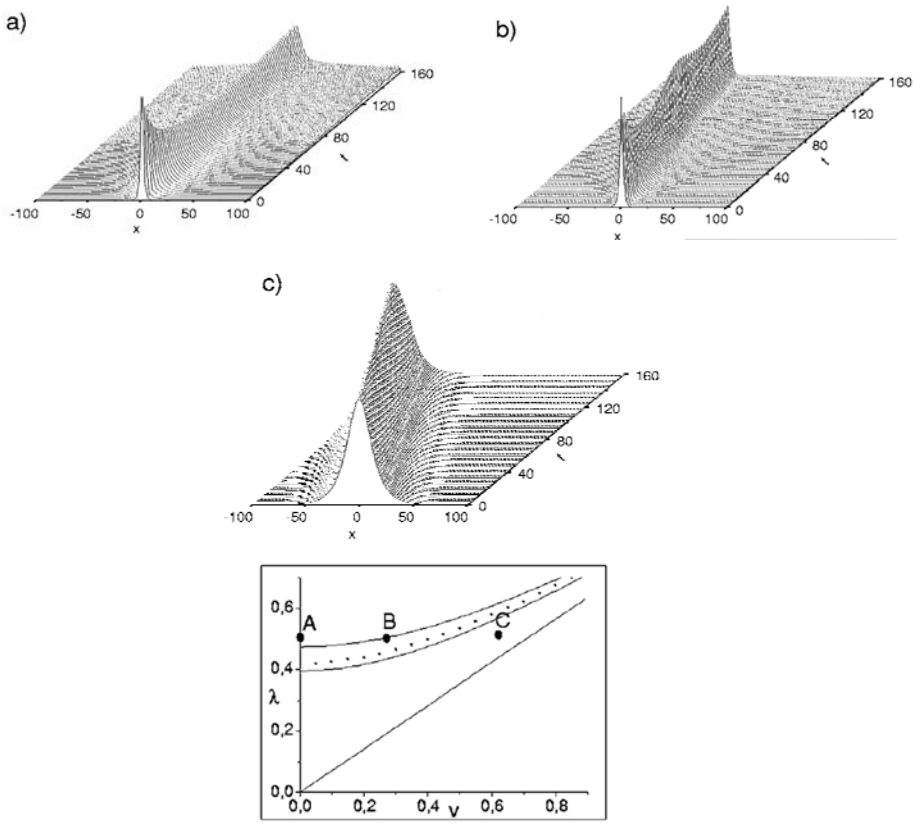

Fig. 5. Different dynamical regimes of the soliton with λ=0.5: a) Standing soliton in the unstable region with amplitude A_0=1.56, P=3.23; b) Moving soliton (v=0.3) in the unstable region, A_0=1.5, P=3.9; c) Moving soliton (v=0.7) in the stable region, A_0=0.26, P=1.34.

The observed long lived oscillations of the soliton amplitude show a similar behavior as in the case of the NLS equation with a local power-law nonlinearity, described in Ref. 24. This nonlinear evolution is illustrated in Fig. 7 in the $P_0(\lambda)$ diagram for the stable soliton $P_0 = 2.727, \lambda_0 = 0.334, v = 0.4$. The introduced perturbations (ε_1) at the stable soliton increase the photon number to $P_1 > P_0$ and excite internal oscillations around the new value of λ_1 which corresponds to the

stable soliton with P_1. During the oscillations, the soliton profile periodically changes its shape. Due to the influence of the nonlocal terms in Eq. (4), the periodic amplitude increase leads toward the cusp shape of the soliton profile. With the further perturbation increase (ε_2) the oscillatory behavior remains until the photon number reaches the value above $P_{\max}$ when the intersection with the curve $P_0(\lambda)$ is absent and the corresponding stable soliton solution cease to exist. In that case, a rapid aperiodic growth of the soliton amplitude creates a collapsing soliton structure up to the point when the amplitude reaches the critical value creating a cusp structure when we can no longer follow dynamic behaviour [25].

Initially launched stable moving solitons with parameters inside the stability region, but closer to the instability threshold, exhibit similar behavior, however, the level of the imposed perturbations that will lead to the soliton aperiodic growth, is much lower.

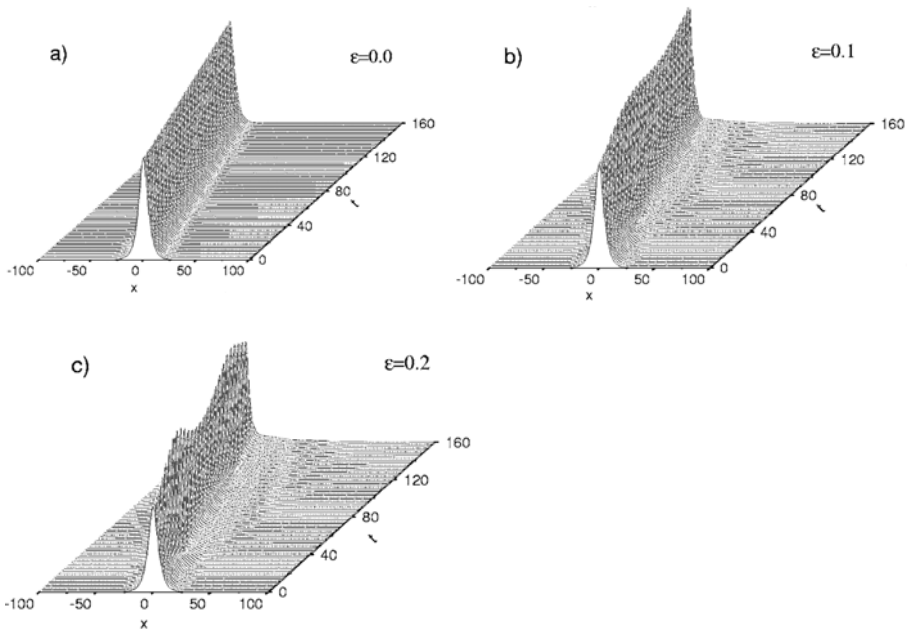

Fig. 6. Spatio-temporal evolution of initially launched moving soliton, in the stable region λ=0.334, v=0.4, A_0=0.6, P=2.73, for different perturbation levels.

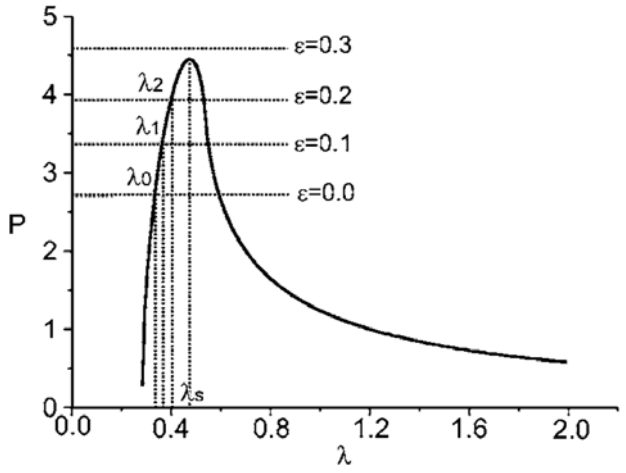

Fig. 7. Typical dependence of the photon number $P_0(\lambda)$ for solitons with v=0.4, P_{max}=4.45, λ_s=0.473. The stable soliton corresponds to the point P_0=2.727, λ_0=0.334. For the perturbation level ε_1=0.1 the photon number is P_1=3.3 and λ_1=0.36 of the corresponding stable soliton (amplitude oscillations around λ_1). For ε_2=0.2, P_2=3.927 and λ_2=0.39 of the corresponding stable soliton (amplitude oscillations around λ_2). For ε_3=0.3, the photon number is P_3=4.61> P_{max} and corresponding stable solution does not exist (soliton collapse-decay).

5. SOLITON INTERACTIONS

The type of soliton interaction depends on the parameters (amplitude, phase, velocity) of the colliding solitons. We restrict our study to symmetric collisions of two solitons with equal amplitudes and opposite velocities $v_1 = v, v_2 = -v$ [26]. Direct numerical simulations of the model equation (1) show that interaction of the small amplitude solitons is always elastic one (Fig. 8a), without energy (momentum) exchange between colliding solitons. By increasing the soliton amplitude, the interaction remains elastic up to the point when the resulting amplitude of the interacting soliton complex reaches the value of ρ_c and creates a highly unstable "cusp" -form structure. (Fig. 8b). Numerical simulations show a break up (annihilation) of the interacting pair. However, it is not possible to further follow chaotic dynamics due to the break up of the spectral numerical scheme (conservation loss for H and P). An introduction of the phase difference between the colliding soliton pair results in decreasing amplitude of the interacting complex and possible turn to the elastic type of interaction (Fig. 8c). Depending, whether during

impact, the soliton pair is in or out of phase, constructive or destructive interference of EM fields determines a fate of their interaction. Based on P-M-H interdependence future attempts to seek conservation laws for soliton interaction will be made.

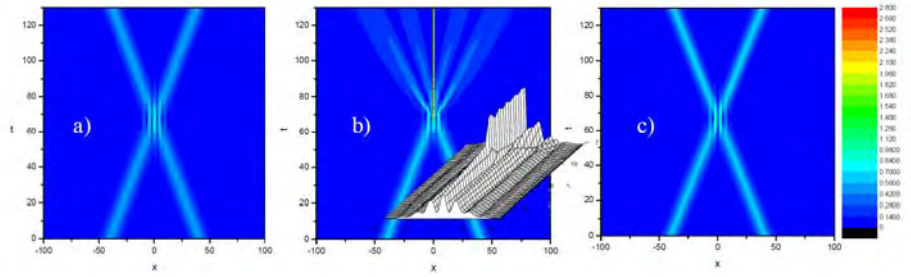

Fig.8. Interaction of two, in phase solitons with equal velocity v = 0:6 and different amplitudes a) $\rho_0 = 0.485$ and b) $\rho_0 = 0.6$½0 = 0:6, and c) solitons with same parameters as (b) with phase difference $\varphi = \pi$. The inserted plot illustrates the creation of the "cusp" structure.

VI. CONCLUSIONS

In this work, moving 1D electromagnetic solitons, formed in a weakly relativistic laser plasma interaction, were studied in the framework of the envelope GNLS equation (4). Moving EM soliton solutions and corresponding soliton photon number (*P*) and Hamiltonian (*H*) were analytically derived in a closed form. The stability analysis shows that the weakly relativistic moving EM solitons are stable; with the stability region shifting toward larger amplitudes in comparison to the standing soliton case. Numerical simulations of the model equation (4) have confirmed our analytical results. Moreover, further studies of the dynamics of the perturbed solitons, shows that the imposed perturbations excite internal oscillation modes leading to the creation of the breather type of structures. A further increase of the perturbation level leads to a further deviation from the stable state and eventually to a rapid aperiodic growth of the amplitude toward the critical amplitude ρ_c, accompanied by a continuous change of the soliton profile toward a highly pointed and unstable structure of a cusp type. Due to the coincidental break up of the model equation (4) and our numerical scheme, we were unable to follow the dynamics of this structure further. This question deserves future attention because our considerations were restricted to a weakly relativistic regime; therefore, the future studies of the obtained large relativistic EM structures are possible with fully nonlinear fluid-Maxwell [15] and particle simulations [27], which are beyond the scope of this work.

ACKNOWLEDGMENTS

This work is supported by the Ministry of Sciences and Protection of the Environment of Republic of Serbia, Project 1964.

REFERENCES

1. A. I. Akkheizer and R. V. Polovin, Sov. Phys. JETP **3**, 696 (1956).
2. A. G. Litvak and A. M. Sergeev, JETP Lett. **27**, 517 (1978).
3. V. A. Kozlov, A. G. Litvak and E. V. Suvorov, Sov. Phys. JETP **49**, 75 (1979).
4. V. E. Zakharov, S. V. Manakov, S. P. Novikov, L. P. Pitaevski, *Theory of Solitons* (Plenum Press, New York, 1984).
5. K. V. Kotetishvili, P. Kaw, and N. L. Tsintzadze, Sov. J. Plasma Phys. **9**, 468 (1983).
6. M. Y. Yu, P. K. Shukla, and N. L. Tsintzadze, Phys. Fluids **25**, 1049 (1982).
7. S. V. Bulanov, I. N. Inovenkov, V. I. Kirsanov, N. M. Naumova, and A. S. Sakharov, Phys. Fluids B **4**, 1935 (1992).
8. P. K. Kaw, A. Sen, and T. Katsouleas, Phys. Rev. Lett. **68**, 3172 (1992).
9. T. Zh. Esirkepov, F. F. Kamenets, S. V. Bulanov, and N. M. Naumova, JETP Lett. **68**, 36 (1998).
10. D. Farina and S. V. Bulanov, Phys. Rev. Lett. **86**, 5289 (2001).
11. S. Poornokala, A. Das, A. Sen, and P. K. Kaw, Phys. Plasmas **9**, 1820 (2002).
12. M. Lontano, M. Passoni, and S. V. Bulanov, Phys. Plasmas **10**, 639 (2003).
13. K. Mima, M. S. Jovanović, Y. Sentoku, Z. M. Sheng, M. M. Škorić, and T. Sato, Phys. Plasmas **8**, 2349 (2001).
14. D. Farina and S. V. Bulanov, Plasma Phys. Control. Fusion **47**, A73 (2005).
15. V. I. Berezhiani, D. P. Garuchava, S. V. Mikeladze, K. I. Sigua, N. L. Tsintsadze, S. M. Mahajan, Y. Kishomoto, and K. Nishikawa, Phys. Plasmas **12**, 062308 (2005).
16. S. V. Bulanov, T. Zh. Esirkepov, N. M. Naumova, F. Pegoraro, and V. A. Vshivkov, Phys. Rev.Lett. **82**, 3440 (1999).
17. Y. Sentoku, T. Zh. Esirkepov, K. Mima, K. Nishihara, F. Califano, F. Pegoraro, H. Sakagami, Y. Kitagawa, N. M. Naumova, and S. V. Bulanov, Phys. Rev. Lett. **83**, 3434 (1999).
18. T. Zh. Esirkepov, S. V. Bulanov, K. Nishihara, and T. Tajima, Phys. Rev. Lett. **92**, 255001 (2004).
19. M. Tushentsov, A. Kim , F. Cattani , D. Anderson, and M. Lisak, Phys. Rev. Lett. **87**, 275002 (2001).
20. M. M. Škorić, Lj. Hadžievski, L. Baiwen, and S. Ishiguro, in *31st EPS Conference on Plasma Physics*, London, 28 June-2 July 2004, ECA (European Physical Society, Petit-Laney, 2004), Vol. 28G, O-2.10. J. Plasma Phys. (to be published)
21. Lj. Hadžievski, M. S. Jovanović, M. M. Škorić, and K. Mima, Phys. Plasmas **9**, 2569 (2002).

22. N. Akhmeidev and A. Ankiewicz, Phys. Rev. E. **59**, 6088 (1999).
23. T. R. Taha and M. J. Ablowitz, J. Comput. Phys. **55**, 203 (1984).
24. D. E. Pelinovsky, V. V. Afanasijev, and Y. S. Kivshar, Phys. Rev E **53**, 1940 (1996).
25. A. Mančić, Lj. Hadžievski and M.M.Škorić, Electromagnetic Solitons in Relativistic Plasmas, Phys. Plasmas, 13, 052309, (2006)
26. A. Mančić, Lj. Hadžievski and M.M.Škorić, Interaction of Electromagnetic Solitons in in Relativistic Plasmas, J. Plasma Phys. 72, 1309-1313 (2006)
27. L. Baiwen, S. Ishiguro, M. M. Škorić, M. Song, and T. Sato, Phys. Plasmas **12**, 103103 (2005).

VI Serbian-Belarusian Symp. on Phys. and Diagn. of Lab. &
Astrophys. Plasma, Belgrade, Serbia, 22 - 25 August 2006
eds. M. Ćuk, M.S. Dimitrijević, J. Purić, N. Milovanović
Publ. Astron. Obs. Belgrade No. 82 (2007), 117-128 *Invited lecture*

APPLICATIONS OF SPECTRAL LINES FOR LOW ELECTRON DENSITY PLASMA DIAGNOSTICS

M. Ivković, S. Jovićević, R. Žikić, N. Konjević

Institute of Physics, 11081 Belgrade, P.O.Box 68, Serbia

Abstract. This work comprises an analysis of optical emission spectroscopy (OES) techniques and results of their application for diagnostics of middle and low electron densities (N_e) in low temperature plasmas. The discussion will be limited primarily to the applications of the methods based on the use of: Stark – widths and shifts of non-hydrogenic neutral and singly ionized atom lines, line shape of neutral helium lines with forbidden components and molecular nitrogen band heads intensities. In this study all these techniques are critically evaluated, tested and applied for diagnostics of microwave induced plasma (MIP), low pressure pulsed arcs or capillary discharge.

1. INTRODUCTION

Low and medium electron density plasmas are extensively used in analytical atomic spectroscopy as a light sources for optical emission spectroscopy (OES), plasma processing and in various technologies, such as laser ablation, thin film deposition, creation of different nanostructures and nanocomposite etc. Therefore, the interest for plasma diagnostics is growing, and the need for improvement of old and development of new techniques is a constant task. Due to their non-perturbative nature, high spatial resolution and variety of different methods, the OES techniques are of particular interest.

In this study, the discussion will be limited primarily to the diagnostics of electron density, N_e, in low temperature plasmas using of non-hydrogenic spectral lines. For other plasma parameters measurements and application of hydrogenic spectral lines for N_e diagnostics, more details can be found in several recent review articles and textbooks [1-5] and references cited therein. Within this work techniques based on Stark – widths and shifts of non-hydrogenic ion and atom spectral lines, thr overall line shape of helium atom lines with forbidden component and molecular nitrogen band heads intensities are studied. All these techniques are

applied and tested in different plasma sources and theirs advantages and drawback discussed.

2. EXPERIMENT

In experimental part of this study two different setups were used. One for the investigations of low pressure pulsed capillary discharge and another one for an atmospheric pressure microwave induced plasma studies. The central part around the axis of the pulsed plasma source is imaged 1 : 1 onto the entrance slit of the 1 m monochromator (inverse linear dispersion 0.833 nm/mm) by means of a 1 m focal length focusing mirror. A 30 mm diaphragm placed in front of the focusing mirror ensures that light comes from the narrow cone about the discharge axis. The spectral line profiles are recorded step-by-step with the instrumental half width of 0.017 nm. Signals from the photomultiplier - PMT are led to a digital storage oscilloscope triggered by the signal from the Rogowsky coil. The main current pulse through the discharge tube induces the trigger pulse. In order to obtain better signal-to-noise ratio an averaging of eight signals at each wavelength step is performed. For more details see references [6, 7].

In cases when radiation from the microwave induced plasma sources – MIP was measured, the 1:1 image is projected on the 20 m wide slit by use of a 0.5 m focal length focusing mirror. In that case, signal from the PMT was amplified by the picoammpermeter. More details about sample introduction, gas flow control when using different versions MIP sources one can find in [5, 8].

3. RESULTS

In the following section in front of the experimental and/or mathematical testing of the methods, short review of theirs fundamental characteristics will be presented.

3. 1. Neutral and Singly Ionized Non-hydrogenic Atom Lines

The use of Stark widths and shift of ionized non-hydrogenic atom lines for diagnostics of the electron densities lower than 10^{22} m^{-3} is very rare. At these densities Stark widths are small and comparable with widths due to the other broadening mechanisms, so that high-resolution spectroscopic instrumentation has to be used and deconvolution procedures must be applied.

3.1.1. The Width and Shift of the Neutral Atom Lines

The shape of the neutral atom line in quasistatic approximation for ions is described by the following expression [9]:

$$j_{A,R}(x) = \frac{1}{\pi} \cdot \int_0^{\infty} \frac{H(\beta)\, d\beta}{1 + \left(x - A^{4/3} \cdot \beta^2\right)^2} \qquad (1)$$

where H(β) is ion microfield distribution, and x is described by $x = (\lambda - \lambda_0 - d_e)/w_e$, λ_0 is the central wavelength of the unperturbed line, d_e is the electron shift and w_e is the electron impact half-halfwidth. Examples of neutral atom plasma broadened line shape for Debye shielding parameter R = 0.8 and different values of ion broadening parameter A are presented in Figure 1.

From a large number of generated profiles Griem [4] found that total Stark (full widths at half maximum FWHM) - w_t of line profiles could be expressed within the quasistatic ion approximation as a function of w_e, A and R

$$w_t(T_e) \cong 2w_e(T_e)[1 + 1.75x10^{-4}N_e^{1/4}A(T_e)(1 - 0.068N_e^{1/6}T_e^{-1/2})]10^{-16}N_e \qquad (2)$$

$$d_t(T_e) \cong [d_e(T_e) \pm 2.0x10^{-4}N_e^{1/4}A(T_e)\, w_e(T_e)(1 - 0.068N_e^{1/6}T_e^{-1/2})]10^{-16}N_e \qquad (3)$$

$$d_{t1/2}(N_e,T_e) \approx [d_e(T_e) \pm 3.2x10^{-4}Ne^{1/4}A(T_e)w_e(T_e)(1 - 0.068N_e^{1/6}T_e^{-1/2})]10^{-16}N_e \qquad (4)$$

where w_t, d_t and $d_{t1/2}$ are measured Stark widths and/or shift of the peak line intensity or shift of the halfwidth, respectively, while w_e, d_e, and A are theoretical electron impact half-halfwidth, d_e shift and A ion broadening parameter calculated for $N_e = 10^{16}$ cm^{-3} and published in Appendix IV of [4].

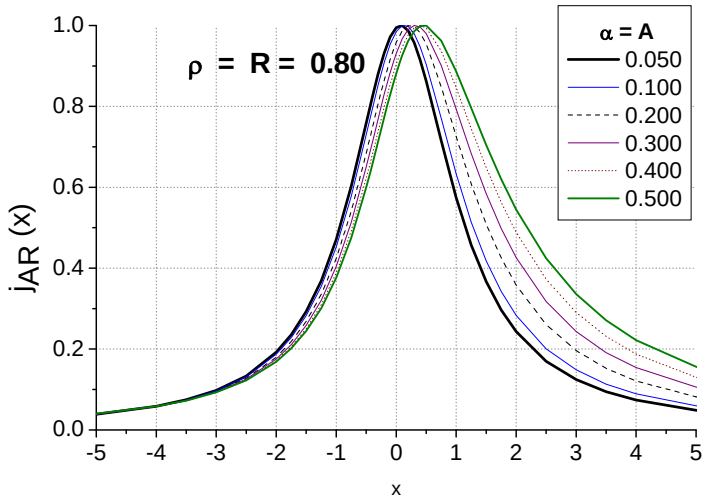

Fig 1. The $j_{A,R}(x)$ profiles of neutral atom lines for R = 0.8 and different values of A

It should be noticed that plasma broadened neutral atom lines are asymmetric and that the deconvolution procedure, see e.g. [10,11], differs from symmetric profiles of, for example, ionic lines, see e.g. [12]. Influence of ion dynamics especially in case of light elements such as helium [13,14] is also important and

must be taken in account. For a number of lines correction factors w_{exp}/w_t determined by Konjevic [15] from the comparison of theory and large number of high accuracy experimental data. This enables more precise electron density determination.

This technique was tested in the capillary discharge with gas mixture of 2.4% Ne, 5.6% He and 92 % H_2 at pressure p = 4 mbar. The maximum discharge current of I = 400 A with t = 2.7 s was obtained by discharging C = 0.36 F, charged up to U = 7 kV. By use of excitation temperature T_{exc} = 33 000 K determined from Boltzmann plot of O II lines, correction factors from [15] and tabulated values of w_e and A [4] the electron density N_e= (4.8 ± 0.2) x 10^{22} m^{-3} from the He I : 388.8, 471.3 and 501.6 nm spectral lines was determined. For the determined electron density and w_e value in Appendix IV of [4] for Ne I spectral line at 594.483 nm very good agreement between experimental and generated Voigt profile was obtained. The observed Ne I lines were symmterical, within the uncertainty of experiment indicating that small ion broadening contribution is small, see Figure 2.

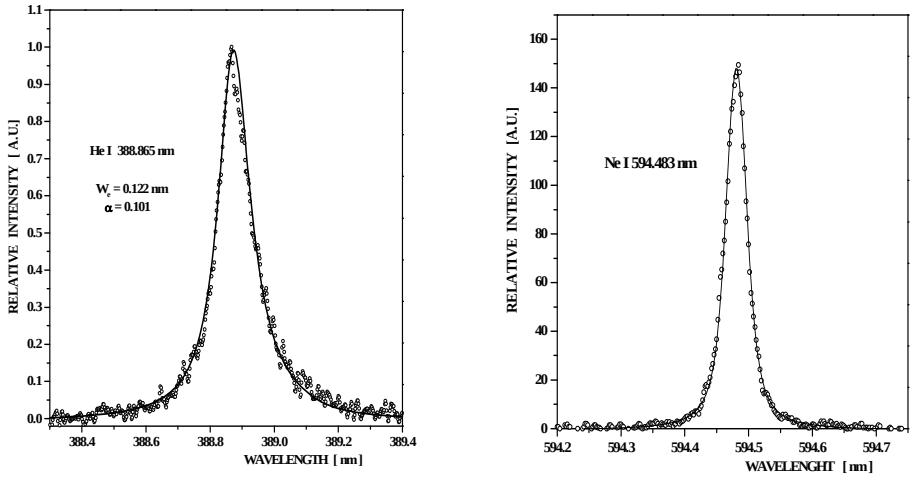

Fig 2. a) The recorded He I 388.865 nm line (○) fitted with j_{AR} (x) theoretical profile with data taken from [4] for N_e = 5.2 x 10^{22} m^{-3} and T_e = 33000 K and b) The recorded Ne I 594.483 nm line (○) fitted with Voigt profile for N_e = 4.8 x 10^{22} m^{-3} and T_e = 33000 K.

It should be notices that from fitted j_{AR} (x) profile of the He I 388.8 nm line We = 0.122 nm i.e. N_e = 5.2 x 10^{22} m^{-3} is obtained, but after applying w_{exp}/w_t correction factor determined in [15] the value of 4.8 x 10^{22} m^{-3} is determined.

3.1.2. The Comparison of the Theoretical and Experimental Profiles

The another and more accurate way for electron density determination is based on comparison of whole experimental and theoretical line profiles, see example in Fig.2 [16-18]. In order to test the possibility of determining plasma and line parameters by using deconvolution techniques and especially the six fit parameter deconvolution - SFPD procedure [18] from one line profile only (without independent plasma parameters and shift measurements) the theoretical line profiles are generated from Eq.(1). We analyzed theoretical profiles $j_{A,R}(x)$ with the following sets of parameters: 1) various R values ($0 \leq R \leq 0.8$) and largest value of A = 0.075 reported in [19]; 2) different pairs of A and R values with fixed electron impact w_e, and ion contribution w_i and 3) fixed total Stark widths w_t and R values for various sets of w_e and A.

The Case 1. is illustrated by Fig. 3. The FWHM of these lines for the whole range of R changes from 2.133 to 2.188, i.e. difference is only 0.055 (in x units) while shapes are very similar. This means that for typical w_e values around 0.1 nm at 10^{17} cm^{-3} [19] the difference in half width corresponds to only 0.0055 nm for the whole range of R values. Such a small difference between profiles in a large range of R values raises a question: Is any deconvolution capable of detecting so small differences of line shapes in particular if one is using pulsed plasma source and shot–to-shot technique for line profile recording or study the astrophysical plasmas.

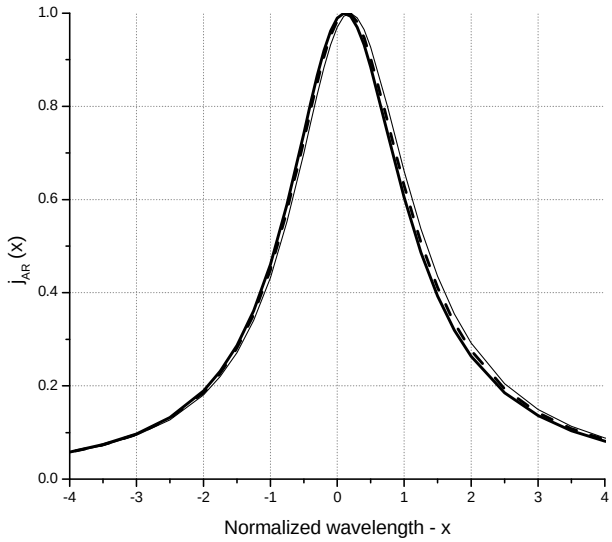

FIGURE 3. The $j_{A,R}(x)$ profiles of neutral atom lines for $w_e = 2$, $d_e = 0$, A = 0.075 and different values of: R = 0 (thick line), 0.4 (dashed line) and 0.8 (thin line).

In the Case 2., from Eq. (2), after several iterations of this approximate formula many (A,R) pairs with the same electron impact, w_e, and ion contribution, w_i, i.e. with the same total Stark width w_t are determined, see several examples in Table 1.

Table 1. Different sets of parameters for the same w_t and total ion shift d_{it}.
A_1- calculated from Eq.(2), A_2- determined by an iteration process.

We	w_t	d_i	R	A_1	A_2
2	2.41	0.47	0.55	0.2	0.2
2	2.41	0.47	0	0.118	0.142
2	2.41	0.47	0.2	0.138	0.162
2	2.41	0.47	0.8	0.294	0.24

The shapes of the lines with parameters given in Table 1 are practically indistinguishable in a typical line profiles presentation. Consequently, the line shape only cannot be used for plasma diagnostics and line parameters determination.

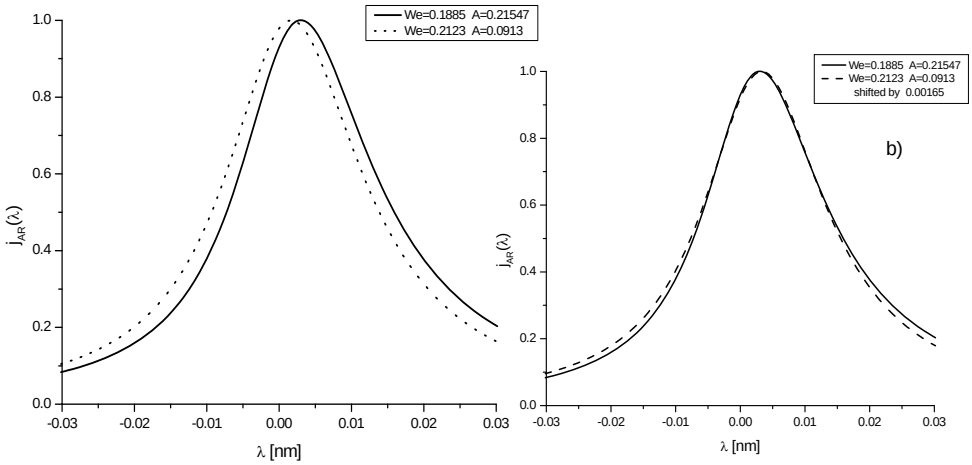

Fig 4. The $j_{A,R}(x)$ profiles for R = 0.48 and different values of w_e and A; w_e = 0.188, A = 0.215 (solid line); w_e = 0.212, A = 0.091 (dotted line). a) shifted profiles and b) profiles with the shift normalized to the same value.

In the Case 3, by using Eq.(2), whole set of (w_e, A) pairs for the same value of w_t and R were calculated. In this case profiles are not identical, but they differ slightly at the line wings, see Fig. 4b. These differences are so small that deconvolution of profiles recorded from pulsed sources using shot-to-shot technique in the presence of impurity lines can't distinguish one from another. Figure 4a illustrates the importance of precise shift measurements for determination of N_e in these cases.

The analysis of line profiles is even more complex when all three parameters w_e, A and R are varied. With different combinations of these parameters profiles with exactly the same w_t with very small differences in shape can be obtained.

3.2. Helium lines with Forbidden Component

In the case of helium plasmas, electron density can be determined by using the shape of some visible He I lines with forbidden components. These strong lines, belonging to the $2^3P - n\ ^3D$ series (n = 4 for 447.1 nm and n = 5 for 402.6 nm) and to the $2\ ^1P - n\ ^1D$ series (n = 4 for 492.2 nm), have in plasma forbidden components 2^3P- $n\ ^3F$ or $2\ ^1P$ - $n\ ^1F$, respectively. The complex structures of these lines, see Fig.5, are extensively studied both theoretically, by applications of unified, MMM or close coupling (CC) theories, and experimentally. The inclusion of ion dynamic effects in theoretical descriptions of helium lines with forbidden components greatly improves agreement with experimental results.

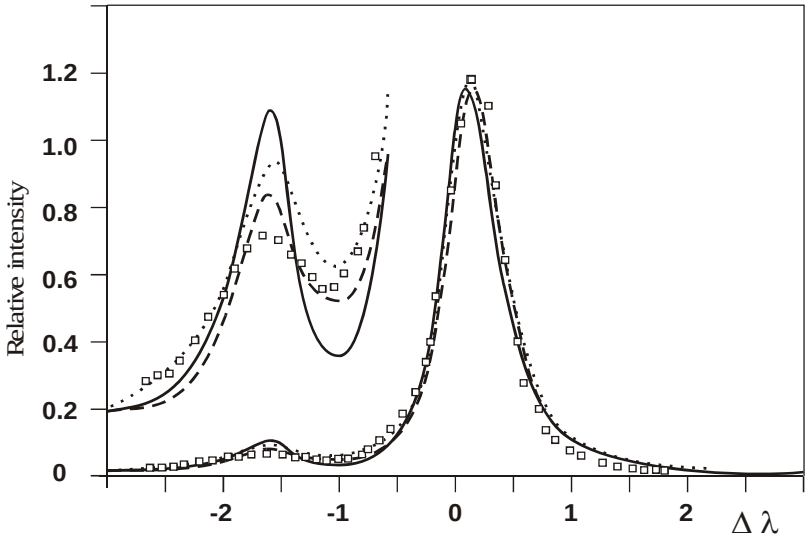

Fig. 5. Comparision of measured He I 447.1 nm line shape (squares) with theory: MMM (full), CC (dashed),and BCS (doted line).Plasma parameters: $N_e = 1 \times 10^{15}$ cm^{-3}, T_e=18 000 K, T_g = 13 000 K. Doppler and instrumental broadening included and all profiles are area normalized.

However, as illustrated in Fig. 5, the discrepancy of predicted forbidden line intensity with the experiment [20] still remains for all three theoretical approaches.

This is a main reason why experimentally determined formulas relating N_e with the parameters of helium lines with forbidden component such as F/A - forbidden (F) to allowed (A) line maximum intensity, D/A - deep (D) i.e. minimum intensity between forbidden and allowed line and A line intensity) and *s* - wavelength separation between F and A. determined by Czernichowski and Chapelle [21] are mainly used. Due to the fact that parameter *s* is not sensitive to distortion of the strong allowed line caused by the possible presence of a self-absorption effect, the following relation was used in this work

$$\log N_e\,[m^{-3}] = 23.056 + 1.586 \log (s[nm] - 0.156) + 0.225\,[\log (s - 0.156)]^2 \qquad (5)$$

where 0.156 nm in Eq.(6) is the separation between unperturbed F and A line.

The application of He I 447.2 nm line for determination of the medium electron densities was applied in the capillary discharge at p=4 mbar of gas mixture 1.5% CO_2, 1.5% N_2 and He, see Figure 6. The capacitor of 0.36 F charged up to the 6 kV was used to obtain peak current with duration of 3.6 s.

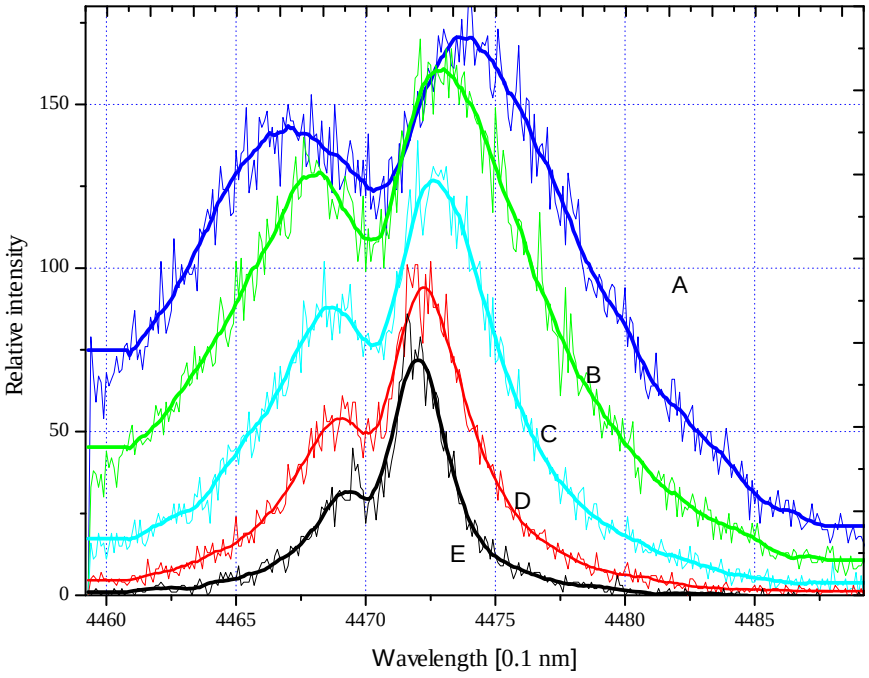

FIGURE 6. The shapes of the 447 nm line during plasma evaluation (A - 3.5; B - 4.5; C - 5.5; D - 6.5 and E - 7.5 s after current maximum),

which corresponds to the Ne = 3.4; 1.9; 1.2; 0.78 and 0.35 *10^{16} cm^{-3} respectively. The same procedure can be used for lower N_e determination, but with a use of a different amplification when recording forbidden or allowed component, as shown in Figure 7. It should be pointed out that great care must be taken when using He I lines with forbidden components for the determination of N_e lower than few times 10^{14} [cm^{-3}]. At these densities, the low intensity of the forbidden component (less than few percents of the allowed one), may be masked by noise or in the presence of traces of nitrogen, molecular lines from 6-8 and 8-10 bands of the first negative system of N_2^+.

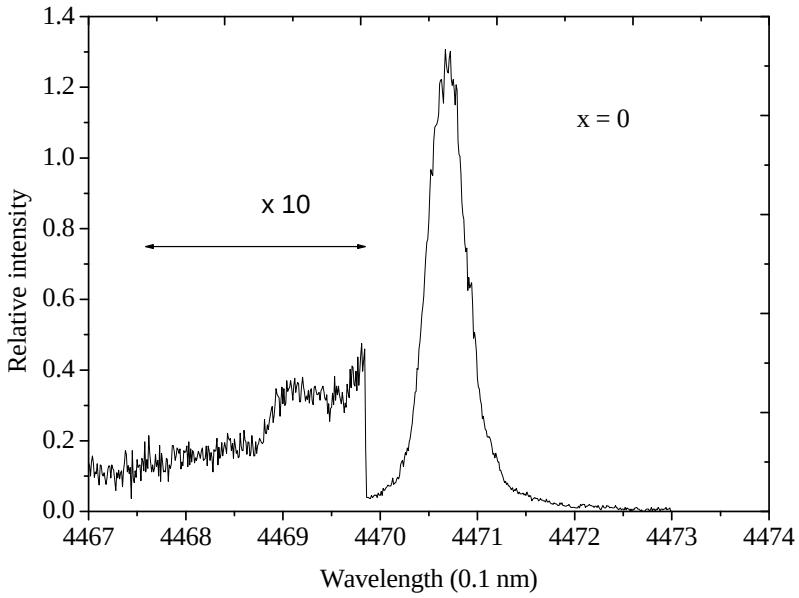

Fig. 7. Illustration of line shape recordings with different amplification of the photomultiplier signal. Line emitted from the center of the Mini MIP at height of 1mm from the torch orifice. The flow rate of He through the outer was 0.6 l/min, and He+ 3% H_2 through the inner capillary was 0.2 l/min.

3.3. Intensity of the N_2 and N_2^+ Molecular Band Heads

According to [22-24], the electron density in nitrogen and nitrogen/He plasmas can be determined from the intensity of N_2 second positive system (SPS) band head (0-0) at 337.1 nm ($C\ ^3\Pi_u \rightarrow B\ ^3\Pi_g$) and N_2^+ first negative system (FNS) band head of (0-0) at 391.4 nm ($B^2\Sigma_u^+ \rightarrow X^2\Sigma_g^+$).

Namely, by using the simplified kinetic model of the N_2 ($C^3\ _u$) state, see e.g. [23] and assuming that the steady-state population of the upper energy state is

equal zero, a linear relation between the 337.1 nm band intensity and the electron density at constant pressure and constant electric field may be obtained. This relation is confirmed with 5% accuracy in a volumetric near field microwave plasma [24].

A similar discussion can be applied to the band head of First Negative System of nitrogen ion ($B^2\Sigma_u^+ \rightarrow X^2\Sigma_g^+$) [23]. Due to an additional excitation process for the upper level population, the intensity of the 391.4 nm line has quadratic dependence upon electron density, i.e. $I_{(391.4\ nm)} \sim N_u \sim A\ N_e^2 + B\ N_e$, where N_u is the population of the $B^2\Sigma_u^+$ state, while A and B are constants, which must be independently determined.

According to the authors [22], this method can be applied even in plasmas with non-Maxwellian electron energy distribution.

To apply the same method for N_e determination in other gas mixtures, N_2^+ ion fraction has to be calculated. The situation is more complex if Ar or H_2 are present in the gas mixture. The reactions $Ar^* + N_2 \rightarrow Ar + N_2^+$, $N_2^+ + H_2 \rightarrow N_2H^+ + H$ and $Ar^* + H_2 \rightarrow Ar\ H^* + H$ and many others, have to be taken into account.

The band intensity method is tested in MIP at atmospheric pressure with power input of 100 W and at constant He flow rate of 0.7 l/min. The radial distributions of the band head intensities and hydrogen Balmer beta line shapes – H are obtained by Abel inversion procedure. From the determined H line shapes electron densities are calculated using approximate experimental formula, see Eq.2 in [5]. Finally, dependence of the molecular nitrogen band head intensities versus log N_e for different values of radius are presented in Figure 8.

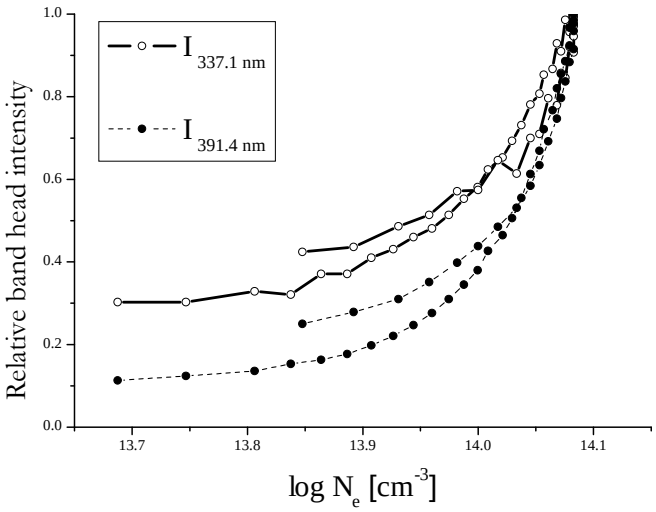

Fig. 8. Dependence of the molecular nitrogen band head intensities versus log N_e for different values of radius in MIP at atmospheric pressure Power input 100 W and flow rate of He 0.7 l/min.

It is evident that the application of this method for N_e determination requires further elaboration and experimental verifications in different plasma sources and gas mixtures. It should be noticed that the calibration of log N_2^+ band intensity vs. log N_e determined using another independent diagnostic technique enables slope parameter determination. The extrapolation of intensity vs. N_e plot may be used for lower N_e plasma diagnostics.

4. CONCLUSIONS

At the end one can conclude that fitting of the neutral atom line profiles is usefull for the medium electron density diagnostics, but a great precautions must be undertaken. This is especially important when more than one parameter fit of only one line without shift measurements is used for several plasma parameters determination.

The helium lines with forbidden components can be used in a very broad range of electron densities and even at lower than 10^{15} cm^{-3}. For lower densities the more complicated procedure must be used and furher theoretical studies will be welcomed.

It should be stressed out that the molecular nitrogen band heads intensities offer a greatest possibility for diagnostics of very low densities, but a both theoretical and experimental studies in different plasma conditions are needed.

ACKNOWLEDGMENTS

This work is partially supported by the Ministry of Science and Environmental Protection of Serbia under projects 141032B.

REFERENCES

1. Q.Jin, Y.Duan, and J.A.Olivares, *Spectrochim.Acta* **B 52,** 131-161 (1997).
2. W.Locchte-Holtgreven, *Plasma Diagnostics*, American Institute of Physics, New York 1995.
3. J.Ropke, P.B.Davies, M.Kaning and B.P.Lavrov, Diagnostics of non-equilibrium molecular plasmas using emission and absorption spectroscopy, in *"Low temperature plasma physics - Fundamental Aspects and Applications"* Eds. R.Hippler, S.Pfau, M.Schmidt, K.H. Schonbach. Wiley-VCH, Berlin, N.Y. Toronto, 2001.
4. H.R.Griem, *Plasma Spectroscopy*, Academic Press, New York 1964.
5. M.Ivković, S.Jovićević and N.Konjević, *Spectrochimica Acta* **B 59,** 591-605, (2004).
6. S.Jovićević, M.Ivković, R.Zikic and N.Konjević, *J.Phys.B* **38**, 1249-1259 (2005).
7. M.Ivković Ben Nessib N and Konjević N, *J.Phys.B* **38**, 715-728 (2005).

8. S.Jovićević, M.Ivković, Z. Pavlovic, and N.Konjević, *Spectrochimica Acta* **B 55,** 1879-1893, (2000).
9. H.R.Griem, M.Baranger, A.C.Kolb and G.Oertel, *Phys.Rev*. **125,** 177 (1962).
10. Z. Mijatović, R.Kobilarov, B.T.Vujičić, D.Nikolić and N.Konjević, *J. Quant. Spectrosc.Radiat. Transfer* **50,** 329-335 (1993).
11. D.Nikolić, Z.Mijatović, S.Đurović, R.Kobilarov and N.Konjević, *J. Quant. Spectrosc.Radiat. Transfer* **70,** 67-74 (2001).
12. J.T.Davies and J.M.Vaughan, A new tabulation of the Voigt profile, *Astrophys.J.* **137,** 1302-1305 (1963).
13. R.Kobilarov, N.Konjević, M.V.Popović, *Phys. Rev.* **A 40,** 3871-3879 (1989).
14. Z.Mijatović, N.Konjević, M.Ivković , R.Kobilarov, *Phys. Rev.* **E51** 4891-4896 (1995).
15. N.Konjević, *Phys. Reports* **316**, 339-401 (1999).
16. T.D.Hahn and L.A.Woltz, *Phys.Rev*.**A 42**, 1450 (1990).
17. D.Nikolić, S.Djurović, Z.Mijatović, R.Kobilarov and N. Konjević, in *Srectral Line Shapes*, International Conf. of Spectral Line Shapes, Pen State University Park, State College, Pensilvania USA, Vol 10, AIP Conf. Proc. **467**, New York AIP, 93, (1999).
18. V.Milosavljević and G.Poparić, Phys.Rev.E **63**, 036404 (2001).
19. V.Milosavljević, S.Djeniže and M.S.Dimitrijević, Phys.Rev.E **68**, 016402 (2003).
20. H. Richter and A.Piel, *J. Quant. Spectrosc.Radiat. Transfer* **33,** 615-626 (1985).
21. A.Czernichowski and J.Chapelle, *J. Quant. Spectrosc.Radiat. Transfer* **33,** 427–435 (1985).
22. K.Behringer and U.Fantz, *J.Phys.D: Appl. Phys.* **27,** 2128– 2135 (1994). .
23. S.D.Popa, *J.Phys.D: Appl.Phys.* **29,** 416-418 (1996).
24. Exton R.J., Jeffrey Balla R., Hering G.C, Popovic S and Vuskovic L. *Proc. 34th AIAA Plasmadynamics and Lasers Conference*, 23–26 Jun 2003, Orlando, Florida, USA, paper 4181.

VI Serbian-Belarusian Symp. on Phys. and Diagn. of Lab. &
Astrophys. Plasma, Belgrade, Serbia, 22 - 25 August 2006
eds. M. Ćuk, M.S. Dimitrijević, J. Purić, N. Milovanović
Publ. Astron. Obs. Belgrade No. 82 (2007), 129-130 *Invited lecture*

NOTES ON THE ROLE OF REACTIVE FIELD EFFECTS OF THE PARTICLE ACCELERATION TO THEIR COLLECTIVE MOTION IN PINCHED PLASMAS IN NATURE AND EXPERIMENTS

M. Jelić[1,2,3], S. Kuhn[2], J. Duhovnik[1]

[1] *LECAD Laboratory, Faculty of Mechanical Engineering, University of Ljubljana, Aškerčeva Street 6, SI-1000 Ljubljana, Slovenia*
[2] *Plasma and Energy Physics Group, Association EURATOM-ÖAW, Department of Theoretical Physics, University of Innsbruck, Technikerstrasse 25, A-6020 Innsbruck, Austria*
[3] *3D Intitut, Ljubljana, Kotnikova 5, SI-1000, Ljubljana, Slovenia*

Abstract. Reactive field due to particle acceleration is one of the most intriguing and controversial phenomena in classical mechanics and classical electrodynamics (see e.g., [1,2]). The appearance of reactive field is apparently easy to understand within a simple pictures based on the retarding fields of moving particles, and seems to be a very universal one in both sub-atomic and cosmological scales (e.g., [3]). It gives nice interpretations of the magnetic field, which turns out to be just a consequence of potential field sources in the space-time structure [4,5]. The Einstein equivalence between the mass and energy was discovered within this theory well before his work on the mass-energy equivalence (e.g., [1]). This theory is also well aligned with the zero point fluctuating field theory [6]. Unfortunately, the pragmatic success of quantum mechanics, which itself yields excellent results (we may say: too formal, i.e., without a real understanding), somehow damped the further development of this branch of physics during the previous and current centuries. In this lecture we would like to point out the relevance of reactive forces in classical electrodynamics to macroscopic systems with strong particle accelerating fields. The test case we propose here is a system consisting of a spherical shell of charged particles accelerated in radial direction in an external field (in general of arbitrary nature), which generates the stationary reactive electric field $\mathrm{E}_{\mathrm{acc}}$ that we calculate as:

$$E_{acc} = \frac{Q}{4\pi\varepsilon_0}\frac{a}{R}\frac{1}{c^2}I(\frac{r}{R}),$$

where, Q is the total charge within the spherical shell of an instant radius *R*, *a* is the acceleration, ε_0 and *c* are the vacuum permeability and the speed of the light, respectively, and $I(r/R)$ is an integral over the spherical angle, (which is finite in the range $0 < r < \infty$ with a sharp maximum of the order of unity for $r = R$). In the case of a number of N particles with elementary charge *e* and mass m_e (e.g., electrons), accelerated in an external electrostatic field E_{ext} the last formula yields the result $E_{acc} = N\frac{r_0}{R}E_{ext}$, where $r_0 = e^2/(4\pi\varepsilon_0 m_e c^2) = 2.8179\times10^{-15} m$ is the classical (or Compton) electron radius. This last expression could have dramatic consequences to plasma systems in nature, laboratory and fusion devices, which are characterized by enough high number of accelerated particles. Namely, the reactive acceleration can strongly compete the external electrostatic force and so could be interpreted as a kind of "electrostatic" confinement mechanism. In addition, consequences of the present approach to subatomic scales should be reinvestigated in a new consistent manner, leading to a reanimation of classical electrodynamics so as to establish the quantum theory only as a special case of the first principles of the nature.

REFERENCES

1. J. D. Jackson: "Classical Electrodynamis", *John Wiley and Sons*, 1975
2. R. P. Feynman, R. B. Leighton, M Sands: *"The Feynman Lectures on Physics"*, *Addison- Wesley Publishing Company*, 1977
3. J. E. Branderburg: "Unification of Gravity and Electromagnetism in the Plasma Universe", *IEE Transactions on Plasma Sciences*, **20**, 944 (1992)
4. A. Bergstrom: "On The origin of the Magnetic Field", *Nuovo Cimento* **14B**, 235 (1973)
5. J R Tessman: "Maxwell – Out of Newton, Coloumb and Einstein", *Am. J. Phys*. **34**, 1048, (1966)
6. "Random electrodynamics: The theory of classical electrodynamics with classical electromagnetic zero-point radiation", *Phys. Rev.* 790-808, (1975)

VI Serbian-Belarusian Symp. on Phys. and Diagn. of Lab. &
Astrophys. Plasma, Belgrade, Serbia, 22 - 25 August 2006
eds. M. Ćuk, M.S. Dimitrijević, J. Purić, N. Milovanović
Publ. Astron. Obs. Belgrade No. 82 (2007), 131 *Invited lecture*

MODELS OF STELLAR ATMOSPHERES FOR EVOLUTIONARY MODELLING

D. Jevremović[1], A. Dotter, E. Baron

[1]*Astronomical Observatory, Volgina 7, 11160 Belgrade, Serbia*
e-mail: darko@aob.bg.ac.yu

Abstract. In our contribution we will review recent modelling of stellar atmospheres using general stellar atmosphere code PHOENIX.. A grid of over four thousand models has been built with temperatures in the range from 3000-10000K, Z from -2.5 to +0.5 and different alpha element enhancement (from -0.2 to +0.8). Application to the better understanding of boundary condition between inner stellar structure and atmosphere and its consequences to the evolutionary modeling will be discussed.

VI Serbian-Belarusian Symp. on Phys. and Diagn. of Lab. &
Astrophys. Plasma, Belgrade, Serbia, 22 - 25 August 2006
eds. M. Ćuk, M.S. Dimitrijević, J. Purić, N. Milovanović
Publ. Astron. Obs. Belgrade No. 82 (2007), 133-147 *Invited lecture*

SHORT LIVE AFTERGLOW IN PURE NITROGEN AND NITROGEN CONTAINING TRACES OF OXYGEN AND METHANE

F. Krčma, V. Mazánková, I. Soural

Brno University of Technology, Faculty of Chemistry, Purkyňova 118, 612 00 Brno, e-mail: krcma@fch.vutbr.cz

Abstract. The work presents results obtained during spectroscopic observations of DC flowing post-discharges of pure nitrogen plasma and nitrogen plasma containing traces of oxygen and methane. The plasma has been studied by the emission spectroscopy of three nitrogen spectral systems, NO^{β} bands (with oxygen impurities) and two CN spectral systems (when methane was added).

The maximum of the pink afterglow intensity of nitrogen 1^{st} positive system decreased more or less exponentially with increasing the oxygen concentration. The position of the maximal pink afterglow emission was shifted to shorter decay times but both nitrogen positive systems showed a slow increase of the decay time of pink afterglow maximum after the initial shift to the earlier post-discharge position. Intensities of both nitrogen positive systems didn't show any significant dependence on the oxygen concentration. The NO^{β} bands were observed with low intensity and their intensities were directly proportional to the oxygen concentration.

The maxima of the pink afterglow intensities for all three nitrogen systems were decreasing proportionally to the increase of the methane concentration. The position of the maximal pink afterglow emission was also more or less linearly shifted to later decay times, it means on the contrary to the oxygen impurity. The strong CN emission is dominant at methane concentrations beyond 7 ppm and its intensity was more or less directly proportional to the methane concentration in the studied range.

On the basis of the experimental results, the appropriate kinetic models of the plasma generated in pure nitrogen and in nitrogen with oxygen or methane traces were designed. The specific state-to-state energy transfer reactions between the studied states are presented.

1. INTRODUCTION

Nitrogen post-discharges in various configurations have been subjects of many studies for a relatively long time [1-6]. Besides the laboratory and technological plasmas the nitrogen post-discharge is studied also in the kinetics of upper atmosphere (corona borealis [7-9]) and these processes are also taken into account in some extraterrestrial systems, for example in Titan atmosphere [10, 11]. Relaxation processes of atomic and various metastable molecular states created during an active discharge lead to the common thermal equilibrium. Besides collisional processes the light emission plays a significant role in the thermalization. Visible light can be observed up to one second after switching off the active discharge.

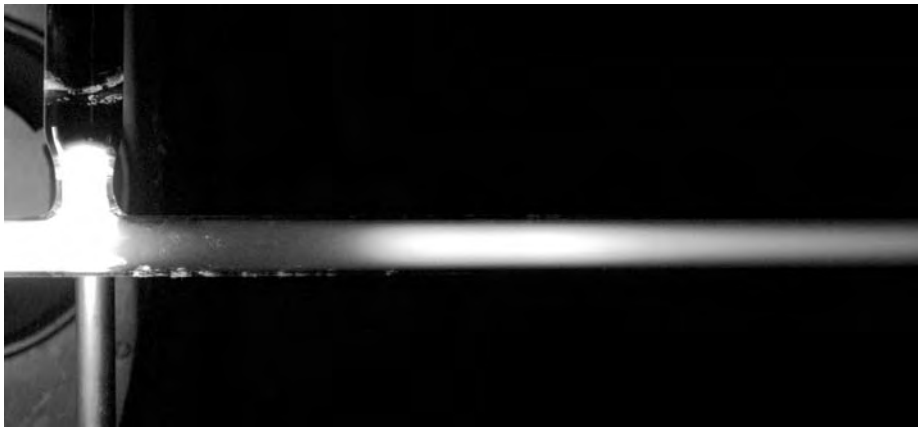

Fig. 1. Pink afterglow in pure nitrogen DC post-discharge.

The first period (up to about 3 ms) of the post-discharge in the pure nitrogen is characterized by a strong decrease of the light emission. After that, the strong light emission at about 5 – 14 ms after the end of an active discharge is known as a pink afterglow (see Fig. 1) and it can be observed in nitrogen only [12, 13]. The pink afterglow is manifested by a strong increase of the pink light emission at the decay times of about 6 – 8 ms in pure nitrogen and of about 28 ms in a nitrogen-argon mixture, while the yellow-orange color is characteristic of the other parts of the nitrogen afterglow. The nitrogen pink afterglow can be characterized as a secondary discharge, because the electron concentration strongly increases due to various collisionally induced ionization processes [14, 15] (see below) and thus the conditions are similar to those in the active discharge. The electron density measurements during the afterglow show the strong increase of the free electron concentration during this post-discharge period [16]. The effect of the nitrogen pink afterglow can be studied only in pure nitrogen; various traces (especially carbon and oxygen) quench it [17]. This work is focused on the experimental study of these

quenching processes. The simplified kinetic model of the post-discharge processes is proposed, too.

2. EXPERIMENTAL SETUP

The DC flowing post-discharge was used for the experimental study. The simplified schematic drawing of the experimental set up is given in Fig. 2.

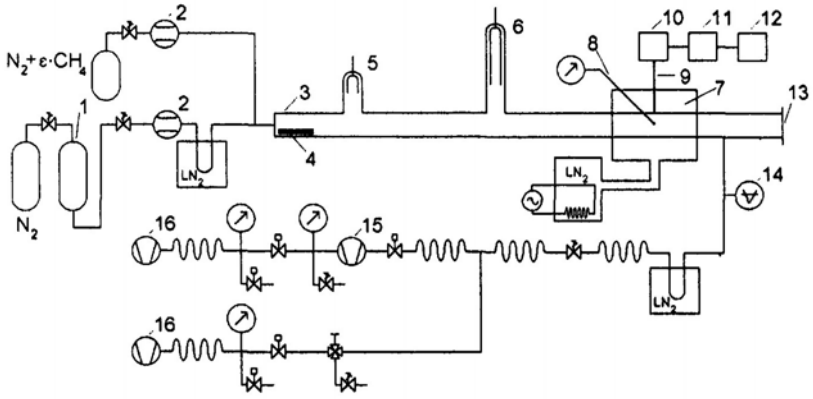

Fig. 2. Siplified scheme of the experimental set-up [17].

An active discharge was created in a Pyrex discharge tube (length: 1100 mm, inner diameter: 16 mm) with a 120 mm electrode distance. Tantalum or molybdenum electrodes were placed in the side arms of the main discharge tube for minimizing the sputtering of the electrode material and also for suppressing the light emitted in the electrode regions. The gas flow was automatically controlled by mass flow controllers. The nitrogen was of 99.999 % purity and it was further cleaned by copper based catalyzer and liquid nitrogen trap. The synthetic air (80 % N_2 + 20 % O_2) and various nitrogen-methane mixtures (except commercial mixture of 1 % of methane in pure nitrogen) were prepared directly in the laboratory and their compositions were measured by the gas chromatography. The system was pumped continuously by a rotary oil pump. The total pressure in the discharge tube during the experimental studies was measured by a baratron and Pirani gauges connected to the end of the discharge tube.

The spectra emitted from the post-discharge were measured by Jobin Yvon monochromator (HR320 or TRIAX 550 with the 1200 grooves per mm grating) coupled with multichannel detectors. The emitted light was led to the entrance slit of the monochromator by the multimode quartz optical fiber movable along the discharge tube. Nitrogen 1st (N_2 ($B\ ^3\Pi_g$) $\rightarrow$ ($A\ ^3\Sigma_u^+$)) and 2nd (N_2 ($C\ ^3\Pi_u$) $\rightarrow$ ($B\ ^3\Pi_g$)) positive and nitrogen 1st negative (N_2^+ ($B\ ^2\Sigma_u^+$) $\rightarrow$ ($X\ ^2\Sigma_g^+$)) systems were recorded

in all spectra. The bands of NO^{β} system ($NO\,(B\,^2\Pi) \rightarrow NO\,(X\,^2\Sigma^+)$) were remarkable with low emission intensity when oxygen was added, CN red ($CN\,(A\,^2\Pi) \rightarrow (X\,^2\Sigma^+)$) and violet ($CN\,(B\,^2\Sigma^+) \rightarrow (X\,^2\Sigma^+)$) systems were observed with higher intensities when methane traces were added. The typical experiment was carried out at total gas pressure of 1000 Pa and discharge current of 150 – 200 mA.

3. QUENCHING BY OXYGEN TRACES

The post-discharge emission intensity profiles of representative bands of all three observed nitrogen spectral systems are shown in Figs. 3 – 5 as a function of the oxygen concentration. The pink afterglow is quenched by oxygen traces. This effect differs for each of the measured nitrogen systems as it is compared in Fig. 6 where the dependences of the pink afterglow maximal intensities on the oxygen concentration are given. At the lower concentrations (up to about 200 ppm), the significant increase of the nitrogen positive band intensity can be seen.

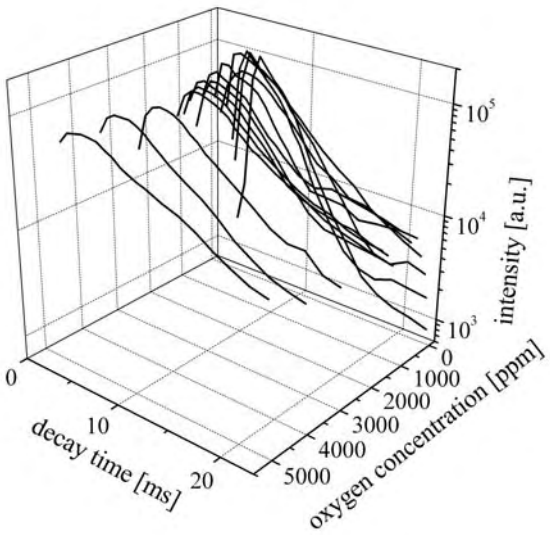

Fig. 3. Intensity of nitrogen 1st positive 2–0 band during the pink afterglow as a function of oxygen concentration.

The slow decrease of emission intensity with the increasing oxygen concentration appeares at higher concentrations but at the highest concentrations, another slight increase can be recognised. The emission from molecular ion decreases more or less exponentially with oxygen concentration increasing in the whole concentration range.

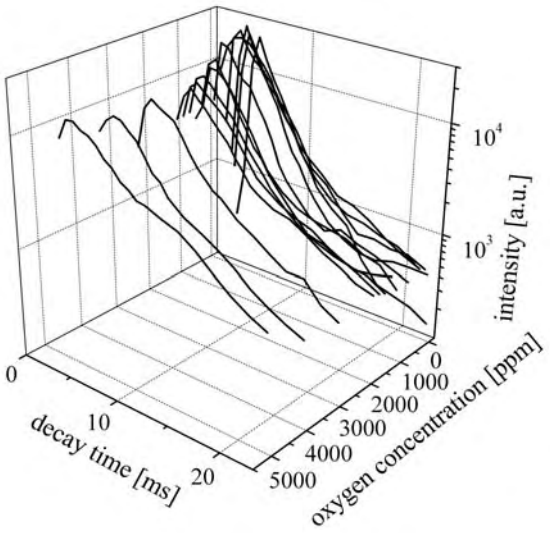

Fig. 4. Intensity of nitrogen 2nd positive 0–0 band during the pink afterglow as a function of oxygen concentration.

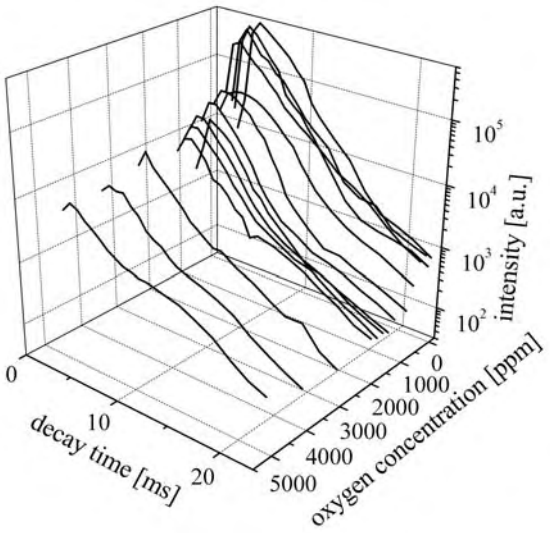

Fig. 5. Intensity of nitrogen 1st negative 0–0 band during the pink afterglow as a function of oxygen concentration.

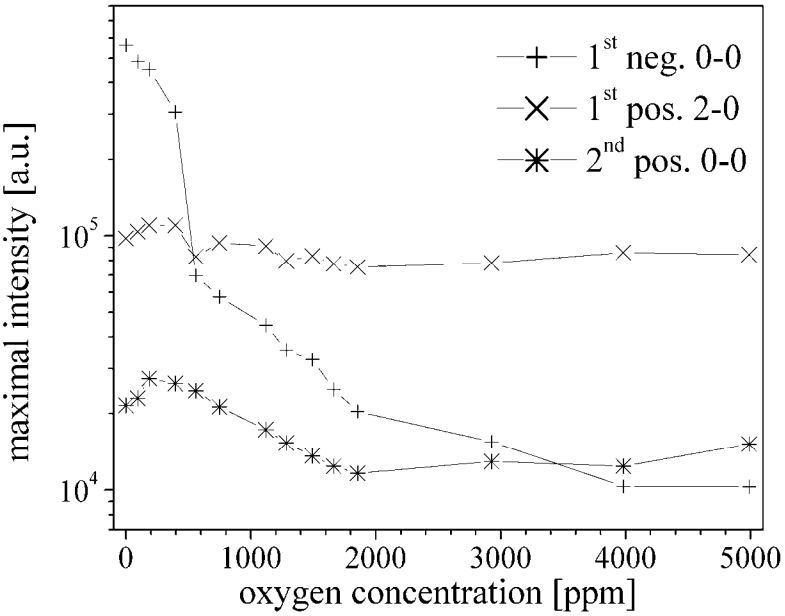

Fig 6. Maximal pink afterglow emission intensity as a function of oxygen concentration.

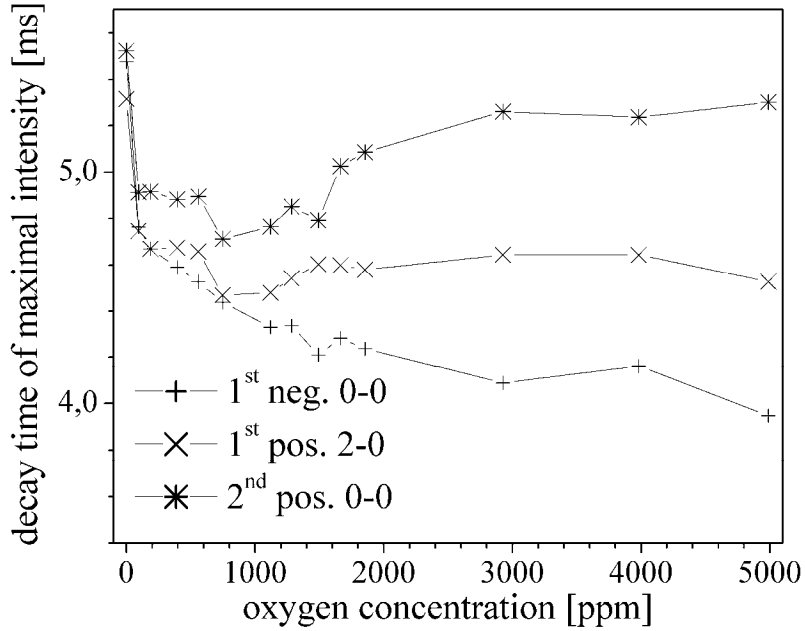

Fig. 7. Position of the maximal pink afterglow emission intensity as a function of oxygen concentration.

The position of the maximal pink afterglow emission intensity depends on oxygen concentration, too, as it is demonstrated in Fig. 7. The positions of maxima were calculated using the fitting of the post-discharge profile by polynomial function of 3rd order in time interval of 3 – 8 ms due to the limited number of experimental points (we didn't expect the observed effect and thus the number of experimental points was not sufficient to use the original time scale). The maximum of the 1st negative system is shifted to earlier post-discharge positions at the lower oxygen concentration (under about 100 ppm), but further increase of oxygen amount has only a slight influence of the same character. Both nitrogen positive systems show a slow increase of the decay time of pink afterglow maximum after the initial shift to the earlier post-discharge position.

4. QUENCHING BY METHANE TRACES

The pink afterglow quenching by methane traces is about two orders stronger than quenching by oxygen. Experiments focused on quenching by methane were carried out using the discharge tube with higher diameter. Due to the fact that the wall processes play a significant role in the post-discharge kinetics the pink afterglow maximum in pure nitrogen is localised at longer decay time of 8 ms in this case.

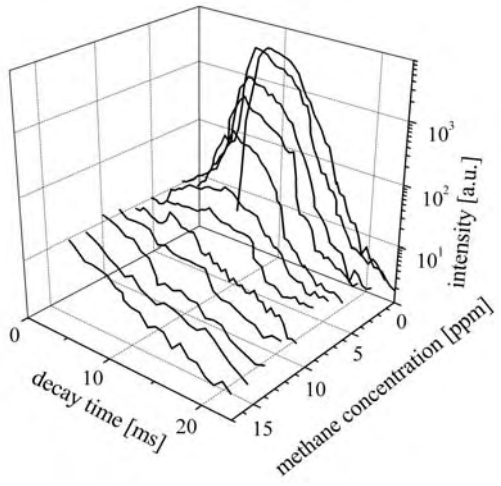

Fig. 8. Intensity of nitrogen 2nd positive 0–2 band during the pink afterglow as a function of methane concentration.

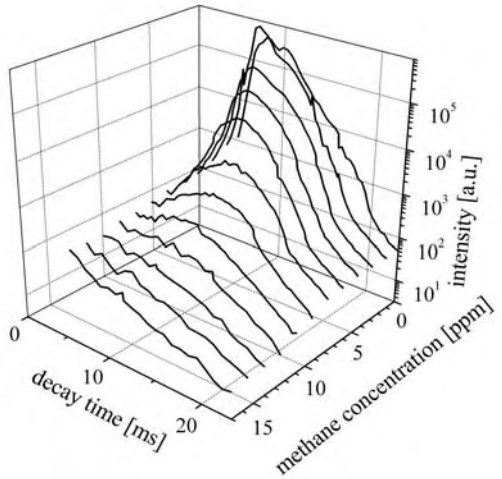

Fig. 9. Intensity of nitrogen 1st negative 0–0 band during the pink afterglow as a function of methane concentration.

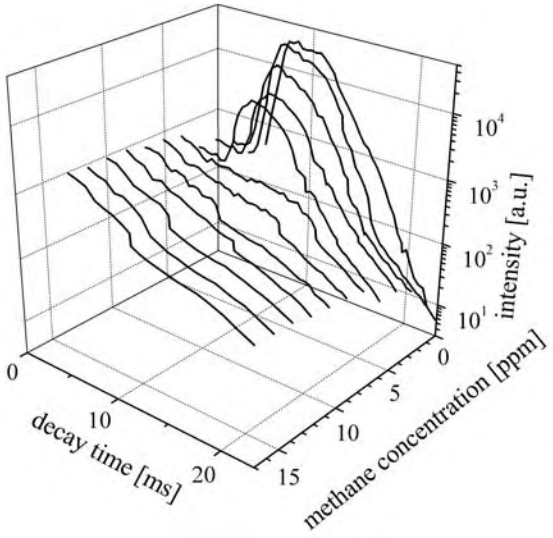

Fig. 10. Intensity of nitrogen 1st negative 1–1 band overlaped by P-branch of CN violet 0-0 band during the pink afterglow as a function of methane concentration.

The influence of methane presence on the pink afterglow has been observed through the emission of the nitrogen 1st negative and 2nd positive and CN violet spectral systems. The other spectral systems (nitrogen 1st positive and CN red) have been observed only in the other experiments and they show similar behaviours. Figures 8 – 10 show measured band head intensities of selected bands as a function of the methane concentration during the pink afterglow. The intensity profiles of the 1st negative 0–0 and 2nd positive 0–2 bands are similar, the second one is less

obvious due to lower intensities. Different situation is in the case of 1st negative 1–1 band which is completely overlapped by the P branch of 0–0 CN violet spectral system (see Figure 10). Thus at methane concentrations up to 7 ppm, the effect of the pink afterglow can be resolved, at higher concentrations, the strong CN emission can be dominant and its intensity is more or less directly proportional to the methane concentration in the studied range (in Fig. 10 it looks like independent due to the overlap by exponentially quenched nitrogen 1st negative band).

Figures 11 and 12 show the quenching of maximal pink afterglow intensity by methane addition and shift of this maximal intensity in the post-discharge time. Fig. 11 shows the dependence of the pink afterglow maximal intensity on the methane concentration. A small increase of the intensity can be seen at methane concentrations up to about 1 ppm and after that the maximum intensity is exponentially quenched by methane. At concentrations higher than 12 ppm, the maximum of the pink afterglow can't be found, however, this effect still exists. Fig. 12 demonstrates the shift of the pink afterglow intensity maximum to later decay times. This effect is more or less directly proportional to the methane concentration. The maximum pink intensity shifts up to 15.5 ms at the highest methane concentration of about 12 ppm when the effect can be measured. The shift of pink afterglow maximal intensity by methane on contrary to the shift by oxygen addition.

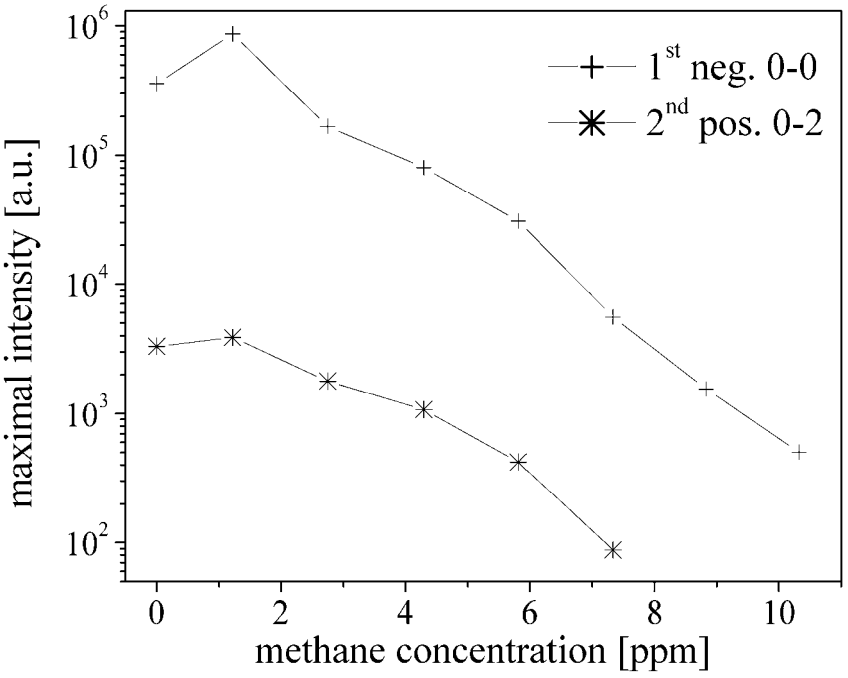

Fig. 11. Maximal pink afterglow emission intensity as a function of methane concentration.

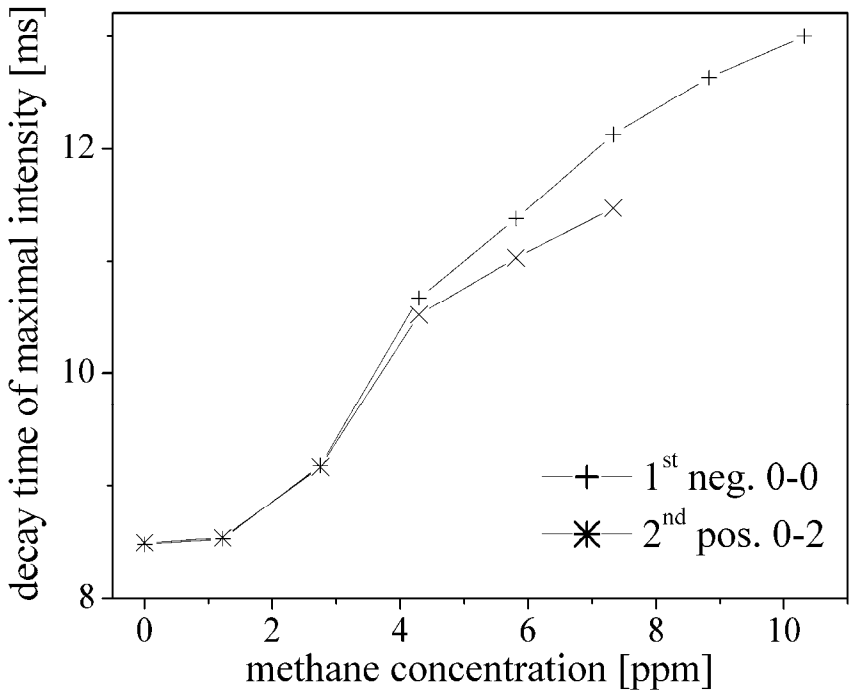

Fig. 12. Position of the maximal pink afterglow emission intensity as a function of methane concentration.

5. KINETIC MODEL

The nitrogen afterglow kinetics is a really complicated problem. The mechanisms that populate the radiative states of a neutral molecule and a molecular ion are different and they must be discussed separately. After that, the kinetics in both nitrogen mixtures is discussed. Only the creation mechanisms are given in the schemes. Besides them, many collisional quenching processes of specific states must be included to the numeric modeling (see [18]).

5.1 Neutral nitrogen

The $N_2(B\,^3\Pi_g)$ and $N_2(C\,^3\Pi_u)$ states are dominantly created by pooling reactions of lower metastable states, especially by the vibrational excited ground state and by the lowest 8 levels of $N_2(A\,^3\Sigma_u^+)$ state [2-4, 19]. These reactions show the creation of both these states, but they cannot explain the strong population enhancement during the pink afterglow. Therefore another process must be considered. It is known that in nitrogen post-discharge kinetics of the ground state

the initial vibrational distribution changes by v-v process into the Treanor-Gordiets distribution that can be characterized by the significant enhancement of populations at higher vibrational levels. In the creation of the $N_2(B\ ^3\Pi_g)$ and $N_2(C\ ^3\Pi_u)$ states by pooling, the ground state must be excited at least to the levels of $v = 4$, or $v = 19$ respectively, when the pooling is with $N_2(A\ ^3\Sigma_u^+)$ state. When two ground states are involved the excitation to the $v = 14$, or $v = 24$ respecitively, is necessary. It is clear that at the end of an active discharge all these species are presented in the gas but their concentrations are much lower than the concentrations of the lowly excited molecules. The creation of higher vibrational levels takes some time, of course, and thus the dark space between the end of the active discharge and the pink afterglow can be observed. The pooling reactions can also lead to the creation of the $N_2(A\ ^3\Sigma_u^+)$ state, and thus the pink afterglow effect is further enhanced. The reaction scheme can be written as follows (for references and rate constants see [20]):

$N_2(X\ ^1\Sigma_g^+, v) + N_2(X\ ^1\Sigma_g^+, w) \rightarrow N_2(X\ ^1\Sigma_g^+, v+1) + N_2(X\ ^1\Sigma_g^+, w-1)$ R1

$2\ N_2(X\ ^1\Sigma_g^+, v \geq 12) \rightarrow N_2(A\ ^3\Sigma_u^+) + N_2$ R2

$N_2(X\ ^1\Sigma_g^+, v \geq 25) + N(^4S_0) \rightarrow N_2(A\ ^3\Sigma_u^+) + N(^4S_0)$ R3

$N_2(X\ ^1\Sigma_g^+, v \geq 25) + e \rightarrow N_2(A\ ^3\Sigma_u^+) + e$ R4

$N_2(X\ ^1\Sigma_g^+, v \geq 35) + N(^4S_0) \rightarrow (N_2(a\ ^1\Pi_g) \text{ or } N_2(a'\ ^1\Sigma_u^-)) + N(^4S_0)$ R5

$N_2(X\ ^1\Sigma_g^+, v \geq 35) + e \rightarrow (N_2(a\ ^1\Pi_g) \text{ or } N_2(a'\ ^1\Sigma_u^-)) + e$ R6

$2\ N_2(X\ ^1\Sigma_g^+, v \geq 14) \rightarrow N_2(B\ ^3\Pi_g) + N_2$ R7

$N_2(X\ ^1\Sigma_g^+, v \geq 4) + N_2(A\ ^3\Sigma_u^+) \rightarrow N_2(B\ ^3\Pi_g) + N_2$ R8

$2\ N_2(A\ ^3\Sigma_u^+) \rightarrow N_2(B\ ^3\Pi_g) + N_2$ R9

$2\ N_2(X\ ^1\Sigma_g^+, v \geq 24) \rightarrow N_2(C\ ^3\Pi_u) + N_2(X\ ^1\Sigma_g^+)$ R10

$N_2(X\ ^1\Sigma_g^+, v \geq 19) + N_2(A\ ^3\Sigma_u^+) \rightarrow N_2(C\ ^3\Pi_u) + N_2$ R11

$2\ N_2(A\ ^3\Sigma_u^+) \rightarrow N_2(C\ ^3\Pi_u) + N_2(X\ ^1\Sigma_g^+)$ R12

$N_2(A\ ^3\Sigma_u^+) + N_2(B\ ^3\Pi_g) \rightarrow N_2(C\ ^3\Pi_u) + N_2(X\ ^1\Sigma_g^+)$ R13

The first six reactions form the precursors, the other lead to the formation of both radiative states. The reaction R1 is well known as v-v pumping process and plays the significant role during the whole nitrogen afterglow. Also the reaction R2 is running about all the time without any significant changes. The reactions R3 – R6 are probably the most important for the pink afterglow creation. They need highly vibrationally excited ground state molecules that are not presented during the afterglow beginning in higher concentrations and they must be created by *v-v* process (reaction R1). This takes some time and after that the electronically excited molecules are created and consequently they can react with molecules excited to the lower vibrational levels. This mechanism can explain the lower radiative afterglow part between the active discharge and the pink afterglow. The other metastable states, especially metastable singlet states, must be, of course, included in the scheme, when a numeric modeling would be used. This simplified reaction scheme clearly demonstrates the main principles of the pink afterglow creation. Much more complex description of the mechanisms was described recently in [12, 21].

5.2 Nitrogen molecular ion

The kinetics of the molecular ion radiative state is more complicated and it can be explained in a two-step scheme. Before the pink afterglow the charged particles concentration is very low [16] but during the pink afterglow it significantly increases. So, the first step must lead to the molecular ion creation.

Due to the fact that the post-discharge is without any external energy source, some of the kinetic processes must be efficient enough for the ionization. The whole process is known as a step-wise ionization [14, 15]. In its principle, the highly excited neutral metastable molecules (excited both electronically and vibrationally) can have energy sufficient for the ionization during their collisions. Precursors for the ionizing collisions are created by the process R1 and by processes similar to R2.

When the molecular ion is created, the excitation to the radiative state must be completed. Recent studies have demonstrated that the main process responsible for the population of the radiative $N_2^+(B\ ^2\Sigma_u^+)$ state is the collisionally induced energy transfer from the vibrationally excited neutral ground state [19] as it is shown as the reaction R18.

The reactions describing kinetics of the molecular ion are, besides the reaction R1, as follows:

$$N_2(X\ ^1\Sigma_g^+, v) + N_2(X\ ^1\Sigma_g^+, w) \rightarrow N_2^* + N_2 \quad \text{R14}$$
$$2\ N_2(X\ ^1\Sigma_g^+, v \geq 32) \rightarrow N_2^+(B\ ^2\Sigma_u^+) + N_2 + e \quad \text{R15}$$
$$N_2(X\ ^1\Sigma_g^+, v) + N_2^* \rightarrow N_2^+ + N_2 + e \quad \text{R16}$$
$$2\ N_2^* \rightarrow N_2^+ + N_2 + e \quad \text{R17}$$
$$N_2(X\ ^1\Sigma_g^+, v \geq 12) + N_2^+(X\ ^2\Sigma_g^+) \rightarrow N_2(X\ ^1\Sigma_g^+) + N_2^+(B\ ^2\Sigma_u^+) \quad \text{R18}$$

The N_2^* in the reactions above means an electronically excited metastable neutral molecule, especially $N_2(A\ ^3\Sigma_u^+)$, $N_2(a\ ^1\Pi_g)$ and $N_2(a'\ ^1\Sigma_u^-)$ states.

5.3 Nitrogen with oxygen traces

Kinetics of pure nitrogen with a small addition of oxygen can be generally described by following additional reactions. The reactions with molecular oxygen can be neglected because we can assume high molecular oxygen dissociation in an active discharge (residence time about 8 ms) and recombination forming molecular oxygen during afterglow can be neglected due to its low concentration.

$$N_2(X\ ^1\Sigma_g^+, v \geq 13) + O \rightarrow NO(X\ ^2\Pi) + N(^4S_0) \quad \text{R19}$$
$$N_2(A\ ^3\Sigma_u^+) + O \rightarrow NO(X\ ^2\Pi) + N(^2D_0) \quad \text{R20}$$
$$N(^4S_0) + O + N_2 \rightarrow NO(X\ ^2\Pi) + N_2 \quad \text{R21}$$
$$NO(X\ ^2\Pi) + N(^4S_0) \rightarrow N_2(X\ ^1\Sigma_g^+, v \cong 3) + O \quad \text{R22}$$
$$N_2(A\ ^3\Sigma_u^+) + NO(X\ ^2\Pi) \rightarrow N_2(X\ ^1\Sigma_g^+, v = 0) + NO(A\ ^2\Sigma^+) \quad \text{R23}$$
$$N_2(X\ ^1\Sigma_g^+, v \geq 23) + NO(X\ ^2\Pi) \rightarrow N_2(X\ ^1\Sigma_g^+) + NO(A\ ^2\Sigma^+) \quad \text{R24}$$

$$N\,(^4S_0) + O + N_2 \rightarrow NO\,(B\,^2\Pi,\ v = 0) + N_2 \qquad R25$$

These reactions show four different channels of NO molecule formation. The reaction R19 has a strong influence on the *v-v* process described by reaction R1. Thus highly excited molecular states are formed with lower probability and the creation of electronically excited states is decreased. Formation of nitrogen molecular ion strongly decreases also due to reactions R20, R23 and R24, and thus the nitrogen 1st negative system is effectively quenched. High vibrationally excited ground state nitrogen molecules (over $v = 22$) play a minor role in the formation of electronically excited states, and thus both nitrogen positive systems are quenched only slightly. Direct confirmation of processes described by reaction R23 and R24 is impossible in our contemporary experimental set up because the NO^{γ} system emission is in UV region under 300 nm and a strong light absorption of the Pyrex reactor walls takes part.

5.4 Nitrogen with methane traces

Situation in nitrogen with methane traces is more or less similar as in the previous case. Again we can suppose high dissociation of methane during the active discharge and CN and NH radicals are formed. The NH radicals have not been identified in the spectra, so we suppose that their role in post-discharge kinetics is negligible. The CN radical kinetics can be described in a simplified form by the following scheme:

$$N\,(^4S_0) + C\,(^3P) + M \rightarrow CN + M \qquad R26$$

$$N_2^{*} + CN \rightarrow N_2 + N + C \qquad R27$$

$$N_2\,(X\,^1\Sigma_g^+,\ v \geq 4) + CN\,(X\,^2\Sigma) \rightarrow N_2\,(X\,^1\Sigma_g^+) + CN\,(A\,^2\Pi) \qquad R28$$

$$N_2\,(X\,^1\Sigma_g^+,\ v \geq 12) + CN\,(X\,^2\Sigma) \rightarrow N_2\,(X\,^1\Sigma_g^+) + CN\,(B\,^2\Sigma^+) \qquad R29$$

Reaction R26 represents the CN radical formation by three body recombination (M means a third body, in our case it is mainly nitrogen neutral molecule or the reactor wall). The other two processes are nearly resonant [19, 22] and due to the high concentration of the vibrationally excited neutral nitrogen ground states, they are very effective sources for the strong CN spectra emission.

The reactions R28 and R29 play a significant role in the *v-v* process described by the reaction R1. Due to the fact that the excited states of the CN radical are radiative, the reactions R28 and R29 can be repeated many times, and thus the *v-v* process could not effectively populate the higher vibrational level needed for the creation of all higher states. Moreover, the reaction R27 effectively decreases the concentration of the electronically excited nitrogen states. Thus the $N_2\,(B\,^3\Pi_g)$, $N_2\,(C\,^3\Pi_u)$ and N_2^+ species could not be formed as effectively as in pure nitrogen, and therefore the pink afterglow is quenched. The strong quenching of nitrogen 1st negative system is caused by the strong depopulation of $N_2\,(X\,^1\Sigma_g^+,\ v \geq 12)$ by reaction R29 that is faster process than reaction R12. Due to this fact, the pink afterglow quenching by methane traces is much more stronger than quenching by

oxygen traces where is no direct reaction depopulating vibrational level of N_2 ($X\ ^1\Sigma_g^+$, $v = 12$).

6. CONCLUSION

The work presents results obtained during spectroscopic observations of DC flowing post-discharges of pure nitrogen plasma and nitrogen plasma containing traces of oxygen and methane. The plasma has been studied by the emission spectroscopy of three nitrogen spectral systems, NO^β bands (with oxygen impurities) and two CN spectral systems (when methane was added).

First, the quenching of the nitrogen pink afterglow by the oxygen traces was studied. It was shown that the maximum of the pink afterglow intensity of nitrogen 1st positive system decreased more or less exponentially with the increasing oxygen concentration. The position of the maximal pink afterglow emission was shifted to shorter decay times at the lower oxygen concentration (under about 100 ppm), but further increase of oxygen amount had only a slight influence of the same character. Both nitrogen positive systems showed a slow increase of the decay time of pink afterglow maximum after the initial shift to the earlier post-discharge position. Intensities of both nitrogen positive systems didn't show any significant dependence on the oxygen concentration. The NO^β bands were observed with low intensity and their intensities were directly proportional to the oxygen concentration.
The quenching of the nitrogen pink afterglow by the methane traces showed different character of behaviors. It was shown that the maxima of the pink afterglow intensities for all three nitrogen systems were decreasing proportionally to the increase of the methane concentration. The position of the maximal pink afterglow emission was also more or less linearly shifted to later decay times, it means on the contrary to the oxygen impurity. The strong CN emission is be dominant at methane concentrations over about 7 ppm and its intensity was more or less directly proportional to the methane concentration in the studied range.
On the basis of the experimental results, the appropriate kinetic models of the plasma generated in pure nitrogen and in nitrogen with oxygen or methane traces were designed. The specific state-to-state energy transfer reactions between the studied states were presented. The full kinetic models of nitrogen-oxygen and nitrogen-methane mixtures are contemporary under preparation.

This work was supported by the Czech Science Foundation, contracts No. 202/98/P258 and 202/05/0111.

REFERENCES

1. G. E. Beale, H. P. Broida: J. Chem. Phys. **31**, 1030 (1959).
2. L. G. Piper: J. Chem. Phys. **88**, 231 (1988).
3. L. G. Piper: J. Chem. Phys. **88**, 6911 (1988).
4. L. G. Piper: J. Chem. Phys. **91**, 864 (1989).

5. V. Guerra, P. A. Sa, J. Loureiro: J. Phys. D, Appl. Phys. **34** (2001) 1745.
6. F. Krčma: Acta Phys. Slovaka **55**, 453 (2005).
7. Ø. Lie-Svendsen, M. H. Rees, K. Stamnes, E. C. Whipple: Planet. Space Sci. **39**, 929 (1991).
8. A. S. Kirillov, G. A. Aladjev: Adv. Space Res. **16**, 105 (1995).
9. J. S. Morrill, W. M. Benesch: J. Geophys. Res. Space Phys. **101** (1996).
10. C. N. Keller, V. G. Anicich, T. E. Cravens: Planet. Space Sci. **46,** 1157 (1998).
11. V. Dimitrov, A. Bar-Nun: Prog. Reac. Kin. Mechanisms **29**, 1 (2004).
12. P. A. Sa, V. Guerra, J. Loureiro, N. Sadeghi: J. Phys. D, Appl. Phys. **37**, 221 (2004).
13. Loureiro J, Sa PA, Guerra V: J. Phys. D, Appl. Phys. **39**, 122 (2006).
14. L. S. Polak, D. I. Sloveckii, A. S. Sokolov: Opt. Spectrosc. **32**, 247 (1972).
15. F. Paniccia, C. Gorse, M. Cacciatore, M. Capitelli: J. Appl. Phys. **61**, 3123 (1987).
16. J. Janča, A. Tálský, N. El Kattan: Folia Physica **27**, 23 (1978).
17. F. Krčma, L. Babák: Czech. J. Phys. **49**, 271 (1999).
18. C. D. Pintassilgo, J. Loureiro, V. Guerra: J. Phys. D, Appl. Phys. **38**, 417 (2005).
19. F. Krčma, E. T. Protasevich: Post-discharges in Pure Nitrogen and in Nitrogen Containing Halogenated Hydrocarbon Traces, Tomsk Polytechnic University Publishing, Tomsk 2003.
20. F. Krčma: http://www.fch.vutbr.cz/home/krcma/publications/95-thesis-appendix1.pdf.
21. N. Sadeghi, C. Foissac, P. Supiot: J. Phys. D, Appl. Phys. **34,** 1779 (2001).
22. J. Hubeňák, F. Krčma: J. Phys. D, Appl. Phys. **33,** 3121 (2000).

VI Serbian-Belarusian Symp. on Phys. and Diagn. of Lab. &
Astrophys. Plasma, Belgrade, Serbia, 22 - 25 August 2006
eds. M. Ćuk, M.S. Dimitrijević, J. Purić, N. Milovanović
Publ. Astron. Obs. Belgrade No. 82 (2007), 149-156 *Invited lecture*

DIODE-PUMPED SOLID-STATE LASERS WITH CONTROLLED PARAMETERS FOR SPECTROSCOPIC APPLICATIONS

V. V. Mashko[1], G. I. Ryabtsev[2], M. V. Bogdanovich[2], A. S. Drakov[1], A. I. Enzhyieuski[2], O. E. Kostik[1], A. V. Pozhidaev[3] , A. G. Ryabtsev[3], M. A. Shemelev[3], L. L. Teplyashin[1]

[1] *Institute of Molecular and Atomic Physics, National Academy of Sciences of Belarus, Minsk, Belarus*
[2] *B.I. Stepanov Institute of Physics, National Academy of Sciences of Belarus, Minsk, Belarus*
[3] *Belarussian State University, Minsk, Belarus*

Abstract. This work is devoted to analysis of possibility of control of frequency, polarization and spatial radiation attributes of diode-pumped solid-state lasers (DPSSLs) fabricated on the base of modern active elements (AEs). Crystals of yttrium aluminum garnet and yttrium vanadate activated by neodymium ions (Nd:YAG и Nd:YVO_4) lasing at the wavelength λ = 1.06 μm and the boro-silico-phosphate glass co-activated by erbium and ytterbium ions lasing in the 1.5 μm spectral region are considered. The schemes of longitudinal and transversal laser diode (or laser diode array) pump are compared.

Compact diode-pumped solid-state lasers (DPSSLs) are perspective sources of coherent light for range finding, metrology, spectral analysis as well as for investigations of impact of the radiation on a substance. The predetermined parameters of laser beam are needed for many of these applications. Because of specific properties of DPSSLs (small dimensions, peculiar pump unit and so on) the well known approaches for control of the laser beam characteristics are not always convenient for utilization in practice. As a result, the task of elaboration of the new methods of the DPSSL control and adaptation of the earlier one is posed.

The tuned single- and double-frequency lasing modes were realized for the Nd:YAG longitudinally pumped radiation source with a composite resonator [1]. The laser scheme is shown in Fig. 1. In spite of monolithic construction [2], it allows quick changing and tuning the lasing frequency in a wide spectral interval. The AE length and diameter were 1.3 mm and 5 mm respectively. Dielectric mirror M1 with the reflection coefficient R = 99.8% for λ = 1.06 μm and transmission coefficient 90% for λ = 0.809 μm (pump radiation wavelength) was deposited on one AE facet. The second facet of the AE crystal was covered with antireflecting coating (λ = 1.06 μm, residual reflection is as high as 1.2%). Output mirror M2 deposited on outer spherical surface (r = 50 mm) of the substrate had R = 98% at λ = 1.06 μm. The second substrate surface was covered with antireflecting coating (λ = 1.06 μm).

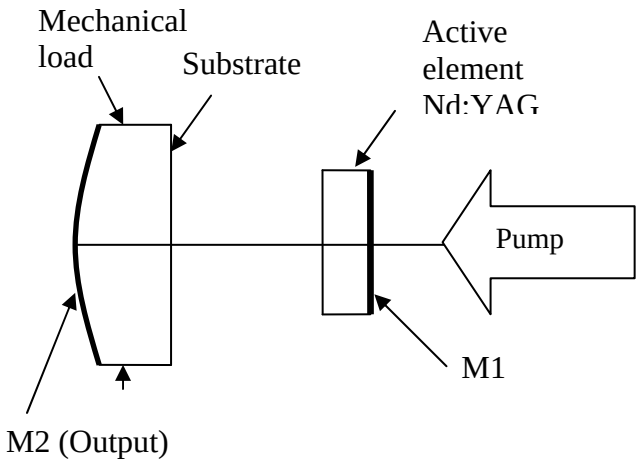

Fig. 1. Optical scheme of the Nd:YAG laser with coupled resonators and longitudinal diode pump unit

Adjustable mechanical load was applied to the output mirror substrate using the piezoelectric cell. This allowed us to achieve lasing at splitted orthogonally polarized modes due to linear phase anisotropy of the resonator.

Minimal optical length of the main resonator formed by the mirrors M1 and M2 was equal to 10.8 mm. This value is related to a frequency difference between the main resonator characteristic modes Δν = 13,9 GHz. Intermode difference for the complementary resonator formed by the AE facets was approximately equal to 64 GHz. During experiments the output mirror was moved along the resonator optical axes with help of piezoelectric cell. Output laser radiation frequency spectrum was controlled by means of scan Fabry-Perot interferometer (the free dispersion interval of 1.5 GHz, the resolution at the level of 50 GHz), high-speed photodiode and spectrum analyzer.

CW laser diode (LD) emitted polarized radiation at λ = 0.809 μm with maximum power of 450 mW was used as a pump light source. The LD beam was focused by the microscope objective on the AE facet (through the M1 mirror).

DPSSL lasing frequency structure was defined by a relative position of the modes of two coupled resonators and power-level overshoot over the threshold value. By varying of these parameters in the absence of the resonator phase anisotropy the following lasing regimes were realized: 1) lasing of single longitudinal mode with a possibility of its tuning within the gain spectrum, and 2) lasing of two adjacent modes with the frequency difference of 7.5 – 13.9 GHz (depending on the optical length of the main resonator). Induction of linear phase anisotropy during pressing of the output mirror substrate allowed lasing of two orthogonally polarized modes with a gradual tuning of the frequency difference within the interval of 50 MHz – 2.4 GHz in the regime 1) and up to 8.4 GHz in the regime 2). Thus, one can conclude that the proposed method allows two modes lasing both with small and large intermode intervals at relatively small-scale elastic strains induced in the output mirror substrate.

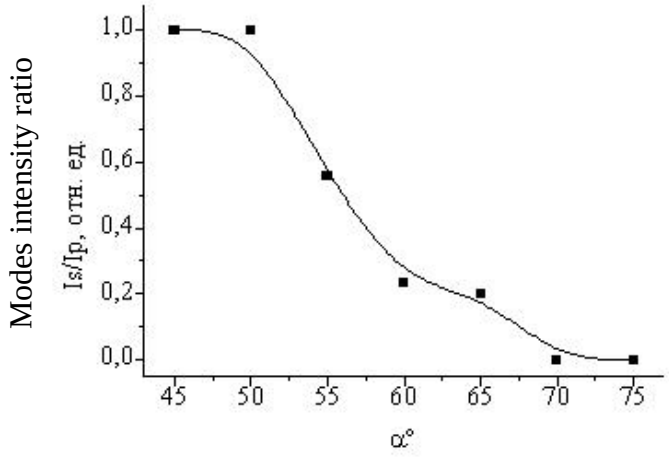

Fig. 2. The dependence of the orthogonally polarized modes intensity ratio on the angle α .

As is well known [3], the polarization of radiation of the Nd:YAG laser with isotropic resonator is coupled with the polarization of the LD beam used in the longitudinal pump unit. Similar phenomenon was investigated in our experiments for the case when the resonator has the linear phase anisotropy being responsible for two orthogonally polarized mode lasing. If the LD polarization azimuth was directed at the angle α = 45° relative to the axis along which the mirror substrate is pressed, the identical conditions were created for lasing of two orthogonally polarized modes. If the frequency of the initial mode was close to the central frequency ν_0 of the coupled resonator transmission line, the intensities of these modes were equal. In other cases the higher intensity was achieved for the mode which polarization vector

is closer to the pump radiation polarization one. Only one mode with the corresponding polarization vector was selected when the pump radiation polarization vector was directed along or perpendicularly to the resonator anisotropy axis (α = 0°, 90°). The lasing frequency was gradually tuned during changing of the anisotropy value (mechanical load).

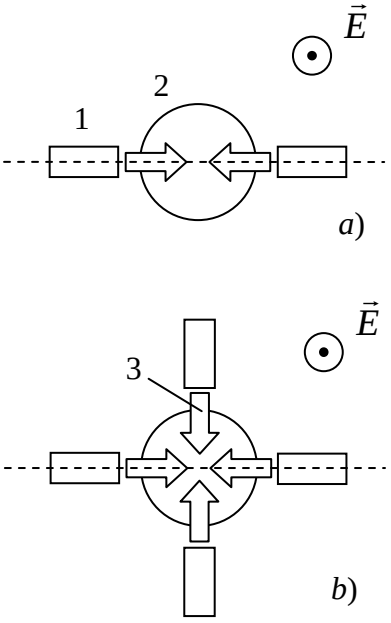

Fig. 3. Scheme of transversal pumping of erbium laser AE using two (a) and four (b) LDAs: LDA (1), AE (2), pump radiation (3)

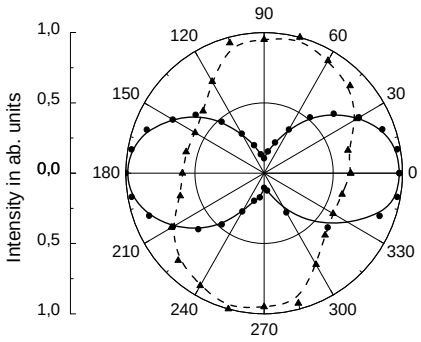

Fig. 4. Intensity azimuth dependence for the Er^{3+} laser beam after its passing through the polarizer: pumping by two (solid) and four LDAs (dashed lines)

The dependence of the orthogonally polarized modes intensity ratio on orientation of the pump radiation polarization vector relative to the selected anisotropy axis is given in Fig. 2 for the case of tuning of the lasing frequencies to the composite resonator transmission line center. Deviation of the pump radiation polarization azimuth from a medium position between the resonator anisotropy directions leads to the change in the intensity ratio for the orthogonally polarized mode components similar to theirs changing during the scan of the modes relative to central frequency of the resonator transmission line, i.e. to theirs spectral selection.

An increase of the output radiation power is a key problem for many application areas of DPSSLs. A rather high level of the power can be reached in the case of the transversal pumping of AE by the laser diode arrays (LDAs) [4]. In the frame of our experiments the spatial-polarization properties of radiation of the solid-

state erbium laser (λ = 1.54 μm) with transversal LDA pump unit have been studied. AE based on the boro-silico-phosphate glass co-activated by Er and Yb ions was fabricated in the form of rod with the diameter of 3 mm and the length of 11 mm. The erbium laser AE facets were covered with the antireflection coatings for the 1.50-1.58 μm spectral region. The erbium laser pump unit had two or four LDAs fabricated from the *InGaAs/AlGaAs* heterostructures. The LDA active layers are placed parallel to the AE axis (Fig. 3). LDA output radiation was linear polarized with the light wave electrical vector $\vec{E}$ parallel to the laser optical axis. Duration of the LDA current pulses was equal to 5 ms at the repetition rate of 1 Hz. The laser output radiation pulse energy was varied within the range of 10-30 (two LDAs) or 10-60 mJ (four LDAs).

It has been determined that output radiation of the erbium laser is polarized with a degree of the polarization $P \approx 0.8$ (pumping by two LDAs) and $P \approx 0.3$ (pumping by four LDAs), where $P = (I_{max} - I_{min})/(I_{max} + I_{min})$, I_{max} and I_{min} are the maximum and minimum values of the signal after passing of the DPSSL beam through the polarizer. Indicatrixes of the laser radiation intensity for these two pumping variants are shown in Fig. 4.

Since the vector $\vec{E}$ of the LDAs is directed parallel to the resonator optical axis the pump radiation can not be the source of the anisotropy of induced optical parameters for the laser active medium. The investigated resonator had no any anisotropic elements. No traces of the dichroism were revealed both the *Er-Yb* glass absorption or transmission measurements. So, polarization of the erbium laser output radiation can be attributed to the anisotropy induced in AE by mechanical and/or thermal strains. The reason for the conclusion is the fact that the polarization degree of the erbium laser is distinctly different in the cases of pumping with help of two and four LDAs.

If the problems concerned with focusing and/or delivering of laser radiation are arisen the beam quality begins to play an important role. The beam quality is usually described with the propagation parameter M^2 [5] reflecting an excess of the product of the real beam divergence and waist diameter over that for the gaussian beam.

It has been revealed that output beam cross-section of the investigated laser has an elliptic form. It can be characterized by two propagation parameters M^2_x and M^2_y (axes *Ox*, *Oy* are directed along major and minor axes of the ellipse). Appling the relation establishing the correlation among the laser beam diameters D_x, D_y along *Ox*, *Oy* axes, the distance *z* from the principal plane of the focusing lens placed for obtaining the beam waist at a plane *A-A* and the beam examination plane $D_{x,y}(z) = D_{0x,y}(1 + 4 M^2_{x,y} \lambda (z - z_{0x,y})/\pi D_{0x,y}^2))^{1/2}$ [6] the parameters M^2_x and M^2_y were determined. Numerical values of the beam waist diameters D_{0x}, D_{0y} at the *A-A* plane, the distance $z_{0x,y}$ from the *A-A* plane as well as the M^2_x and M^2_y were treated as the adjustable parameters. They have been found by the least-squares technique in the course of making the match between the above given function $D_{x,y}(z)$ with a set of the $D_x(z)$,$D_y(z)$ data calculated based on the experimental beam cross-section profiles [5].

The M^2_x,M^2_y measurements were performed for different resonator lengths and configurations using two or four LDAs in the pump unit. The best results (M^2_x =

1.9 and M^2_y = 1.2) were obtained for the 85 mm-length parallel-plane resonator of the *Er-Yb* laser pumped by four LDAs.

The beam propagation parameter M^2 was also investigated for the high-power Nd^{3+}:YVO_4 laser with longitudinal pumping through the fiber depending on the AE exciting power P_{pump}, degree of overlapping of the AE pump and lasing volumes, uniformity of the Nd^{3+} ion distribution within AE. It has been shown that in the case of considerable excess of the lasing mode cross-section over that for the pump radiation the limiting dimension of the beam spot is rose when a sharp focusing is carried out. The regularly varying intervals of an abrupt increase of the beam propagation parameter were obtained on the background of the M^2 (P_{pump}) monotonous dependence. This phenomenon can be explained by action of the AE nonlinear lenses originated both from the lasing radiation and the pump one.

The active elements with uniform (Nd^{3+}:YVO_4) and nonuniform (YVO_4/Nd^{3+}:YVO_4) distributions of the activator ions within the AE volume were studied with the aim of search of the most effective lasing medium for DPSSLs. In the first case the Nd^{3+} concentration was at the level of 0.4 at. %, and the AE crystal was a parallelepiped 4x4x8 mm. In the second case the 3x3x10 mm crystal was used. From its length of 10 mm the main part of 8 mm was the uniform activated section, whereas the rest 2 mm-section was the passive one. It has been ascertained that the AE with the passive section allows us to improve noticeably the output beam quality: the M^2 parameter takes on the value of 1.4 – 1.8. Probably, this is a consequence of diminishing the thermoelastic strains developing at the AE active region border.

For the purpose of quantitative comparative analysis the internal loss coefficient ρ was determined for the laser active elements with uniform and nonuniform distributions of the activator ions. A method based on the measurements of the lasing output power P_{out} as a function of the output cavity losses $\alpha_R = (1/L)\ln(1/\sqrt{R_1 R_2})$, where R_1 and R_2 are the reflection coefficients for cavity mirrors was used [7]. With this object in view the $P_{out} = F(\alpha_R)$ dependence was presented in the following form:

$$\frac{P_{out}}{\alpha_R} = Ls \cdot n \cdot h\nu_l \left[\frac{\eta\beta P_{pump}}{\rho + \alpha_R} - \frac{\eta\beta P_{pump} + (p_{31} + p_{32})}{\chi} \right],$$

where *Ls* is the lasing volume of the active element, *n* is the concentration of the active particles, $h\nu_l$ is the lasing photon energy, $\eta\beta P_{pump}$ is the pump rate, p_{31} and p_{32} are the optical transition probabilities for the lasing energy levels, χ is the maximum gain value.

Typical dependences of normalized output power on the pump level are shown in Fig. 5. The results of measurement of the internal loss coefficient for DPSSLs on the base of the Nd^{3+}:YVO_4 and YVO_4/Nd^{3+}:YVO_4 active elements are summarized in Table 1 It should be noted that in the case of the YVO_4/Nd^{3+}:YVO_4 DPSSL two different variants of the AE orientation were studied: 1) YVO_4 passive

region is directed towards income of the pump beam, 2) YVO_4 passive region is directed in the opposite direction.

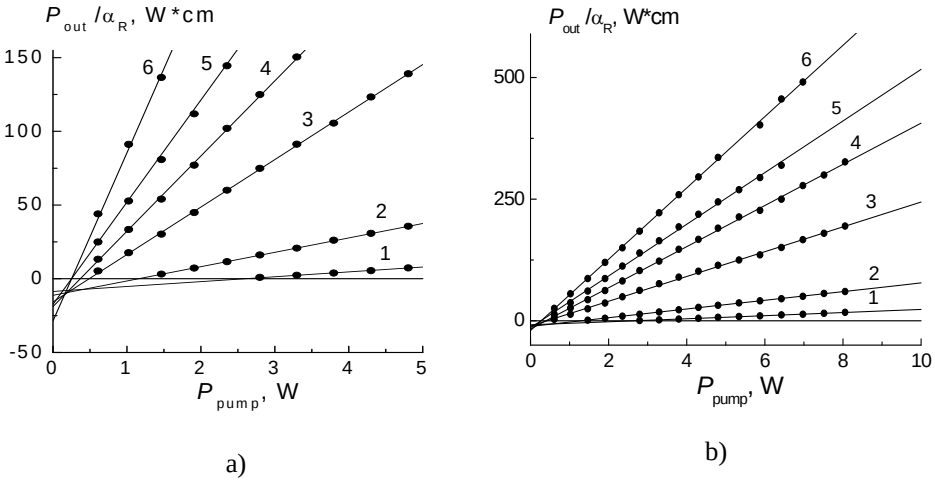

Fig. 5. Watt-Watt characteristics normalized to the α_R coefficient for DPSSLs on the base of the $Nd^{3+}:YVO_4$ (a) and $YVO_4/Nd^{3+}:YVO_4$ (b) active elements with uniform and nonuniform distributions of activator ions respectively. In the (b) case the YVO_4 passive region of the active element was orientated towards income of the pump beam. The output laser mirror reflection coefficient R_2 = 20 (1), 53 (2), 83 (3), 90 (4), 95 (5), 98 (6) %.

Table 1. Magnitudes of the internal loss coefficient ρ for DPSSLs with different types of AE.

Type of active element	Internal loss coefficient, cm^{-1}
AE with uniform ($Nd^{3+}:YVO_4$) distribution of activator ions	0,0091
AE with nonuniform ($YVO_4/Nd^{3+}:YVO_4$) distribution of activator ions, passive region is directed towards the pump beam	0,0089
AE with nonuniform ($YVO_4/Nd^{3+}:YVO_4$) distribution of activator ions, passive region is directed away from the pump beam	0,0093

As may be seen from Table 1, obtained results show that the DPSSL emitter with nonuniform distribution of activator ions and orientation of the passive region directed towards the pump beam has the minimum optical losses, all things being equal. In other words, this type of the DPSSL emitter is the best suited for powerful applications.

The obtained data demonstrate new possibilities for control of the frequency, polarization and spatial characteristics of the DPSSLs radiation. One perspective application is the development and fabrication of the narrowband laser sources with tuning of the lasing frequency within the range approximately 10 GHz for the purpose of spectroscopy. Another possible application is dealt with the development of the relatively powerful compact lasers with the output radiation pulse energy of several tens of mJ and a very high beam quality which are sufficient for a precise focusing manipulation. Such laser installations can be used as the atomizer suitable for portable spectrometers, just as the intensive light sources adjusted to the investigation of interaction of radiation and solids as well as to obtaining the plasma technology.

REFERENCES

1. V.G. Gudelev et al., Appl. Phys. B, **76**, 249 (2003)
2. A. Owyoung, P. Esherick, Optics Letters, **12**, 999 (1987)
3. N.V. Kravtsov, et al., Quantum. Electron. (in Russian), **34**, 839 (2004)
4. G.I. Ryabtsev, et. al., J. Optical Technology (in Russian), **73**, 10 (2006)
5. B.J. Neubert, et. al., Journal of Physics D: Applied Physics, **34**, 2414 (2001)
6. N. Reng, B. Eppich, Optical and Quantum Electronics, **24**, 973 (1992)
7. B.I. Stepanov, editor, Method of calculations of optical quantum generators (in Russian), Nauka i Technika, Minsk, **1**, 403 (1966)

VI Serbian-Belarusian Symp. on Phys. and Diagn. of Lab. &
Astrophys. Plasma, Belgrade, Serbia, 22 - 25 August 2006
eds. M. Ćuk, M.S. Dimitrijević, J. Purić, N. Milovanović
Publ. Astron. Obs. Belgrade No. 82 (2007), 157 *Invited lecture*

THE SHAPE OF Fe Kα LINE EMITTED BY ACTIVE GALACTIC NUCLEI: MICROLENSING EFFECTS

L. Č. Popović, P. Jovanović

Astronomical Observatory, Belgrade
e-mail: lpopovic@aob.bg.ac.yu, pjovanovic@aob.bg.ac.yu

Abstract. The Fe Kα line is emitted from an accretion disk around a massive black hole located in the center of Active Galactic Nuclei (AGN). Here we present a model of the Fe Kα emitting accretion disk in Kerr metrics. We discuss the different Fe Kα line shapes as a function of different disk parameters. Moreover, the influence of microlensing on the Fe Kα line shape will be presented.

VI Serbian-Belarusian Symp. on Phys. and Diagn. of Lab. &
Astrophys. Plasma, Belgrade, Serbia, 22 - 25 August 2006
eds. M. Ćuk, M.S. Dimitrijević, J. Purić, N. Milovanović
Publ. Astron. Obs. Belgrade No. 82 (2007), 159-170 *Invited lecture*

PLASMACHEMICAL REDUCTION FOR THE CONSERVATION OF ARCHAEOLOGICAL ARTEFACTS

Z. Rašková[1], F. Krčma[2]

[1]*Technial museum in Brno, Purkyňova 105, 612 00 Brno,*
raskova@technicalmuseum.cz
[2]*Faculty of Chemistry, Brno University of Technology, Purkyňova 118, 612 00 Brno*

Abstract. This work deals with the plasmachemical treatmant influence on the chlorides removal from the corrosion layers that are present on the surface of an archaeological artefact. The plasma was analysed by optical emission spectroscopy. The OH, N_2 CN, NO band integral intensities as well as hydrogen line intensities were observed as a function of the treatment time. It was found that OH band intensity measurment is sufficient for the reduction process monitoring in practice. Results obtained with a real artefact were compared with the other from model samples treatment. Moreover, the corrosion layer analyses were carried out by means of X-ray diffraction. These results confirmed that the plasmachemical method is very effective.

1. INTRODUCTION

It was proved that the using of hydrogen plasma allows reduction of chlorinated products as well as oxides from the corrosion layers of archaeological objects [1, 2, 3]. Plasmachemical treatment is much more shorter than the mechanical or chemical treatment that have been commonly used till this time. The main advantage of this method is the fact that it is possible to treat the artefact of big size, the hollow artefacts or artefacts with broken relief [2, 4, 5].

Furthermore, it could be appreciated that the plasmachemical treatment is regardful of the artefacts. Obviously, the effect of UV radiation should not be neglected.

Internal corrosion layers of steel objects, surrounding the metalic core, are mainly made of magnetite Fe_3O_4. External corrosion layers consist of oxides, chlorides, α-FeOOH, β-FeOOH, α-Fe_2O_3 in combination with other minerals such as FeOCl, $FeCl_2$, Fe_2SiO_4, $Fe_3(PO_4)_2$ $8H_2O$, and many other compounds.

Corrosion layers of copper or bronze artefacts include for example Cu_2O, CuO, $Cu(OH)_2$, $Cu_2Cl(OH)_3$, CuS, Cu_2S, $CuFeS_2$, etc… It is well known that especially chlorinated products are dangerous in term of new corrosion occurance. The chlorinated products can be decomposed to the chlorides which cause the active corrosion. Our aim is to remove the corrosion layers and to protect the artefacts against new corrosion. Besides the corrosion products, the real corrosion layers contain also many other compounds originating in the artifact surrounding. Thus, for example, the sand grains are build up in the corrosion layer structure and they furthermore complicate the conservation procedures.
Mechanical and chemical treatment in alcaline sulphite bath is often used to eliminate the chlorides from the layers. The main disadvantage of this method is its long duration which can take several months. In 1980, the plasmachemical method was developed [1, 2, 3]. This method is based on the reduction processes by means of low-pressure hydrogen plasma and it included:

1. Partial reduction of external corrosion layers in the mixture of hydrogen with 25 % of methane. Duration of this step was about 2 h and the gas temperature increased up to 300 °C.

2. Mechanical removing of the corrosion layers.

3. Reduction corrosion layer from the artefact bulk. It taked about 20 houres, the temperature was about 400 °C. The mixture of 39 % of hydrogen, 17 % of metane, 22 % of nitrogen a 22 % of argon was applied. Besides reduction, the carbonitridation and passivation of the object surface was provided.

4. The conservation using the commonly used hydrophobic wax.

The original method of prof. Veprek was changed and improved on the basis of further experience. Presently, it is given priority to pure hydrogen utilization and in some cases, the argon and much lower temperature is used (up to 250 °C) to decrease the negative higher temperature effects, especially in case of sensitive archaeological objects their composition is not fully known..
The reduction process is based on the presence of atomic hydrogen created in the plasma. The main reactions in pure hydrogen plasma are as following:

$e + H_2 \rightarrow e + H + H$
$e + H_2 \rightarrow e + H_2^*$
$e + H_2 \rightarrow 2e + H_2^+$
$e + H_2 \rightarrow 2e + H + H^+$

Depending on the corrosion layer character, the reduction can be fully completed up to the metal. For example, the reduction of ferrous corrosion products can be described by following reactions:

$10\ FeOCl + 3H_2 \rightarrow 2Fe_3O_4 + 4FeCl_2 + 2HCl + 2H_2O$
$FeCl_3\ H_2O \rightarrow FeOCl + 2H_2O$
$2FeCl_3 + H_2 \rightarrow 2FeCl_2 + 2HCl$
$FeCl_2 + 2H + \rightarrow Fe + 2HCl$

Many corrosion layers contain also the ammonia complexes. The amonium is liberated under the plasma conditions and by photolysis it can be the additional source of atomic hydrogen:

$h\nu + NH_3 \rightarrow NH_2 + H$
$h\nu + NH_3 \rightarrow NH + 2H$

2. EXPERIMENT

The plasmachemical treatment was carried out in two reactors that differed from each other by their dimensions. The simplified scheme of the experimental set up is shown in Fig. 1.

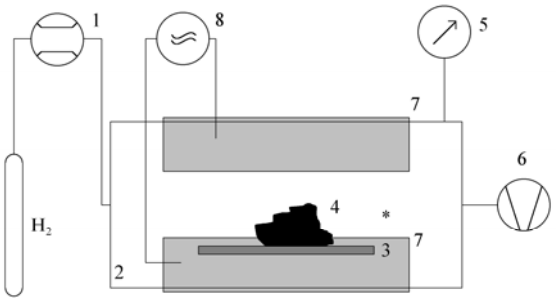

Fig. 1. 1 – mass flow controller; 2 – Pyrex glass reactor (length 100 cm, inner diameter 10 cm); 3 – Pyrex artifact holder; 4 – the treated archaeological artifact; 5 – baratron gauge; 6 – rotary oil pump; 7 – outer cylindrical copper electrodes; 8 – RF power supply; * – point of spectroscopic measurements.

Both reactors consist from a Pyrex glass tube with a pair of outer copper electrodes. The created capacitivelly coupled RF discharge has a good spatial homogeneity and thus it could be applied for treatment of objects with large range of dimensions. The main part of presented results was provided in the simplified small model device with inner diameter of 10 cm and length 100 cm. Fig. 2 shows the real wiev on this small scale device. The working pressure was kept between 100 and 110 Pa, hydrogen flow rate was 100 sccm. The capacitively coupled RF power supply gave the total power of 400 - 450 W, and the sample temperature was estimated at 280 °C. The second experimental device uses a Pyrex tube of 40 cm in diameter with length of 150 cm. This device is continualy developed and improved.

The optical emission spectroscopy was applied to study the processes during the plasma treatment. The spectra emitted from the discharge were recorded by spectrometer Jobin Yvon 550 with CCD detector.

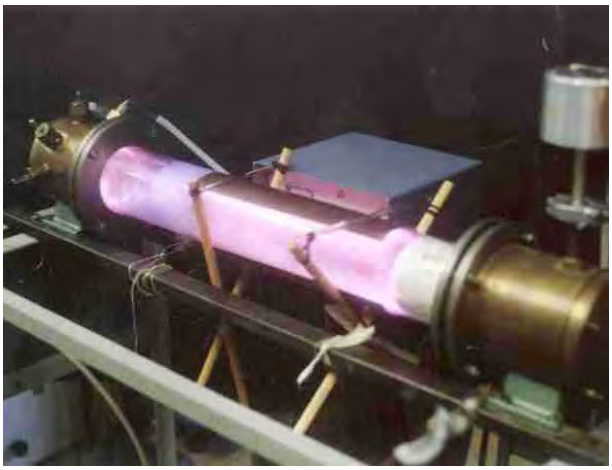

Fig. 2. Photography of the small scale experimental device during the operation.

3. RESULTS AND DISCUSSION

The optical emission (OE) spectra were recorded with and without an artefacts inside the reactor.

In the spectra, various lines and bads were found, as it is shown in Fig. 3. The hydrogen lines and bands as well as OH radical bands were the most intensive. The band and line intensities were observed as a function of the treatment time.

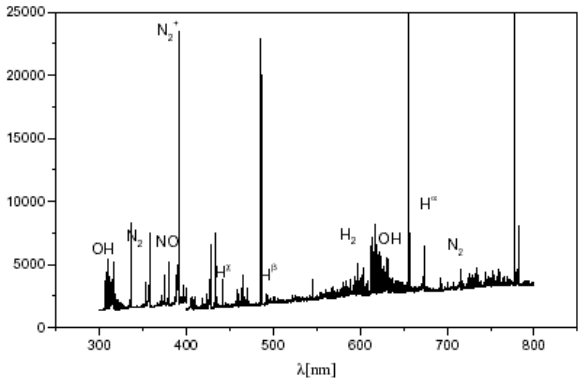

Fig. 3. An example of the optical emission spectra obtained during the plasma treatment of archaeological bronze coin.

It was found that the integral intensity of OH is changed during the reduction process. The plasmachemical reduction was carried out in several stages. Each of them consits of the reduction in the discharge and mechanical removal of the rest of corrosion layer. At the begining of the cyclus, the small increase was observed first, and then, the intensity decreased, as presents Fig. 4. The relation between oxides reduction and OH intensity was found. It could be appreciated that its integral intensity decrease to the value of 10 % of its maximum corresponds to the „end“ of the cyclus of the redution process. For the removal of corrosion layers and for their reduction to the metal it is necessary to apply several treatment steps which are combined with the soft mechanical cleaning and desalination in the LiOH solution or in the distilled water. The desalination process was controlled by the determination of chloride concentration in the solution using the titration method. The Fig. 5 shows that plasmachemical treatment influence the desalination process. The chloride amount in the layer is lower than in the case of classical mechanical treatment and besides, the desalination time is much shorter.

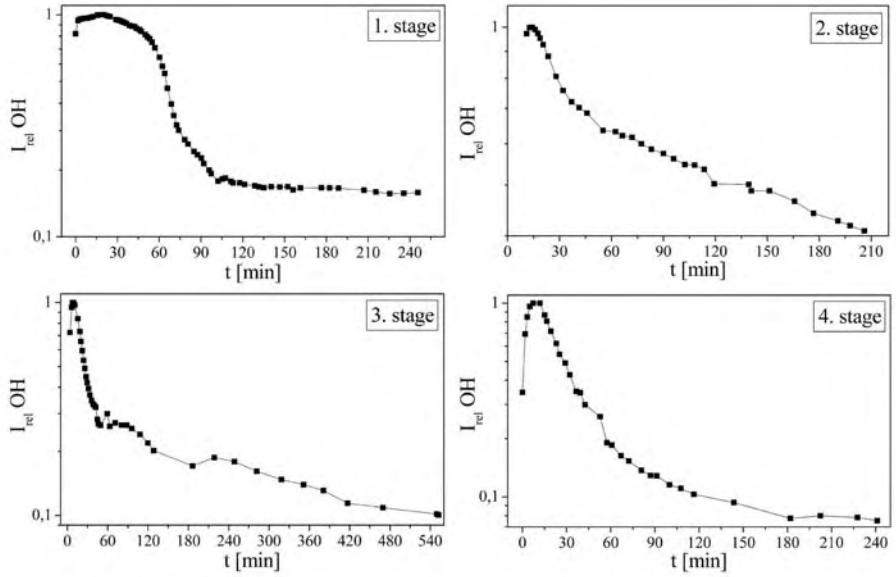

Fig. 4. The dependence of the OH band integral intensity as a function of the treatment time during four different stages.

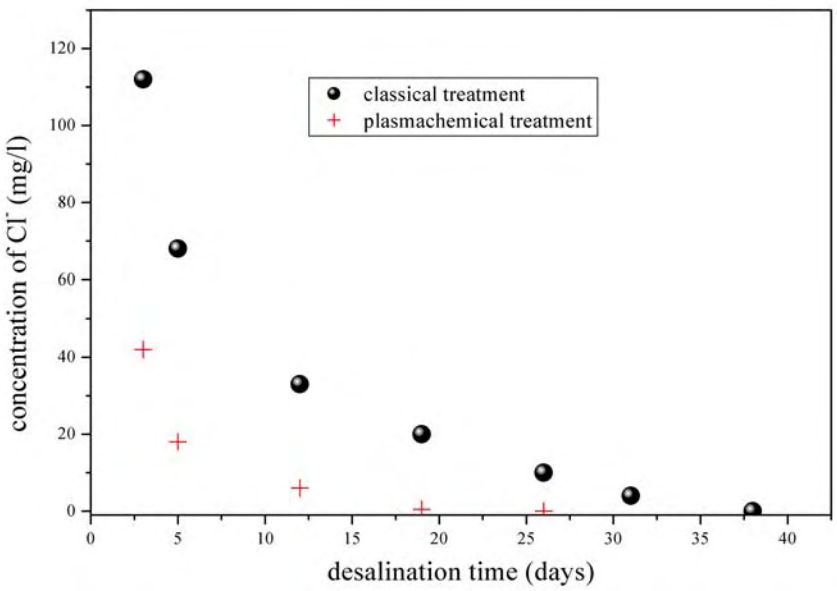

Fig. 5. The dependence of the concentration of Cl^- as a function of the desalination time in the case of classical and plasmachemical treatment of iron artefacts. The concentration was determined by titrimetric (mercurimetric) method.

Moreover, the model samples of corrosion layers were made and treated in our experiments, too. Two sets of copper corroded samples were prepared for the study. First one was created in acid atmosphere that consisted of 18.5% HCl, 32.5 % HNO_3 and mixture of HCl, Na_2CO_3 + Na_2SO_3. So, theree different corrosion layers were obtained (chloride, sulphate and carbon). For the other set of samples, basic atmosphere of ammonia was applied. The diameter of copper samples was 70x100x0.6 mm. Initially, they were cleaned by an alkaline galvanic solution and they were placed on a glass grating in the dessicator at the temperature of 20 °C. The sampels were removed after six days and dried at ambient air. The $CuCO_3$, $CuCO_3$ $2Cu(OH)_2$, $CuSO_4$ $Cu(OH)_2$ compounds were dominant in the corrosion layers. The CuO, CuO_2 represented only about 10 %.

The emission spectroscopy was used to find out all changes those had been resulting from plasmachemical reactions in a hydrogen RF discharge. Identification of the atomic lines and the molecular bands was the first step to be done. After that some atomic and molecular spectrograms were chosen to be suitable for later studies of plasma catalysed reactions. $OH(A^2\Sigma \rightarrow X^2\Pi)$ (305 – 320 nm) and $N_2(C^3\Pi_u \rightarrow B^3\Pi_g)$ 0-0 (337 nm) bands and H^β (486,1), resp. H^γ (434,0 nm), lines were chosen as the best describing makers of their intensities, those had changed mostly in the spectra during whole plasma operation. Those emitted spectra intensities were measured as a function of treatment duration and results were

enregistered into diagrams. Spectra emitted from the discharge during the plasmachemical treatment were measured also as a function of the treatment time. The hydrogen lines and OH, N_2 CN, NO bands were the most intensive in the spectra. The bands of metal were observed, too.

The results obtained during the treatment were compared with the results obteined using real archeological artefacts. The results show, that the OH radical intensity slowly decreases in the both cases while nitrogen bad intensities decrease very fast (almost exponentially). In the case of hydrogen lines, it was found the difference during the „basic“ corrosion treatment and the acid corrosion treatmnet. During the basic corrosion reduction, the hydrogen line intensity increases and then it is constant or it slowly decreases. But during the acid corrosion layer reduction, this intensity decreases, first and then strongly increases.

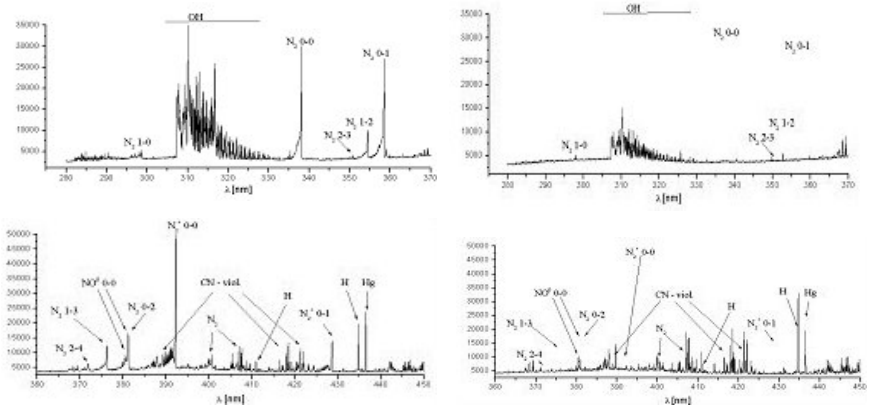

Fig. 6. An example of the OE spectra obtained during the plasmachemical treatment of model samples with created corrosion layers [7]. The pictures on the left side show the emitted spectrum recorded at the begining of the treatment. The pictures on the right side present spectra emitted after 1 hour of treatment.

Green layers : $CuCO_3$, $CuCO_3.2Cu(OH)_2$
Green-blue layers: $CuSO_4$, $CuSO_4.Cu(OH)_2$
Dark blue layers: NH_3 complex compounds
Brnown layers: CuO, CuO_2

Fig. 7. Various kinds of corrosion on model copper layers.

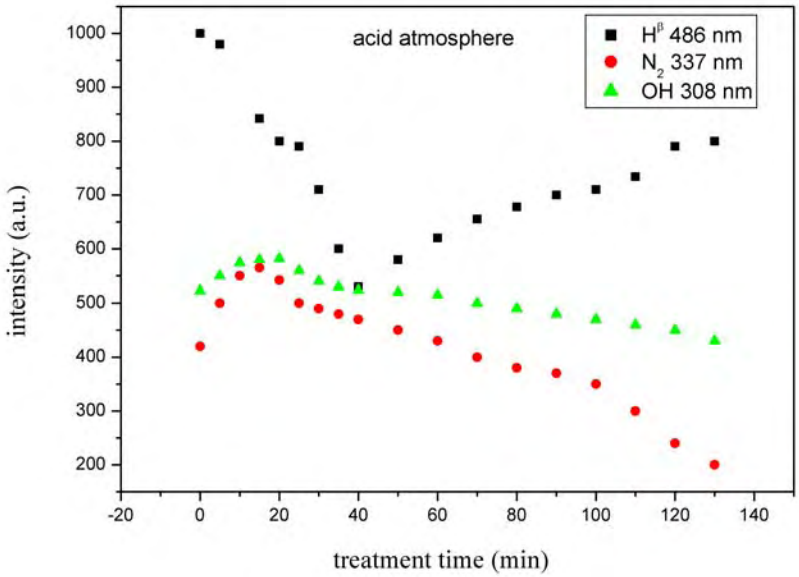

Fig. 8. The dependence of the spectral band integral intensity as a function of the treatment time during the plasma model samples treatment. The corrosion layer was made in acid atmosphere.

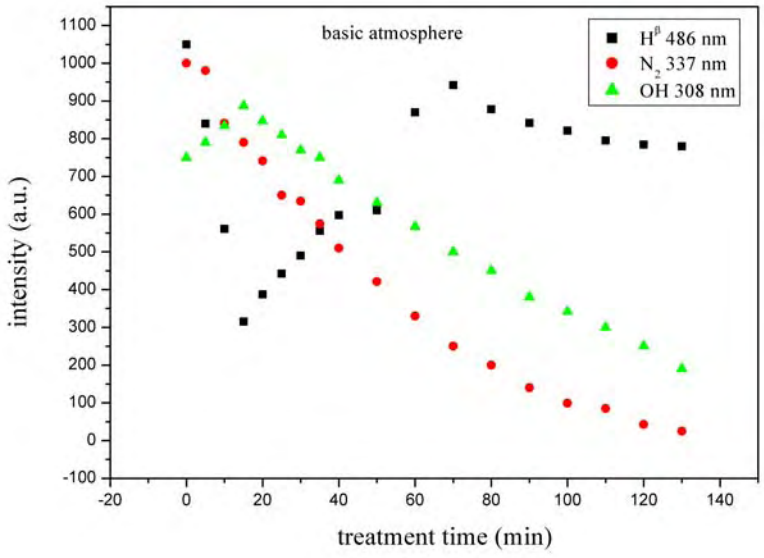

Fig. 9. The dependence of the spectral band integral intensity as a function of the treatment time during the plasma model samples treatment. The corrosion layer was made in basic atmosphere.

Outcome graphs (Figs. 8 and 9) showed explicitly that nitrogen is removed from the corroded samples as first. Its intensity maximum was in the time of about 5 to 10 minutes after the treatment beginning and in time of 1 hour it became extinct at latest. Intensity of OH radical had its maximum in time period 10 to 25 minutes, depending on the corrosion character and it is decreasing to constant minimum level in time about 180 minutes after start of measurement. In the case of iron object, the treatment time of 120 minutes for each step is sufficient.

These results proved that copper oxides reduction took longer time than removal of the other elements contained in the corrosion compounds. Due to detected facts, monitoring of the OH radical spectrum could be suitable for the plasma treatment of more types of corrosions than only the oxide ones.

It was also found that the simplified monitoring device would be useful for the purpose of practical conservation in the museum. The device consists of lens, interference filter, UV sensitive photodiode, low noise amplifier, AD converter, grounded box and digital signal output [4, 7].

Furthermore, the X-ray diffraction analysis was provided during our experiments. The results shows the strong decrease of the chloride content in the layer during the treatment. We also observed the difference between the layer composition at the begining of the treatament and the composition identified after several hours of treatment. The diagrams obtained from X-ray diffraction are given in Figs. 10 and 11. The chlorine removal from the corrosion layer is shown in Fig. 12 as a function of hydrogen discharge treatment time.

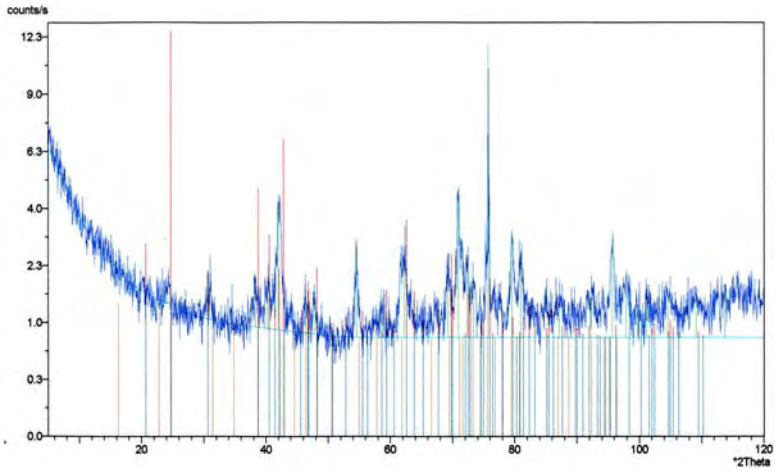

Fig. 10. X-ray diffraction diagram of corrosion layers on the surface of iron object before plasma treatment. The main peaks correspond to the geothite FeO(OH), lepidocrocite Fe_2O_3 H_2O and FeOCl

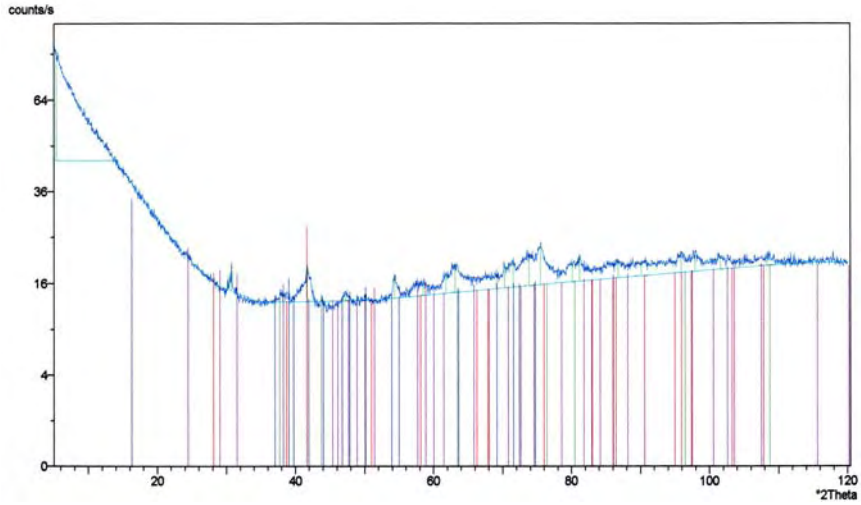

Fig. 11. X-ray diffraction diagram of corrosion layers on the surface of iron object after 60 minutes of the plasma treatment. The main peaks correspond to the magnethite,Fe_3O_4, hematiteFe_2O_3 and calcium iron oxide $CaFe_3O_5$.

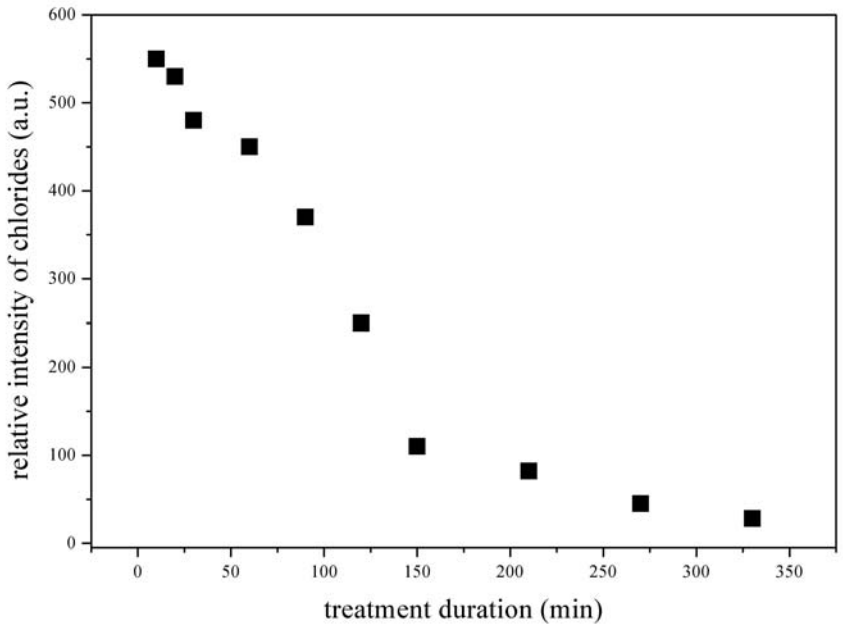

Fig. 12. The intensity of chlorides in the corrosion layer of silver coin as a function of treatment duration in the hydrogen discharge. The chloride content was determined using X-ray diffraction analysis.

4. CONCLUSION

The low pressure plasma chemical treatment of various metallic archaeological objects and model samples was studied. It was found that the whole process can be monitored by using optical emission spectroscopy. Mainly the OH radical band intensity is useful to observe. The plasmachemical treatment consists of several steps and it is possible to determine the end of the reduction in the each step according to the OH integral intensity decrease. Moreover, the gas temperature can be estimated from the rotational spectrum of this band. The N_2 second positive band intensities can also interesting for this purpose. It was found that plasmachemical treatment has positive influence to the chloride ions removal from the corrosion layers. Thus, the deionisation time is shorter than during classical mechanical treatment.

Furthermore, the X-ray diffraction analysis was carried out before and afret plasmachemical reduction. The results show that the reduction process is very effective and in some cases, the reduction to the pure metal was observed.

In the second part of the experiment, the model corrosion layers were created to better comprehension of reduction processes in the plasma. With defined corrosion it was much more simple to observe and to distinguish the bands in the spectrum. The evolution of nitrogen and hydroxyl radical intensity was similar like in the case of real archaeological artefacts. Due to the fact that OH radical monitoring is sufficient during the plasmachemical treatment, the simple monitoring device was presented in [4]. For the practical application, the exact plasma conditions for the treatment are required in dependence on the metallic treated material. So, the searching these condition on the basis of the results from corrosion layer and plasma diagnostics will be aim of further studies for the other materials.

The plasmachemical method is still developed and upgraded. Up to now, it was used mainly for the iron objects treatment. But one of the objective of our work is to find the working conditions for plasma treatment of the other metals, wood and textile materials. Those materials require low temperature up to 80 °C. The pulse plasma utilisation could be very useful to solve the problem with the low temperature keeping. The plasmachemical method is still developed and upgraded. Up to now, it was used mainly for the iron objects treatment. But one of the objective of our work is to find the working conditions for plasma treatment of the other metals, wood and textile materials. Those materials require low temperature up to 80 °C. The pulse plasma utilisation could be very useful to solve the problem with the low temperature keeping.

REFERENCES

1. S. Veprek, J. Patscheider, J. Elmer: Plasma Chem. Plasma Process, **5,** 201 (1985).
2. F. Dalard, Y. Gourbeyre, Ch. Degrigny: Research on Metal Conservation, Studies in Conserv. **47**, 117 (2002).

3. D. Perlík: Vliv plazmy na metalografii a deionizaci železných archeologických nálezů, Konzervátorský a restauratorský seminař, České Budějovice, (2001).
4. Z. Rašková, F. Krčma, M. Klíma, J. Kousal, Characterisation of Plasmachemical Treatment of Archaeological Artefacts, Czech. J. Phys., **52**, D927 (2002).
5. C. N. Chave, P. Leprince, F. Dussere, Plasma treatment of artefacts, Surf. Engeneering **17**, 236 (2000).
6. M.J. Graaf, R.J. Severens et al, Cleaning of iron archaeological artefacts by cascaded arc plasma treatment, Surf. Coat. Technol. **74-5**, 351 (1995).
7. M. Cihlář: Diagnostic of plasmachemical removal of copper corrosion layers, Diploma Thesis, Brno University of Technology, Brno 2005.

VI Serbian-Belarusian Symp. on Phys. and Diagn. of Lab. &
Astrophys. Plasma, Belgrade, Serbia, 22 - 25 August 2006
eds. M. Ćuk, M.S. Dimitrijević, J. Purić, N. Milovanović
Publ. Astron. Obs. Belgrade No. 82 (2007), 171-181 *Invited lecture*

THE METHODS FOR DETERMINATION OF HF CHARACTERISTICS OF NONIDEAL PLASMA

N. M. Sakan[1], V. A. Srećković[1], V. M. Adamyan[2],
I. M. Tkachenko[3], A. A. Mihajlov[1]

[1]*Institute of Physics, Pregrevica 118, Zemun, 11000 Beograd*
[2]*Department of Theoretical Physics, Odessa National University, Dvoryanska 2, 65026 Odessa, Ukraine*
[3]*Department of Applied Mathematics, ETSII, Polytechnic University of Valencia, Camino de Vera s/n, Valencia 46022, Spain*

Abstract. In this work the previously developed method of calculation of HF electro-conductivity of non-ideal plasma is applied to the area of higher electron densities, up to 10^{24} cm^{-3} and in the temperature range 30 000 K ≤ T ≤ 200 000 K. The computations are carried out in the frequency range [0, $1\cdot\omega_p$], ω_p being the plasma frequency. A good agreement with the previously published data is obtained.

1. INTRODUCTION

This work is a continuation of the works [2, 1, 3, 4]. In [1] we presented data for slightly non-ideal plasma HF conductivity, while in [2] we have covered the area of moderately non-ideal plasma, while in [3] and [4] we have reached extreme dense concentrations in a range of $1\cdot 10^{21}$ $cm^{-3} \le Ne \le 1\cdot 10^{23}$ cm^{-3} and for 30 000K ≤ T ≤ 200 000K. Here we present and compare the data for extremely dense non-ideal fully ionized hydrogen plasmas with thermodynamic conditions data presented in [5]. There are two values that was reproducible from their data $\Gamma = 0.5$ $r_s = 4$, and $\Gamma = 0.5$ $r_s = 1$ which yields $N_e = 2.517 \cdot 10^{22}$ cm^{-3}, T = 15 7882 K and $N_e = 1.611 \cdot 10^{24}$ cm^{-3} T = 63 153 K respectively. Here $\Gamma = \beta e^2/a$, where β is inverse temperature in energy units and $a = r_s$ is the mean interionic distance (electronic Wigner-Seitz radius).

In this work a completely ionized hydrogen plasma is considered in a homogenous and monochromatic HF external electric field

$$\vec{E}(t) = \vec{E}_0 \exp\{-i\omega t\}$$

The dynamic electric conductivity σ(ω) is given by a complex function of the field frequency:

$$\sigma(\omega) = \sigma_{\mathrm{Re}}(\omega) + i \cdot \sigma_{\mathrm{Im}}(\omega)\,, \tag{1}$$

and, according to [1, 2], σ(ω) is taken in the integrated Drude-like form:

$$\sigma(\omega) = \frac{4e^2}{3m}\int_0^\infty \frac{\tau(E)}{1-i\omega\tau(E)} \cdot \left[-\frac{dw(E)}{dE}\right]\rho(E)EdE \tag{2}$$

where ρ(E) is the density of electronic states in the energy space and w(E) is a Fermi-Dirac distribution function τ(E) is the static electronic relaxation time. The basic feature of our theory [8, 9, 10, 11] is the evaluation of the relaxation time within the following approach: each electron (carrier) moves in a self-consistent field generated by all other free charges in the system. The finite values of the transport coefficients result from electron's scattering on the self-consistent field fluctuations. It is based on the paper [12], which related the Lorenz-model expression for the fully-ionized plasma electrical conductivity to the strict quantum-statistical calculation involving the Green's function formalism with the self-consistent field potential. It was shown that thus obtained static conductivity is in semi-quantitative agreement with available experimental data and also possesses correct limiting forms of Ziman and Spitzer, corresponding to high and low densities, respectively [11].

A detailed comparison with alternative methods of theoretical investigation of the dynamic conductivity, see, e.g., [13] and [14] is presented in this paper.

New methods:

$$\sigma(\omega) = \frac{\omega\dfrac{i\omega_p^2}{4\pi} - \Omega^2\sigma_0}{\omega^2 - \Omega^2 + i\omega\Omega^2\dfrac{4\pi\sigma_0}{\omega_p^2}}\,, \tag{3}$$

$$\Omega^2 = \frac{\omega_p^2}{3n_e V}\sum_j^N \left\langle 2\sum_\nu f(\varepsilon_\nu)\left|\psi_\nu(R_j)\right|^2 \right\rangle_0 , \tag{4}$$

where,
ε_ν - energy levels
ψ_ν - corresponding eigenfunction in one-electron states ν
$f(\varepsilon)$ - Fermi distribution function.

1. First method

$$\Omega^2 = \frac{\omega_p^2}{3}\left(1+\frac{2m^2e^2}{\pi^2 \mathrm{h}^4 n_e}\int_0^\infty \frac{1}{\exp\beta(\varepsilon-\mu)+1}\arctan\left(\frac{2}{\kappa}\sqrt{\frac{2m\varepsilon}{\mathrm{h}^2}}\right)d\varepsilon\right), \tag{5}$$

$$\frac{1}{2\pi^2}\left(\frac{2m}{\mathrm{h}^2}\right)^{\frac{3}{2}}\int_0^\infty \frac{1}{\exp\beta(\varepsilon-\mu)+1}\sqrt{\varepsilon}\,d\varepsilon = n_e , \tag{6}$$

2. Second method

$$\Omega^2 = \frac{\omega_p^2}{3}\left\{1+\frac{\beta e^2}{\lambda_T(1+\lambda_T/\lambda_D)}\right\}, \tag{7}$$

where,

$\lambda_T = \mathrm{h}/2\sqrt{\beta/m}$ - electronic thermal wavelength

$\lambda_D^{-2} = 4\pi e^2\beta\sum_{j=0}^{s} Z_j^2 n_j$ - the Debye radius

2. RESULTS

Comparison with the other data: On the basis numerical calculations presented earlier in [3, 4], both σ_{Re} and σ_{Im} are computed, but for the previously mentioned thermodynamic conditions. The results are displayed in the figures 1-4. The figures represent the data from several separate sources [5, 6, 7] as compared to our data. A good agreement with existing data [5, 6, 7] in a wide range of dimensionless frequency ω/ω_p.

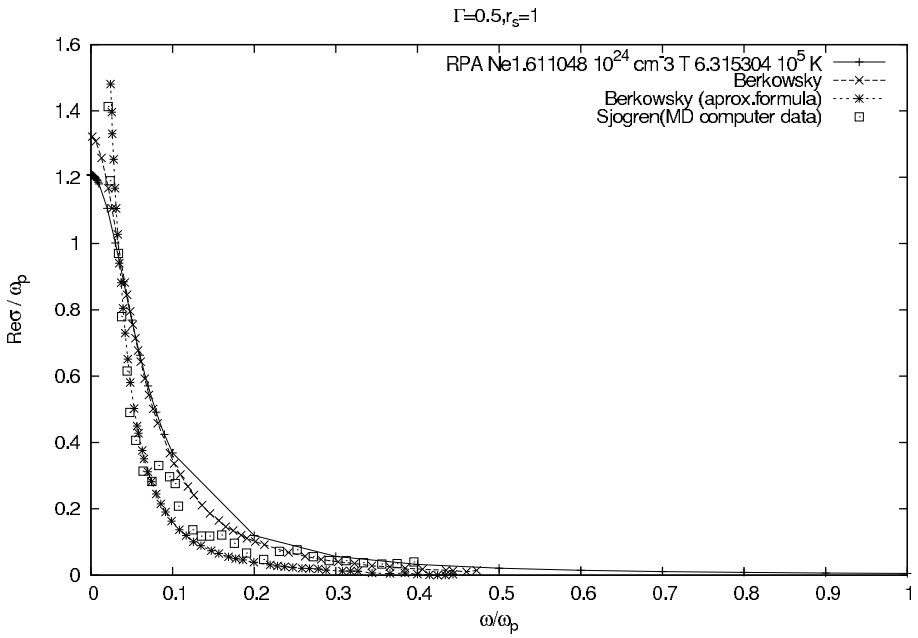

Fig. 1 The real part of HF electrical conductivity of fully ionized Hydrogen plasma for $\Gamma = 0.5$ $r_s = 1$, compared with other authors [5], [6] and [7].

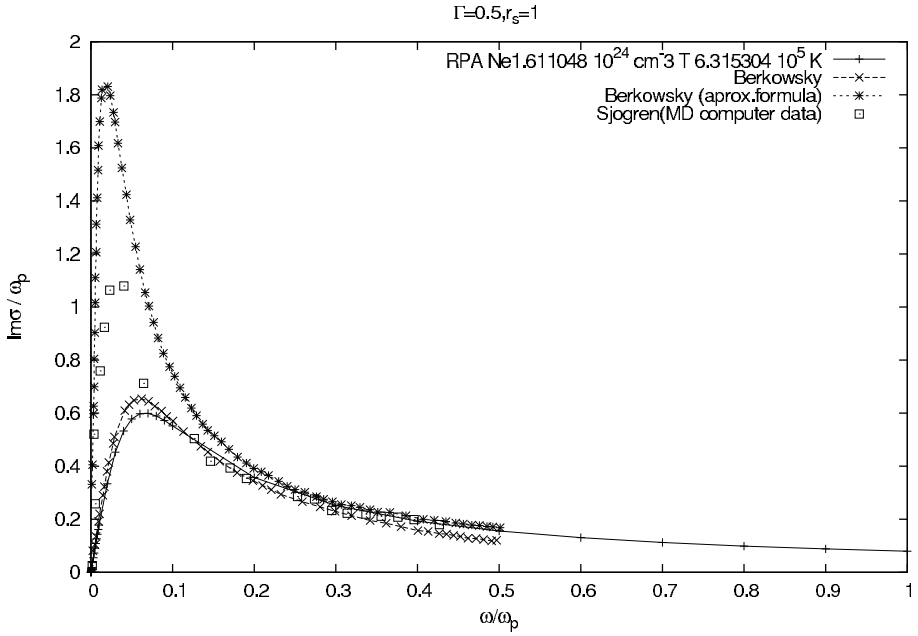

Fig. 2 The imaginary part of electro conductivity, same as Fig. 1.

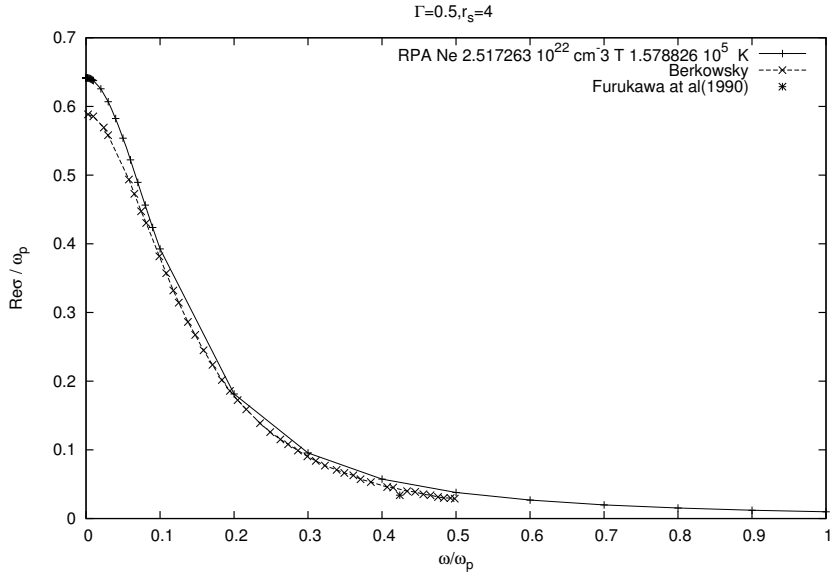

Fig. 3 The real part of HF electrical conductivity of fully ionized H plasma for $\Gamma = 0.5$ $r_s = 4$, compared with other authors [5] and [7].

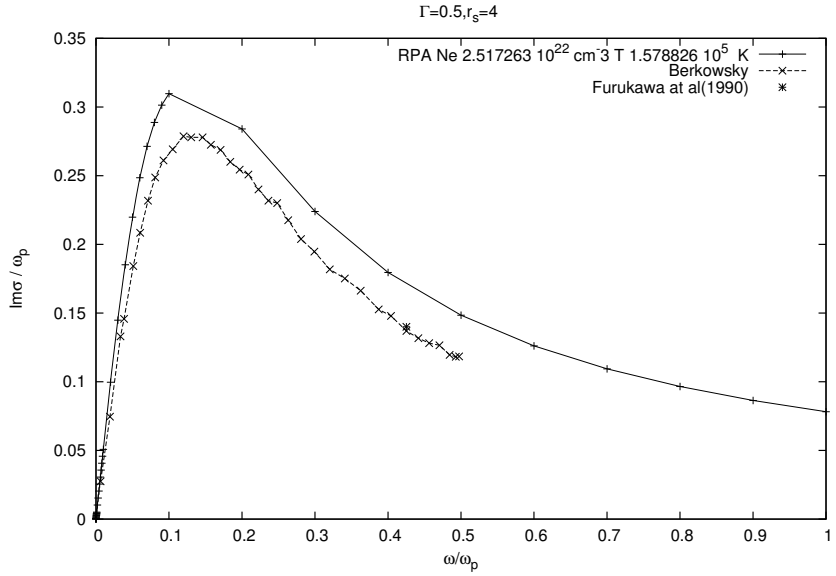

Fig. 4. The real part of HF electrical conductivity of fully ionized H plasma for $\Gamma = 0.5$ $r_s = 4$, compared with other authors [5] and [7].

Comparison of the methods: Results of numerical calculations using equations (5), (6), (7) presented earlier in this paper are displayed in the figures 5 – 13.

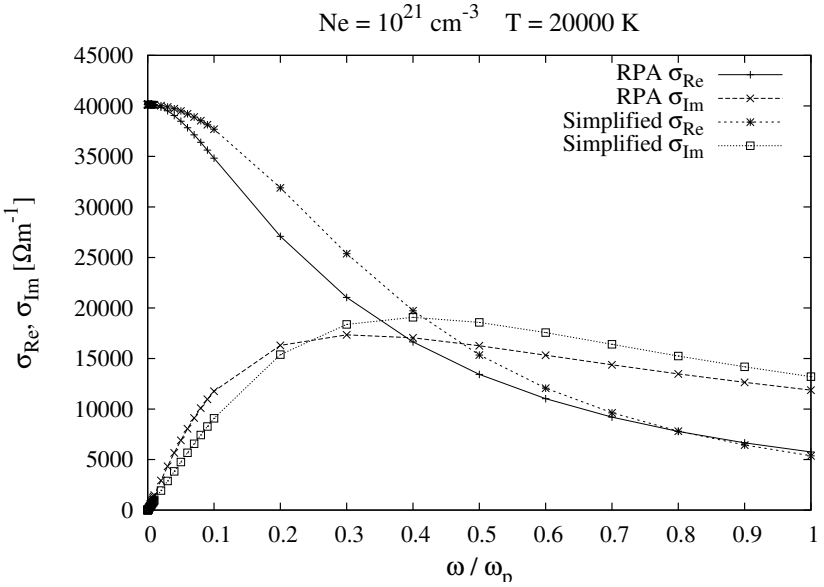

Fig. 5. The comparison of the simplified calculation method and the basic modified RPA method for the fully ionized hydrogen like plasma with the electron density $10^{21}cm^{-3}$, and tempereture 20000K.

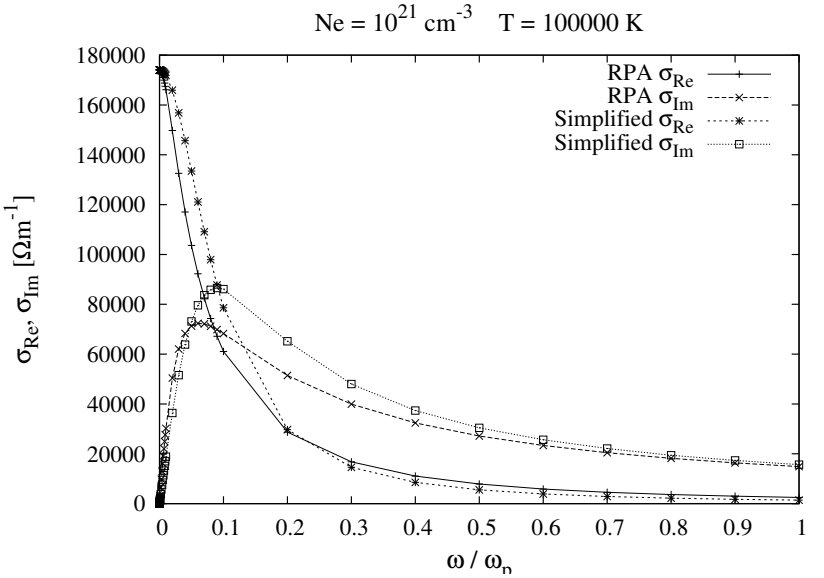

Fig. 6. Same as Fig. 5 but for Ne = $10^{21}cm^{-3}$ and T = 100000K.

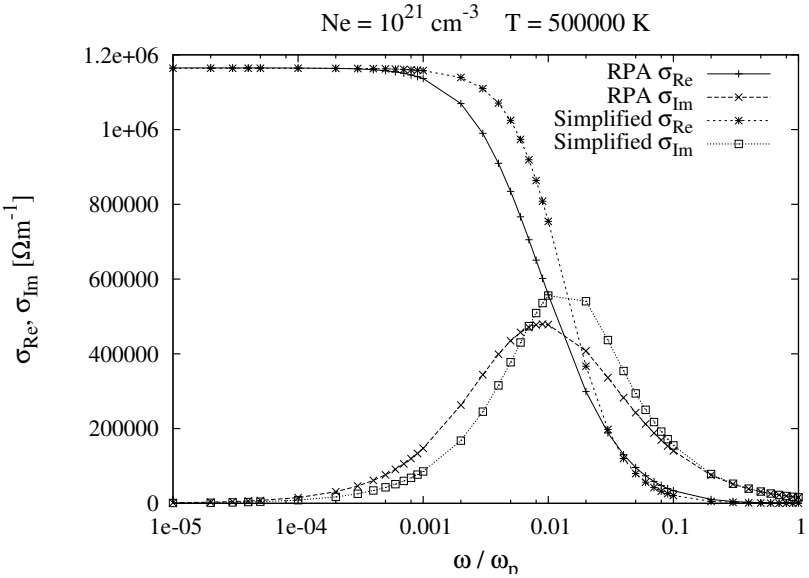

Fig. 7. Same as Fig. 5 but for Ne = 10^{21}cm^{-3} and T = 500000K.

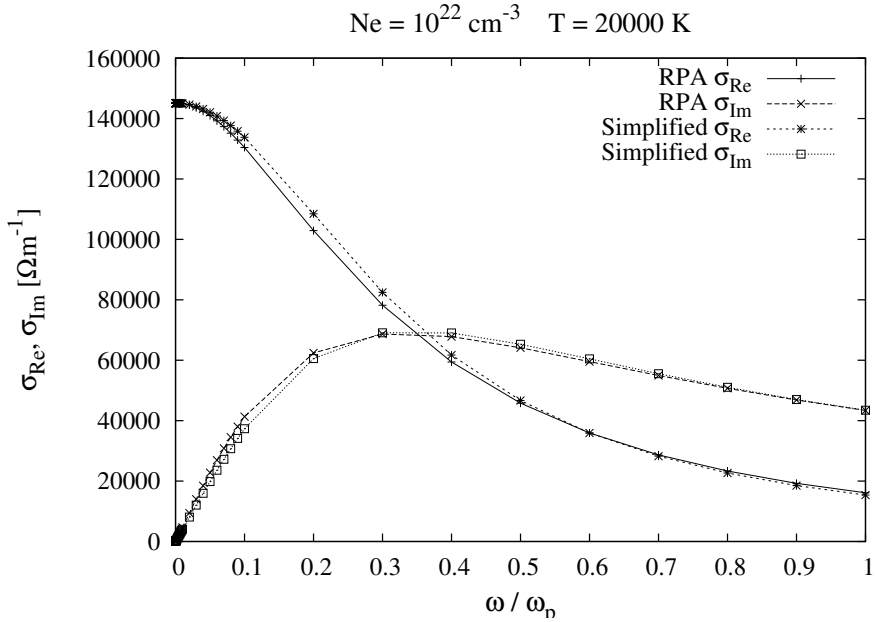

Fig. 8. Same as Fig. 5 but for Ne = 10^{22}cm^{-3} and T = 20000K.

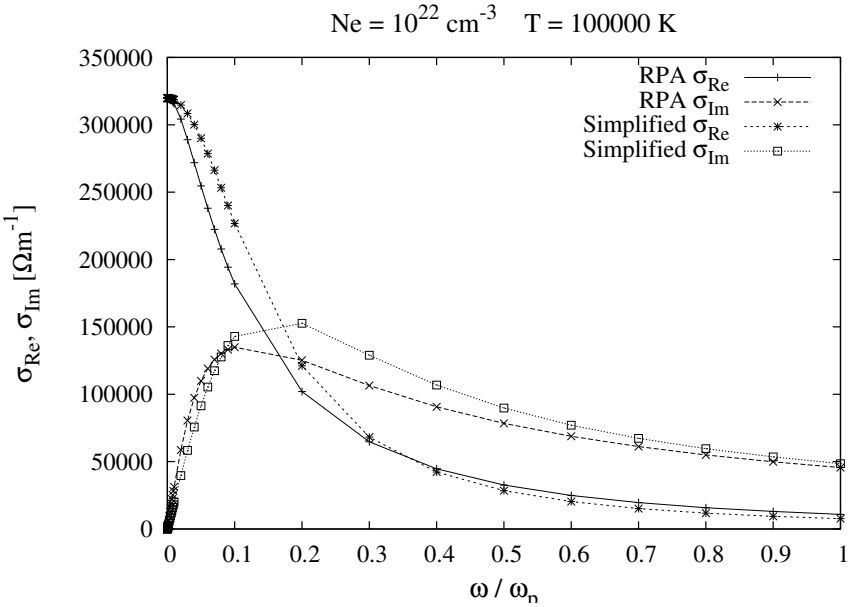

Fig. 9. Same as Fig. 5 but for Ne = 10^{22}cm^{-3} and T = 100000K.

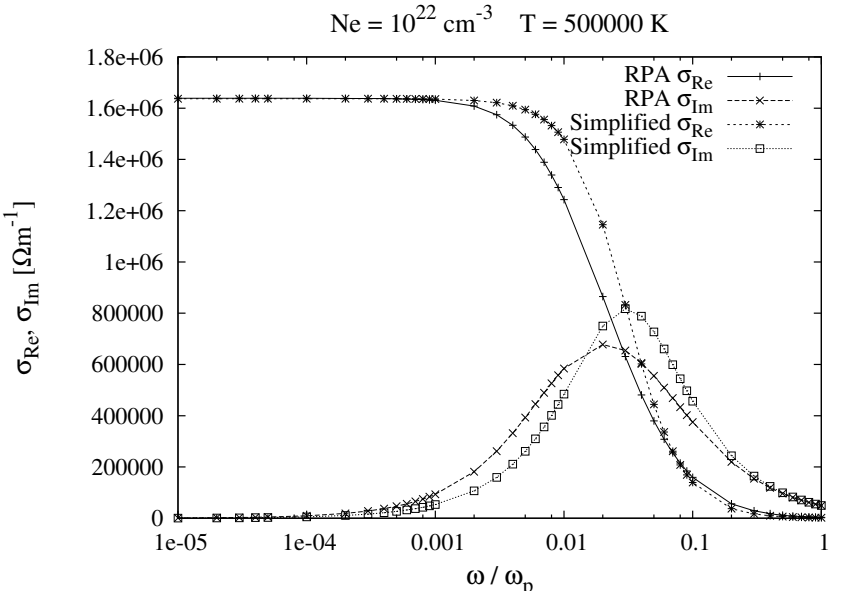

Fig. 10. Same as Fig. 5 but for Ne = 10^{22}cm^{-3} and T = 500000K

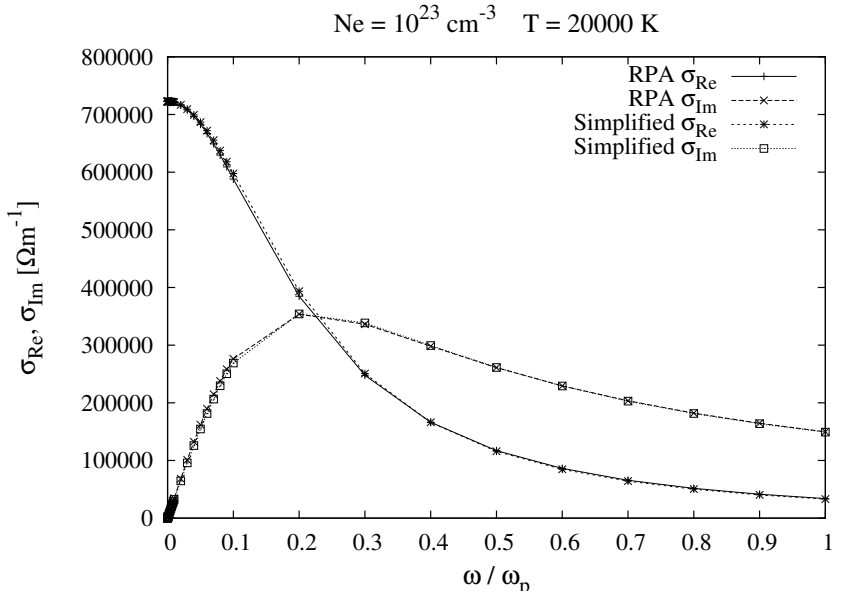

Fig. 11. Same as Fig. 5 but for Ne = 10^{23}cm^{-3} and T = 20000K

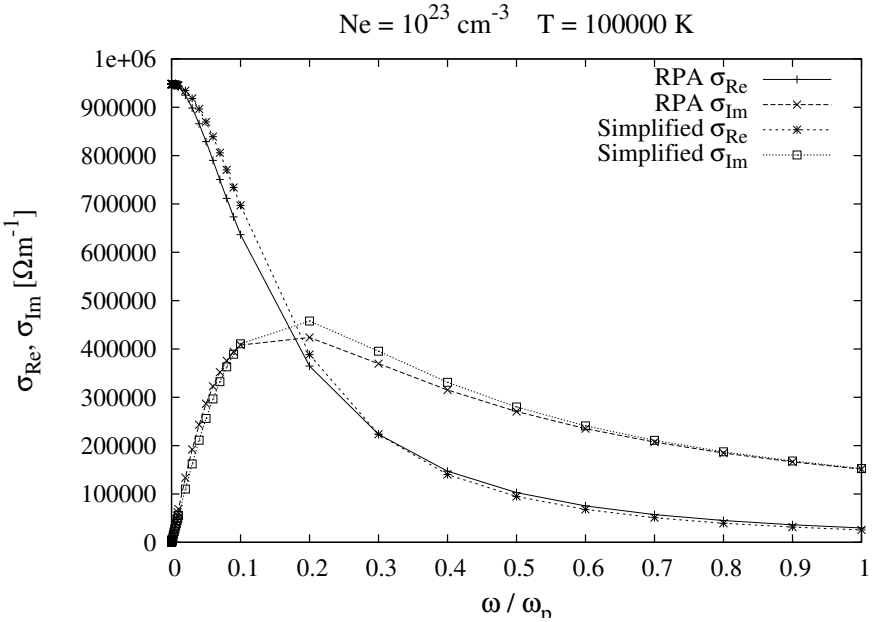

Fig. 12. Same as Fig. 5 but for Ne = 10^{23}cm^{-3} and T = 100000K.

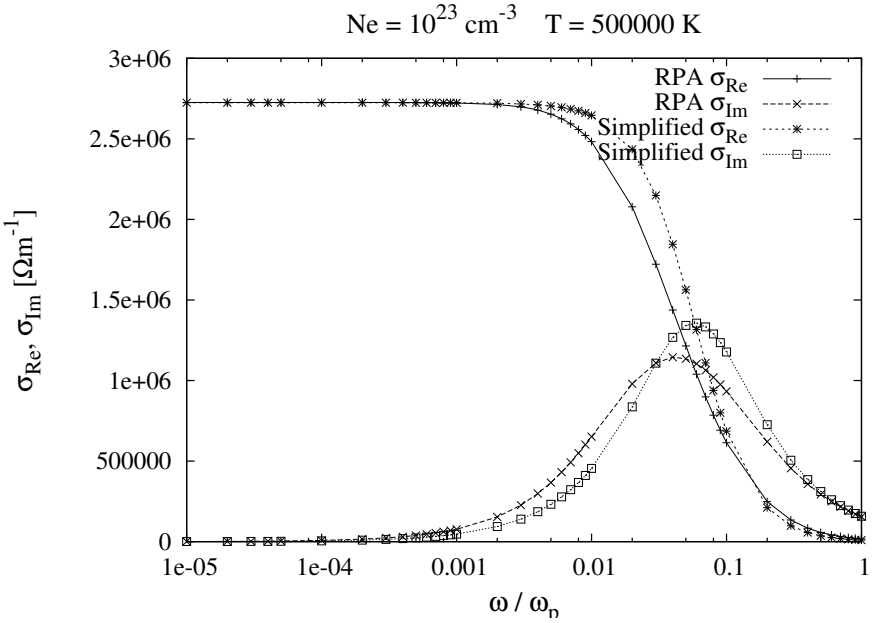

Fig. 13. Same as Fig. 5 but for Ne = 10^{23}cm^{-3} and T = 500000K.

With the help of the presented results the other, easily measurable, dynamical characteristics of dense plasma could be obtained [2, 3, 4].

3. CONCLUSIONS

Method of calculations has been proven, and simplified using formulas (5), (6), (7) . Method works well in a much broader area then expected. Work is in progress on inclusion of neutrals, and preliminary calculations with multifold ionized states. Heading towards the area of more dense plasma where a good experimental data exists.

ACKNOWLEDGMENTS

This work is a part of the project 141033 “Radiation and transport properties of non-ideal laboratory and ionospheric plasmas” of the Ministry of Science and Environmental Protection of Serbia.

REFERENCES

1. A. A. Mihajlov, Z. Djurić, V. M. Adamyan and N. M. Sakan, J.Phys.D. **34**, 3139-3144 (2001).
2. V. M. Adamyan, Z. Djurić, A. A. Mihajlov, N. M. Sakan and I. M. Tkachenko, J.Phys.D. **37**, 1896-1903 (2004).
3. V. M. Adamyan, D. Grubor, A. A. Mihajlov, N. M. Sakan, V. A. Srećković and I. M. Tkachenko, J.Phys.A. **39**, 4401-4405 (2006).
4. I. M. Tkachenko, V. M. Adamyan, A. A. Mihajlov, N. M. Sakan, D. Šulić, and V. A. Srećković, J.Phys.A. **39**, 4693-4697 (2006).
5. M. A. Berkovsky, D. Djordjević, Yu. K. Kurilenko, H. M. Milchberg and M. M. Popović, J.Phys.B. **24**, 5043-5053 (1991).
6. L. Sjőgren, J. P. Hansen, E. L. Pollock, Phys. Rev. A. **24**, 1544 (1981)
7. H. Furukawa et. al., 1990, Strongly coupled plasma physics ed S. Ichimaru, Japan, Elsevier, p613
8. Z. Djurić, A. A. Mihajlov, V. A. Nastasyuk, M. Popović, and I. M. Tkachenko, Phys. Lett. A **155**, 415 (1991).
9. V. M. Adamyan, Z. Djurić, A. M. Ermolaev, A. A. Mihajlov, and I. M. Tkachenko, J. Phys. D: Appl. Phys. **27**, 111 (1994).
10. V. M. Adamyan, Z. Djurić, A. M. Ermolaev, A. A. Mihajlov, and I. M. Tkachenko, J. Phys. D: Appl. Phys. **27**, 927 (1994).
11. I. M. Tkachenko, P. Ferndez de Cdoba, Phys. Rev. E. **57**, 2222 (1998) .
12. S. F. Edwards, Philos. Mag., **3**, 1020, (1958).
13. H. Reinholz et al., Phys. Rev. E, **68**, 036403, (2003).
14. D. Ballester and I. M. Tkachenko, Contrib. Plasma Phys. **45**, 293, (2005).

VI Serbian-Belarusian Symp. on Phys. and Diagn. of Lab. &
Astrophys. Plasma, Belgrade, Serbia, 22 - 25 August 2006
eds. M. Ćuk, M.S. Dimitrijević, J. Purić, N. Milovanović
Publ. Astron. Obs. Belgrade No. 82 (2007), 183-200 *Invited lecture*

EXCESSIVE DOPPLER BROADENING OF H_α AND D_α LINE IN A HOLLOW CATHODE GLOW DISCHARGE

N. M. Šišović[1], G. Lj. Majstorović[2], N. Konjević[1]

[1] *Faculty of Physics, University of Belgrade, 11001 Belgrade, P.O. Box 368, Serbia*
[2] *Military Academy, 11105 Belgrade, Pavla Jurišića – Šturma 33, Serbia*

Abstract. A review of experiments dealing with excessive Doppler broadening (EDB) of hydrogen and deuterium Balmer lines in hollow cathode gas discharge(s) is presented. The experimental data of excessive line broadening are discussed from the point of view of the sheath-collision model and the resonance transfer model. The results of new experiments reported here indicate that EDB part of hydrogen Balmer lines may be used for discharge-cathode surface interaction monitoring.

1. INTRODUCTION

Since the discovery of excessive Doppler broadening of hydrogen Balmer lines [1,2], experimental studies, see e.g. Refs. 3-4, have been conducted to resolve and understand processes related to this phenomena. The shape of these lines emitted from some low-pressure gas discharges operated with hydrogen isotopes or hydrogen gas mixtures with inert gases exhibits unusual multi component behavior, see e.g. Figures 1a-4a. The same EDB shapes of H_α and H_β lines are detected in a plane cathode glow discharge operated with various gas mixtures with hydrogen [5].

The origin of the narrowest part of the profile in Figure 1a is related to the Doppler broadening of the thermalized excited hydrogen atoms H^* in the negative glow region of the discharge. The broader middle part of the line profile is related to excited hydrogen atoms generated in electron collisions with H_2. The pedestal of the line profile is very broad indicating that energetic excited hydrogen atoms having energies larger than hundreds of electron volts are generated in (the) discharge. The presence of large energy excited hydrogen atoms implies that fast hydrogen atoms H_f of higher energy exist in the discharge [6]. As pointed out already, the origin of the narrow- and medium-width part of the line profile may be explained on the basis of well-established processes.

The primary explanation of the broadest part - pedestal of the line profile comes from the sheath-collision model. In this model ions H^+ and H_3^+ are accelerated in a high-voltage discharge sheath and produce fast H atoms in charge transfer/dissociation collisions with the matrix gas–molecular hydrogen. The fast H atoms are then excited and scattered in another collision. The same excitation process is occurring with H atoms backscattered from the cathode [3,7,8]. In the Ar-H_2 discharge, see the H_α profile in Figure 1b, the contribution of H^+ ion is negligible in comparison with that of H_3^+ ion, see e.g. [6,9]. The latter ions fragment in collisions with matrix gas or at the cathode surface generating H_f atoms of lower energy, and consequently lower energy excited atoms H^* are produced. For EDB in DC discharges see [1-13].

Another model of EDB has been proposed by Mills *et al.*, see e.g. [14,15]. According to this model, in the resonance transfer (RT) process H atoms react with certain ions, for instance He^+, Ar^+ or other "resonance catalysts" produced by the electric discharge, to generate excess energy. The RT process is followed by excessive Doppler broadening of the hydrogen Balmer lines, which according to references [14,15] reveals the presence of high energy excited hydrogen atoms-carriers of excess energy produced in the RT process.

In this paper a review of publications dealing with the excessive Doppler broadening hydrogen and deuterium Balmer lines in hollow cathode gas discharge will be presented and discussed from the point of view of both models, when it is possible. Also, it will be demonstrated that some new results dealing with this subject may be used for discharge-cathode surface interaction monitoring [16].

2. THE INFLUENCE OF CATHODE MATERIAL, GAS COMPOSITION AND ELECTRIC FIELD DIRECTION ON EDB IN HOLLOW CATHODE DISCHARGE

In the recent paper [15] the authors of RTM reported study of the excessive H_α broadening in various discharges including hollow cathode discharge. The results in Table I [15] and discussion firmly state that excessive broadening is detected only in Ar and He mixtures with hydrogen while in H_2, and in mixtures Ne-H_2 and Xe-H_2 no effect is found. This result is expected on bases of their RTM. The aim of a recent experiment [13] in our laboratory is to test these results.

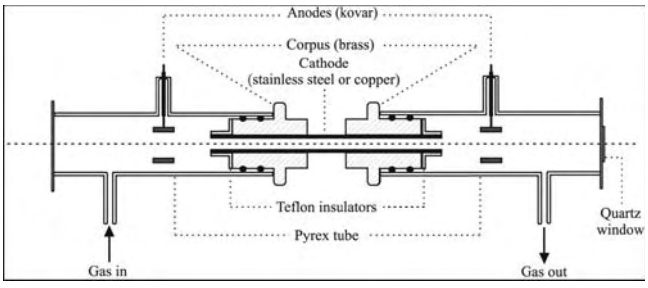

Fig 1. The hollow cathode discharge tube [13].

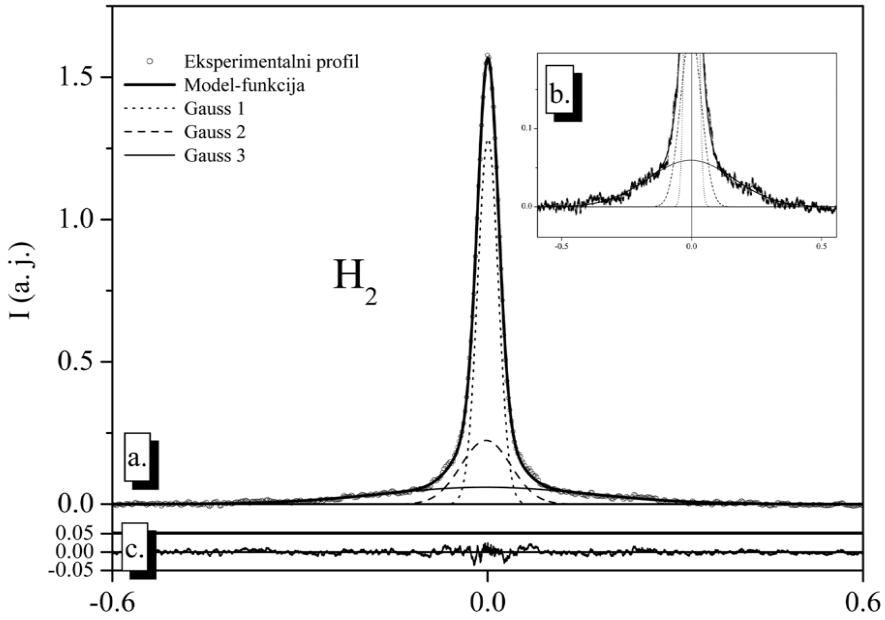
Eksperimentalni profil
Model-funkcija
Gauss 1
Gauss 2
Gauss 3
H2
I (a. j.)
a.
b.
c.
1.5
1.0
0.5
0.0
0.05
0.00
-0.05
-0.6
0.0
0.6

A

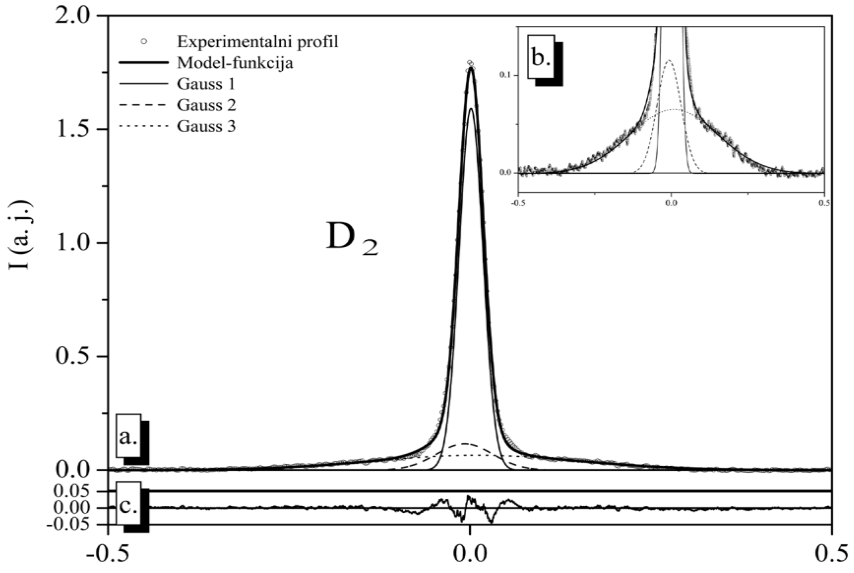
Experimentalni profil
Model-funkcija
Gauss 1
Gauss 2
Gauss 3
D2
I (a. j.)
a.
b.
c.
2.0
1.5
1.0
0.5
0.0
0.05
0.00
-0.05
-0.5
0.0
0.5

B

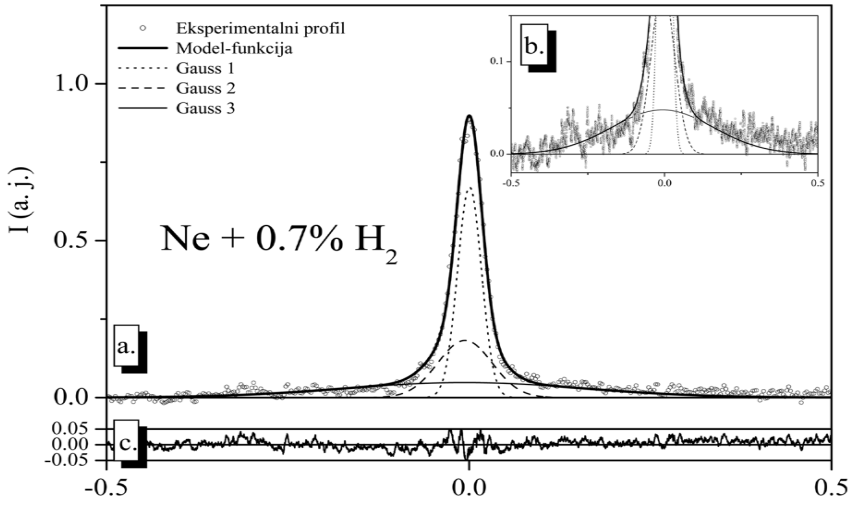

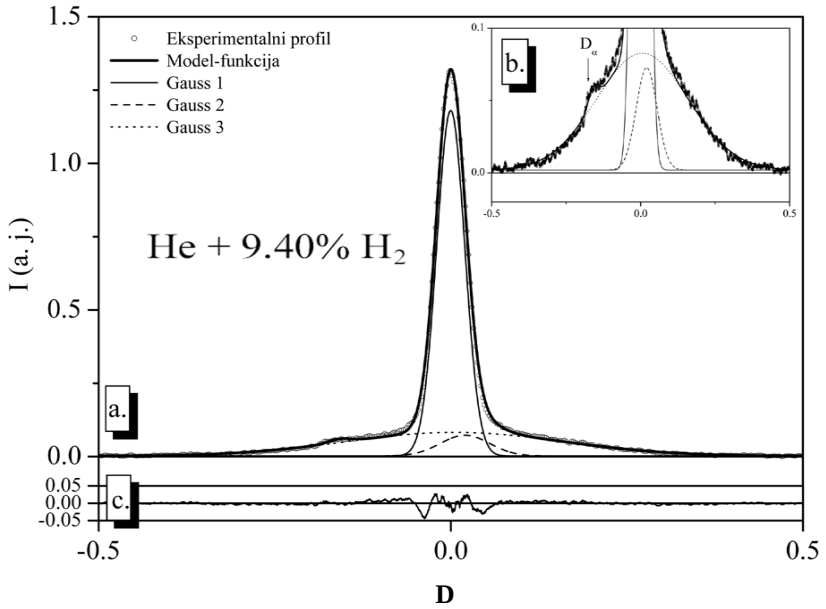

Fig. 2. Typical H_α line shapes recorded end-on from high pressure low-voltage copper hollow cathode glow discharge and fitted with three Gaussians: (a) H_α line shape, (b) the enlarged part of H_α line shape excessively broadened; and (c) the residual plot. **A.** Discharge conditions: pure hydrogen; front anode, *p*=2mbar, *U*=440V, *I*=90mA. **B.** Discharge conditions: pure deuterium; front anode, *p*=2mbar, *U*=490V, *I*=90mA. **C.** Ne-H_2 mixture (99.3%:0.7%); front anode, *p*=2mbar, *U*=250V, *I*=90mA. **D.** He-H_2 mixture (90.6%:9.4%); front anode, *p*=2mbar, *U*=323V, *I*=90mA. [13]

Newly developed hollow cathode glow discharge with stainless steel or with copper cathode is used, see Fig.1. The construction details follow basic concept of pyrex-kovar design reported in [17]. Both cathodes were 100 mm long with 6 mm internal diameter. Kovar anodes, 5 mm long with 15 mm dia, are located at the both ends of cathode at a distance of 15mm.

Typical examples of the H_α line shape recordings from the central region of copper hollow cathode high pressure low-voltage glow discharge are given in Fig. 2. Three components can be distinguished in the overall fit of the symmetric H_α and D_α line shapes in pure gases and gas mixtures, see Fig. 2: central narrow peak, broader middle part and far drawn-out pedestal. The overall fit involving convolution of three Gaussians in Fig. 2 may be justified in two ways: *(i)* three groups of excited hydrogen atoms are expected in the negative glow region: thermalized H^* typical for negative glow (Gauss 1); a group of H^* atoms produced by dissociation of H_2 molecules in collisions with high energy electrons (Gauss 2); and a group of H_f^* atoms generated in collisions of H_f reflected from the cathode with H_2 (Gauss 3) and *(ii)* a good quality of three gaussian fit, see the residue plot in Fig. 2.

The examples in Fig. 2 show that the excessive H_α or D_α line broadening is present in both hollow cathodes discharges under all studied experimental conditions. Furthermore, there is nothing exceptional about discharge operating in $He\text{-}H_2$ mixture, where, according to RTM, resonance transfer catalysts He^+ are present: the profiles, recorded from our discharges operating in $He\text{-}H_2$ mixtures, have a typical multipart component structure in contrast to a single excessive broadened profile recorded in the same gas mixture and reported in [15].

On the basis of earlier experiment, see Fig.9 in [3], high D_f^* temperatures are expected and they are detected in both hollow cathode discharges. The presence of high energetic neutrals D_f^* in this case is related to large back scattering coefficients of D^+ from the cathode surface, which exceeds ~50% same coefficients of H^+ [18]. These ions are neutralized at the cathode and reflected back in the form of D_f, which collide with matrix gas D_2 and produce observed D_f^* [2]. High voltage in deuterium discharge plays an important role in D^+ acceleration and in this way to generation of high temperature D_f^*.

The comparison of data obtained for different cathodes shows also that Gauss 3 contribution to the overall profile is significantly larger in case of copper than stainless steel hollow cathode discharge. This result is in qualitative agreement with results from PCGD discharge, see Fig.7 in [3,4] and may be explained by larger back scattering coefficients of H^+ from Cu surface in comparison with Fe [3,4,18]. It proves that the concentrations and energies of H_f^* depends of cathode material and that, most likely, is associated with sputtering yield and characteristic back-scattering coefficients [4].

As pointed out already in Introduction, the electric field is essential for the CM to explain basic processes related to excessive Doppler broadening. The only fact in this experiment that looks in favor of RTM: the H_α line shape measurements are performed primarily by observing the negative glow region of discharge where large electric fields do not exist. Since the excessive broadening is detected in this region one may conclude that this proves validity of RTM. However, one should also bear in mind that accelerated H^+ and H_3^+ ions in a cathode fall region of

discharge operated at high pressure and low-voltage regime are back-scattered towards the center of hollow cathode in the form of fast hydrogen atoms, which generate H_f^* in collisions with matrix gas. Thus, the presence of observed excess Doppler H_α broadening, Gauss 3, may be well explained within CM.

In order to examine further the importance of electric field for excessive Doppler broadening an experiment with stainless steel hollow cathode glow discharge in a low pressure, high-voltage regime is carried out. This is the case when electric field vector is coaxial with hollow cathode axis and its direction may be changed by applying rear or front anode, see Fig. 3.

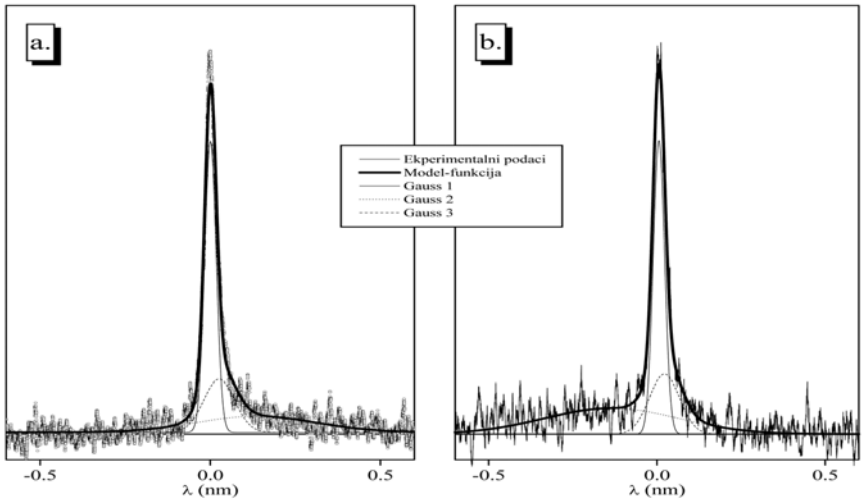

Fig. 3. Typical H_α line shapes recorded end-on from low pressure high-voltage discharge (He-H_2) mixture; stainless steel cathode) and fitted with three gaussians: **(a)** front anode and **(b)** rear anode. Discharge conditions: p=1mbar, U=1030V, I≈5mA. [13]

The results in Fig. 3 clearly show that Gauss 3 may be shifted into blue or red wavelength direction by simply changing the direction of electric field vector. Similar experiment with hollow cathode glow discharge operated with higher voltages in pure hydrogen is reported in [17,19]. The dependence of shift direction of high temperature component upon electric field vector is the same as in Fig. 3. Both experiments, [17] and this one, undoubtedly prove the importance of electric field for the excess Doppler broadening. The RTM in contrast to CM does not depend upon electric field and can't be used to explain results in Fig. 3.

Moreover, Phelps [20,21] reported recently a thorough comparative analysis of Mills and co-workers RT experiments and most of the other EDB Balmer line studies. On the bases of this analysis and the fact that Mills and co-workers [14,15] do not provide a set of elementary processes with cross sections for converting the energy of RT products into the fast excited hydrogen atoms, one may conclude that RT model cannot be used to explain EDB of hydrogen Balmer lines.

On the other hand, a number of experiments disagree with RT model predictions, see e.g. [20,21] and references therein. Therefore, the sheath-collision model will be used from this point forward for the interpretation of EDB results.

3. EXCESSIVE BROADENING OF HYDROGEN BALMER LINES FOR DISCHARGE-SURFACE INTERACTION MONITORING

Several experiments [10,11], in particular the recent ones [6,9,13] carried out with measurements perpendicular to the electric field, showed symmetric line profiles, which can be precisely analyzed. The possibility of separating the EBD part of the H_α profile has enabled determination of cross section data for $H \rightarrow H_2$ collisions in an abnormal glow discharge [6]. Also, it has been demonstrated that the EDB part of hydrogen Balmer lines may be used for discharge-cathode surface interaction monitoring [16].

In this experiment, the H_α line shape and the effective sputtering rates were monitored using intensities of Ti or Fe, Ni, and Cr resonance lines in a hollow cathode (HC) discharge operated using H_2 or (a) the Ar-H_2 mixture at a pressure of 2 mbar. For comparison with the Ar-H_2 experiment, all relevant measurements are also carried out in an Ar discharge. During the discharge operation, cathodes were either air cooled or gradually heated by switching off the fan. The temperature of the outer wall of the HC tube is measured by a K-type thermocouple.

Three components of the line profile are determined by fitting the H_α line with three Gaussians, see Figs. 4 and 5. Due to low sputtering yield of hydrogen ions, observations of resonance lines are performed in Ar–H_2 and Ar only. Line intensities were measured at different electrical power inputs induced by a change of discharge voltage at constant current, see Figs. 6(c) and 7(c). Line intensities normalized to the unit electrical power input are given in Figs. 6(a) and 7(a).

Titanium. Figure 6 shows for H_2 and Ar–H_2 discharges, a gradual increase of G_3/G_{total} with temperature, where G_i (i=1,2,3) is the area of the corresponding line component. This is in agreement with earlier results, showing that implanted hydrogen in Ti lowers the reflection of H after bombardment with protons [22]. Experimentally, it is determined that the H particle reflection coefficients R_N of TiH_2 is less than 30% lower than for Ti [23], while simulations predicted 50% [24]. During an increase of cathode temperature, a lowering of the TiH_2 concentration is expected and consequently G_3 increases. At elevated temperatures (>230^0C), not reached in this experiment, no hydride contribution is expected [25]. Figure 6(b) supports an assumption of the TiH_2 influence to the G_3 contribution. The intensity of Ti I resonance lines at lower temperatures in Ar–H_2 discharges are smaller than in Ar discharges in spite of energetic ArH^+ ions present in the mixtured-species discharge [26]. At higher temperatures, Ti line intensities in the Ar–H_2 case gradually overcome those in Ar as a consequence of the lowering H/Ti ratio.

Stainless steel. Similar to the Ti surface case, the G_3 contribution in H_2 discharge increases with temperature, see Fig. 7(b), and may be related to an increase of SS reflectivity with decreasing H/Fe ratio [24]. The large and almost constant G_3 in Ar–H_2 is explained by: *i)* a large presence of H_3^+ ions; and *ii*) negligible influence of iron hydrides at the SS surface under the influence of

energetic ArH^+ sputtering. Generally, hydrogen in the SS matrix may be characterized by fast diffusion and reemission leading to a smaller surface concentration [22]. Consequently, in contrast with the Ti case, see Fig. 6(a), Fe, Cr and Ni resonance lines in Ar-H_2 are always larger intensity than in the Ar discharge, see Fig. 7(a). From the sputtering point of view, SS is considered to behave as a single-component system [27]. Ratios of line intensities in Fig. 7(a) show, at lower cathode temperatures, good agreement with values expected from SS composition. At higher cathode temperatures when sputtering yield increases, the intensity of Fe resonance line shows slower increase due to the self-absorption effect.

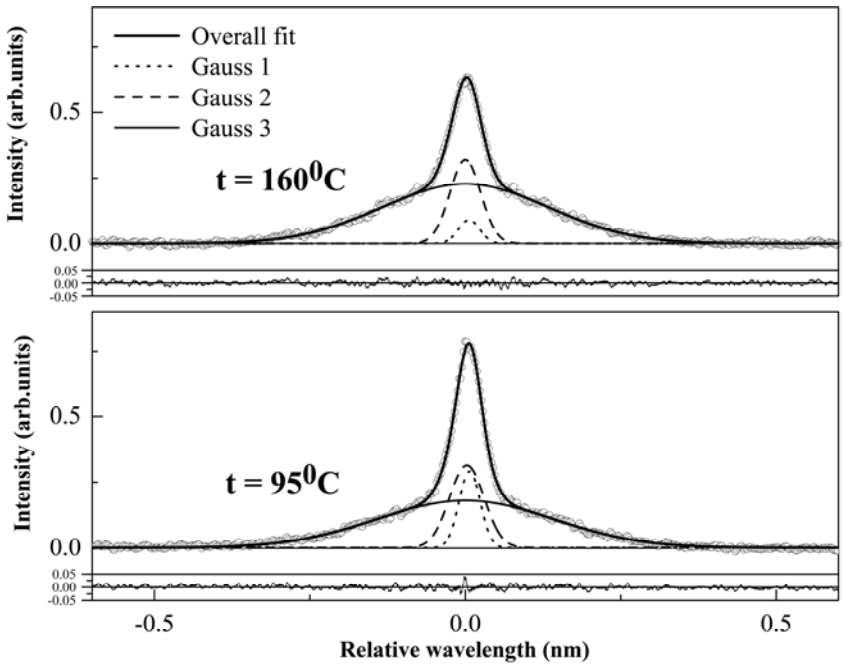

Fig. 4. The H_α line profiles recorded along the axis of titanium hollow cathode glow discharge in Ar–H_2 fitted with three Gaussians. Discharge conditions: I=90 mA and p=2 mbar [16].

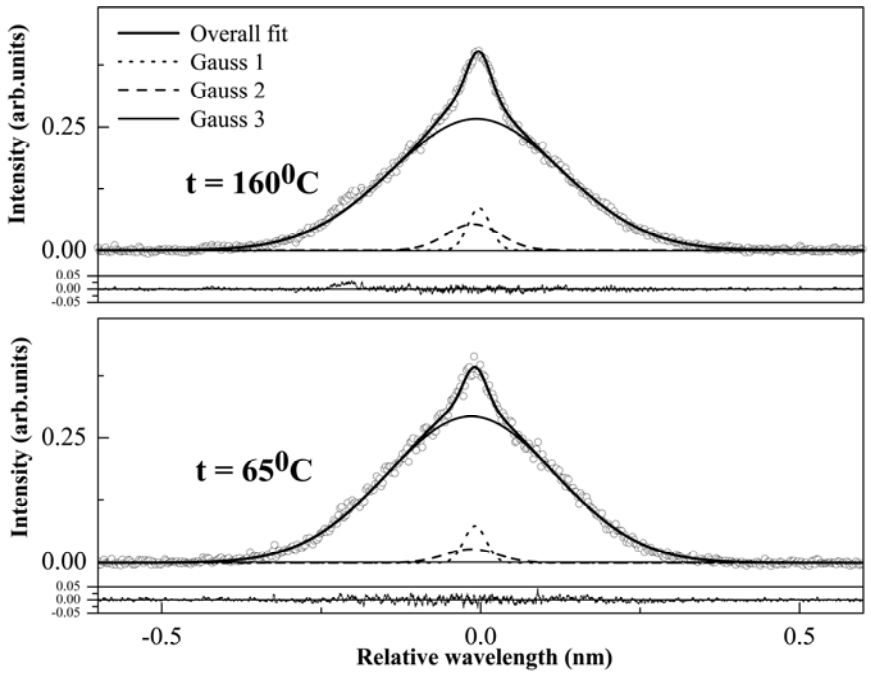

Fig. 5. The H_α line profiles recorded along the axis of stainless steel hollow cathode glow discharge in Ar–H_2 fitted with three Gaussians. Discharge conditions: I=90 mA and p=2 mbar [16].

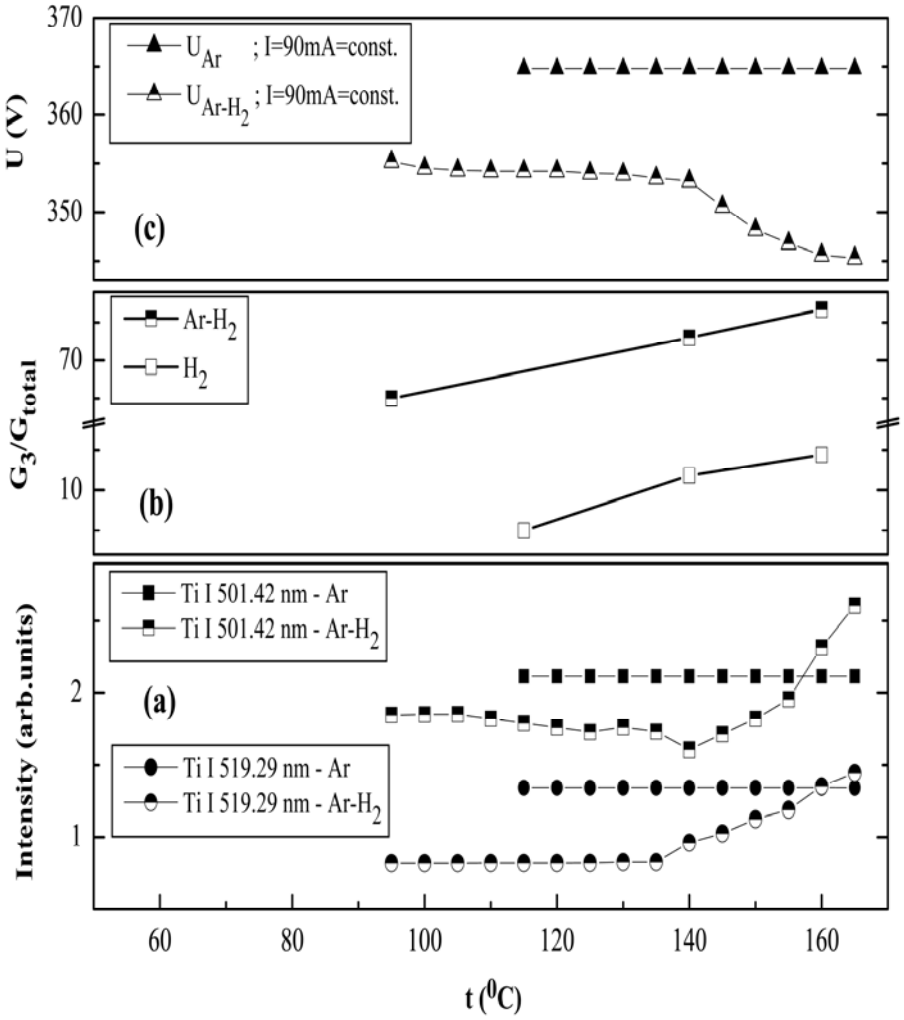

Fig. 6. The temperature dependence of: (a) Ti resonance lines intensity; (b) contribution of G_3/G_{total} to the H_α profile in H_2 and in Ar–H_2 ; and (c) discharge voltage for constant current of 90 mA in Ar–H_2 and in pure Ar [16].

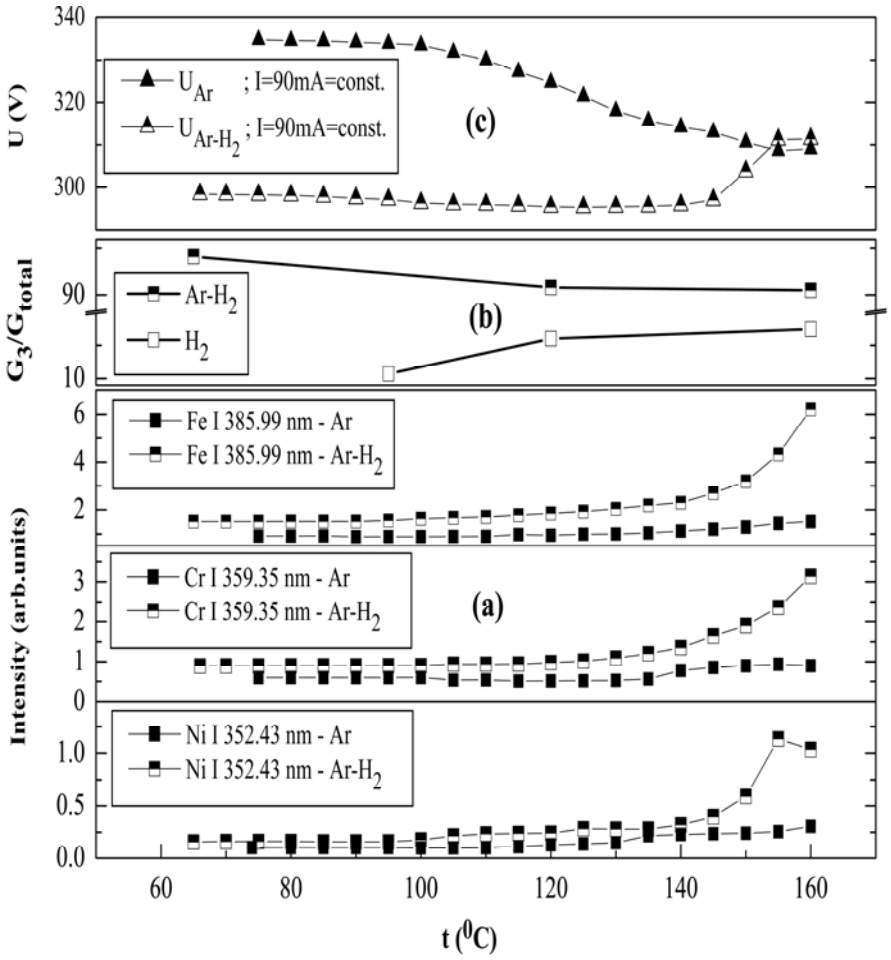

Fig. 7. The temperature dependence: of (a) Fe, Cr and Ni resonance lines intensity**;** (b) contribution of G_3/G_{total} to the H_α profile in H_2 and in Ar–H_2 **;** and (c) discharge voltage for constant current of 90 mA in Ar–H_2 and in pure Ar [16].

4. RADIAL DISTRIBUTION, INFLUENCE OF SURFACE COVERAGE AND TEMPERATURE EFFECT

The experiment in Ref. 16 was carried out using HC discharges observed end-on without attempting to achieve spatial resolution of the EDB of the Balmer lines. Our

recent study [28] is an extension of earlier ones [13,16], but with an emphasis on the radial distribution of the EDB of the H_α line in HC discharge in H_2 and Ar-H_2 mixtures.

The details of the HC discharge source are described earlier, see also [13]. The only difference is the cathode – anode distance, which was on one side 20 mm, and 15 mm on the other. In this way the discharge voltage can be changed using one or the other anode. During the discharge operation, the cathode was either air cooled with a fan, placed 150 mm from the discharge tube, or gradually heated by changing the cooling rate of the fan. The temperature of the outer wall of the HC tube is measured by a K-type thermocouple. The radial distribution spectra recordings were performed with unity magnification in equidistant steps perpendicular to the discharge axis, with an estimated spatial resolution of 0.25 mm or 0.40 mm. For radial intensity measurements the discharge was run between HC and rear anode, located at 20 mm from the cathode.

Three H_α line profiles recorded at various radial positions from the axis of HCGD operated with SS cathode in H_2 are presented in Figure 8a. In the upper right corner of this figure the experimental H_α profile recorded at the radial position *r=2.8 mm* and the best fit with three Gaussians are presented. The experimental conditions, relative contributions G_i/G_{total} (i=1,2,3) and energies E_i (i=1,2,3) of excited hydrogen atoms obtained by fitting the H profiles from titanium HC disharges are given in Tables 1 and 2.

An experimental study of the excessively broadened part G_3 of the Balmer alpha line in HCGD operated with H_2 and Ar-H_2 gas mixture with SS or Ti cathodes shows considerably different radial distribution depending upon the choice of operating gas. The differences between radial G_3 distribution with SS and Ti cathode are evident, see Figs. 9 and 10, and an increase with the HC temperature is always detected, see Tables 1 and 2.

With both HC operated in pure H_2, the radial distribution of the G_3 component is flat and therefore the overall profile has a bell shape, see Figures 9a and 10a. In order to explain the difference between G_3 contributions for HCGD with SS and Ti cathodes, the number R_N and the energy R_E coefficients for incident H^+ ions are calculated first for clean metal surface and than for surfaces covered with metal hydride layers. For this purpose we have utilized a FORTRAN subroutine [29] which implements a code described by Tabata and Ito [30]. This is not the only process of interaction between energetic particles and the cathode surface. The fast hydrogen atoms H_f, resulting from collisions of fast H^+ and H_3^+ ions with H_2, are also back scattered from the cathode surface. To analyze this process the results of a simulation with Fe and Ti targets using the binary collision cascade program MARLOWE [24] are used. Both sets of results for R_N and R_E, calculated and [24], show that the fraction of particles and energy reflected decreases with increasing hydrogen content of the metal hydride. Furthermore, both scattering coefficients are larger for Fe (very close to SS) than for Ti, see also Table 5 in Ref. 28 and [24]. For this reason the energy of excited hydrogen atoms (half-width of G_3 inenergy units) is larger for SS (E_3*=59 eV*) than for Ti HC (E_3*=50 eV*), in spite of similar voltage for both discharges. Thus, the results of both simulations, from Table 5 in Ref. 28 and [24], for Fe or SS and for Ti are in qualitative agreement with G_3 values

(proportional to R_N and R_E) and their temperature trend in Tables 1 and 2. The increase of G_3 contribution versus temperature may be related to the decrease of the metal hydride layer with an increase of HC temperature.

The secondary emission processes, which can affect the sheath field profile, and consequently the ion acceleration, are neglected in our analysis of discharge-surface interaction. This is due to the lack of secondary emission coefficients data for SS and Ti surfaces covered with a hydride layer having variable hydrogen/metal ratio.

At least, but not last, it is interesting to notice that similar line shapes of the H_α and D_α lines, see Figure 8a and [21], are detected close to the first wall and in plasma diverters of large plasma fusion devices, see e.g. [33-36] and references therein. Although in these cases Doppler broadening is combined with the Zeeman line splitting, the same elementary atomic and molecular collisions and interaction with the wall surface are also present. Therefore, the shape of the Balmer lines in high temperature plasma reactors must bear certain resemblance to those reported here. On the other hand, simple devices like HCGD may be used for material testing and for study of elementary processes relevant for large plasma devices.

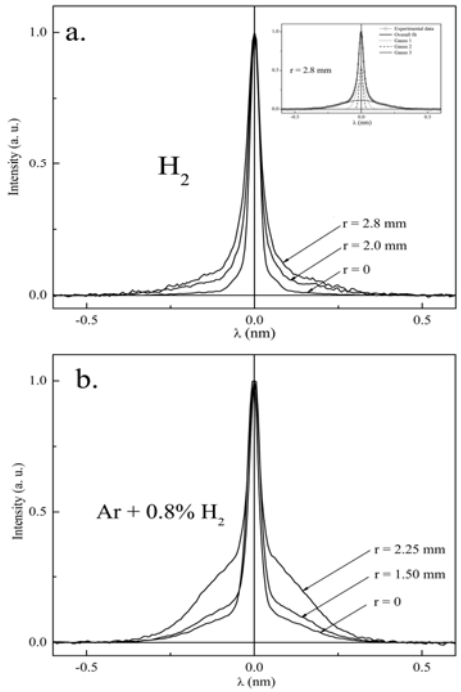

Fig. 8. Typical H_α profiles recorded at different radial positions in: (a) stainless steel hollow cathode; upper right corner depicts the H_α line shape at radial position *r=2.8 mm* fitted with three Gaussians; and (b) titanium hollow cathode. Discharge conditions: (a) pure H_2 at *p=4 mbar; I=90 mA; U=427V* and $T_{wall}=74^OC$; (b) Ar-H_2 mixture at *p=4 mbar; I=90 mA; U=338V* and $T_{wall}=75^OC$ [28].

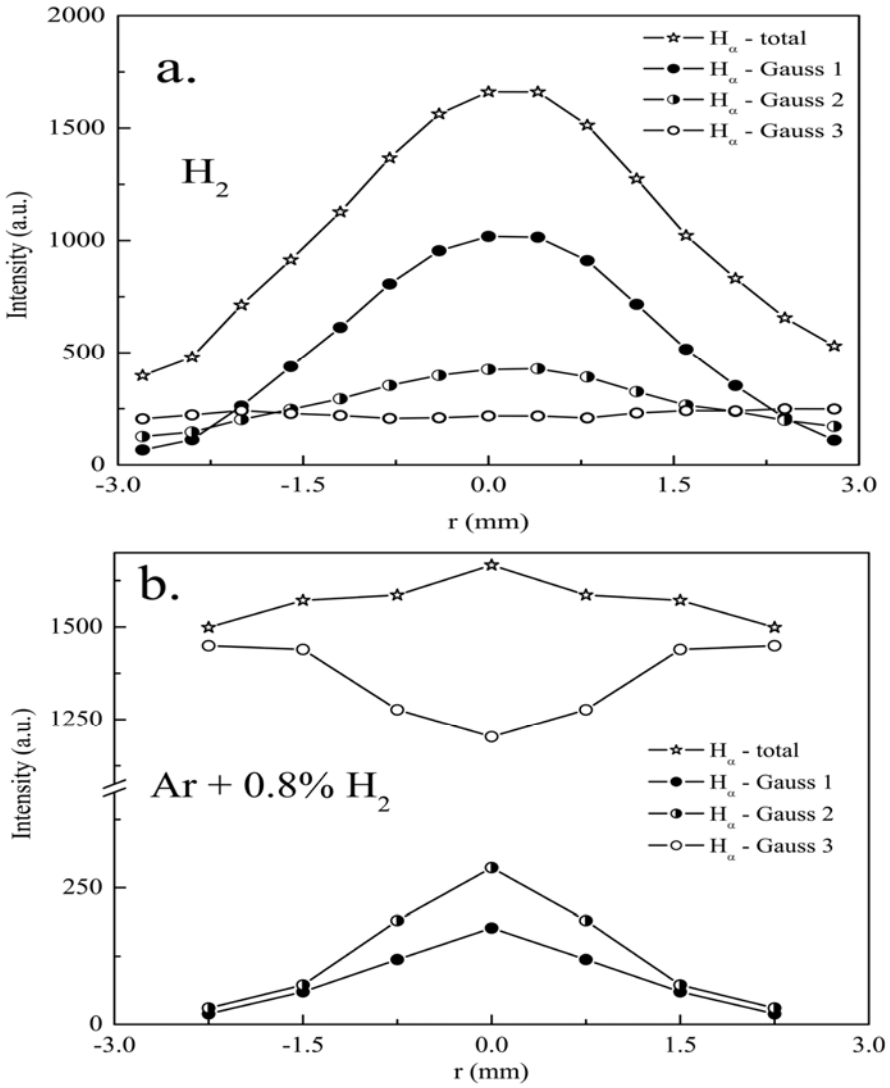

Fig. 9. The intensity distribution of the H spectral line and its Gaussian components vs. radial coordinate *r*. Experimental conditions: stainless steel hollow cathode discharge in (a) pure H_2 at *p=4 mbar; I=90 mA; U=427V* and $T_{wall}=74^{O}C$; (b) Ar-H_2 mixture at *p=4 mbar; I=90 mA; U=300V* and $T_{wall}=55^{O}C$ [28].

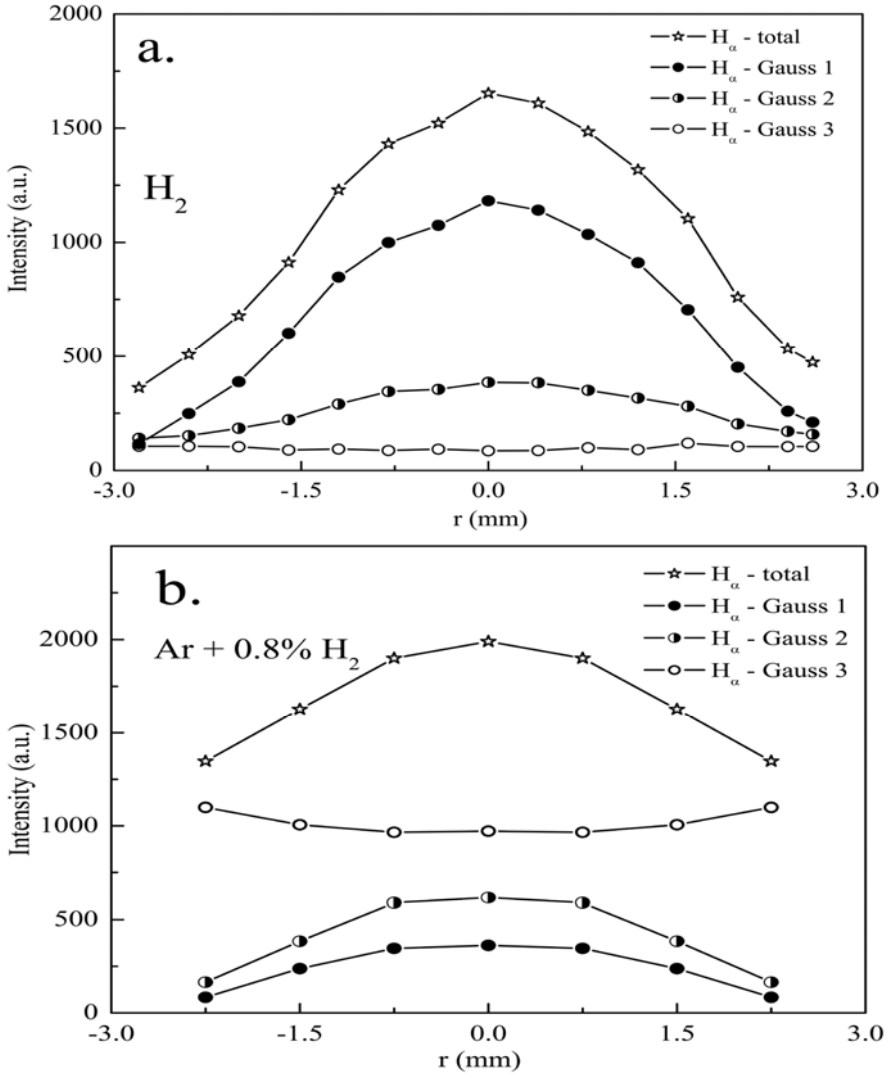

Fig. 10. The intensity distribution of the H spectral line and its Gaussian components vs. radial coordinate. Experimental conditions: titanium hollow cathode discharge in (a) pure H_2 at *p=4 mbar; I=90 mA; U=424V* and $T_{wall}=75^{O}C$; (b) Ar-H_2 mixture at *p=4 mbar; I=90 mA; U=338V* and $T_{wall}=75^{O}C$ [28].

Table 1. Experimental conditions, relative contributions G_i/G_{total} ($i=1,2,3$) and energies E_i ($i=1,2,3$) of excited hydrogen atoms obtained by applying three Gaussian fit to the H profiles for titanium hollow cathode glow discharge in pure H_2 at *p=4 mbar; I=90 mA*; *r* denotes radial position. [28]

T. (°C)	Voltage (V)	r (mm)	G_1/G_{total} (%)	G_2/G_{total} (%)	G_3/G_{total} (%)	Hydrogen Atom Energy		
						E_1 (eV)	E_2 (eV)	E_3 (eV)
74	424	0	71.4	22.3	6.3	0.3	5	50
		0.75	65.4	23.7	10.9		4	
		1.50	48.4	29.6	21.9			
		2.25	33.6	38.9	27.5		3	
100	435	0	66.5	25.3	8.2	0.3	5	
		0.75	59.8	27.0	13.2		4	
		1.50	39.6	35.8	24.6			
		2.25	20.9	42.9	36.2		3	
125	448	0	65.7	25.2	9.1	0.3	5	
		0.75	59.5	27.6	12.9		4	
		1.50	42.0	34.0	24.0			
		2.25	19.3	44.7	36.0		3	

Table 2. Same as for Table 1, but for glow discharge in argon-hydrogen mixture at *p=4 mbar; I=90mA.* [28]

T. (°C)	Voltage (V)	r (mm)	G_1/G_{total} (%)	G_2/G_{total} (%)	G_3/G_{total} (%)	Hydrogen Atom Energy		
						E_1 (eV)	E_2 (eV)	E_3 (eV)
75	338	0	19.0	31.0	51.0	0.3	1	37
		0.75	18.2	31.0	50.8			
		1.50	14.6	23.6	61.8			
		2.25	6.2	12.2	81.6			
100	336	0	14.8	28.7	56.5			
		0.75	16.9	26.7	56.4			
		1.50	10.5	18.2	71.3			
		2.25	4.9	8.5	86.6			
135	340	0	15.1	20.0	64.9			
		0.75	12.1	21.9	65.9			
		1.50	8.9	13.9	77.1			
		2.25	4.4	6.8	88.9			

ACKNOWLEDGMENT

This work within the Project 141029B "Low-temperature plasmas and gas discharges: radiative properties and interaction with surfaces» is supported by the Ministry of Science and Environmental Protection of the Republic of Serbia.

REFENECES

1. W. Benesh and E. Li, Opt. Lett. **9**, 338 (1984).
2. E. Li Ayers and W.Benesh, Phys. Rev. A **37**, 194 (1988).
3. M.R. Gemišić Adamov, B.M. Obradović, M.M. Kuraica and N. Konjević, IEEE Trans.Plasma Sci. **31**, 444 (2003).
4. M.R. Gemišić Adamov, M.M. Kuraica and N. Konjević, Eur.Phys.J. D **29**, 393 (2004).
5. N. Konjević and M. M. Kuraica, in The Physics of Ionized Gases, Eds: Lj. Hadžievski, T. Grozdanov, and N. Bibić, 22nd Summer School and International Symposium on the Physics of Ionized Gases, August 23 - 27, 2004, National Park Tara - Bajina Bašta, AIP Conference Proceedings 740 (2004) 268-281.
6. N. Cvetanović, M.M. Kuraica, N. Konjević, J.Apppl.Phys. **97**, 033302 (2005).
7. Z.Lj. Petrović, B.M. Jelenković, A.V. Phelps, Phys.Rev.Lett. **68**, 326 (1992).
8. S.B. Radovanov, K. Dzierzerga, J.R. Roberts, J.K. Ollthoff, Appl.Phys.Lett. **66**, 2637 (1995).
9. I.R. Videnović, N. Konjević, M.M. Kuraica, Spectrochim.Acta **51B**, 1707 (1996).
10. M. Kuraica and N. Konjević, Phys. Rev. A **46**, 4479 (1992).
11. M. Kuraica, N. Konjević, M. Platiša and D. Pantelić, Spectrochim. Acta **47B**, 1173 (1992).
12. M. Kuraica and N. Konjević, Phys. Scripta **50**, 487 (1994).
13. N.M. Šišović, G.Lj. Majstorović and N. Konjević, Eur. Phys. J. D **32**, 347–354 (2005).
14. R.L. Mills, P.C. Ray, B. Dandapani, R.M. Mayo, J. He, J.Appl.Phys.. **92**, 7008 (2002).
15. R.L. Mills, P.C. Ray, M. Nansteel, X. Chen, R.M. Mayo, J. He, B.Dandapapanii, IEEE Trans. Plasma. Sci. **31**, 338 (2003).
16. N. Konjević, G.Lj. Majstorović, N.M. Šišović, Appl.Phys.Lett. **86**, 251502 (2005).
17. B.P.Lavrov, A.S.Mel'nikov, Optics and Spectroscopy **75**, 1152 (1993).
18. T. Tabata, R. Ito, Y. Itikawa, N. Itoh, K. Morita, At. Data Nucl. Data Tables **31**, 1 (1984).
19. B.P.Lavrov, A.S.Mel'nikov, Optics and Spectroscopy **79**, 922 (1995).
20. A.V. Phelps, J.Appl.Phys. **98**, 066108 (2005).
21. NotesOnMills.pdf may be requested from avp@jila.colorado.edu
22. J. Roth, Chap.7 in Sputtering by Particle Bombardment II: Topics in Applied

Physics (Berisch, R., ed.) Vol.52, Springer-Verlag, Berlin (1983).
23. W. Eckstein and H. Verbeck, J.Nucl.Mat. **76&77**, 365 (1978).
24. O.S. Oen and M. T. Robinson, J.Nucl.Mat. **76&77**, 370 (1978).
25. J. Rooth, W. Eckstein and J. Bohdansky, J.Radiat.Eff. **48**, 231 (1980).
26. C. V. Budtz- Jorgensen, P. Kringhoj and J. Bottiger, Surf.Coat.Technol. **116-119**, 938 (1999).
27. J. Bohdansky, Nuclear Fusion, Special Issue, Data Compendium for Plasma Surface Interactions (1984) p.61.
28. N.M. Šišović, G.Lj. Majstorović and N. Konjević, Eur. Phys. J. D, accepted for publication.
29. M. Warrier, R. Schneider, X. Bonnin, Computer Phys.Comm. **160**, 46 (2004).
30. T. Tabata, R. Ito, Present status of data compilation on ion backscattering, Institute of Plasma Physics Report, Nagoya, Japan, IPPJ-AM-64:84–89, 1989.
31. A.V.Phelps, J.Phys.Chem.Ref.Data **19**, 653 (1990).
32. A.V.Phelps, J.Phys.Chem.Ref.Data **21**, 883 (1992).
33. J.D. Hey, C.C. Chu, E. Hintz, Contrib. Plasma Phys. **40,** 9 (2000).
34. M. Koubiti, Y. Marandet, A. Escarguel, H. Capes, L. Godbert-Mouret,R. Stamm, C. De Michelis, R. Guirlet, M. Mattioli, Plasma Phys.Control.Fusion **44,** 261 (2002).
35. J. D. Hey, C. C. Chu, Ph. Mertens, S. Brezinsek, B. Unterberg, J.Phys.B: At.Mol.Opt.Phys. **37**, 2543 (2004).
36. J. D. Hey, C C Chu, Ph. Mertens, J.Phys.B: At.Mol.Opt.Phys. **38**, 3517 (2005).

VI Serbian-Belarusian Symp. on Phys. and Diagn. of Lab. &
Astrophys. Plasma, Belgrade, Serbia, 22 - 25 August 2006
eds. M. Ćuk, M.S. Dimitrijević, J. Purić, N. Milovanović
Publ. Astron. Obs. Belgrade No. 82 (2007), 201-211 *Invited lecture*

LASER ABLATION PLASMAS IN LIQUIDS FOR FABRICATION OF NANOSIZE PARTICLES

N.V. Tarasenko, V.S. Burakov, A.V. Butsen

Institute of Molecular and Atomic Physics National Academy of Sciences of Belarus
70 Nezalezhnasty Ave., 220072 Minsk, Belarus
e- mail: tarasenk@imaph.bas-net.by

Abstract. The capabilities of laser ablation in liquids for fabrication of metallic and composite nanoparticles were analyzed. The properties of Ag, Au and Cu as well as bimetallic Ag-Cu and Ag-Au nanoparticles synthesized in different liquids (water, acetone, ethanol) were examined.

The results obtained showed both the mean size of the nanoparticles and their stability could be controlled by proper selection of the parameters of laser ablation such as temporal delays between pulses, laser fluence and a sort of liquid used. The optimal conditions favoring the formation of nanoparticles with a desired structure were found.

1. INTRODUCTION

Last years considerable efforts have been directed to preparation and investigation of nanostructured materials. Broadly defined, nanostructured materials are solids composed of structural elements (mostly crystallites) which characteristic size falls in the range of 1 – 100 nm [1]. They include nanocomposites, loosely aggregated nanoparticles, cluster-assembled materials, nanocrystalline thin films, metal colloids as well as semiconductor nanostructures such as quantum dots, wires and wells.

Due to the reduced size of their constituent elements nanostructured materials have electronic, magnetic and chemical properties, which differ considerably from those of the corresponding bulk materials. For example, nanostructured materials have been found to exhibit increased strength and hardness, higher electrical resistivity, enhanced diffusivity, reduced density, etc. compared to the bulk. Hence, these materials are promising candidates for a variety of applications, which include heterogeneous catalysis, gas sensor technology, microelectronics, nonlinear optics, etc. [2-4].

Depending on the size range, shape and chemical composition of nanoparticles different techniques have been used for producing of such samples. Among them are wet chemical processes, physical methods and combined techniques [5-7]. The ultimate goal of each technique is a fabrication of monodisperse particles with a predetermined size and shape.

Recently, plasma assisted methods based on laser ablation and electrical discharges have become a focus of many studies [8-11]. The capabilities of laser ablation technique and the results of its application for fabrication of metallic and composite nanoparticles are discussed in the present paper.

Laser ablation plasma is formed above the surface of the solid target when an intense laser beam strikes the target. Laser ablation provides a simple and contaminant-free method which can be used for a large number of materials. The important advantages of laser ablation technique are:

- laser ablation can be used for metals, semiconductors and insulators,
- conditions during the laser ablation can be fairly well controlled,
- in the case of multi – component samples, the stoichiometry of the ablated material can be achieved to closely resemble that of the target.

Typically, laser ablation experiments are carried out in gas or vacuum environments. The technique allows changing the diameter of nanoparticles by means of changing the energy of laser radiation, sort and pressure of an ambient gas. But efficiency of this technique is not very high in result of material depositions on walls of the vacuum chamber.

The more effective collection of synthesized particles can be achieved by laser ablation in liquid environment. Additional advantage of this approach - experiments are performed at the normal atmosphere.

It should be noted that the processes of laser ablation in liquids have been much less investigated. But the feasibility of using laser ablation in transparent liquids for nanoparticle synthesis has been recently demonstrated [8-10].

We developed the double-pulse laser ablation approach in liquid environment for fabrication of metallic and bimetallic nanoparticles with a controlled size distribution. Double-pulse approach of laser ablation has been recently shown to enhance considerably the line emission from the plume that is highly important for improvement of sensitivity of laser spectral analysis (LIBS) [12-15]. As concerns of the nanoparticles formation, the double-pulse laser ablation seems to be also more favorable than single pulse regime. The developed technique offers the better control over the particle formation process. The definite size reduction of particles in ablation plume can be achieved under conditions of suitable temporal delays between two laser pulses in result of heating and fragmentation of the ablated material produced by the first laser pulse [16].

2. EXPERIMENTAL

Experiments were made by using two 10 Hz pulsed Nd:YAG lasers, operating at the fundamental (1064 nm) and frequency-doubled (532 nm) wavelengths each with 50 mJ pulse in a 5-mm beam. The laser beams were focused on the surface of the metallic sample (Ag, Cu, Au) or combined target consisted of two tightly pressed (silver/copper or silver/gold) plates immersed into the cell with liquid. In the case of the combined target the laser beams were focused on the Ag-Cu or Ag-Au interface. Laser beams were employed for ablation both singly and together with appropriate temporal delays between pulses. The ablation laser power densities at the target surface were in the range of $5 \cdot 10^8$ - $5 \cdot 10^9$ W/cm^2. Experiments were performed using different liquids like acetone, ethanol, and distilled water.

We used two different laser beam configurations: (1) the double-pulse approach based on collinear beams focused onto the same place of the target surface and (2) the configuration based on crossed beams when the second unfocused laser beam at λ=532 nm runs parallel to the sample surface, providing additional irradiation of the formed nanoparticles.

The fabricated nanoparticles were characterized by optical absorption spectroscopy for monitoring the changes in the plasmon absorption characteristics, transmission electron microscopy (TEM), X-ray diffraction (XRD) and energy dispersive X-ray microanalysis (EDX) in order to analyze the final size and composition of nanoparticles.

3. RESULTS AND DISCUSSION

Two main mechanisms of nanoparticle formation during laser ablation process can be distinguished.

- The first mechanism, associated with aggregation of the ablated atoms and clusters into small embryonic nanoparticles and their growth by assembling the clusters and attachment of free atoms.
- The second one, attributed to the plasma-induced heating and ablation of particulates from the target.

According to the first mechanism the density of ablated species (atoms) in the gas phase plays an important role in the nanoparticles growth. By controlling the density of the ablated species it is possible to control the final size of the formed nanoparticles. The density of the ablated species can be changed by adjusting the laser fluence. It should be noted that the second mechanism gives rise to much larger particle sizes and broader size distributions.

Relative contributions of the both mechanisms determine the final size distribution of the produced particles. That’s why for optimization of synthesis process the detailed information about plasma parameters is required.

Spectroscopic characterization of the ablated plume was performed by the time resolved emission spectroscopy and gated intensified CCD imaging technique (Fig.1).

The optical observation of the plasma emission was executed by imaging the plasma plume onto the entrance slit of the spectrograph such that the expansion direction (z) lies along the orientation of the entrance slit of the spectrograph. At the output of the spectrograph, in the image plane, a time-gated ICCD camera was installed. So, at its output the spectrograph produced a one-dimensional spatial and spectral image of the expanding plasma, in which the vertical axis corresponds to the expansion direction z and the horizontal axis to the wavelength of the emission of plasma species.

The emission spectrum was recorded at different time delays. Typical gate steps and gate widths used were 100 and 50 ns, respectively, which were selected in order to give the optimal signal/amplitude ratio and temporal resolution.

Plasma emission spectra were recorded and compared for different ablation regimes (single pulse, two pulses in coincidence and in sequence at various delays between pulses).

Summarizing the results of our investigations and results of previous studies of double-pulse laser ablation plasma for spectral analysis [15,17], the main features of double-pulse laser ablation in liquids can be characterized as following:

- A hemispherical cavitation bubble originated from gaseous ablation products is formed above the sample.
- Arising after the ablating pulse and expanding steadily, the bubble reaches its maximum size after several tens of microseconds (depending on the sample material and laser fluence) and then collapses.
- The dimension of laser ablation plasma in liquid is significantly smaller, vertically and horizontally, than the plume produced in air. For illustration Fig.2 presents intensity profiles in the direction of the normal to the sample surface for emission from the 1064-532 nm double-pulse laser-induced plasma of a copper sample (z = 0 mm), obtained under air and water environment.
- Plasma radiation after single-pulse ablation is weaker (compared to gaseous environments) because it is strongly quenched. The spectrum of the plume is dominated by continuum radiation.
- But from double-pulse ablation plasma sharp atomic line spectra were observed. The Fig. 2B presents the fragments of the spectra of the laser-induced plasma of a copper sample in case of the 532 nm single (A) and in the 1064-532 nm double-pulse ablation modes for gate delays with respect to the 532 nm laser 200 (b), 400 (c) and 600 ns (d). The mechanism responsible for the distinct line excitation produced by the second pulse has been attributed to the formation of a bubble at the surface by the first laser pulse. The second pulse fired into the bubble under gaseous environments. The optimal values of pulse separations are determined by larger bubble volume that leads to increase the emission intensity and to decrease quenching of emitting atoms.

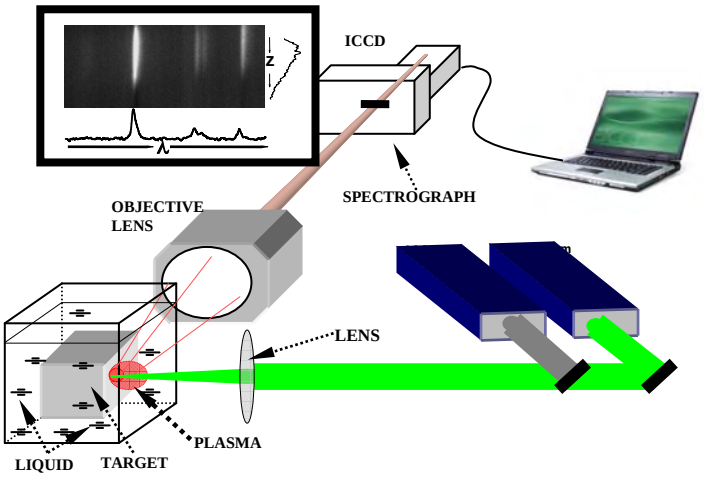

Fig.1. Experimental set-up for time-resolved spectroscopic plasma characterization.

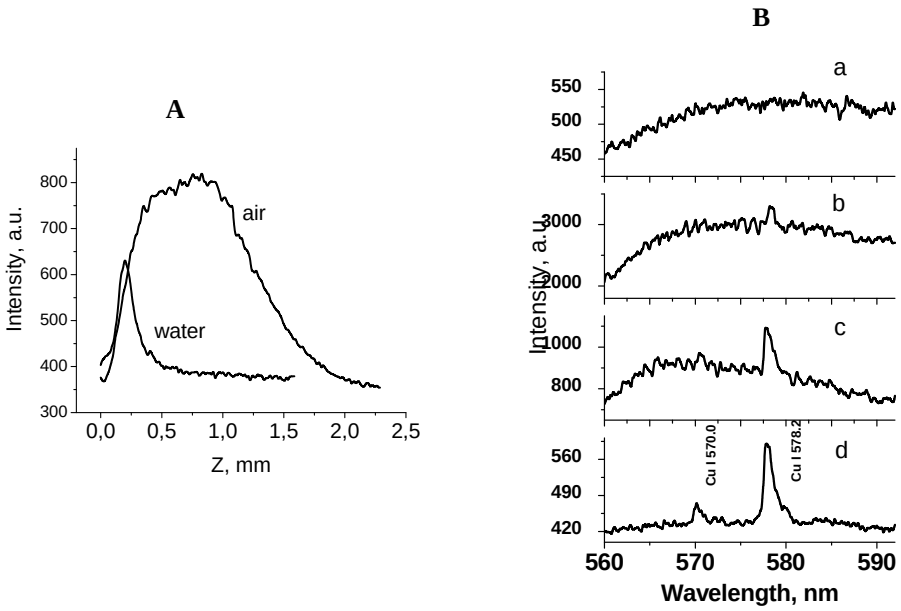

Fig.2. A - Intensity profiles in the direction of the normal to the sample surface for emission from the 1064-532 nm double-pulse laser-induced plasma of a copper sample (z = 0 mm), obtained under air and water environment; **B -** fragments of the spectra of the laser-induced plasma of copper sample in case of the 532 nm single (a) and in the 1064-532 nm double-pulse ablation mode for gate delays with respect to the 532 nm laser 200 (b), 400 (c) and 600 ns (d).

During the repeated (10 Hz) laser ablation of the metal samples the solution in the cell became visibly contaminated with the ablated material. The properties of metal nanoparticles fabricated by laser ablation were studied by recording their extinction spectra as a function of preparation conditions. Typical spectra of the prepared colloids are shown in Fig.3 and Fig.4. The spectra exhibit characteristic absorption bands with peaks located at 400 nm for silver nanoparticles and at 520 nm for gold nanoparticles. The spectral features of copper colloids are characterized by a peak of absorbance at 570 nm (Fig.4).

These bands were clearly seen in all solutions and they are related to the collective excitation of conduction electrons (surface plasmon resonances SPR). The position and shape of the plasmon absorption are known to be dependent on the particle morphology, dielectric functions of the metal and the surrounding medium as well as surface-absorbed species [1]. The presence of the single surface-plasmon peaks implied that the formed nanoparticles were nearly spherical. In the case of ellipsoidal particles the absorption spectrum would have two plasmon peaks [18].

According to Mie theory spectra of the particles with radii between about 2 and 10 nm are independent of the particle size. For particles with dimensions beyond 10 nm the absorption peak broadens and shifts to longer wavelength. The broadening and lowering of the absorption peak can be related to a reduced mean free path for conduction electrons. The peak position at 400 nm observed for silver in our experiments indicated a formation of Ag nanoparticles with sizes in the range of 10 –30 nm.

Gold colloids exhibit the characteristic peaks of the surface plasmon resonance (SPR) on the tail of the broad band extending toward the UV- wavelength range and originating from the interband transitions of gold nanoparticles [19]. It is known that the absorption due to the interband transition does not change appreciably with the particle size but is sensitive to the particle quantity.

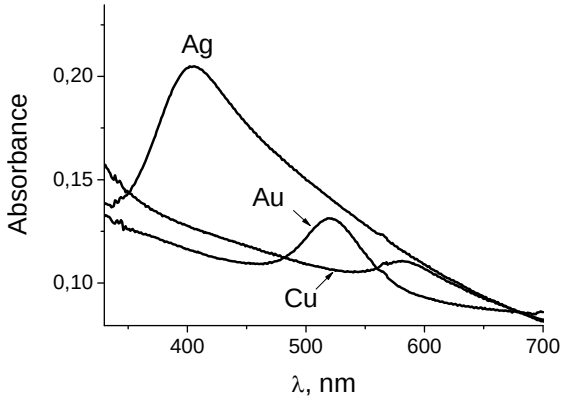

Fig.3. Extinction spectra of silver, gold and copper colloids prepared by laser ablation in ethanol.

Therefore, the absorption of the solution at the wavelengths of interband transitions can be used as a measure of the total amount of gold in the solution including the nanoparticles of different sizes, clusters and free gold atoms. Conversely, the height of the plasmon peak is proportional to the concentration of the Au nanoparticles with sizes in the range of 5 – 30 nm. The absorbance in the vicinity of 200 nm can be assigned to the small gold clusters, which begin to contribute to the optical absorption in the range of the surface plasmon resonance as they grow into nanosized particles, by aggregation and attachment processes [20].

Analogous considerations can be made for the absorption spectra of copper nanoparticles. In this case the size effect is similar to that of gold. At very small sizes limitation of the mean free path by the particle boundary broadens and decreases peak absorption, while at larger sizes the peak shifts to longer wavelengths and broadens as high order modes are excited. For example, the copper particles with a diameter below 4 nm are characterized by such a strong broadening of the plasmon resonance that it practically disappeared [21]. A progressive appearance of the peak at 570 nm occurs upon increasing the size of the copper nanoparticles.

Owing to the high reactivity of copper, it was practically impossible to observe the copper plasmon band near 570 nm by laser ablation in water. But Cu nanoparticles with the average diameter of 5-7 nm exhibiting the characteristic plasmon band were synthesized by laser ablation of a copper metal plate immersed in the aqueous solution of sodium dodecyl sulfate (SDS) [22].

In our experiments [16] the shape and intensity of the plasmon bands in the absorption spectra of colloidal solutions were also dependent on the regime of laser operation (double-pulse or single pulse mode). By using the double pulse laser ablation and the same total number of laser pulses, the efficiency of ablation was greater and the absorption bands were more intense. The observed spectra were also changed with changing of the temporal delay between two pulses in double pulse mode. It should be noted that particles prepared by the double-pulse laser ablation had smaller diameters than those prepared in the single pulse ablation regime. The size reduction of particles in ablation plume is most likely to achieve under conditions of suitable temporal delays in result of heating and fragmentation of the ablated material produced by the first laser.

It is important to mention that the particles produced in acetone show a long-term stability towards coagulation/aggregation as compared to that in water. This function of acetone most probably is connected with the interaction between the acetone carbonic group and the metal nanoparticle surface.

The spectra findings were confirmed by TEM data. The size and size distribution of the nanoparticles were found to be functions of the laser ablation parameters (laser wavelength and fluence). Typical TEM images and histograms of the diameter distributions for Cu nanoparticles synthesized by the 532 nm laser ablation in acetone are presented in Fig.4. TEM images show the presence of nearly spherical particles with an average diameter of 10±2 nm.

The TEM of the Ag particles fabricated by laser ablation indicated that the average size of the particles was around 15 nm with an asymmetrical distribution of sizes ranging from approximately 5 to 35 nm. The average size of gold

nanoparticles, formed at the same experimental conditions was about 15 nm. The average diameter was found to be decreased as the laser fluence increased. Some of the nanoparticles were loosely agglomerated, some presented chains of welded particles.

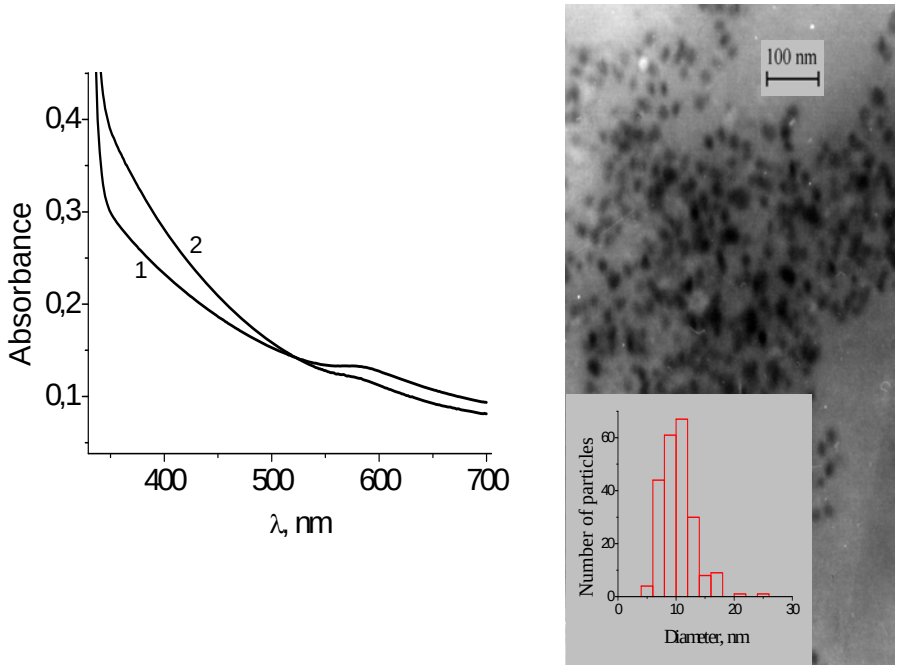

Fig. 4. Extinction spectra of copper nanoparticles prepared in acetone: (1) by the repetitive (10Hz) 1064 nm single-pulse laser ablation for 5min; (2) by the double-pulse laser ablation (10 μs separation between the 1064nm and 532 nm pulses) (**left**) and TEM image with corresponding size distribution histogram of Cu nanoparticles prepared in single pulse regime in acetone (**right**).

In the case of combined target consisted of two tightly pressed silver/copper or silver/gold plates immersed into the cell with acetone when the laser beams focused on the Ag-Cu or Ag-Au interface, the spectra of the solutions do not exhibited a pronounced maximum attributable to the monometallic particles. These spectra showed a single SPR whose position was dependent on a ratio of element concentrations, which can be changed by the variation of the ratio of the irradiated areas of both metals in the focal plane of a lens focusing the laser radiation on the target surface. It should be noted, that the absorption curve of the bimetallic dispersion could not be obtained by simple overlapping of the absorption curves of the monometallic Ag and Cu (Au) particles. Two separate maxima that correspond to the plasmon bands of individual metals should be observed in case of a mixture of monometallic particles or bimetallic particles of a core-shell structure. Therefore

based on the spectra analysis, it is reasonable to conclude that bimetallic (composite) nanoparticles are formed. It is known that silver and copper exhibit very limited miscibility in the bulk, while gold and silver are completely miscible. Therefore, most likely in case of Ag-Cu target, the silver/copper particles are phase-separated composites, which are made partly of silver and partly of copper atoms and in the case of Ag-Au sample a formation of alloys is preferable.

EDXS and XRD analysis also pointed to the bimetallic composition of the formed nanoparticles. Scanning electron micrographs when viewed with greater magnification showed that the rather large grains formed after deposition of the colloidal solution onto silicon substrate were seen to be clusters of many smaller grains (Fig.5). The EDX spectra showed the presence of both constituent elements along the line of scanning. XRD analysis of the produced powders showed that the characteristic peaks for a Ag–Cu bimetallic system became broader and accordingly suggested the formation of bimetallic nanoparticles with smaller sizes.

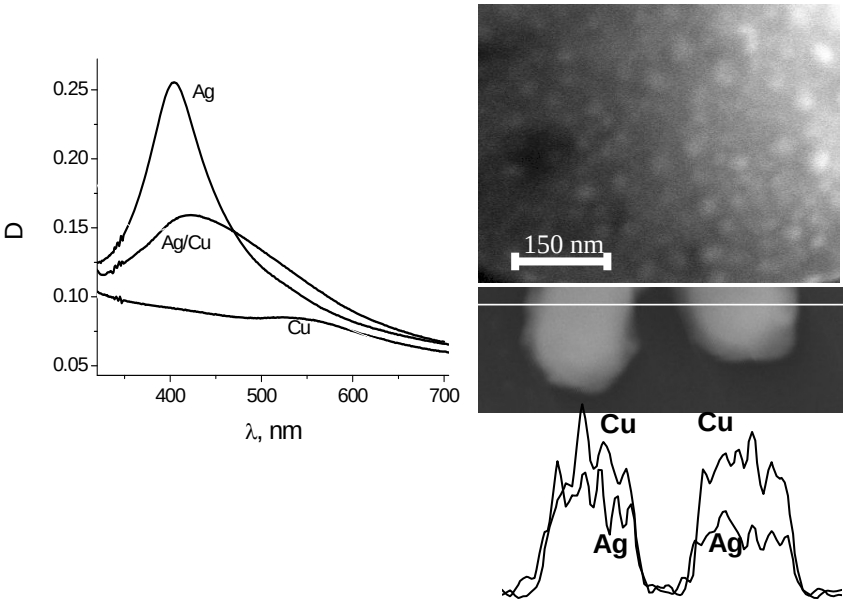

Fig. 5. Extinction spectra of silver, copper and bimetallic silver/copper colloids prepared by single-pulse laser ablation **(left)** and SEM images of bimetallic Ag-Cu nanoparticles with distribution of elements along the line of scanning measured by EDX **(right).**

TEM data confirmed that the laser ablation of the combined target produced the particles of smaller (5-7 nm) sizes than the particles formed under the laser ablation of the monometallic samples. From the diffractions patterns, it was revealed that the individual particles were polycrystalline.

It is important to note that bimetallic nanoparticles, are even of greater interest than the monometallic ones because of their composition-dependent optical and catalytic properties. For example, the enhanced catalytic performance of bimetallic nanoparticles compared with the single metal ones is well established [23,24].

4. CONCLUSION

It is expected, that the obtained results will find applications in the synthesis of new materials with modified properties, in the fabrication of catalysts with optimized selectivity and efficiency, in medicine for preparation of nanoparticle-based probes with great potential for targeting, imaging and treating different diseases etc.

ACKNOWLEDGEMENTS

The work has been partially supported by the Belarusian Foundation for Fundamental Researches under grant F 06-094 and by the Presidium of the National Academy of Sciences under grant № 02.

REFERENCES

1. U. Kreibig, M. Vollmer, Optical Properties of Metal Clusters, Springer, Berlin (1995).
2. M.S. Sibbald, G. Chumanov, T.M. Cotton, J. Phys. Chem. **45**, 721 (1998).
3. R.A.Ganeev, A.I.Ryasnyanskii, T.Usmanov, Quantum Electronics **31**, 185 (2001)
4. J. Neddersen, G. Chumanov, T. Cotton, Appl. Spectr. **47**, 1959 (1993).
5. Ю.В. Бокшиц, Г.П. Шевченко, В.В. Свиридов, Весці НАН Беларусі, сер. хім. навук, **1**, 19 (2001).
6. Mark T.Swihart, Current Opinion in Colloid and Interface Science **8**, 127 –133 (2003).
7. C.-H. Jung, H.-G. Lee, C.-J. Kim and S.B. Bhaduri, J. of Nanoparticle Research **5**, 283-388 (2003).
8. N.V. Tarasenko, E.A. Nevar, A.V. Butsen, N.A. Savastenko, Appl. Surf. Sci., **252**, 4439-4444 (2006).
9. A. Simakin, V. Voronov, G. Shafeev, R. Brayner, F. Bozon-Verduraz, Chem. Phys. Lett. **348**, 182 (2001).
10. A.V. Kabashin, M. Meunier, C. Kingston, and John H.T. Luong, J. Phys. Chem. B **107**, 4527 (2003).
11. N. Parkansky, B. Alterkop, R.L. Boxman, S. Goldsmith, Z. Barkay, Y. Lereah, Powder Technology **150**, 36 – 41 (2005).

12. M. L. Petukh, V. A. Rozantsev, A. D. Shirokanov, A. A. Yankovskii, J. Appl. Spectr. **67**, 1097-1101 (2000).
13. S. M. Pershin, Quantum Electronics **16**, 325-330 (1989).
14. L.St-Onge, V.Detalle, M.Sabsabi, Spectrochimica. Acta B **57**, 121-135 (2002).
15. A. Pichahchy, D. Cremers, M. Ferris, Spectrochimica Acta B **52**, 25-39 (1997).
16. V.S. Burakov, N.V. Tarasenko, A.V. Butsen, V.A. Rozantsev, M.I. Nedel'ko, Eur. Phys. J. Appl. Phys. **30**, №2, 107-113 (2005).
17. R. Nyga, and W. Neu, Opt. Lett. **18**, 747-749 (1993)
18. S. Link, C. Burda, B. Nikoobakht, and M.A. El-Sayed, J. Phys. Chem. B **104**, 6152 (2000).
19. C.F. Boren, D.R. Huffman, Absorption and Scattering of Light by Small Particles, Wiley, New York, 1983.
20. F. Mafune, J. Kohno, Y. Takeda, and T. Kondow, J. Phys. Chem. B **106**, 8555 (2002).
21. M. Aslam, G. Gopakumar, T.L. Shoba, et.al. J. Colloid. Inter. Sci. **79**, 255 (2002).
22. V.S. Burakov, E.A. Nevar, P. Ya. Misakov, N.A. Savastenko, and N.V. Tarasenko, Proceedings IV International Symposium “Laser Technologies and Lasers”. October 8-11, Plovdiv, Bulgaria, 277-281.
23. Chen Yu-Hung and Yeh Chen-Sheng, Chem. Commun., 371–372 (2001).
24. J.F. Sanchez-Ramirez, C. Vazquez-Lopez, U. Pal, Superficies y Vacio **15**, 16–18 (2002).

VI Serbian-Belarusian Symp. on Phys. and Diagn. of Lab. &
Astrophys. Plasma, Belgrade, Serbia, 22 - 25 August 2006
eds. M. Ćuk, M.S. Dimitrijević, J. Purić, N. Milovanović
Publ. Astron. Obs. Belgrade No. 82 (2007), 213 *Invited lecture*

INTRINSIC RADIATIVE COLOR CENTERS IN ALKALI HALIDES CRYSTALS AND FILMS: FORMATION AND APPLICATIONS

A. P. Voitovich

Institute of Molecular and Atomic Physics of National Academy of Sciences,
Belarus, 220072, Minsk, pr. Nezalejnosti, 70
e-mail: voitovich@imaph.bas-net.by

Abstract. Alkali halides (AH) crystals, containing radiative color centers (CCs), are widely applied as active and passive laser media. They are also used in optoelectronics and in radiation dosimetry. Among them, lithium fluoride (LiF) crystals and films with CCs have found the most successful applications. LiF samples can be colored by irradiation with ionizing radiation, as X-rays, γ-rays, elementary particles and ions.

The processes of CCs formation under LiF irradiation with ionizing radiation and electrons are considered in the report. Charged particles are appeared into the crystals or films during their irradiation. The most numerous and important particles are electrons, fluorine ions, shifted from the lattice site into the interstitial position, and positively charged vacancies F^+, positioned on the lattice sites where the fluorine ions were situated before shifting. All of these particles are moving inside the crystal or film. Their diffusion results in the CCs formation.

The formation processes and efficiency hardly depend on the temperature during and after irradiating and the temperature of particles mobility. The formation features which depend upon these temperatures are discussed in the report. Two cases are considered: a) irradiating temperature is higher than temperature of vacancies mobility, b) irradiation temperature is lower than temperature of vacancies mobility but temperature of annealing which followed the irradiation is higher than last one. The difference in the CCs formation processes is noted for these two cases.

The particularities of the CCs formation processes in a bulk, a near-surface layer, a film, nano-sized structures of LiF crystals are given. They are determined by concentrations of electrons, vacancies, different kinds of traps and ratio of electrons and vacancies concentrations.

The examples of CCs applications are presented. Lasers, optoelectronics, dosimetry are considered as an illustration of such applications.

CONTRIBUTED PAPERS

VI Serbian-Belarusian Symp. on Phys. and Diagn. of Lab. &
Astrophys. Plasma, Belgrade, Serbia, 22 - 25 August 2006
eds. M. Ćuk, M.S. Dimitrijević, J. Purić, N. Milovanović
Publ. Astron. Obs. Belgrade No. 82 (2007), 217-221 *Contributed paper*

VARIATIONS OF ABNORMAL GLOW DISCHARGE PROPERTIES WITH CATHODE HEATING

N. Cvetanović[1], B. M. Obradović[2], M. M. Kuraica[2]

[1]*Faculty of Trans. and Traff. Engineering, University of Belgrade, V. Stepe 305, Belgrade,Serbia*
[2]*Faculty of Physics, University of Belgrade POB 368, 11001 Belgrade, Serbia*

Abstract. In this paper the influence of cathode temperature on abnormal glow discharge properties is examined. A Grimm type glow discharge with no cathode cooling, operating in argon was used. Spectral line intensities of argon and cathode material are measured simultaneously with cathode temperature and were observed to change significantly. Change of discharge voltage with measured cathode temperature is also reported. The behavior of the discharge was the same for two different cathode materials. Variations of the discharge properties may be attributed to the rise of gas temperature due to the heat transfer form the cathode.

1. INTRODUCTION

In this paper the influence of cathode temperature on abnormal glow discharge properties is examined. A Grimm type glow discharge with no cathode cooling, operating in argon was used. Spectral line intensities of argon and cathode material are measured simultaneously with cathode temperature and were observed to change significantly. Change of discharge voltage with measured cathode temperature is also reported. The behavior of the discharge was the same for two different cathode materials. Variations of the discharge properties may be attributed to the rise of gas temperature due to the heat transfer form the cathode.

Glow discharges are widely used today for many different purposes. One of them is the use of glow discharges for analysis of solid samples by optical emission spectrometry or mass spectrometry. In these sources sample material is sputtered leading to detection of sample atoms or ions in the discharge. Grimm type lamp, used in this experiment, is used for optical emission spectrometry.

Fair knowledge of discharge properties is needed if the discharge is to be applicable for analytical purposes. On the other hand, all processes that may influence discharge properties must be taken into account when analyzing and

modeling these sources. The Grimm abnormal glow discharge source operating in argon has so far been the subject of many analysis see for instance [1-3]. Many different processes may contribute to gas heating in glow discharges. Electric field accelerates the ions and electrons which then collide elastically with atoms of working gas giving rise to gas temperature. Sputtering of cathode material may also contribute to gas heating. It is well known that the cathode, in glow discharges, may reach a temperature much higher than room temperature due to the bombardment by heavy particles [1,4] and [5]. In order for the discharge to operate stably, cathode is usually cooled. Since it is heated the cathode contributes to the energy transfer to the gas [1, 6]. Concrete value of cathode temperature surface determines the boundary condition in the heat equation [1], but is usually not well known. Higher cathode temperature increases the gas temperature, at constant pressure this means lower gas density and a change of discharge parameters. Further more at constant current, voltage becomes higher giving rise to average electron energy [1, 6, 7]. Through this order of events, rise of cathode temperature changes the current--voltage characteristic and the intensity of spectral lines emitted form the discharge.

This paper presents results of an experiment that investigates the influence of cathode temperature on the Grimm type discharge properties operating in argon. This was done by measuring the discharge voltage and spectral line intensities of working gas and sputtered atoms with simultaneous measurement of the cathode temperature.

2. EXPERIMENTAL SETUP

The experimental setup is presented schematically in Fig.1. The discharge source is a modification of the Grimm type glow discharge, described in detail elsewhere [2]. Here, for completeness, minimum details will be given. Anode is hollow, 30 mm long with 8.00 mm inner diameter. Cathode is 7.60 mm wide and 10 mm long made of copper (99.998%) or Ti (99.5%) and placed in a 12 cm long cathode holder made of brass. In standard operation the cathode holder is water cooled, but here no cooling was used. Before every measurement the discharge operated for an hour at low current.

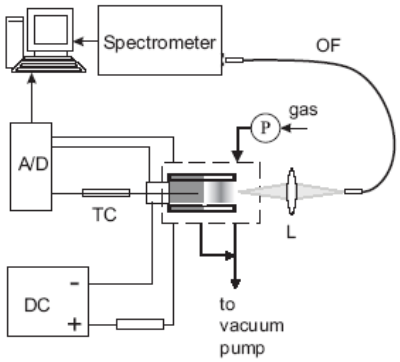

FIGURE 1. Experimental setup.

A gas flow of about 300 cm^3/min of argon (purity 99.995%) is sustained at a selected pressure of 6 mbar. To run the discharge a current stabilized power supply with voltage up to 1.1 kV was used. A ballast resistor of 15 kΩ is placed in series with the discharge.

The measuring end of a K-type thermocouple was placed in a drilled vacancy inside the cathode reaching 1.7 mm distance from the surface. Signal from the thermocouple was led to the multi channel A/D converter. Discharge voltage was measured by a high voltage probe connected to the mentioned A/D converter. Values of voltage and temperature were taken with 2 Hz sample rate.

Spectral line intensities were recorded end on by projecting the image of the discharge to the optical fiber, which was connected to the entrance slit of 1 m Cherny-Turner monochromator, see Fig. 1, equipped with CCD multichannel detector. This configuration enabled simultaneous monitoring of cathode temperature, discharge voltage and line intensities.

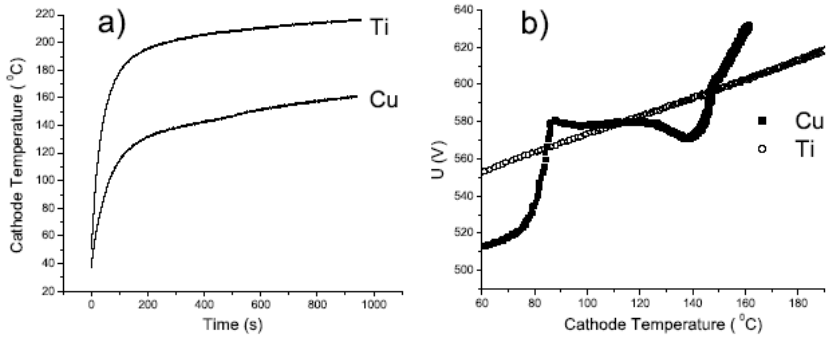

FIGURE 2. Measured dependences for two different cathode materials: a) Cathode temperature vs time; b) Discharge voltage vs cathode temperature; Discharge conditions: $I = 18$ mA, $p = 6$ mbar of Argon

3. RESULTS AND DISCUSSION

Exchangeable cathode holder enabled us to investigate the influence of cathode material by performing two separate measurements, with two cathode materials: titanium and copper. In both cases the discharge current was kept stable at I=18 mA at pressure of 6 mbar, with argon as a working gas. The cathode had neither external cooling nor heating. The temperature we have recorded may be presumed to be several degrees lower than at cathode surface due to the temperature gradient in the cathode material along the 1.7 mm distance.

Obtained cathode temperature dependence on time is given in Fig. 2a. Temperature shows a steep rise in the first tens of seconds and rises slowly for several minutes till it reaches its maximum value. This may be expected since there ought to be a short period needed to establish the continuous heat transfer form and to the cathode. After this period cathode temperature reaches a steady-state value. Cathode made of titanium is heated much faster and reaches higher maximum

temperature than the copper cathode (Fig. 2). This effect comes from a large difference in heat conductivity of these two materials (Ti: 22 W/Km, Cu: 400 W/Km).

Voltage dependence on cathode temperature is given in Fig. 2b. Calculations by Revel in [6] and by Bogaerts in [1] show that an increase in the cathode temperature leads to an almost linear increase in the argon gas temperature. For a fixed current and gas pressure model shows an increase in discharge voltage [6] with increase of gas temperature. Results in Fig. 2b correspond to this, showing rise in discharge voltage for both cathodes. However the curve dependence is quite different for two materials. Discharge voltage with copper cathode shows at first a period of instability corresponding to fast rise of temperature in Fig. 2a, after that it rises slowly and has another jump at high temperature. Operating with titanium cathode, discharge shows a much smoother, monotonous rise of voltage. After the temperature perturbation, the discharge tends to stabilize itself, reaching its steady state parameters after some short time [4]. Due to the large difference in thermal conductivity of titanium and copper cathode, the discharge behaves differently.

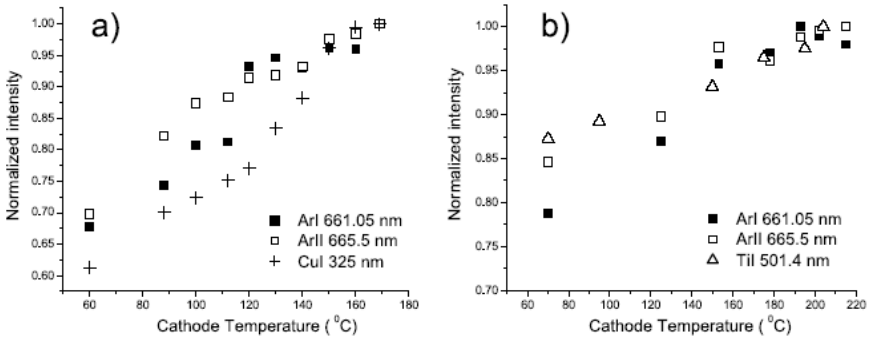

FIGURE 3. Measured line intensities dependance on cathode temperature: a)Discharge with Cu cathode; b) Discharge with Ti cathode; Discharge conditions: $I = 18$ mA, $p = 6$ mbar of Argon

Difference in sputtering yields for two materials must also be taken into account.

Results of spectral line intensities measurements are given in Fig. 3a - for copper cathode and Fig. 3b - for titanium cathode. Line intensities of argon and of cathode material are normalized at their maximum reached value for the sake of comparison. Again, the change is more drastic with copper cathode, both copper and argon lines are changed from about 60% to 100% with cathode heating. Discharge operating with titanium cathode shows a smaller change of about 80% to 100%. In both cases lines of cathode material follow the same behavior as lines of the working gas. It may be concluded that excitation of all lines is changed by the same mechanism i.e. rise of cathode temperature gives rise to gas temperature and changes electron energy distribution which is reflected on atom excitation.

4. CONCLUSION

Experimental investigation of influence of cathode temperature on abnormal glow discharge is reported in this paper. Discharge used is of Grim type operating in argon with non--cooled cathode made of copper and titanium. Simultaneous measurements of cathode temperature, discharge voltage and spectral line intensities were performed. It is shown that rise of cathode temperature gives rise to discharge voltage. Curve dependence of voltage on cathode temperature is significantly different for two cathode materials.

Line intensities of working gas and cathode material are also increased with cathode heating. Increase of discharge voltage and line intensities is attributed to rise of gas temperature and consequent change of electron density and energy distribution.

REFERENCES

1. A. Bogaerts, R. Gijbels and V. V. Serikov, J. Appl. Phys. **87**, 8334 (2000).
2. M. Kuraica, N. Konjevic, M. Platisa, D. Pantelic, Spectrochim. Acta B **47**, 1173 (1992).
3. N. P. Ferreira, H.,G.,C. Human, L., R. ,P. Butler, Spectrochim. Acta B **35**, 287 (1980).
4. Y. P. Raizer, Gas Discharge Physics, Springer-Verlag, Berlin, 1991.
5. A. Bogaerts, R. Gijbels, J. Anal. At. Spectrom., **19**, 1206 (2004).
6. I. Revel, L.,C. Pitchford and J. P. Boeuf, J. Appl. Phys., **88**, 2234 (2000).
7. A. Bogaerts , R. Gijbels, G. Gamez, G. M. Hieftje, Spectrochim. Acta B **59**, 449 (2004).
8. M. Kasik, C. Michellon and L.,C. Pitchford, J. Anal. At. Spectrom., **17**, 1398 (2002).

VI Serbian-Belarusian Symp. on Phys. and Diagn. of Lab. &
Astrophys. Plasma, Belgrade, Serbia, 22 - 25 August 2006
eds. M. Ćuk, M.S. Dimitrijević, J. Purić, N. Milovanović
Publ. Astron. Obs. Belgrade No. 82 (2007), 223-227 *Contributed paper*

SPECTROSCOPIC MEASUREMENTS OF NITROGEN COMPRESSION PLASMA FLOW ELECTRON DENSITY AND TEMPERATURE

I. P. Dojčinović[1,2], M. Nikolić[1], B. M. Obradović[1,2],
M. M. Kuraica[1,2], J. Purić[1,2]

[1]*Faculty of Physics, University of Belgrade, POB 368, 11001 Belgrade, Serbia*
[2]*Center for Science and Technology Development, Obilićev venac 26,*
11000 Belgrade, Serbia
e-mail: ivbi@ff.bg.ac.yu

Abstract. Magnetoplasma compressor with a semi-transparent electrode system that operates in the ion current transfer regime is studied. The thermodynamic parameters of the discharge and the compression plasma flow generated in N_2 + 5% H_2 mixture at 500 Pa pressure with input energy 4.9 kJ have been measured. Special construction of the accelerator electrode system enable the electrode shielding by the self-magnetic field resulting in protection from the erosion. Fully predominant N II spectrum is observed in the compression plasma flow during quasistationary phase. The plasma flow velocity and electron temperature maximum values are measured close to 35 km/s and 4 eV, respectively. It was found that electron density values are close to $2 \cdot 10^{16}$ cm^{-3} during discharge quasistationary phase.

1. INTRODUCTION

A quasistationary plasma accelerators are sources of supersonic compression plasma flows in which the duration of the stable state is much longer (~100-1000 μs) then the flight time of the plasma in the acceleration channel (~1 μs) [1]. In these plasma accelerators an ion current transport in the accelerating system occures through the transparent anode [2]. Heavy electrode erosion, which is characteristics of traditional pulsed plasma accelerators, is avoid in the quasistationary plasma systems.

Magnetoplasma compressor (MPC) is the source of quasistationary compression plasma flows (CPF) [1-4]. The importance of research connected with the MPC is in enabling the study of fundamental processes in plasma flows and, also, in application of such systems and their plasma flows in different plasma technologies such as plasma solid surface modification, plasma deposition of the

materials to the sample surfaces etc. Plasma flow parameters optimization with nitrogen as working gas is very important because this plasma accelerating system was used for solid surface modification [5].

2. EXPERIMENTAL SETUP

The MPC used in this experiment was described elsewhere [3,4,6]. In this experiment, CPF parameters have been measured in N_2 + 5% H_2 mixture in the regime of residual gas at 500 Pa pressure. Hydrogen is added because of spectroscopy electrone density measurement. The electrode system is connected through an ignitron with 800 μF capacitor banks at 3.5 kV. Time and space developments of CPF and plasma flow velocity were determined using the photographs obtained by IMACON 790 high speed camera. The electron density and temperature time dependences are obtained from side-on observations. The profiles of spectral lines were obtained by Jobin Yvon HR 320S spectrometer equipped with PI·MAX 1024×256 UV CCD camera gated at 2 μs exposure time and synchronized with the discharge. Spectroscopy measurements of H_β and N II lines radiation from MPC plasma have been performed at eight positions along z axis starting from the outlet of the cathode with 1 cm separation up to 8 cm distance. It gives a possibility to obtain a set of the line profiles, from Balmer beta up to Balmer alpha line in one shot at each positions from the cathode and at each time in order to obtained electron densities and temperatures. Line profiles are scanned from 20 up to 60 μs with 10 μs separation at each position. Calibration of spectroscopy system was made by standard of spectral irradiance (FEL F-000 lamp).

3. EXPERIMENTAL RESULTS AND DISSCUSION

Plasma flow electron density and temperature are measured using spectroscopy methods. Plasma reproducibility was found to be within ±10%. The estimated experimental errors of plasma electron density and temperature measurements are within ±10% and ±15%, respectively. When MPC working with pure nitrogen at 500 Pa pressure, highly predominant spectrum in the CPF radiation is N II spectrum. The axial and temporal distributions of the electron temperature are given in Fig. 1.

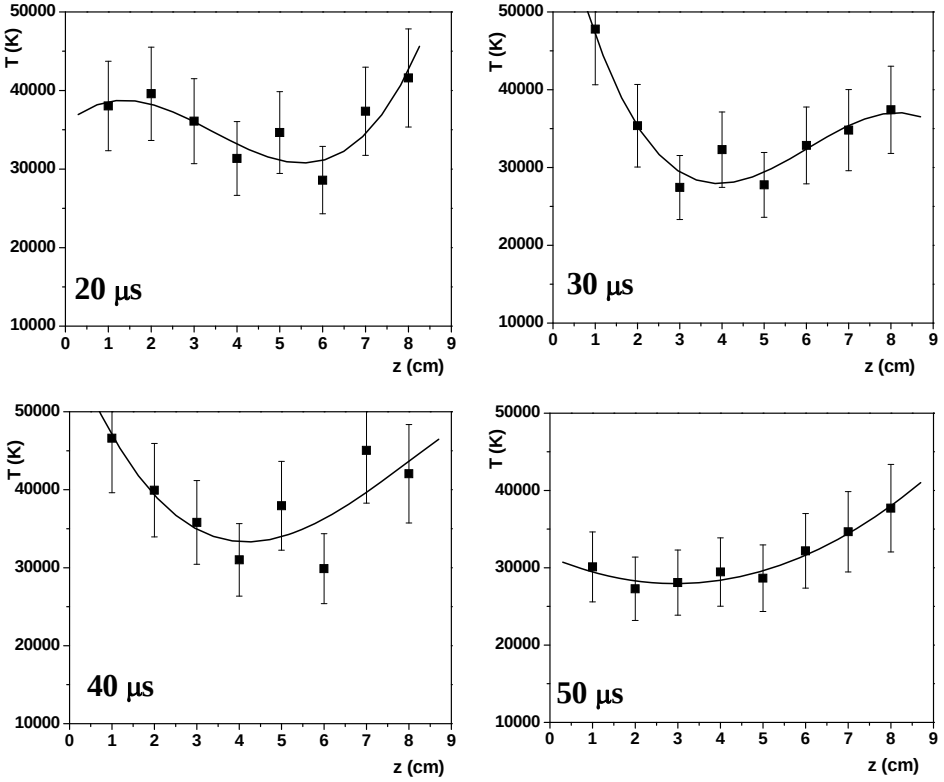

Fig 1. Electron temperature axial and temporal dependences in N_2 + 5%H_2 at 500 Pa pressure.

The electron temperature was measured using a method based on the relative intensity measurements of N II spectral lines, i. e. Boltzman plot. The measurement has been done using the following ten N II spectral lines: 471.8 nm, 478.8 nm, 480.3 nm, 489.5 nm, 504.5 nm, 566.7 nm, 571.1 nm, 589.3 nm, 594.2 nm and 634.7 nm. It was found that during quasistationary phase in the CPF region the average temperature is 35.000 K, what is in good agreement with the results obtained in previous experiments [7,8]. From Fig. 1 one can conclude that two regions can be observed along z axis. One, starting from the top of the cathode up to 3-4 cm, is compression plasma flow. Further from 4 cm is zone of thermalization, because CPF kinetic energy is transformed to thermal energy.

The axial and temporal electron density distributions of the CPF are obtained from the Stark halfwidth of Balmer beta line profiles comparison with theoretically calculated ones [9] and presented in Fig. 2. The profiles were obtained in the single shot.

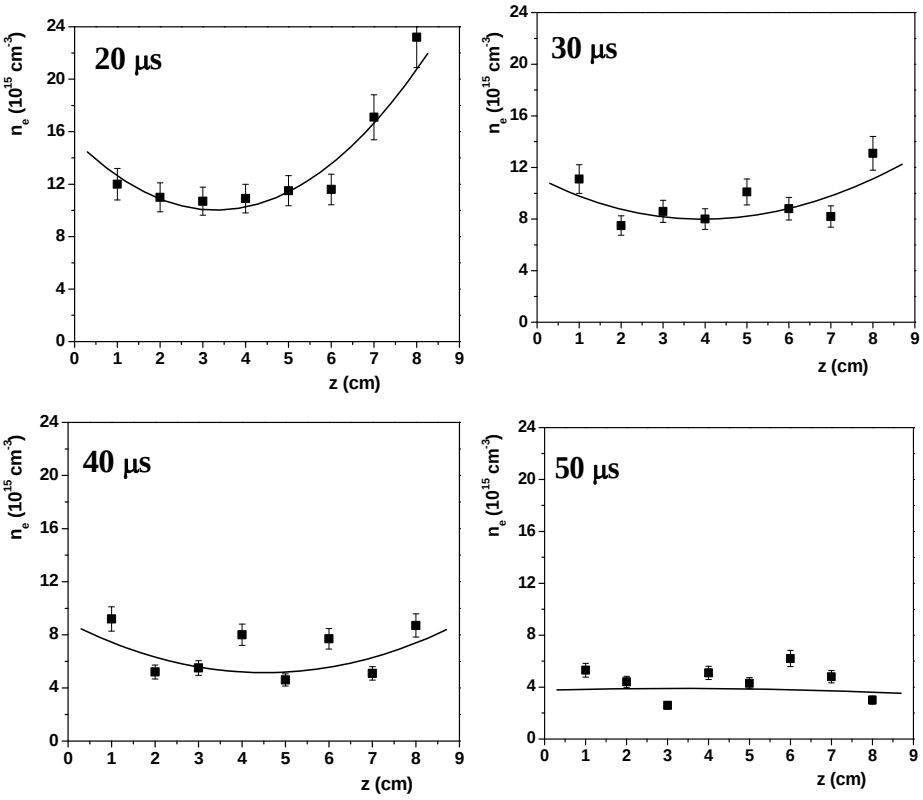

Fig. 2. Electron density axial and temporal dependences in N_2 + 5% H_2 at 500 Pa pressure.

Electron density has maximum at 20 μs and is approximately constant ~10^{16} cm^{-3} within the region up to 4 cm along the z axis with origin at the top of the cathode. For distances larger then 6 cm the higher electron density can be explained by the action of shock wave on the ionization of working gas.

The discharge evolution of MPC was registered by high speed camera. It has been found that the CPF length and diameter in these experimental conditions are about 4 cm and 1 cm, respectively [3]. Plasma flow velocity determined in nitrogen is found to be 35 km/s.

By comparing the obtained electron temperature (Fig. 1) and the electron density axial distribution in time (Fig. 2) one can come to the following conclusions: (i) both distributions have maximum 10-20 μs after the discharge beginning, gradually decreasing later on; and (ii) two regions are observed, one from the top of the cathode up to 3-4 cm along z axis is zone of compression plasma flow and, second, region beyond 4 cm is zone of termalization. During CPF decay, 60-70 μs after the discharge beginning, plasma parameters in this zone are higher than those in CPF.

The advantages of MPC, as compared to other types of accelerators, are high stability of a generated quasistationary compression plasma flows in nitrogen, size and plasma parameters, as well as the discharge time duration sufficient for practical applications (up to 100 μs). During quasistationary phase the continual ionization processes are taking part in working gas introduced into the interelectrode region. The ionized gas (plasma) is steadily accelerated and permanently compressed and within CPF region only this, accelerated, plasma exists. During this phase the plasma flow parameters are slowly changing in time within certain volume. It is a consequence of an ion-drift acceleration of magnetized plasma realised using specially shaped accelerating channel [2].

Beside that, the operation in the ion current transfer mode with the minimization of the electrodes erosion represents an additional and very important advantage of the MPC in comparison with the classical ones. An especially designed electrode system has self magnetic field shielding and it causes a reduction of the electrodes erosion. Also, in order to obtain as pure as possible plasma flow by MPC the ion separation per M/q has to be acheived and therefore the cathode top is shaped as a divertor. If particular ion leave the cathode the high pressure zone (~10 kPa) of the plasma flow push it back into divertor. As a consequence, highly predominant N II spectrum is observed in the CPF during quasistationary phase. Therefore, MPC described here is a favorable one for performing of plasma surface treatment of different materials and for the other plasma technologies.

REFERENCES

1. A.I. Morozov, Sov. J. Plasma Phys., **1**, 95-107 (1975).
2. A.I. Morozov, Sov. J. Plasma Phys., **16**, 69-84 (1990).
3. J. Purić, I.P. Dojčinović, V.M. Astashynski, M.M. Kuraica and B.M. Obradović, Plasma Sources Sci. Technol., **13**, 74-84 (2004).
4. S.I. Ananin et al., Sov. J. Plasma Phys., **16**, 102-112 (1990).
5. J. Purić, V.M. Astashynski, I.P. Dojčinović and M.M. Kuraica, Vacuum, **73**, 561-566 (2004).
6. I.P. Dojcinovic, M.R. Gemisic, B.M. Obradovic, M.M. Kuraica, V.M. Astashinskii and J. Puric, J. Appl. Spectroscopy, **68**, 824-830 (2001).
7. V.M. Astashinskii et al., J. Appl. Spectroscopy, **33**, 629-633 (1980).
8. V.M. Astashinskii et al, J. Appl. Spectroscopy, **40**, 540-545 (1984).
9. M.A. Gigosos and V. Cardenoso, Journal of Phys. B, **29**, 4795-4838 (1996).

VI Serbian-Belarusian Symp. on Phys. and Diagn. of Lab. &
Astrophys. Plasma, Belgrade, Serbia, 22 - 25 August 2006
eds. M. Ćuk, M.S. Dimitrijević, J. Purić, N. Milovanović
Publ. Astron. Obs. Belgrade No. 82 (2007), 229-233 *Contributed paper*

CLEAVAGE OF SILICON SINGLE CRYSTAL SURFACE PRODUCED BY COMPRESSION PLASMA FLOW ACTION

I. P. Dojčinović[1,3], D. Randjelović[2], M. Matić[2],
M. M. Kuraica[1,3], J. Purić[1,3]

[1]*Faculty of Physics, University of Belgrade, POB 368, 11001 Belgrade, Serbia*
[2]*Institute HTM-CMTM, Njegoševa 12, 11000 Belgrade, Serbia*
[3]*Center for Science and Technology Development, Obilićev venac 26, 11000 Belgrade, Serbia*
e-mail: ivbi@ff.bg.ac.yu

Abstract. Modification of silicon single crystal surface by the compression plasma flow (CPF) action is studied. It has been found that during single pulse surface treatment regular fracture features are obtained on the Si (111) and Si (100) surface in the target central part. Some of these regular structures can become free from the underlying bulk, formed as blocks ejected from the surface. These surface phenomena are results of specific conditions during CPF interaction with silicon surface.

1. INTRODUCTION

High-power pulsed energy streams interaction with material surfaces results in surface modification, as well as the material removing from surface in the form of vapor, liquid droplets, or solid flakes due to evaporation, sputtering, ablation, exfoliation etc. High temperatures and consequent thermal stresses, as well as mechanically strained surface during treatment, result in significant deformation and fracture of the layer, induced defects, cracking and exfoliation of the coating. Also, cracks are occurng being characteristic of a molten material which is resolidified very quickly. Surface and interface properties are very important for semiconductor devices and their engineering applications. In this experiment supersonic compression plasma flow (CPF) is used for silicon single crystal surface modification. In central part of treated silicon surface regular fracture features are obtained. It was found that some of these structures as blocks can be ejected from the surface. In the periphery part of silicon samples surface highly oriented periodic cylindrical shaped structures are obtained. Surface cleavage and exfoliation

phenomena, as well as ripple structures formation, as the results of specific conditions during CPF interaction on silicon surface are, also, observed and studied.

2. EXPERIMENTAL SETUP

Si (100) and Si (111) surfaces of single crystal were treated with quasistationary CPF produced by magnetoplasma compressor (MPC). This quasistationary plasma accelerator (plasma gun) is described elsewhere [1-3], therefore only a few details are given here for the sake of completeness. The MPC consists of the specially designed electrode system [1]. Conically shaped cathode of MPC defines the profile of acceleration channel. Using nitrogen as working gas at 500 Pa pressures and 800 μF, 4 kV capacitor bank, the obtained current maximum was up to 100 kA and time duration up to 150 μs with current half period ~70 μs. The continual ionization processes are taking part in working gas introduced in interelectrode region. The ionized gas (plasma) is steadily accelerated and permanently compressed.

The advantages of MPC, as compared to other types of plasma accelerators, are high stability of generated CPF and high plasma parameters (electron density up to $4 \cdot 10^{17}$ cm^{-3} and temperature up to 4 eV), as well as the CPF time duration (quasistationary stable phase is 40-50 μs) and large flow velocity (~40 km/s in nitrogen) sufficient for material surface modification. Beside that, the operation in the ion current transfer mode with the minimization of the electrodes erosion represents an additional and very important advantage of the quasistationary plasma accelerators in comparison with the classical ones. Magnetic flux conservation is a particular characteristic of CPF. During the action of CPF on a sample surface, due to CPF deceleration and frozen-in magnetic field, current loops (vortices) are formed.

For the studies of CPF interaction with silicon surfaces, commercial one-side polished n-type silicon wafers (100 and 111 orientation) 300 μm thick and 10 mm in diameter were used. The sample is mounted on the cylindrical brass holder of the same diameter, and placed in front of the MPC cathode at the distance of 5 cm. Silicon samples are exposed to a single plasma pulse. To investigate the morphology of treated silicon surface, optical microscopy (OM), scanning electron microscopy (SEM) and atomic force microscopy (AFM) were used.

3. RESULTS

OM micrographs of central part of the treated Si (111) and Si (100) surfaces are given in Fig. 1a and Fig. 1b, respectively. Rhombic and triangular regular fracture features are obtained in the case of Si (111) (Fig. 1a), as expected for threefold symmetry. On Si (100) surface treated by CPF, two sets of fracture lines intersecting at 90º form a grid that divides the surface into rectangular blocks (Fig. 1b). Length of a cleavage along crystal planes is up to 1 mm. It is worth to emphasize that, in the same conditions, the length of cleavage lines at Si (100)

surface is much larger than one at Si (111). SEM micrographs of the treated Si (100) surfaces are given in Fig. 2a. On the central part of the sample, some of the blocks are ejected from the surface, and large holes at the surface emerged. In this case development of subsurface fracture, parallel to the surface, is occured. Thickness of these blocks is about 10 μm. A typical hole is shown in Fig. 2a. In order to determine cleavage plane, treated silicon surface is observed by atomic force microscopy. AFM micrographs of treated Si (100) surfaces are given in Fig. 2b. Surface profile indicates cleavage along crystal plane. Cleavage height in this figure is (1.3 ± 0.1) μm. Estimated angle between Si (100) surfaces and cleavage plane is (54 ± 3)º. This indicates that cleavage plane is Si (111).

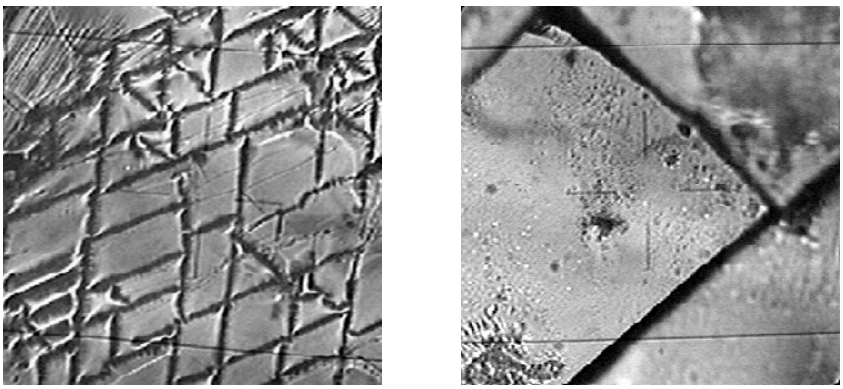

a) **b)**

Fig 1. OM micrograph of silicon single crystal surface after CPF treatment: a) Si (111), image size 100 × 100 μm^2, b) Si (100), image size 50 × 50 μm^2.

The formation of observed surface features may be explained by energetic action of CPF on the surface (absorbed energy 10-15 J per pulse, flow power density ~1·10^5 W/cm^2 [4]). Interaction of CPF with silicon sample surface causes the evaporation of a thin surface layer and formation of a shock-compressed plasma layer (plasma plume) [5]. Formation of this cloud of dense target plasma results in the shielding of a processed surface from a direct action of a CPF and surface protection from further excessive evaporation. A thickness of shock-compressed plasma layer is about 1 cm. Using the high speed camera, time of interaction was estimated to be ~40 μs [5].

Energetic action of CPF causes the fast heating and melting of the surface layer and the presence of high dynamic pressure of CPF of the order of several atmospheres [4]. Namely, CPF kinetic energy thermalization causes the heating of target surface and high gradient of thermodynamic parameters occurred.

Formation of regular fracture features (Figs. 1,2) can be explained by considerable fraction of the absorbed plasma flow energy trapped into fractures rather than converted to heat energy [6]. Single crystal silicon is well known as a

typical anisotropic material and it is very brittle at room temperature [7]. Similar to silicon surface cleavage, obtained in this experiment, laser interactions with MgO single crystal caused regular fracture features [6]. Plastic deformation in MgO typically involves the growth of a relatively few dislocations that form extremely long, convoluted structures known as dislocation "multiplication". During laser interaction with MgO (111) surface triangular features are typical fracture patterns.

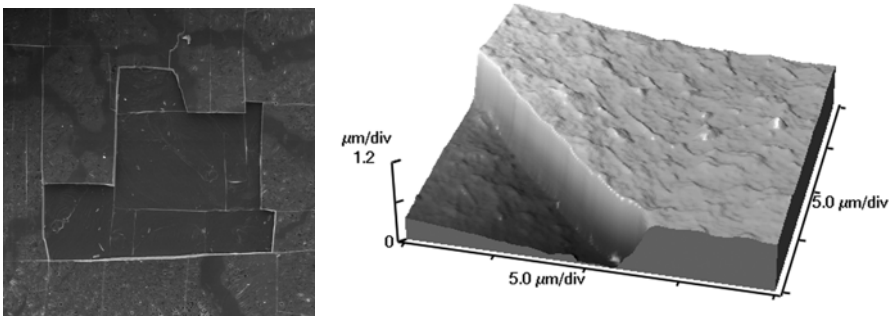

a) **b)**

Fig. 2. a) SEM micrograph of a typical fracture features and holes on the treated Si (100) surface, image size 800 × 800 μm^2; b) AFM three-dimensional view of the Si (100) surface morphologies after CPF treatment.

The anisotropy of crack propagation direction from energetic point of view is explained with Griffith criterion [8]: in equilibrium, the mechanical energy released upon crack advance must be in balance with the energy required to create the two new surfaces. This is a necessary condition for fracture and leads to conclusion that crystal lattice planes with low surface energies are energetically favored as cleavage planes. The lowest energy cleavage planes in silicon are the {111} planes.

When a silicon single crystal is loaded to fracture, the cracks tend to initiate along a family of favoured crystallographic planes. In the case of plasma flow treatment of Si (100) surface, favoured cleavage planes are Si {111}, as are given in Fig. 2b. Angle between Si (100) surface and cleavage Si (111) plane is 54.74^o.

Low adhesion between blocks and silicon bulk, and eventual ejection of blocks from the CPF treated surface (Fig. 2), can be explained by development of subsurface fracture, parallel to the surface. Cracking between the block and the bulk is growing due to local energy absorption.

4. CONCLUSION

Regular fracture features and exfoliations are observed on silicon single crystal surface treated by CPF. Surface modification is performed by fast heating of the surface in the presence of high dynamic pressure, thermodynamic parameters gradients and induced magnetic field from the CPF. During surface treatment and fast cooling phase, differential stresses in surface layer occurred. As the results of all

of these processes rhombic and rectangular regular fracture features are obtained on the Si (111) and Si (100) surface, respectively. Some of these blocks are ejected from the surface.

REFERENCES

1. J. Purić, I.P. Dojčinović, V.M. Astashynski et al., Plasma Sources Sci. Technol.**,** **13**, 74-84 (2004).
2. I.P. Dojčinović, M.M. Kuraica, B.M. Obradović, N. Cvetanović and J. Purić, Plasma Sources Sci. Technol., **16**, 72 (2007).
3. I.P. Dojcinovic, M.R. Gemisic, B.M. Obradovic et al., J. Appl. Spectroscopy**, 68,** 824-830 (2001).
4. V.V. Uglov, V.M. Anishchik, V.V. Astashynski et al., Surf. Coat. Technol.**, 158-159**, 273-276 (2002).
5. J. Purić, V.M. Astashynski, I.P. Dojčinović and M.M. Kuraica, Vacuum, **73**, 561-566 (2004).
6. R.L. Webb, L.C. Jensen, S.C. Langford and J.T. Dickinson, J. Appl. Phys. **74**, 2323-2337 (1993).
7. J.A. Hauch, D. Holland, M.P. Marder and H.L. Swinney, Phys. Rev Lett.**, 82**, 3823-3826 (1999).
8. A.A. Griffith, Philos. Trans. R. Soc. London A, **221**, 163 (1921).

VI Serbian-Belarusian Symp. on Phys. and Diagn. of Lab. &
Astrophys. Plasma, Belgrade, Serbia, 22 - 25 August 2006
eds. M. Ćuk, M.S. Dimitrijević, J. Purić, N. Milovanović
Publ. Astron. Obs. Belgrade No. 82 (2007), 235-240 *Contributed paper*

PROPERTIES OF DIAMONDLIKE CARBON FILMS DEPOSITED ON SILICON, QUARTZ AND GLASS SUBSTRATES USING LASER PLASMA DEPOSITION

V. Goncharov, D. Ismailov, S. Petrov, M. Puzyrou

Scientific-Research Institute of Applied Physical Problems,
Kurchatova 7, 220064, Minsk, Belarus,
e-mail: puzyrev@bsu.by

Abstract. Investigation of diamondlike carbon films using Raman spectroscopy method has showed, that deposited coatings according to substrate material can show graphite, nanocrystalline carbon or amorphous diamondlike carbon films' properties with the content of sp^3 hybridized carbon atoms of ~20 %.

1. INTRODUCTION

Nanostructured diamondlike films have been the object of intensive study for world scientific community for several decades. This interest is caused mainly by two basic directions of use of diamondlike structures: in electronics and as a protective coating. The first direction includes exploration of ways to create low-voltage and highly stable autoelectronic emitters for flat displays and microwave vacuum electronic devices [1], this is mainly caused both by the presence of a low emission threshold and MIS structures, thin-film transistors for solar elements, electromechanical structures on the basis of diamondlike carbon coverings building [2] with the purpose of practical realization of diamond semi-conductor electronics. The second direction is based on high durability and wear resistance of diamondlike coverings, besides they possess low friction coefficient, high heat conductivity and chemical inertness. It makes them very attractive for use as coating for critical mechanical technical units, and for magnetic storage devices [3]. The high transparency in visible and IR-range allows to use carbon films for mechanical protection of optical elements.

Properties of carbon films depend on several parameters characterizing their structure and composition. For pure carbon films, obtained using laser plasma vacuum deposition, such main parameters are the ratio of the sp^3/sp^2 bonds content and a measure of orderliness of carbon atoms in a film and clusterization degree. [4]

It is known that physical properties of substance can cardinally change when transition to nanostuctured state takes place. In particular such law can be observed during formation of diamondlike carbon films. It is related to great variety of phase microstructural organizations in these films, having different forms and sizes that compose the film of carbon nanoclusters. These clusters possess unique quantum-dimensional and other properties depending on formation conditions. For example, it is known, that emission properties of diamondlike films are improved considerably with increase of defectiveness upto formation of an amorphous material which essential attribute is a diamond hybridization type of valent electrons pertinent to carbon atoms [5].

Recently a set of techniques for obtaining diamondlike carbon coatings is in use. Among them are deposition using vacuum-arc discharge [6,7], chemical-plasma deposition [6,8] or magnetron beam deposition. Every method has its own advantages and disadvantages.

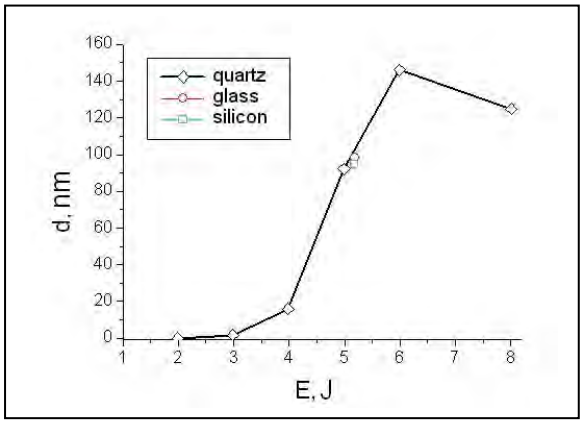

The number of laser pulses – 100, the temperature of the substrate - 225 °C.

Fig. 1. Thickness of a diamondlike film dependence on acting laser radiation energies for different types of substrates

Use of lasers as an energy source for graphite evaporation has a number of advantages such as process purity (there are no impurity gases), high accuracy and productivity. Use of pulse lasers makes vacuum requirements less rough due to short time of interaction.

2. EXPERIMENTAL

The diamond-like carbon films were deposited by laser ablation of graphite, using Nd-glass laser (λ=1.06 μm). The pulse laser duration was 30 ns. Films were deposited in vacuum. The pressure was 10^{-3} Pa. The graphite target had angle 45 degree to the axis of the acting laser radiation. Substrates were placed in parallel to

the graphite target. The distance from a target to a substrate was 10 cm. A system heating substrates was used during deposition. A Spectroscopic Ellipsometry, Rutherford Back-Scattering **(RBS)** and Raman Spectroscopy systems have been used to analyze the obtained films' properties.

3. RESULTS AND DISCUSSION

Some parameters of diamondlike carbon films such as optical transparency or coefficient or microhardness can significally depend on thickness of deposited coating. Therefore measurements of diamondlike carbon (DLC) films' thicknesses have been carried out depending on energy of acting laser radiation and substrate material. Films' thickness was measured by ellipsometry method using WVASE ellipsometer. Films were deposited on quartz, glass and silicon substrates. Corresponding to a range of influencing laser radiation energy of 2 – 8 J films were deposited on quartz substrates. The figure 1 shows that thickness significantly changes for different laser radiation energies. Besides, measurements have shown, that thickness of (DLC) films, deposited on silicon, glass and quartz substrates using the same laser energy of 5 J actually does not depend on substrate type.

In order to determine layer content of carbon atoms in samples, obtained under different conditions of films' deposition, the Rutherford He+ ions Back-Scattering method (RBS) was used [9]. Films were deposited on silicon substrates having <110> orientation.

Substrate temperature, number of laser pulses and vacuum level in the vacuum chamber had been varied during the experiment. Results are shown in Table 1. Energy of acting laser radiation was equal to 5 J. Calculations were carried out using a method that includes computer plotting of a reference spectrum and its subsequent adjustment in the area under the carbon peak in an experimental spectrum to perfect match.

Table 1. Layer content of carbon atoms in diamondlike films deposited on silicon substrates. The energy of acting laser radiation amounts to 5 J.

№	Number of pulses	Vacuum, Torr	Temperature, K	Layer content of carbon atoms, cm-2
1	100	$2•10^{-5}$	498	$1{,}15•10^{18}$
2	100	$2•10^{-5}$	373	$3{,}5•10^{17}$
3	100	$8•10^{-6}$	293	$2{,}0•10^{17}$
4	100	$1•10^{-3} – 7•10^{-4}$	293	$1{,}9•10^{17}$
5	380	$2•10^{-5}$	293	$1{,}7•10^{17}$

Indication of layer content in the table instead of film thicknesses is related to the feature of method RBS in which ions with energies about MeV order of magnitude are used as an analyzing beam, it makes the method insensitive to the nature of chemical bounds and the electronic structure of the investigated material.

Having assumed that the nuclear density of obtained films is approximately equal to nuclear density of diamond that comes to $1{,}76\ 10^{23}$ cm^{-3}, it is possible to

estimate films' thickness for samples shown in table 1. It comes practically to 10 – 65 nanometers [9].

Additional research of obtained films' structure is made using the method of Raman spectroscopy. In our case parameters of the film deposited on silicon, glass and quartz substrates were investigated. Energy of acting laser radiation was 5 J. All substrates were heated to temperature of 498 K. Residual gases pressure in the vacuum chamber was $2 \cdot 10^{-3}$ Pa. Obtained Raman spectra were processed using Lorents curves approximation.

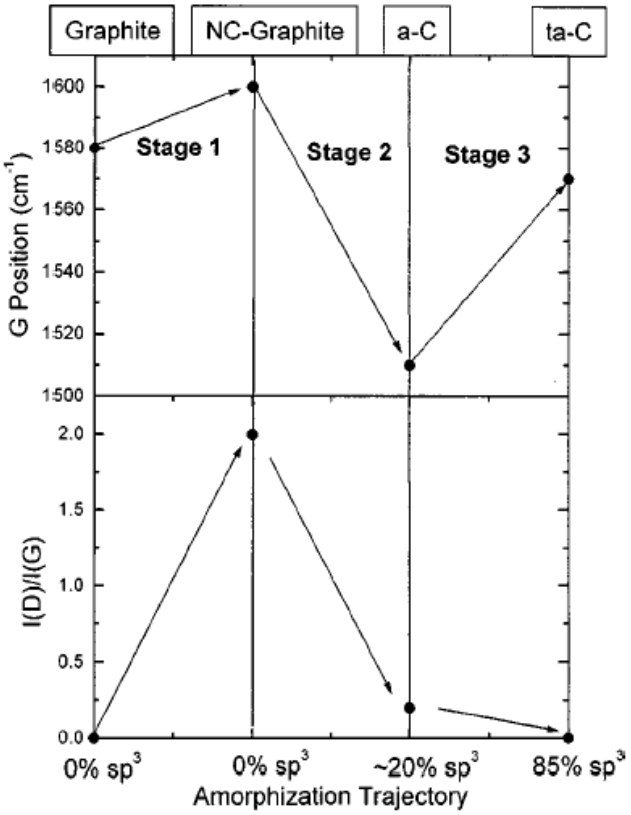

Fig. 2. The trajectory of carbon transition from graphite to tetrahedral amorphous state with contingent schematic variation of G-peak position and I_D / I_G ratio [10].

Most of amorphous carbon experimental Raman spectra can be interpreted by phenomenological three-stage model [4] that defines transition of carbon from graphite to tetrahedral carbon (ta-C). This process consists of three stages as shown on figure 2:

a) graphite → nanocrystalline graphite (nc–C);
b) nanocrystalline graphite → amorphous carbon (a–C);
c) a–C → ta–C (→ ~ 100 % sp^3, defective diamond).

Let's consider change of G-peak position and I_D/I_G ratio corresponding to obtained films (Table 2).

Table 2. Results of Raman scattering spectra processing using Lorentz curves approximation

I_D, cm^{-1}	I_G, cm^{-1}	I_D/ I_G
Glass		
1350	1579	0,57
Quartz		
1327	1544	0,42
Bronze		
1330	1529	0,86
Silicon		
1430	1561	0,72

As we can see from the table 2 structure of the film deposited on a glass substrate lies on boundary of graphite structure to nanocrystalline graphite structure transition. Films deposited on quartz, bronze and silicon substrates are characterized by transitional structure between nanocrystalline graphite and amorphous carbon film and the sp^3 carbon atoms content amounts to 10 – 20 %.

It should be noted separately that obtained spectra contain pronounced peaks near 1332 cm^{-1} that correspond to natural diamond peaks [10].

4. CONCLUSIONS

It is experimentally shown that the material of a substrate has weak effect on thickness of deposited diamondlike films. Films thicknesses depend on both energy of laser radiation affecting graphite target and substrate temperature. Films' thicknesses obtained by the ellipsometry method are consistent with the thicknesses measured on basis of mathematical processing of obtained Rutherford Back Scattering spectra.

REFERENCES

1. А.Н. Гладкий, С.Ю. Суздальцев, Р.К. Яфаров, ЖТФ, **70**, 133 – 135 (2000).
2. W. I. Milne, Electronic devices from diamond-like carbon Semiconductor science and technology **18**, 81 (2003).
3. V.U. Uglov, A.K. Kuleshov, D.P. Rusalsky, J.I. Onate, Si-Ze Yang, Surface and coatings technology **128, 129**, 150–155 (2000).
4. A.C. Ferrari, J.Robertson, Physical review., **61**, No. 20, 14095–14105

5. А.П. Семенов, А.Ф. Белянин, И.А. Семенова, П.В. Пащенко, Ю.А. Барнаков, ЖТФ, Т. 74, Вып. 5, 101 – 104 (2004).
6. И. Поло, Ф. Тьерри, Ж. Пелетье, В.В. Углов, А.К. Кулешов, М.П. Самцов, В.М. Амнищик, Н.Н. Череда, С.Н. Дуб, Перспективные материалы, № 5, 13–19 (2002).
7. Youshiyuki Show, Mitso Iwase, Tomio Izumi, Thin Solid Films, **274**, 50-54 (1996)
8. А.Н. Гладкий, С.Ю. Суздальцев, Р.К. Яфаров, ЖТФ, Т. 70, Вып. 5, 133–135 (2000).
9. Бойко Е.Б., Гончаров В.К., Лагутин А.Е, Петров С.А., Пузырев М.В., Мат. 6-ой межд. конф. "Взаимодействие излучений с твердым телом". Минск, Беларусь, 28-30 сентября 285-287 (2005).
10. Горелик В.С. Современные проблемы спектроскопии комбинационного рассеяния света Под ред. М.М. Сущинского. М.: Наука, 28-47 (1978).

VI Serbian-Belarusian Symp. on Phys. and Diagn. of Lab. &
Astrophys. Plasma, Belgrade, Serbia, 22 - 25 August 2006
eds. M. Ćuk, M.S. Dimitrijević, J. Purić, N. Milovanović
Publ. Astron. Obs. Belgrade No. 82 (2007), 241-243 *Contributed paper*

ASTEROID CLOSE ENCOUNTERS WITH (704) INTERAMNIA

A. Kovačević

Department of Astronomy,Faculty of Mathematics,Belgrade
andjelka@matf.bg.ac.yu

Abstract.Interamnia is the seventh largest known asteroid with an estimated diameter larger than 300 km and was discovered (surprisingly late for such a large object) on October 2, 1910 by Vincenzo Cerulli. The technique of asteroid mass determination from perturbation during close approach requires as many as possibledifferent close approaches in order to derive reliable mass of a perturber. Here is presented list of newlyfound close encounters with the asteroid (704) Interamnia which could be used for its mass determination..

1. INTRODUCTION

The number of papers devoted to mass determinations of large asteroids is raising in recent years.There are several facts that influenced such a determination-the discovery of satellites of asteroids (e.g. [1, 2]), measurements by space probes that visited asteroids [3] and growing number of astrometrical measurements with increased precision [4].

As is well known, the method of minor planet mass determination that considers gravitational perturbations produced by asteroid on other bodies during mutual close encounter was developed first.

The aim of this paper is to introduce close encounters suitable for mass determination of seventh largest asteroid (704) Interamnia by astrometric methods.

2. SELECTION PROCESS

The initial osculating orbital elements for epoch JD 2451600.5, were taken from E. Bowell database (http://www.lowell.edu/users/elgb/). Perturbations due to all planets, Moon and seven largest main belt asteroids were taken into account. The

numerical integration of differential equations of motion of perturbed bodies is carried out by Everhart code.

The close encounters between (704) Interamnia and 12970 numbered main-belt asteroids for the period 1996-2054 were investigated. For searching of the close encounters a multistep selection procedure was applied that consists in the following:

- by means of a simple geometrical consideration the minimum possible distances between pairs of asteroid orbits were found
- by using two-body dynamics it was checked for a given pair whether such an approach might occur within the given period.
- a numerical integration in the framework of a dynamical model which include major planets and four largest asteroids was performed to determine the parameters of the close encounters.

Each of this steps significantly reduces the number of potential interesting cases of close encounters

3. RESULTS AND DISCUSSION

As a result of our procedure, we found 8 perturbed asteroids due to gravitational influence of the mass of (704) Interamnia. In order to calculate dynamical characteristics of close encounters we used its estimated (based on IRAS data) mass $2.40 \cdot 10^{-11}$ M sun . Geometrical and kinematical parameters of these close encounters between perturbing body Interamnia (Ast. 1) and perturbed (Ast. 2) asteroids are given in Table 1, where:

JD - the moment of the closest encounter
ρ - the minimum distance
Vr - the relative velocity
θ - the angle of deflection
ΔV_2 - the velocity change of the perturbed body

Table 1.: Geometrical and kinematical parameters of close encounters.

Ast.1	Ast. 2	JD	ρ[AU]	V_r [kms^{-1}]	θ["]	ΔV_2 [kms^{-1} x 10^{-9}]
704	651	2457499.0	0.005434	6.808	0.04	1170
704	977	2453653.8	0.009134	9.545	0.01	497
704	1467	2451214.0	0.006471	4.687	0.06	1427
704	1484	2458351.4	0.006955	11.854	0.01	524
704	6001	2450621.3	0.009895	6.327	0.02	691
704	7152	2461553.5	0.008935	6.002	0.03	807
704	7461	2450599.5	0.007481	5.300	0.04	1092
704	10034	2451851.2	0.008073	3.497	0.09	1533

The close encounters that occurred between the seventh largest body in main asteroid belt and recorded asteroids have some common characteristics.

The relative velocities are particularly high (greater than 5kmsec^{-1}) implying that these close encounters are not long lasting. As can be seen from Table

1, the minimum distances are small (lower than 0.01 AU). Consequently, gravitational influence (Table 2) of (704) Interamnia on these perturbed asteroids is not significant.

However, it could be seen that its close encounter with (1467) Mashona exhibits significant gravitational effects.

Table 2.: Dynamical parameters of close encounters. Absolute values of gravitational effects for all selected close encounters in right ascensions ($\Delta\alpha$) and declinations ($\Delta\delta$).

Ast.1	Ast. 2	$\Delta\alpha$ ["]	$\Delta\delta$ ["]
704	651	2.50	1.25
704	977	1.00	0.40
704	1467	6.05	3.24
704	1484	0.68	0.50
704	6001	0.30	0.10
704	7152	1.80	0.70
704	7461	1.04	0.35
704	10034	2.00	1.00

The relative velocity is low. Combining this fact with small value for minimum distance it was not surprising that gravitational influence is significant. Among found perturbed bodies, the four of them are high numbered. Namely, their designation is larger than 5000. It means they are relatively faint objects.

4. CONCLUSION

The most suitable geometrical, kinematical and dynamical parameters are exhibited in the case of close encounter with (1467) Mashona. It could be useful for mass determination of (704) Interamnia.

The cases of close approaches with bodies (6001), (7452), (7461) and (10034) indicate the existence of other close encounters of Interamnia with faint objects with similar dynamical characteristics, which could be observed by ESA astrometric mission GAIA during the next decade. Using faint objects will provide an enlargement of the number of close encounters and perturbed asteroids suitable for asteroid mass determination.

REFERENCES

1. M.E. Brown, J.L. Margot, IAUC, 7588 (2001)
2. A. Storrs, F. Vilas, R. Landis, et al, IAUC , 7599 (2001)
3. P.C. Thomas, J. Veverka, J.F. Bell, et al., Icarus, **140**, 17 (1999)
4. G. Michalak, A&A, **374**, 703 (2001)

VI Serbian-Belarusian Symp. on Phys. and Diagn. of Lab. &
Astrophys. Plasma, Belgrade, Serbia, 22 - 25 August 2006
eds. M. Ćuk, M.S. Dimitrijević, J. Purić, N. Milovanović
Publ. Astron. Obs. Belgrade No. 82 (2007), 245-250 *Contributed paper*

ОСОБЕННОСТИ ДВИЖЕНИЯ КРУПНЫХ ЧАСТИЦ В КОМЕТНЫХ АТМОСФЕРАХ. ЧАСТЬ 1

(PARTICULARITIES OF LARGE PARTICLE-MOTION IN COMETARY ATMOSPHERES. PART 1)

О. П. Кузнечик, В. Н. Горенков, В. О. Кузнечик

Белорусский государственный университет, Обсерватория,
4, Пр.-т Независимости, г. Минск, 220030, Беларусь
E-mail: kuznechik@bsu.by

Abstract. The analysis of the motion of the largest particles in cometary atmospheres with the dimensions of the order of centimeter was performed. Their velocities in the atmospheres as a function of initial conditions are obtained.

1. ВВЕДЕНИЕ

В работе [1] была выявлена возможность возникновения состояния устойчивого равновесия твердых частиц в кометных атмосферах. Оказалось, что для слабозапыленной атмосферы кометы при различных состояниях поверхности ее ядра все пылинки могут быть классифицированы по размерам на три типа (I, II, III) в зависимости от их фазового изображения. Начальная скорость и размер являются параметрами, которые полностью определяют траекторию пылинки постоянной массы.

Из выделенных трех типов особый интерес представляют самые крупные частицы сантиметровых размеров (тип III). На фазовом изображении этих частиц [1] видны две особые точки, вторая из которых – точка устойчивого равновесия – находится дальше от ядра. Траектории частиц этого типа наиболее разнообразны. Наличие в атмосфере кометы точек устойчивого равновесия указывает на возможность появления частиц, колеблющихся вокруг положений равновесия, и частиц, медленно двигающихся в сторону ядра после поворота на больших расстояниях от него. Такие особые траектории требуют более детального рассмотрения, поскольку это может привести к появлению в

атмосфере фрагментов с очень большим временем жизни. К тому же часть пылинок может накапливаться в зоне точек устойчивого равновесия. Ввиду особого значения начальной скорости частиц проведен анализ их скорости выхода из пристеночного слоя кометного ядра в случае плоского слоя для сферически-симметричного радиального течения газа с твердыми фрагментами в узком угловом диапазоне вокруг направления комета – Солнце. Для этого случая приведены результаты исследования динамики твердых частиц типа III. Получены их скорости движения в атмосфере в зависимости от начальных условий.

2. НАЧАЛЬНЫЕ УСЛОВИЯ ДЛЯ ПЫЛЕВЫХ ЧАСТИЦ

Для слабозапыленной кометной атмосферы, начальная скорость пылинки является основным параметром определяющим ее траекторию в атмосфере кометы [1]. Значения начальных скоростей пылинок V_0 зависят от механизма их появления. Если рассматривается движение мелких минеральных или органических пылинок, то их появление в атмосфере кометы связано с их высвобождением из матричного вещества ядра в результате сублимации [2]. В этом случае можно ожидать, что скорость такой пылинки при выходе с поверхности ядра V_s будет близка к нулю. Однако это не означает, что течение газопылевой смеси в запыленной атмосфере или движение пылинок в слабозапыленной атмосфере можно расчитывать при нулевых начальных скоростях последних. Поскольку при расчете течения газа начальные условия следует накладывать на внешней границе пристеночного слоя, как это было сделано в работах [1, 3], то и для пылинок скорость необходимо задавать там же. Эта начальная для газодинамической задачи скорость V_0 связана с температурой и состоянием поверхности ядра, а также с размером и структурой самой пылинки. Для крупных твердых частиц, кроме этого, необходимо исследовать зависимость V_0 от стартовой скорости, так как механизм их появления в пристеночном слое может существенно отличаться от механизма появления мелких пылинок.

Значение скорости твердой частицы на выходе из слоя можно получить на основе общей методики определения импульса, переданного частице газом с известным законом распределения молекул по скоростям [4]. Для получения распределения молекул по скоростям можно воспользоваться подходом, предложенным в работе [4], когда внутри кнудсеновского слоя неизвестная неравновесная функция распределения аппроксимируется взвешенной суммой двух известных функций распределения, одна из которых соответствует внутренней границе пристеночного слоя, а вторая — внешней. Весовые коэффициенты можно определять как линейную [3] или экспоненциальную функции расстояния до поверхности сублимации. С помощью такой методики в работе [3] для мелких пылинок получены результаты, свидетельствующие об определяющем влиянии температуры поверхности на скорость выхода пылинок из пристеночного слоя. При моделировании дальнейшего движения пылинок в околоядерной области был

сделан вывод о незначительном влиянии скоростей выхода на скорость движения при удалении от ядра. Исходя из наших исследований, мы считаем, что полученные в работе [3] результаты ограничены размерами пылинок: они справедливы только для части наиболее мелких пылинок типа I, для которых в атмосфере кометы можно пренебречь гравитацией ядра, и в движении которых нет особых точек. Уже для более крупных частиц типа II траектории, а значит и скорость в околоядерной области, могут принципиально отличаться при небольшой разнице в начальных скоростях. Так, при изменении начальной скорости V_0 от 29 см/с до 30 см/с траектория описывает либо падающую на ядро частицу размером 2.5 см, либо уходящую в область ускоренного движения. Заметим, что такая структура поля направлений, когда траектория в зависимости от скорости изменяется скачком, характерна для особых точек типа «седло», к которым относятся положения точек ветви возрастания относительно ядра OT1 [1].

Учитывая, что положение особых точек в голове кометы изменяется в процессе ее орбитального движения, для крупных твердых частиц необходимо исследовать начальные скорости в широком диапазоне их размеров и для различных гелиоцентрических расстояний. Сантиметровые частицы принципиально отличаются от субмикронных тем, что при расчете их движения следует учитывать гравитацию. Кроме того, наиболее крупные из них должны выделяться с поверхности ядра со скоростью V_s, больше нулевой, поскольку, скорее всего, являются его фрагментами и могут появляться только в результате разрушения поверхностного слоя. Механизмы разрушения, при которых частицы образуются с начальным импульсом, неоднократно рассматривались рядом авторов, например, в связи с исследованиями состояния кометных льдов [5], поверхности ядра [6] или вспышечной активности комет [7].

Для определения начальных скоростей было принято, что на внутренней границе пристеночного слоя темп сублимации определяется законом Герца – Кнудсена, распределение молекул по скоростям полумаксвелловское с температурой T_s равной температуре поверхности сублимации [3, 4], что справедливо при отсутствии пористой коры. На внешней границе – распределение локально-максвелловское с температурой, равной начальной температуре газодинамической задачи $T_0 = T_s\,\Delta T$, где ΔT – скачок температуры. Обратный поток молекул тоже локально-максвелловский с температурой T_0 и слабее прямого с коэффициентом η от 0.14 до 0.25, у нас он равен 0.20 [1]. При таких условиях уравнение движения фрагмента внутри пристеночного слоя можно записать в виде

$$m_d \frac{dV}{dt} = [F(0, T_s) - F(0, T_0)](1 - K_x) + F(H, T_0)K_x - F_g, \qquad (1)$$

где m_d, V – масса и скорость пылинки, $F(0, T_s)$, $F(H, T_0)$ – силы увлечения пылинки прямым потоком газа на внутренней и внешней границах слоя, $F(0, T_0)$ – сила у поверхности, обусловленная обратным потоком молекул, $K_x = x/H$ – весовой коэффициент линейной аппроксимации, x – расстояние от

поверхности сублимации, H – толщина пристеночного слоя, F_g – сила гравитационного притяжения ядра.

Для скачка параметров в кнудсеновском слое мы используем значения [3] справедливые для плоского слоя. Силы, входящие в уравнение (1), созданы потоками молекул. При однородной толщине слоя сублимации эти потоки обладают симметрией относительно перпендикуляра к поверхности. В этом случае тангенциальные составляющие сил, действующих на фрагмент, зависят только от расстояния до поверхности. Если стартовая скорость пылинки имела тангенциальную составляющую, то в пристеночном слое это никак не повлияет на нормальную составляющую. Поскольку в создании равновесия частицы тангенциальная составляющая силы непосредственно не участвует, то в кнудсеновском слое уравнением (1) можно описывать движение фрагмента, нормальное к поверхности сублимации, где V – нормальная составляющая вектора скорости. Соответственно вместо векторов сил можно брать их нормальные составляющие. Далее приводятся соотношения и результаты, характеризующие именно нормальное движение.

Коэффициент увлечения пылинки потоком газа в случае максвелловского распределения известен, для полумаксвелловского он был получен в предположении смешанного (зеркального плюс диффузного) закона распределения отраженных молекул [3]. Здесь, как и в предыдущей работе [1], мы использовали косинус-максвелловский закон распределения отраженных молекул по скоростям. Он приводит только к изменению по отношению к работе [3] числового коэффициента [4]. Силы, действующие на пылинку, запишутся в виде

$$F(0, T_s) = \rho_s \pi \alpha^2 k T_s [3/4 + 2/3(T_r / T_s)]^{1/2}, \quad (2)$$

$$F(H, T_0) = \rho_0 \pi \alpha^2 (u_0 - V)^2 C_d / 2, \quad (3)$$

$$F(0, T_0) = \eta \rho_0 \pi \alpha^2 (u_0 - V)^2 C_d / 2, \quad (4)$$

$$C_d = 4/3\pi^{1/2}(T_r T_0)^{1/2}/s + (2s^2+1)\exp(-s^2)/(\pi^{1/2}s^3) + (4s^4+4s^2-1)\mathrm{erf}(s)/(2s^2), \quad (5)$$

где

$$\mathrm{erf}(s) = \frac{2}{\sqrt{\pi}} \int_0^s \exp(-\varsigma^2) d\varsigma, \quad s = \left|\bar{u} - \bar{V}\right| / \sqrt{2kT/m},$$

m – масса молекулы, ρ, и ρ_0 – плотность газа на внутренней и внешней границах пристеночного слоя, u – скорость газа, u_0 – скорость газа на внешней границе. Температура пылинки принята равной температуре ядра T_s, T_r – температура отраженных от пылинки молекул [1, 4]. Здесь вторая и третья силы записаны с учетом движения пылинки, а первая сила, как и в работе [3], соответствует неподвижной пылинке, что является здесь достаточным приближением, поскольку пристеночный слой тонок.

Используя приведенную методику, мы рассчитали ряд зависимостей, характеризующих движение сантиметровых фрагментов в пристеночном слое на разных расстояниях от Солнца. Рис. 1 представляет значение скорости V_0

выхода частицы из слоя в зависимости от стартовой скорости V_s на поверхности ядра кометы на расстоянии R_h = 2 а.е. от Солнца. Видно, что частицы, размер которых меньше некоторого критического $\alpha_{кр}$ (в данном случае $\alpha_{кр}$ = 1 см), выходят из слоя ускоряясь, а размером больше – с торможением. Первые частицы достигают газодинамической области даже при нулевых стартовых скоростях, вторые – нуждаются в начальном импульсе. Если стартовая скорость достигает десятков сантиметров за секунду, то для всех размеров скорость выхода в газодинамическую область V_0 практически равна скорости старта V_s. Дальнейшее увеличение стартовой скорости до метра за секунду практически ведет к нивелированию зависимости скорости выхода фрагмента в газодинамическую область от размера. Зависимость для значения $\alpha_{кр}$ проведена пунктирной линией, частицы этого размера всегда выходят из слоя со скоростью V_s. Это означает, что наибольшими фрагментами, которые попадают в газодинамическое течение без начального импульса на поверхности ядра (V_s = 0), являются частицы размером $\alpha_{кр}$. Отметим, что этот размер вдвое меньше, чем критический на поверхности ядра, определяемый из условия равенства силы гравитационного притяжения и подъемной силы газа.

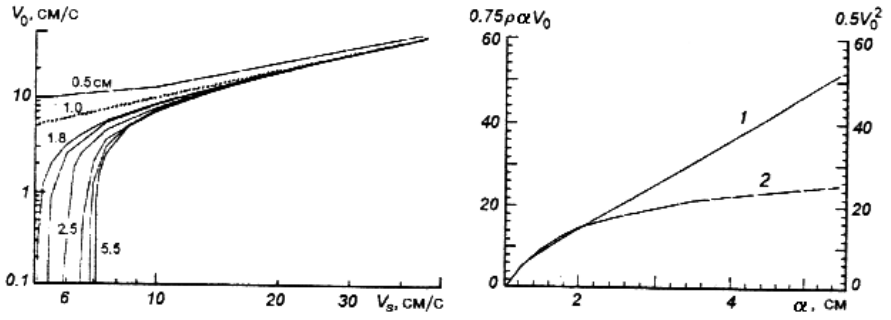

Рис. 1. Зависимость скорости выхода пылинок из пристеночного слоя от стартовой скорости на поверхности ядра. Размер пылинок проставлен возле кривых при плотности 1 г $см^{-3}$. (Свободная поверхность сублимации; R_h = 2 а.е.)

Рис. 2. Значения наименьшего стартового импульса (1) частицы, нормированного на ее площадь сечения, и наименьшей кинетической энергии (2), нормированной на объем, при которых фрагменты выходят из слоя, в зависимости от размера частиц. (Свободная поверхность сублимации; R_h = 2 а.е.)

Фрагменты размером > $\alpha_{кр}$, чтобы выйти из п ристеночного слоя, должны получить стартовую скорость, превышающую некоторое значение $V_{кр}$. Таким образом, фрагменты этих размеров (тип III, II и частично тип I) могут появиться в атмосфере только тогда, когда на поверхности ядра они получили положительный начальный импульс, например, при взрывном разрушении поверхности. Зависимость критического импульса, необходимого для этого, приходящегося на единицу поперечного сечения частицы, является линейной функцией размера, она представлена на рис. 2 кривой 1. Кривая 2 – кинетическая энергия, отнесенная к единице массы частицы.

СПИСОК ИСПОЛЬЗОВАННЫХ ИСТОЧНИКОВ

1. O.P. Kuznechik, N.I. Stetyukevich, V.N. Gorenkov, Research of Cometary Atmospheres and Solar Plasma for Results of Cometary Observations. Part IV. Proc. of the 12th International annual seminar “Nonlinear phenomena in Complex System” (May 17-20, 2005, Minsk, Belarus). – Minsk: Joint Institute of Power and Nuclear Research, **12**, 54-63 (2005).
2. Л.М. Шульман Ядра комет. – М.: Наука, 1987. – 232 с.
3. М.Я. Маров, А.В. Колесниченко, Ю.В. Скоров, Численное моделирование газопылевого потока в приповерхностном слое кометной атмосферы. Астрон. вестник, **29** 3, 243-252 (1995).
4. Л.М. Шульман, Динамика кометных атмосфер. Нейтральный газ. – Киев: Наук. думка, 243 с (1972).
5. A.V. Morozhenko, L.O. Kolokolova, E.A. Kajmakov, I.S. Lysunkova, Possible nature of cometary atmosphere particles. Icarus. **66** 2, 223-229 (1986).
6. И.С. Лизункова, В. А. Драневич, Преобразование вещества в кометах. Лабораторные исследования и интерпретация наблюдений. – С.-Петербург (1997) 19 с. (Препринт / РАН; Физико-технический ин-т им. Иоффе, № 1705).
7. D. Hughes, Meteoroid / Asteroid collisions with cometsry nuclei and the P/Halley outburst – Workshop on the Activity of Distant Comet. Proc. of the workshop on the activity of distant comet, Lenggries, Oct. 18-21, 1992 / Eds W. F. Huebner, H. U. Keller, D. Jewitt, et al. – San Antonio, Texas: Southwest research institute 83-99 (1993).

VI Serbian-Belarusian Symp. on Phys. and Diagn. of Lab. &
Astrophys. Plasma, Belgrade, Serbia, 22 - 25 August 2006
eds. M. Ćuk, M.S. Dimitrijević, J. Purić, N. Milovanović
Publ. Astron. Obs. Belgrade No. 82 (2007), 251-256 *Contributed paper*

МЕРИДИОНАЛЬНЫЙ ДРЕЙФ СОЛНЕЧНЫХ МАГНИТНЫХ СТРУКТУР

(MERIDIONAL DRIFT OF SOLAR MAGNETIC STRUCTURES)

О. П. Кузнечик, В. Н. Горенков, В. О. Кузнечик

Белорусский государственный университет, Обсерватория,
4, Пр.-т Независимости, г. Минск, 220030, Беларусь
e-mail: kuznechik@bsu.by

Abstract. Analysis of drift motion of Solar spots and filaments was performed.

1. ВВЕДЕНИЕ

Для объяснения дифференциального вращения Солнца предлагалось много теорий, но ни одна из них не стала общепризнанной [1]. Изменить ситуацию могут комплексные наблюдательные данные о меридиональном дрейфе различных активных образований на поверхности и в более глубоких слоях Солнца. Таких подробных данных пока не имеется. Наиболее полные сведения о вращении Солнца были получены по пятнам и волокнам [1]. Ниже проведен анализ их дрейфовых движений. При этом необходимо отметить, что все явления солнечной активности обусловлены выходом на поверхность Солнца магнитных полей.

2. ДЕЙСТВИЕ ГИДРОДИНАМИЧЕСКИХ СИЛ НА МАГНИТНЫЕ СТРУКТУРЫ

Для выявления воздействия гидродинамических сил на дрейф магнитных структур, рассмотрим вращающуюся газообразную сферу, которая удерживается силами гравитации. Примем ось z, направленную вверх, за ось вращения сферы и точку 0 за центр притяжения. Возьмем тело в точке M внутри сферы, тогда расстояние его от начала координат равно $R = (x^2 + y^2 +$

$z^2)^{1/2}$, а от оси вращения – $r = (x^2 + y^2)^{1/2}$. При этом $r = R\cos\varphi$, где φ – широта точки М.

Если обозначить через ω угловую скорость вращения сферы, которая направлена по z, то линейная скорость

$$\mathbf{v} = [\boldsymbol{\omega} \times \mathbf{r}], \tag{1}$$

а ее составляющие равны

$$v_x = -\omega y, \qquad v_y = \omega x, \qquad v_z = 0. \tag{2}$$

С учетом (1-2) при $\omega = \text{const}$ уравнение Эйлера принимает вид

$$\nabla \mathbf{P} = \rho(\omega^2 \mathbf{r} - \nabla \boldsymbol{\Omega}), \tag{3}$$

где $\boldsymbol{\Omega}$ – гравитационный потенциал, $\mathbf{P}$ – давление, ρ – плотность плазмы.

Выражение (3) определяет силу давления плазмы во вращающейся газообразной сфере. Примем, что во вращающуюся плазму плотности ρ_ρ погружено тело плотности ρ_m. На тело действует сила давления. При равномерном вращении гравитирующей массы плазмы она равна (3) архимедовой подъемной силе (на единицу объема тела)

$$\mathbf{F_A} = -(\rho_m - \rho_\rho)\nabla \boldsymbol{\Omega} \tag{4}$$

и центробежной силе, отнесенной к единице объема

$$\mathbf{f} = (\rho_m - \rho_\rho)\omega^2 \mathbf{r}. \tag{5}$$

Архимедова сила направлена вдоль радиуса $\mathbf{R}$ гравитирующей массы плазмы Солнца, а центробежная сила – вдоль радиуса-вектора $\mathbf{r}$, перпендикулярного к оси вращения сферы. Центробежная сила для Солнца мала по сравнению с архимедовой силой. На экваторе вблизи поверхности Солнца она составляет $2.14 \cdot 10^{-5}$ от архимедовой подъемной силы. Центробежная сила $\mathbf{f}$ имеет радиальную составляющую

$$\mathbf{f_R} = (\rho_m - \rho_\rho)\omega^2 \mathbf{R}\cos^2\varphi \tag{6}$$

и меридиональную составляющую, параллельную поверхности Солнца:

$$\mathbf{f_L} = -(\rho_m - \rho_\rho)\omega^2 \mathbf{R}\cos\varphi\sin\varphi. \tag{7}$$

Поскольку $|\ \text{grad}\ \boldsymbol{\Omega}\ | = \mathbf{g}$ – ускорение свободного падения, то вдоль радиуса гравитирущей массы плазмы действует подъемная сила на единицу объема тела (4, 6)

$$\mathbf{F_R} = (\rho_m - \rho_\rho)(\mathbf{g} - \omega^2 \mathbf{R}\cos^2\varphi). \tag{8}$$

Она равна архимедовой подъемной силе в неподвижной гравитирующей газовой сфере и дополнительной силе, обусловленной вращением сферы. Из (8) следует, что более легкие тела всплывают, а более тяжелые – тонут. При этом центробежная сила уменьшает действие силы гравитации.

Сила f_L обуславливает движение в меридиональном направлении тела, погруженного в равномерно вращающуюся плазму. Если плотность тела ρ_m меньше плотности плазмы ρ_ρ на данном уровне, то сила направлена от экватора к полярным зонам. Однако если $\rho_m - \rho_\rho > 0$, то сила f_L направлена в противоположную сторону и приводит к движению тела от полярных зон к экватору. Учитывая (7) и данные наблюдений дрейфа магнитных структур на Солнце [1], по аналогии получаем: магнитные структуры общего магнитного поля движутся во вращающейся газовой сфере к полярным зонам подобно всплыванию легких тел в более тяжелой плазме, а тяжелые пятна, наоборот, движутся к экватору; магнитные структуры общего магнитного поля являются

более легкими, а пятна – более тяжелыми образованиями по сравнению с окружающей плазмой.

3. ПАРАМЕТРЫ ПЛАЗМЫ В МАГНИТНЫХ ОБРАЗОВАНИЯХ

На движущееся тело в плазме действует сила сопротивления. Ее величина зависит от формы тела и состояния плазмы. В атмосфере Солнца плазма является сильно турбулентной, по крайней мере в фотосферных слоях. На это указывает уширение спектральных линий. Из него следует, что в невозмущенной фотосфере скорость микротурбулентности равна $v_l \approx 1.25$ км/с [2]. Считается [3], что характерный размер l элемента микротурбулентности составляет доли толщины слоя, в котором образуется спектральная линия. Для слабых фотосферных линий можно взять $l \leq 1$ км. В области размеров макротурбулентности, согласно [3], $v_l \approx 1.5$ км/с и $l \approx 560$ км. Вязкость обусловлена в основном ионами и нейтральными атомами плазмы, поскольку влиянием электронов можно пренебречь. Для оценки коэффициента кинематической вязкости достаточно точности, которая получается из кинетической теории газов. Коэффициент кинематической вязкости в этом случае определяется выражением

$$\nu = \frac{0.179}{\sqrt{\pi}} \frac{\sqrt{mkT}}{S_{\alpha i}\rho},$$

где m – масса атома водорода, k – постоянная Больцмана, T и ρ – температура и плотность плазмы, $S_{\alpha i}$ – эффективное сечение столкновений протон – атом водорода.

При $m = m_\alpha = m_i$, $T = 1.4 \cdot 10^4$ К, $S_{\alpha i} = 5 \cdot 10^{-20}$ м^2, $\rho = 10^{-4}$ кг/м^3 находим $\nu \approx 0.365$ м^2/с. В области размеров микротурбулентности число Рейнольдса $Re \approx v_l\, l/\nu \approx 3.4 \cdot 10^6$ и в области размеров макротурбулентности $Re \approx 2.3 \cdot 10^9$. Приведенные величины указывают на большое число Рейнольдса для плазмы таких масштабов движений.

В подфотосферных слоях магнитные поля обычно сконцентрированы в трубках, которые движутся под действием турбулентных движений. Для определенности примем, что сечения их круглой формы. Решение задачи об обтекании цилиндра перпендикулярно к его оси жидкостью с очень большим числом Рейнольдса приведено в [4]. Согласно решению сила $\mathbf{F_P}$ давления набегающего потока жидкости на цилиндр (сила сопротивления, испытываемая движущимся в жидкости цилиндром) выражается формулой

$$\mathbf{F_P} \approx \alpha h \rho_p \mathbf{u}^2, \qquad (9)$$

где **u** – скорость набегающего потока плазмы, обтекающей цилиндр, α – радиус сечения цилиндра и h – высота его. Сила $\mathbf{F_P}$ отнесена ко всему цилиндру. Примем, что сила, с которой действует движущаяся плазма на магнитные структуры, определяется также выражением (9). При этом плотность плазмы по объему всей магнитной структуры принята одинаковой. Умножая выражение (7) на объем элемента магнитной петли $\pi\alpha^2 h$ и приравнивая его (9), находим

$$\frac{\rho_p - \rho_m}{\rho_p} = \pm \frac{u^3}{\pi\alpha\omega^2 R\cos\varphi\sin\varphi}. \quad (10)$$

Знак «плюс» относится к магнитным структурам с $\rho_p - \rho_m > 0$ (структурам с пятнами), а «минус» – к структурам с $\rho_p - \rho_m < 0$ (структурам общего магнитного поля). Следовательно, сила (9) меняет направление в соответствии с изменением знака у $\rho_p - \rho_m$. Относительная разность плотностей плазмы $(\rho_p - \rho_m) / \rho_p$ в магнитной петле зависит от напряженности магнитного поля. На основании условия равновесия

$$P_m + \frac{H_m^2}{8\pi} = P_p, \quad (11)$$

где P_m – давление плазмы, $H_m^2/(8\pi)$ – давление магнитного поля внутри магнитной петли, P_p – давление окружающей плазмы и m – масса атома водорода. Так как $P = kT\rho/m$ (k – постоянная Больцмана, T – температура), то при однородной плотности внутри петли и одинаковой температуре плазмы как внутри, так и вне магнитной структуры ($T_m = T_p$) условие равновесия (11) дает:

$$\frac{\rho_p - \rho_m}{\rho_p} = \frac{H_m^2}{8\pi P_p}. \quad (12)$$

Между $(\rho_p - \rho_m)/\rho_p$ и $H_m^2/(8\pi P_p)$ для магнитных структур с пятнами такой связи (12) не имеется. На основании (12) для магнитных структур без пятен, т. е. для структур общего магнитного поля,

$$H_m^2 = \frac{8P_p u^2}{\alpha\omega^2 R\cos\varphi\sin\varphi}. \quad (13)$$

Для магнитных структур с пятнами по (10) были вычислены $(\rho_p - \rho_m) / \rho_p$ для различных значений скорости дрейфа u зон пятнообразования к экватору и разных φ. Средняя глубина α расположения магнитных структур под фотосферой взята равной 1000 и 3000 км. Результаты вычислений приведены в табл. 1. Они показывают, что при наблюдаемой скорости дрейфа зон пятнообразования к экватору u = 2 м/с и $\varphi = 30°$ $(\rho_p - \rho_m) / \rho_p \approx 1.72 \cdot 10^{-4}$. Скорость дрейфа u быстро увеличивается по мере увеличения $(\rho_p - \rho_m) / \rho_p$ в магнитных структурах с пятнами, а также с уменьшением широты φ.

Таблица 1. Вычисленные значения $(\rho_p - \rho_m) / \rho_p$ для структур с пятнами при разных u и φ

u, м/с	$(\rho_p - \rho_m) / \rho_p$		
	φ = 10°	φ = 20°	φ = 30°
2	$4.35 \cdot 10^{-4}$	$2.31 \cdot 10^{-4}$	$1.72 \cdot 10^{-4}$
5	$2.72 \cdot 10^{-3}$	$1.45 \cdot 10^{-3}$	$1.07 \cdot 10^{-3}$
10	$1.09 \cdot 10^{-2}$	$5.78 \cdot 10^{-3}$	$4.29 \cdot 10^{-3}$
20	$4.35 \cdot 10^{-2}$	$2.31 \cdot 10^{-2}$	$1.72 \cdot 10^{-2}$
30	$9.78 \cdot 10^{-2}$	$5.20 \cdot 10^{-2}$	$3.86 \cdot 10^{-2}$
40	$1.74 \cdot 10^{-1}$	$9.25 \cdot 10^{-2}$	$6.87 \cdot 10^{-2}$
50	$2.72 \cdot 10^{-1}$	$1.45 \cdot 10^{-1}$	$1.07 \cdot 10^{-1}$

Вычисленные $(\rho_p - \rho_m) / \rho_p$ при разных u и φ и α = 1000 км для структур общего магнитного поля даны в табл. 2. Средние напряженности в структурах общего магнитного поля при тех же u, φ и α при $P_p = 1.413 \cdot 10^{-5}$, отвечающем глубине 1000 км, вычислены по формуле (13) и приведены в табл. 2. При φ = 45° для наблюдаемой скорости дрейфа магнитных структур к полярным зонам u = 5 м/с $(\rho_p - \rho_m) / \rho_p \approx 2.79 \cdot 10^{-3}$, а средняя напряженность поля в магнитных структурах $H_m \approx 31.5$ мТл. С увеличением скорости увеличиваются значения $(\rho_p - \rho_m) / \rho_p$ и H_m .

Таблица 2. Вычисленные значения $(\rho_p - \rho_m) / \rho_p$ и H_m для структур общего магнитного поля при разных u и φ

u, м/с	φ = 45°		φ = 55°		φ = 65°	
	$(\rho_p - \rho_m) / \rho_p$	H_m, мТл	$(\rho_p - \rho_m) / \rho_p$	H_m, мТл	$(\rho_p - \rho_m) / \rho_p$	H_m, мТл
2	$4.46 \cdot 10^{-4}$	12.6	$4.75 \cdot 10^{-4}$	13.0	$5.82 \cdot 10^{-4}$	14.4
5	$2.79 \cdot 10^{-3}$	31.5	$2.97 \cdot 10^{-3}$	32.5	$3.64 \cdot 10^{-3}$	35.9
10	$1.11 \cdot 10^{-2}$	62.9	$1.19 \cdot 10^{-2}$	64.9	$1.46 \cdot 10^{-2}$	71.9
20	$4.46 \cdot 10^{-2}$	125.8	$4.75 \cdot 10^{-2}$	129.8	$5.82 \cdot 10^{-2}$	143.8
30	$1.00 \cdot 10^{-1}$	188.7	$1.07 \cdot 10^{-1}$	194.7	$1.31 \cdot 10^{-1}$	215.7
40	$1.78 \cdot 10^{-1}$	251.7	$1.90 \cdot 10^{-1}$	259.6	$2.33 \cdot 10^{-1}$	287.6
50	$2.79 \cdot 10^{-1}$	314.6	$2.97 \cdot 10^{-1}$	324.6	$3.64 \cdot 10^{-1}$	359.5

При напряженности $H_m \approx 150$ мТл, отвечающей появлению пятен [5] в магнитной структуре, скорость дрейфа оказывается равной 25 м/с, что существенно выше наблюдаемой. Если бы напряженность в магнитных структурах общего магнитного поля действительно составляла 150 мТл, как это вытекает из эффектов насыщения сигналов [6], и занимала бы значительную часть их объема, то скорость дрейфа магнитных структур к полярным областям была бы близка к 25 м/с (табл. 2). Поскольку это не так, то приходится считать, что областей с напряженностью поля 150 мТл нет или же они занимают незначительный объем. Это, конечно, имеет место при условии, что дрейф магнитных структур обусловлен вращением Солнца.

4. ЗАКЛЮЧЕНИЕ

Вклад магнитных структур с сильным полем, но без пятен, в зонах пятнообразования значителен. Причем структуры с пятнами и без пятен в этих образованиях очень тесно связаны, что должно сказаться, в частности, на уменьшении скорости дрейфа зон пятнообразования. Для структур с пятнами $(\rho_p - \rho_m) / \rho_p \approx 1.72 \cdot 10^{-4}$ величина очень малая, но ее оказывается достаточно, чтобы магнитная структура двигалась как целое к экватору.

Скорость дрейфа магнитных структур зависит от многих параметров (выражение (10)). Добавление конвекции и силы Кориолиса может повлиять на скорость осевого вращения Солнца с глубиной и существенно изменить скорость дрейфа магнитных структур. Естественно, что решение этих проблем должно основываться на данных наблюдений.

СПИСОК ИСПОЛЬЗОВАННЫХ ИСТОЧНИКОВ

1. The Astronomy and Astrophysics encyclopedia. – New York: van Nostrand Reinhold, 1002 (1992).
2. R.I. Kostik, T.V. Orlova, On the microturbulence in the solar photosphere, Solar Phys., **62**, 89-92 (1979)
3. Р.И. Костык, Тонкая структура фраунгоферовых линий и строение фотосферы Солнца: Дис. ...д-ра физ.-мат. наук., Киев (Машинопись), 322 (1983).
4. Я.Е. Кочин, И.А. Кабель, Я.В. Розе, Теоретическая гидродинамика, Физматгиз, Ч. II, 728 (1963).
5. Я.В. Стешенко, Магнитные поля мелких солнечных пятен и пор, Изв. Крым, астрофиз. обсерватории, **37,** 21-28 (1967).
6. J.O. Stenflo, Magnetic-field structure of the photosheric network, Solar Phys., **32**, 41-63 (1973).

VI Serbian-Belarusian Symp. on Phys. and Diagn. of Lab. &
Astrophys. Plasma, Belgrade, Serbia, 22 - 25 August 2006
eds. M. Ćuk, M.S. Dimitrijević, J. Purić, N. Milovanović
Publ. Astron. Obs. Belgrade No. 82 (2007), 257-260 *Contributed paper*

EXPERIMENTAL STUDY OF A HOLLOW CATHODE GLOW DISCHARGE IN HYDROGEN

G. Lj. Majstorović[1], N. M. Šišović[2], N. Konjević[2]

[1] *Military Academy, 11105 Belgrade, Pavla Jurišića – Šturma 33, Serbia*
[2] *Faculty of Physics, University of Belgrade, 11001 Belgrade, P.O. Box 368, Serbia*

Abstract. The optical emission spectroscopy is used for the temperature measurement of excited hydrogen atoms T_{exc}, from the shape of the Doppler broadened hydrogen H_α line in a titanium (Ti) hollow cathode glow discharge operated at various pressures of hydrogen. Measurements of molecular rotational and vibrational temperatures have been carried out as well. The rotational temperature is determined from the population of the H_2 excited state $d^3\Pi_u^-$ rotational-vibrational levels ($\nu' = 0$). The vibrational temperature is measured from the H_2 Fulcher-α diagonal bands, $d^3\Pi_u^- \rightarrow a\ ^3\Sigma_g^+$ transition, Q-branches, $\nu'=2, 3$. To reveal the discharge length at various pressures in a hollow cathode, plasma potential probe measurements are performed.

1. INTRODUCTION

It has been demonstrated recently that the excessive Doppler broadening (EDB) of hydrogen Balmer lines may be used for discharge-cathode surface interaction monitoring [1]. The EDB of hydrogen Balmer lines in low-pressure DC discharges operated with hydrogen isotopes and in inert gases with small admixtures of H_2 have been studied recently in some details, see e.g. [1-3] and references therein. The characteristic shape of these lines exhibits unusual multi component behavior, see Figure 1. The presence of high-energy hydrogen atoms in discharge may induce change of the vibrational energy levels population, see cross section data [4]. In this case modeling of cold hydrogen plasma should include these processes as well.

The aim of the present work is to study whether fast hydrogen atoms present in discharge influence other discharge parameters like rotational and vibrational temperature. To achieve this goal precision measurements of the rotational T_{rot} and vibrational temperature T_{vib} must be performed.

The experiment [1] is carried out by observing hollow cathode discharge end-on. This work is an extension of the earlier studies [2,5,6] with an emphasis to the influence of hydrogen pressure in Ti HC discharge to T_{rot}, T_{vib} and EDB of the H_α line.

2. EXPERIMENTAL

The hollow cathode glow discharge (HCGD) source with two symmetrically positioned kovar anodes and Ti cathode is used as a discharge source. The HC tube was 100 mm long with 6 mm internal diameter and 1 mm wall thickness. The construction details of HC discharge source are described elsewhere [2].

All HCGD experiments were carried out with hydrogen. The continuous flow of H_2 was 50-350 cm^3/min (at room temperature and atmospheric pressure). The working gas was sustained at the pressure in the range 2-8 mbar by means of needle valve and two-stage mechanical vacuum pump. To prevent oil vapor back streaming from the vacuum pump, the zeolite trap is placed between discharge chamber and the pump. The gas pressure measurements are performed on the both sides of discharge tube with standard U-shaped oil manometers.

To operate discharge in a DC mode, a current stabilized power supply (0–2 kV, 0–100 mA) is used. The air-cooled variable 10 kΩ ballast resistor is placed in series with the discharge and power supply. For all measurements, the anode was grounded. During the discharge operation, the cathode was either air cooled with a fan (110 mm dia; AC 220V/13W), placed 150 mm from discharge tube, or gradually heated by changing cooling rate of the fan. The temperature of the outer wall of the HC tube is measured by a K-type thermocouple.

To determine discharge length at various pressures a plasma potential probe was used. The probe, made of thoriathed tungsten rod 250 mm long with 2 mm dia, was pushed from the back side of HCGD source along the optical axis towards discharge located inside cathode. The discharge length is determined when probe reaches potential of 25V. This potential was chosen arbitrarily and it was constant in all measurements of discharge length.

The spectra recordings were performed with unity magnification and discharge was run between HC and front anode. The light from the discharge was focused with an achromatic lens (focal length 75.8 mm) onto the entrance slit of PGS-2 spectrometer (2 m focal length; reciprocal dispersion of 0.74 nm/mm with 651 g/mm reflection grating in first diffraction order). All spectral measurements were performed with an instrumental profile very close to Gaussian with measured full half-width of 0.018 nm. Signals from CCD detector (29.1mm, 3648 channels) are A/D converted, collected and processed by PC.

3. RESULTS AND DISCUSSION

The optical emission spectroscopy (OES) is used for all temperature measurements.

Three components can be distinguished in experimental H_α line shape in hydrogen, see Figure 1: central narrow peak, broader middle part and far drawn-out pedestal. The overall fit involving convolution of three Gaussians in Fig. 1 may be justified by the fact that three groups of excited hydrogen atoms are expected in the negative glow region: thermalized H^* typical for negative glow (Gauss 1); a group of H^* atoms produced by dissociation of H_2 molecules in collisions with high energy electrons (Gauss 2); and a group of H_f^* atoms generated in collisions of H_f reflected from the cathode with H_2 (Gauss 3). A subject of our main interest is the broadest Gaussian G_3, which is related to EDB and proportional to the number of fast excited atoms emitting the H_α line. Pressure trend of relative contributions G_i/G_{total} (i=1,2,3) and energies E_i (i=1,2,3) of excited hydrogen atoms obtained by fitting the H_a profiles for Ti HCGD are given in Table 1.

Table 1. Experimental conditions, relative contributions G_i/G_{total} (i=1,2,3) and energies E_i (i=1,2,3) of excited hydrogen atoms obtained by applying three Gaussian fit to the H_a profiles for titanium hollow cathode glow discharge in H_2 at *I=90 mA* and different pressures.

p (mbar)	Voltage (V)	G_1/G_{total} (%)	G_2/G_{total} (%)	G_3/G_{total} (%)	Hydrogen Atom Energy E_1 (eV)	E_2 (eV)	E_3 (eV)
2	389	74.1	22.1	3.8	0.2	4	56
4	389	73.7	22.4	3.9			50
6	388	71.0	24.8	4.2			40
8	387	68.7	28.4	2.9			41

For the rotational temperature T_{rot} determination we follow procedure described in [7]. Logarithmic plots of emission intensities of the Fulcher-α system, Q-branches lines, divided by line strengths and fourth degree of its wave number against term values for upper level are straight line whose slope is hc/k $T_{rot}(n', v')$. We used Q-branches from $d^3\Pi_u^-$ state and the H**ö**nl-London factors, for this electronic transition may be written as in [8], while rovibronic term values are taken from [7].

The transitions of the H_2 Fulcher-α diagonal bands ($d\ ^3\Pi_u^- \rightarrow a\ ^3\Sigma_g^+$ electronic transition; Q-branches with ν′=2,3) are used for T_{vib} temperature measurement. The intensity ratio of the two consecutive vibration bands of the same sequence according to [9] is used.

The temperature of fast excited hydrogen atoms, T_{rot}, T_{vib} and discharge length at various pressures are shown in Figure 2.

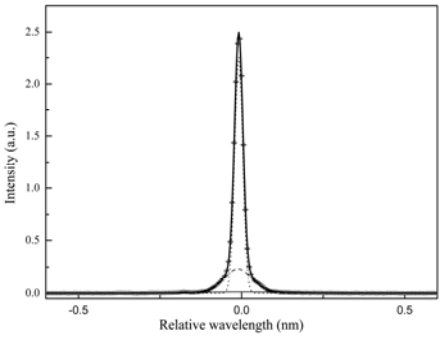

Fig 1. Typical H_α line shape recorded end-on in hydrogen with Ti cathode fitted with three Gaussians. Discharge conditions: U=388V; I=90 mA; T_{wall}=55 ^{O}C.

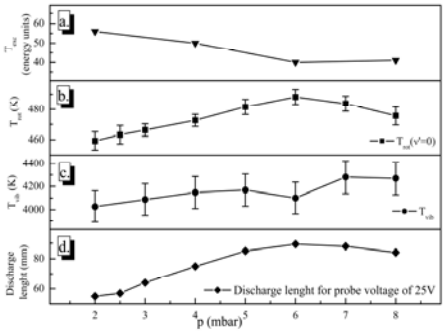

Fig. 2. (a) Fast excited hydrogen atoms energy; (b) rotational temperature; (c) vibrational temperature; and (d) discharge length in titanium hollow cathode glow versus working gas pressure p. Discharge conditions: U_{middle}=395V; I=90 mA; T_{wall}=55 ^{O}C.

In the Figure 2. one can notice different behavior of measured temperatures versus pressure. The rotational and vibrational temperatures increase with an increase of pressure up to 6 mbar. Simultaneously, the discharge length is changing with pressure and consequently the discharge current density on HC changed from 8.68mA/cm^2 to 5.34mA/cm^2 in pressure range from 2 mbar to 6 mbar. Further study is in progress and results will be reported.

REFERENCES

1. N. Konjević, G. Lj. Majstorović and N. M. Šišović, Appl.Phys.Lett. **86**, 251502 (2005).
2. N.M. Šišović, G.Lj. Majstorović, N. Konjević, Eur.Phys.J. D **32**, 347 (2005).
3. N. Cvetanović, M.M. Kuraica, N. Konjević, J.Apppl.Phys. **97** (2005).
4. A.V. Phelps, J.Phys.Chem.Ref.Data **21**, 883 (1992).
5. M. Gemišić-Adamov, B. M. Obradović, M. M. Kuraica and N. Konjević, IEEE Trans.Plasma Sci. **31**, 444 (2003).
6. S. B. Radovanov, K. Dzierzerga, J. R. Roberts and J. K. Ollthoff, Appl.Phys.Lett. **66**, 2637 (1995).
7. A. Astashkevich, M. Kaening, E. Kaening, N. V. Kokina, B. P. Lavrov, A. Ohl and J. Roepcke, J. Quant. Spectrosc. Radiat. Transfer **56**, 725-751 (1996).
8. I. Covacs, "Intensity distribution in rotational bands" in Rotational Structure in the Spectra of Diatomic Molecules, Budapest, 1969, pp. 131-139.
9. J.C. Philips, Optical Spectrometric Measurements of High Temperature, P. J. Dickeman, ed.,Univ. Chicago Press, Chicago, III.,(1961), p.217.

VI Serbian-Belarusian Symp. on Phys. and Diagn. of Lab. &
Astrophys. Plasma, Belgrade, Serbia, 22 - 25 August 2006
eds. M. Ćuk, M.S. Dimitrijević, J. Purić, N. Milovanović
Publ. Astron. Obs. Belgrade No. 82 (2007), 261-268 *Contributed paper*

A METHOD FOR DETERMINING ORBITS OF SMALL PLANETS AND THEIR 3D REPRESENTATION

N. Pejović, M. Marić, Ž. Mijajlović

Faculty of Mathematics, University of Belgrade, Belgrade, Serbia

Abstract. We propose a method for determining elements of orbits of small planets and comets from data obtained by series of measurements. The partic ular benefit of the method is seen in the easy and accurate determination of the type of the orbit when the measured points are closely arranged on the trajectory of the body, i.e. the time intervals between observations are small. It is done by computing four quantities related to conics that represent trajectories. Also, software is developed for the 3D graphical representation of trajectories and enveloping surfaces that they make in the course of time in the heliocentric coordinate system.

1. INTRODUCTION

As it is well known, the computing of elements of the orbit of a small celestial body for the given two heliocentric positions r_1 , r_2 in moments t_1 , t_2 is simple if the parameter p of the orbit is known. The problem of finding the parameter p is solved by Gauss (Theoria motus corporum coelestium, 1809) and it is still basic for contemporary computing. In this computation appears a quantity x, the solution of the system of equations:

$$\eta^3 - \eta^2 = mX(x), \quad x = m\eta^{-2} - l.$$

Then the orbit of the body is: elliptic, if $x > 0$; parabolic, if $x = 0$; hyperbolic if $x < 0$.

Now, suppose that we have a series of measurements of positions of a celestial body. The result is the cloud of points, i.e their coordinates that represent the trajectory of the body with certain precision. We propose an algorithm and it's implementation for finding the algebraic equation representing the trajectory. In fact we did more, we proposed the method for finding the equation of the second order surface *S* from a set *SP* of measured points. Then, the trajectory, a second order algebraic curve is obtained simply choosing $z = 0$ for an appropriately chosen coordinate system.

The classification of second order surfaces is the key part of the method. We use in the classification two matrices of small order having as elements coefficients of the surface. i.e. it's equation. The surface is determined according two the number of their eigenvalues and their signs. This approach permits simple implementation and good results in recognition of the surface, in particular when the points from the set P are concentrated in the small area on the surface S. The recognition of the surface is performed in the three stages. The first step consists of the finding an approximate equation of the surface, in the second, eigenvalues of matrices are determined, and finally, the type of the surface is concluded. The determination of the equation is done by solving of a system of linear equations, where the method of singular decomposition of matrices is used. Eigenvalues of matrices are computed by the Jacoby method. The algorithm in the details is as follows.

The second order surfaces are presented by the equation:

$$f(x, y, z) = ax^2 + by^2 + cz^2 + 2\,fyz + 2gxz + 2hxy + 2\,px + 2qy + 2rz + d \quad (1)$$

where $a^2 + b^2 + c^2 + f^2 + g^2 + h^2 \neq 0$

Another form of this equation is:

$$f(x, y, z) = \langle Mr, r \rangle + 2\langle n, r \rangle + d. \quad (2)$$

where r = [x, y, z]^T is the position vector in R^3, u, v denotes the scalar product of vectors u, v, and

$$M = \begin{bmatrix} a & h & g \\ h & b & f \\ g & f & c \end{bmatrix}, \quad n = \begin{pmatrix} p \\ q \\ r \end{pmatrix}.$$

The advantage of the method we are proposing is that it gives good results when collected data are concentrated in the small area of the supposed surface. This is achieved by introducing the matrix N, usually not considered in other methods, and to which the following theorem refers. This theorem has the crucial role in determination of the type of the surface.

Theorem: Let

$$N = \begin{bmatrix} a & h & g & p \\ h & b & f & q \\ q & f & c & r \\ p & q & r & d \end{bmatrix} \quad (3)$$

and *r3 = rank M, r4= rank N and* δ *=det(N)*. Further, *M-sign* and *N-sign* denote the signs of eigenvectors of matrices *M* and *N* respectively. Then the corresponding surface is:

r3	***r4***	***δ***	***M-sign***	***N-sign***	***Surface***
3	4	<0			Ellipsoid
3	4	>0	different		One-sheet hyperboloid
3	4	<0	different		Two-sheet hyperboloid
3	3		different		Conus
2	4	<0	same		Elliptical paraboloid
2	4	>0	different		Hyperbolical paraboloid
2	3		same	different	Elliptical cylinder
2	3		different		Hyperbolical cylinder
2	2		different		Two intersecting planes
1	3				Parabolical cylinder
1	2			different	Two parallel planes
1	1				Two coincident planes

Imaginary surfaces and degenerate cases (points) are omitted from the table, although they are characterized also by values *r3*, *r4*, δ and *M-sign* and *N-sign*. The proof of the theorem is long, and we omit it from this presentation.

2. THE ALGORITHM

Suppose that the set P of measurements consists of m points. Instead of determining the equation (1), we are computing the normalized form:

$$k_1x_2 + k_2y_2 + k_3z_2 + 2k_4yz + 2k_5xz + 2k_6xy + 2k_7x + 2k_8y + 2k_9z = -1 \quad (4)$$

having one unknown less. Here $x_2 = x^2$, $y_2 = y^2$ and $z_2 = z^2$. We form the matrix S of measured positions of dimension m × 9,

$$S = \begin{pmatrix} x_2^1 & y_2^1 & z_2^1 & 2y^1z^1 & 2x^1z^1 & 2x^1y^1 & 2x^1 & 2y^1 & 2z^1 \\ x_2^2 & y_2^2 & z_2^2 & 2y^2z^2 & 2x^2z^2 & 2x^2y^2 & 2x^2 & 2y^2 & 2z^2 \\ . & . & . & . & . & . & . & . & . \\ . & . & . & . & . & . & . & . & . \\ . & . & . & . & . & . & . & . & . \\ x_2^{10} & y_2^{10} & z_2^{10} & 2y^{10}z^{10} & 2x^{10}z^{10} & 2x^{10}y^{10} & 2x^{10} & 2y^{10} & 2z^{10} \\ . & . & . & . & . & . & . & . & . \\ x_2^m & y_2^m & z_2^m & 2y^mz^m & 2x^mz^m & 2x^my^m & 2x^m & 2y^m & 2z^m \end{pmatrix}.$$

The vector $k = [k_1, k_2, k_3, k_4, k_5, k_6, k_7, k_8, k_9]^T$ of coefficients k_i is the solution of the system $S \cdot k = P$, where $P = [-1, -1, -1, -1, -1, -1, -1, -1, -1]^T$. The number $m \geq 9$ of measured points might be large, therefore we have more equations (4) then unknowns k_i, so we minimize the function:

$$\Gamma = \sum_{i=1}^{m} \left[\sum_{j=1}^{n} s_{i,j} k_j + 1 \right]^2, \qquad S = \left\| s_{i,j} \right\|.$$

The minimum of Γ is achieved in the zero of the derivate of Γ along all coefficients k_i, i.e. by solving:

$$\Gamma = \sum_{i=1}^{m} \left[\sum_{j=1}^{n} s_{i,j} k_j + 1 \right]^2, \qquad l = 1, .., 9. \quad (5)$$

so k is solution of $Ak = B$, where $A = S^T S$ and $B = S^T P$. This system is solved then by the method of singular decomposition in order to minimize the computing

error. In fact, $k = VW^{-1} U^T B$ where U, V are orthogonal matrices such that $U^T AV = D$, and D is a diagonal matrix:

$$D = \begin{pmatrix} W & 0 \\ 0 & 0 \end{pmatrix}.$$

The matrix W is also diagonal and it has on the diagonal as elements the eigenvalues of the matrix $A^T A$. The singular decomposition of the symmetric matrix A is given by

$$A = U DV^T.$$

The approximate equation of the surface is not sufficient for determination of the type of the surface. For this we need to find eigenvalues and rank of matrices directly from measured points. Therefore, the next step is to compute the eigenvectors of matrices
M, N. This goal is done using the Jacobi method [1].

This method is iterative, and it reduces the starting matrix $A = \|a_{p,q}\|$ to the matrix in the diagonal form by the sequence of unitary transformations $T_{p,q} = T_{p,q}(\varphi)$, φ is the angle of an appropriate chosen rotation. In each step the non-diagonal element $a_{p,q}$ is annulated, i.e. $a'_{p,q} = 0$ and $a'_{q,p} = 0$ as well by the symmetry of A. As transformations are unitary, they do not change metric properties of the surface. If $A' = T_{p,q}^T A T_{p,q}$ is the iteration step, $A' = \|a'_{p,q}\|$, the angle φ is obtained from:

$$\frac{1}{2}(a_{qq} - a_{pp}) \sin 2\phi + a_{pq} \cos 2\phi = 0$$

i.e. by computing θ from:

$$\theta = \cot 2\phi \frac{\cos^2 \phi - \sin^2 \phi}{2 \sin \phi \cos \phi} = \frac{a_{qq} - a_{pp}}{2a_{pq}}. \tag{6}$$

Therefore, for $t = \tan\theta = \frac{\sin\theta}{\cos\theta}, \theta = (1 - t^2)/2t$, and we take the smaller root $\bar{t}$ of the equation $t^2 + 2t\theta - 1 = 0$. The reason is that to this smaller root $\bar{t}$ value, the rotation angle φ is smaller than 45°, and rotation appears to be more stable. The value t is given by:

$$t = \frac{sign(\theta)}{\sqrt{\theta^2 + 1} + |\theta|}. \tag{7}$$

Finding the final, diagonal form $\bar{A}$ of the matrix A, we read the eigenvalues on the diagonal of $\bar{A}$, while the number of non-zero elements on the diagonal gives the rank(A). So computed elements are sufficient to determine the type of the surface according to the displayed table.

A few words about the convergence and program implementation of the algorithm. The convergence is achieved after at most $5n^2$ rotations. Each rotation consists of $4n$ arithmetical operations, therefore the complexity of the procedure is $20n^3$. The algorithm is first implemented in Matlab. However, it appeared that this package is to slow, so the procedure is implemented again in C++ using OpenGL, the library for graphical presentation. We tested the program on various examples, most of them consisting of several thousands measured points. The obtained results were at least comparable, or better than implementations of other authors.

In astronomical applications we tested procedure for finding distribution characteristics of observations of asteroids Ceres and Pallas. So derived results are quite agreeable with results obtained with other methods.

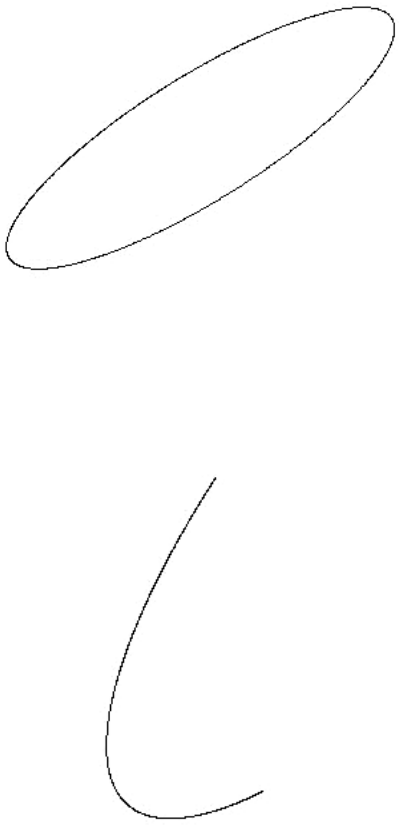

Fig 1. Ellipse and Parabola.

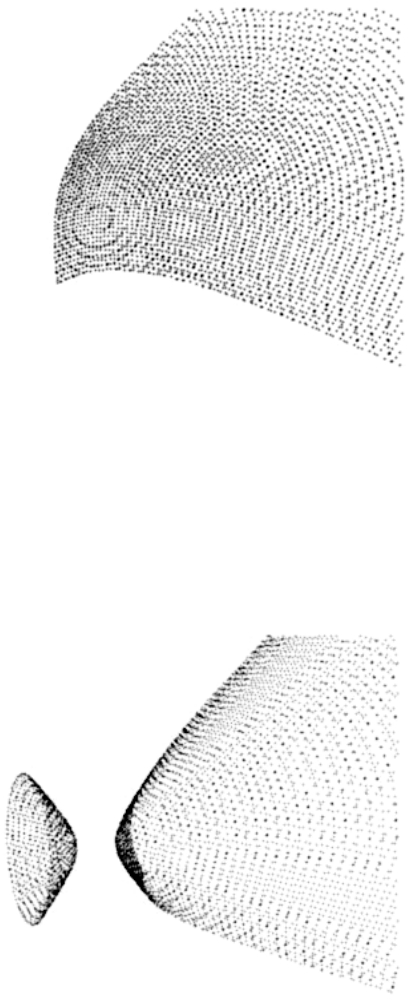

Fig 2. Paraboloid and Hyperboloid

In order to analyze performance of our method, sets of observational data of two largest asteroids in main asteroid belt were downloaded from the public database AstDys (http://hamilton.dm.unipi.it/astdys). We choose as test bodies Ceres and Pallas because of large number of their observations. As a consequence, their

orbits could be determined with high accuracy. We made several tests with different number of used observations. In almost all cases our method has shown that observations concentrate around an elipse. Our method should be tested on other asteroids, with smaller number of observations. We expact to determine what are the most suitable bodies for appllying our method. Our method could be used in preliminary investigations of distribution characteristics of asteroid observations.

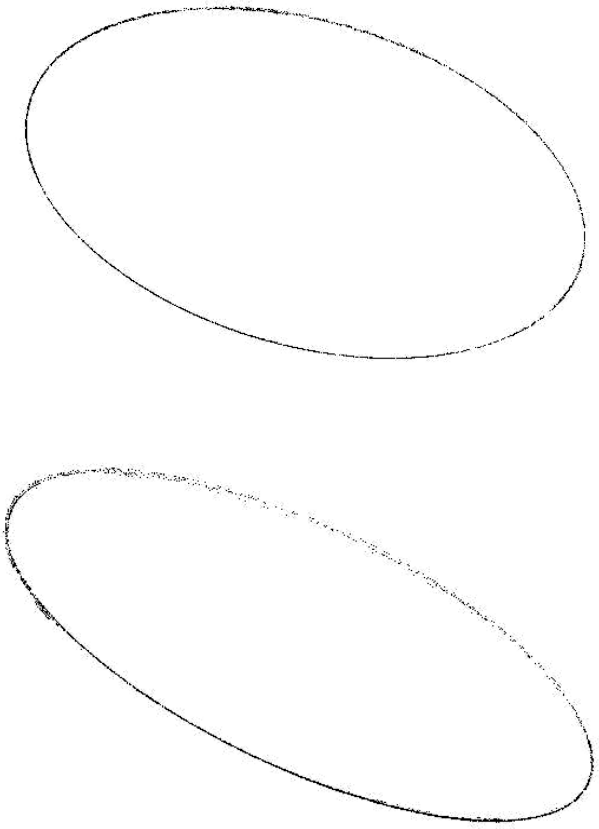

Fig 3. Ceres and Pallas.

REFERENCES

1. William H. Press, Saul A. Teukolsky, William T. Vettering, and Brian P Flannery, *Numerical Recipes in C++: The Art of Scientific Computing*, second edition, Cambridge University Press, 2002.

VI Serbian-Belarusian Symp. on Phys. and Diagn. of Lab. &
Astrophys. Plasma, Belgrade, Serbia, 22 - 25 August 2006
eds. M. Ćuk, M.S. Dimitrijević, J. Purić, N. Milovanović
Publ. Astron. Obs. Belgrade No. 82 (2007), 269-273 *Contributed paper*

ХАРАКТЕРИСТИКИ ИЗЛУЧЕНИЯ ДЖЕТОВ АКТИВНЫХ ГАЛАКТИЧЕСКИХ ЯДЕР НА РАННИХ СТАДИЯХ ЭВОЛЮЦИИ

(CHARACTERISTICS OF ACTIVE GALACTIC NUCLEI JET RADIATION IN EARLY EVOLUTION STAGES)

А. Л. Поплавский, О. П. Кузнечик, Н. И. Стетюкевич

Обсерватория Белорусского государственного университета
4 пр-т Независимости, 220030 Минск, Беларусь
E-mail: poplavsky@rambler.ru

Abstract. Integral and spectral characteristics of active galactic nuclei jets in their early propagation stages are simulated. We analyze two main mechanisms of jet emission: synchrotron emission in the inner regions of jet and Compton scattering of background photons and photons of surrounding sources by jet particles in outer regions. We show only these two mechanisms of jet emission provide the total jet luminosity. Synchrotron emission are effective mainly in radio band of spectrum, Compton one — in hard X-rays and Gamma-rays.

1. ВВЕДЕНИЕ

Одним из наиболее загадочных и менее всего изученных проявлений активности черных дыр являются струйные выбросы плазмы (джеты). Подобные структуры в настоящее время наблюдаются у целого ряда астрофизических объектов: активные галактические ядра [1], микроквазары, протозвезды и протопланетные туманности. Джеты активных галактических ядер являются самыми энергетически мощными и обладают характеристиками, исключительными с точки зрения современной физики.

В настоящее время существует много данных наблюдений структуры джетов, полученных с помощью крупнейших наземных оптических и радиотелескопов, Космического телескопа им. Хаббла и космических рентгеновских и гамма-обсерваторий [1,2]. Однако физика этого явления до сих пор остается

непонятой и неизученной. В данной работе мы строим модель излучения джетов в рамках синхротронного и комптоновского механизмов.

2. СИНХРОТРОННОЕ ИЗЛУЧЕНИЕ

При движении джета в межгалактической среде частицы окружающей плазмы будут двигаться относительно него с ультрарелятивистскими скоростями. При этом интенсивность их суммарного излучения на расстоянии r от оси джета [3]

$$I_{\nu,\theta} \square B_{\varphi}^{2}(r)\cos\theta, \tag{1}$$

где θ — угол в плоскости перпендикулярной оси джета между лучом зрения и точкой излучения. Можно записать следующее интегральное соотношение:

$$I_{\nu}(y) = 2\int_{R_J}^{\sqrt{R_0^2-y^2}} B_{\varphi}^{2}\left(\sqrt{x^2+y^2}\right)\frac{\sqrt{x^2+y^2}}{R_0}\,dx, \tag{2}$$

где R_0 — условно внешний радиус излучающей области, $\cos\theta = \sqrt{x^2+y^2}/R_0$. Интеграл (2) имеет аналитическое решение:

$$I_{\nu}(y) = \frac{K}{R_0}\left[arcsinh\left(\frac{\sqrt{R_0^2-y^2}}{|y|}\right) - arcsinh\left(\frac{R_0}{|y|}\right)\right], \tag{3}$$

где K – постоянная, определяемая экспериментально. На рис. 1 представлено модельное распределение нормированной интенсивности синхротронного излучения плазмы, окружающей джет. Луч зрения на рисунке перпендикулярен прямой джета.

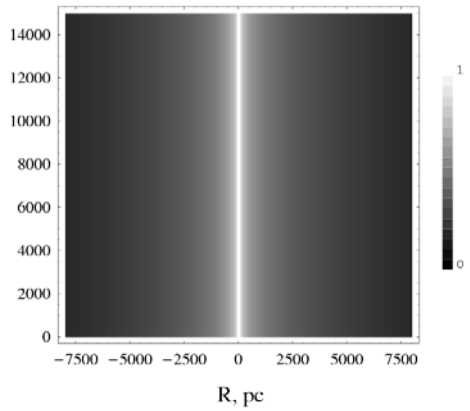

Рис. 1. Модельное двухмерное распределение нормированной интенсивности синхротронного излучение джета в перпендикулярной к его оси плоскости. Шкала интенсивности – линейная.

При построении данного распределения, величина внешнего радиуса принималась равной $R_0 = 12,5$ кпк (радиус Галактики). Сходство полученных модельных результатов с наблюдаемым излучением джетов в радио, рентгеновском, гамма-, ультрафиолетовом и оптическом диапазонах позволяют сделать заключение о правильности модели синхротронного излучения и подбора параметров.

2. ОБРАТНЫЙ ЭФФЕКТ КОМПТОНА

Рассмотрим излучение джета вследствие рассеяния квантов реликтового излучения на его релятивистских электронах. Пусть направления скоростей реликтовых квантов распределены изотропно и ε_0 — их начальная энергия. Тогда энергия рассеянных квантов [4]

$$\varepsilon_{sc} = \frac{4}{3}\varepsilon_0 \frac{K}{mc^2} = \frac{4}{3}\varepsilon_0(\Gamma - 1), \tag{4}$$

$K = mc^2(\Gamma - 1)$ — кинетическая энергия электронов джета. Рекуррентное выражение для фактора Лоренца имеет вид:

$$\Gamma_{k\delta h} = \Gamma_{(k-1)\delta h} - \frac{4\varepsilon_0}{3mc^2}\Gamma_{(k-1)\delta h} + \frac{7\varepsilon_0}{3mc^2}. \tag{5}$$

Из (4) и (5) следует

$$\Gamma(t) = \Gamma_0\left(1 - \frac{4\varepsilon_0}{3mc^2}\right)^{ct/2R_h} + \frac{7\varepsilon_0}{3mc^2 \ln\left(1 - \frac{4\varepsilon_0}{3mc^2}\right)}\left[\left(1 - \frac{4\varepsilon_0}{3mc^2}\right)^{ct/2R_h} - 1\right]. \tag{6}$$

С учетом малости выражения под логарифмом, (6) перепишется в виде

$$\Gamma(t) = \Gamma_0\left(1 - \frac{4\varepsilon_0}{3mc^2}\right)^{ct/2R_h} + \frac{7}{4}\left[1 - \left(1 - \frac{4\varepsilon_0}{3mc^2}\right)^{ct/2R_h}\right]. \tag{7}$$

С помощью полученных выражений, рассчитаем энергетические потери электрона. Рассматривались два вида источников фотонов. Первый – непосредственно реликтовый фон [5], второй – абсолютно черное тело с температурой $T = 10^6$ К.

Учитывая, что современный возраст Вселенной составляет $ct/(2R_h) \approx 10^{15}$ (а возраст типичного джета — на три порядка меньше), приходим к неизбежному выводу об отсутствии влияния комптоновских потерь на скорость джета. Однако обратный эффект Комптона может оказать значительное влияние на излучательные характеристики джета. Рассчитаем спектр фотонов после их диффузии в потоке электронов джета [4]:

$$\frac{\partial N}{\partial y} = \frac{1}{x^2}\frac{\partial}{\partial x}\left[x^4\left(\frac{\partial N}{\partial x} + N + N^2\right)\right], \tag{8}$$

где $x = \hbar\omega / kT_e$, $y = ukT_e/(m_e c^2)$, $u = nc\sigma_T t$, $\sigma_T = (8\pi/2)e^4/(m_e c^2)^2$, N – число фотонов на одну моду, n – концентрация электронов, T_e – электронная температура. Вследствие однородности задачи можно рассматривать только стационарные решения:

$$N(x) = -4\gamma e^{-x} + 4e^{-x}Ei(x) - 4\ln x. \qquad (9)$$

Полученное выражение является спектром излучения джета вследствие обратного эффекта Комптона (рис. 2).

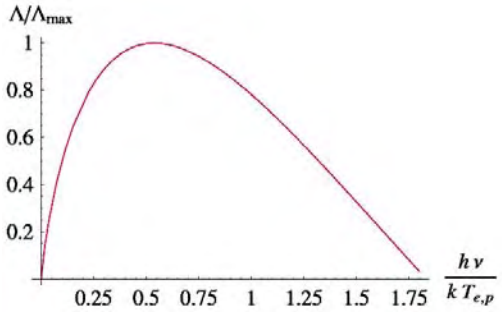

Рис. 2. Спектр излучения джета, образующийся вследствие рассеяния квантов реликтового излучения со средней равновесной температурой $\langle T \rangle \approx T_{eff\,0} = 2,7$ К на ультрарелятивистских электронах (обратный эффект Комптона).

4. ЗАКЛЮЧЕНИЕ

Следует отметить, что несмотря на значительную энергию квантов комптоновского излучения, лежащую в жестком рентгеновском и гамма-диапазоне электромагнитного спектра, само излучение, в отличии от синхротронного, локализовано в очень узком цилиндре, радиус которого равен радиусу джета. В настоящее время это должно служить препятствием для его непосредственного наблюдения с помощью внеатмосферных обсерваторий, т.к. такой размер лежит за пределами разрешающей способности современных рентгеновских и гамма-телескопов.

Результаты данной работы следующие. Рассчитаны интегральные и спектральные характеристики излучения джетов. Рассмотрены два механизма излучения: синхротронный в области $r > R_J$ и комптоновское рассеяние квантов реликтового излучения $r < R_J$. Показано, что только эти механизмы обеспечивают полную светимость джетов: синхротронное излучение — в основном в радиодиапазоне, комптоновский механизм — в жесткой рентгеновской и гамма- диапазонах спектра.

ЛИТЕРАТУРА

1. A.H. Bridle, Astron. J. **108**, 766 (1994).
2. D.A. Schwartz et al., Preprint astro-ph/0306317, (2003).
3. A.L Poplavsky, Dynamics of AGN Jets and Structure of Supermassive Black Hole Magnetospheres. MS Thesis, Belarusian State Uneversity, Minsk, Belarus, section 3.2 (2005).
4. A.L Poplavsky, N.I. Stetyukevich, O.P. Kuznechik, in Proceedinds of the V Symposium PDP-2004, V.S. Burakov, A.F. Chernyanskii eds, p. 48 (2004).
5. M.V. Zombeck, Handbook of Astronomy and Astrophysics. Second Edition. Cambridge, UK: Cambridge Univ. Press, (1990).

VI Serbian-Belarusian Symp. on Phys. and Diagn. of Lab. &
Astrophys. Plasma, Belgrade, Serbia, 22 - 25 August 2006
eds. M. Ćuk, M.S. Dimitrijević, J. Purić, N. Milovanović
Publ. Astron. Obs. Belgrade No. 82 (2007), 275-283 *Contributed paper*

EVOLUTION OF ACTIVE GALACTIC NUCLEI JETS IN GALACTIC HALOS

A. L. Poplavsky, O. P. Kuznechik, N. I. Stetyukevich

Observatory of Belarusian State University
4 Nezaliezhnasti Av., 220030 Minsk, Belarus
E-mail: poplavsky@rambler.ru

Abstract. We analyze long-term evolution of jets from their origin in accretion disks of active galactic nuclei to their destruction in far-halos of galaxies. Based on the analytical solutions of RMHD equations we show that magneto-hydrodynamical interactions of charged jet with intergalactic medium are not effective in jet destruction. High stability of jet in the nearest halo region are explained and proved. We show that the only mechanism of jet particles changing their trajectories is their interaction with cold dark matter (CDM) particles in far regions of galactic halos. Numerical simulations result in the most probable candidate for such CDM particles - primordial micro black holes.

1. INTRODUCTION

Jets are observed in various astronomical objects, such as active galactic nuclei (AGNs), X-ray binaries (XBs), and young stellar objects (YSOs). These astrophysical jets have variety in the linear size. In AGNs, jets extend more than several hundreds kpc and are several times larger than the host galaxies. In XBs and YSOs, the jets are much smaller than those in AGNs. The size of the jets ranges from 0.1 pc to 100 pc. Astrophysical jets show variety also in the velocity and luminosity. Despite all these varieties in the scale, astrophysical jets have common features. (1) Velocities of jets are of the order of the escape velocity of the source. (2) Jets are collimated well and essentially cylindrical. (3) Jets involve complex internal structure, such as wiggling and knots. (4) Jets show often S-shaped point symmetry around the source. (5) Jets vary their shapes and directions on short time scales. (6) Jets associate disks of which planes are perpendicular to the jet axis. These similarities suggest that astrophysical jets have common physical mechanisms in the formation and collimation. Many researchers have studied various aspects of astrophysical jets both observationally and theoretically to shed light on the

mechanisms of formation and collimation. In observations, jet sources have been studied in wide range of wavelength, from radio to X-ray. In radio region, hundreds of jets have been found in AGNs. Their velocities or morphologies are studied statistically. In infrared and optical region, internal structure of jets from YSOs is studied. In X-ray region, using spectra and their variabilities, the structure and dynamics of the most inner region of jet sources, at which the jets accelerate, are investigated. Recently, data of higher spatial or energy resolution are available with interferometer techniques and space observatories. For examples, in radio, with very long baseline interferometer (VLBI) techniques images of radio jets with resolution of milli-arcsecond are obtained. In infrared and optical, the NASA's Hubble space telescope has taken images of 0.1 arcsecond resolution, which are not available with ground-based telescopes. In X-ray, the ASCA satellite observes several KeV images with 0.2 KeV energy. Moreover, multiwavelength observations are carried out owing to cooperation of observatories with different target wavelength. In multiwavelength observations, targets are observed in different wavelengths simultaneously. The multiwavelength observations of the X-ray binary GRS1915+105, known as a transient X-ray source, reveal that there is the time correlation between X-ray flares and superluminal radio jet ejections. In theories, formation and collimation of jets are investigated in various fields: structure of accretion disks, acceleration and collimation processes of jets with numerical simulations, shock waves in accretions disk, particle acceleration mechanisms at shocks, etc. There are two main branches of accretion disk models: Standard accretion disk model and advection dominated accretion flow (ADAF) model, The standard accretion disk models were initiated by Shakura & Sunyaev (1973) [1]. Although the standard models explain many aspects of observational features of accretion disks, there are still some features that can not be accounted for, e.g., spectra of low luminosity AGNs. Other accretion solutions, ADAF models, are the spectra of low luminosity AGNs. Various kinds of jet acceleration mechanisms have been proposed. Jets are accelerated by gas pressure, magnetocentrifugal force, magnetic pressure, or radiation pressure. There are some collimation processes proposed: collimation by funnel flow, pinch effect of plasma, or cylindrical environment.

The velocities of astrophysical jets are known to be of the order of the escape velocities of the central objects. In AGNs and XBs, the velocities of jets range from mildly relativistic ($v \approx 0.2c$) to ultra-relativistic ($v \approx 0.2c$ or the Lorentz factor $\Gamma \approx 10$) [2].

In AGNs, relativistic jets are suggested by the fact that one-sided radio jets are commonly observed [3]. Since these one-sided jet sources associate double radio lobes, and since the lobes are supplied with their energy by the jets, the jets are intrinsically bipolar. The apparent asymmetry of the jets comes from a relativistic beaming effect, i.e., we observe a strong approaching jet as a one-sided jet and hardly observe a week receding jet. Another observational evidence of the relativistic jets is a super luminal motion. For examples, in 3C120 [4] and the quasar 1928+738 [5], proper motion of knots in the radio jets exceeds the speed of light apparently. This super luminal motion is interpreted as a relativistic effect caused by radio jets with bulk velocity close to the speed of light pointing toward the observer.

Also in the X-ray binaries, GRS 1915+105 and GRO 1655-40 [6], super luminal motion is observed. The intrinsic velocities of the jets are estimated to be about $0.9c$. In YSOs, the velocities of jets are of the order of 100 km s^{-1}, which are close to the escape velocities of the protostars with the mass of ≈1M [7].

Collimation of astrophysical jets is known very well. The collimation factor, which is defined as the ratio of the length to the diameter of jets, is several hundred for AGNs and 3-30 for XBs and YSOs. Radio jets from AGNs are extremely well collimated. The radio jets extend more than several tens kpc. Radio jets from the powerful AGNs are typically straighter and better collimated than those associated with weaker AGNs [8].

Astrophysical jets often take straight filled morphology. If we observe the jets with higher spatial resolution, we find their internal structures: knots and wiggling.

Knots are often observed in astrophysical jets. Wiggling is observed in some jet sources. The wiggling is seen not only in the radio intensity morphology but also in the directions of the magnetic field in the jets. These internal structures in astrophysical jets are thought to originate from episodic ejection or the precessing ejection of jets from the central object

Astrophysical jets generally show S-shaped point symmetry with respect to the source [9]. The jets, including the knots and kinks, are highly shaped point symmetric for the length of 30 kpc. Although most AGN jets show point symmetry, some AGNs jets have mirror symmetry (e.g., 3C449). The mirror symmetry is thought to be due to sweeping back of point symmetric jets by the proper motion of the galaxy through the surrounding intergalactic medium, since mirror symmetric jets are found almost exclusively in clusters of galaxies. In fact 3C449 is a member of the open cluster of galaxies Zw2231.2+3732. In the mirror symmetric jets, knots are also distributed mirror symmetrically.

Point symmetry is also seen in jets from XBs. The jets from SS433 show clear S-shaped point symmetry of knots, with the jet axis precessing. Point symmetric distribution of knots is also seen in HH jets. The degree of the symmetry is higher in the inner region.

These S-shaped point symmetries of jet morphology and knots distribution suggest that the morphology and internal structure of jets originate from activities (e.g., precession and episodic ejection of jets) of the central source (internal origin), not from inhomogeneous distribution of the environmental gas (external origin).

Observations have revealed various aspects of astrophysical jets: (1) jets are very fast (relativistic jets are common in AGNs and XBs) and are highly collimated (the ratio of length to width ranges from 10 to 100); (2) jets often associates accretion disks perpendicular to the jet axis (e.g., NGC4261, M87, and HH31); (3) jets ejections have close relation to activities of accretion disks, (in some XBs radio jets emanate after X-ray flares episodically). To account for these observations, many theorists have investigated accretion disks and jets therefrom. Accretion disk models have widely succeeded in accounting for many observational aspects of AGNs, CVs, and YSOs, e.g., the UV bump in AGN spectra, high and low states of CVs. Although accretion disk models succeed in understanding the spectra, they are not effective tools to understand the formation and collimation mechanisms of jets. Jet

formation and collimation mechanisms have been intensively investigated with numerical simulations. Mainly by solving hydrodynamical equations numerically, many researchers propose various kinds of jet acceleration and jet collimation mechanisms [10].

2. INITIAL STAGE OF JET PROPAGATION

Lets consider the process of jet slowing down via its mass increase by means of charged particle capture in the interstellar and intergalactic medium by jet magnetic field. Applying impulse conservation law:

$$\dot{M}_J t \frac{v_0}{\Gamma_0} = \frac{v}{\Gamma}(\dot{M}_J t + rS\rho), \tag{1}$$

where $\dot{M}_J$ — rate of jet matter transfer, v_0, Γ_0 — its initial velocity and Lorentz factor, S — effective cross section of particle capture by magnetic field, ρ — density of surrounding medium. From the last formula we have expression for jet moving away velocity

$$\vec{v}_J(z,t) = -\frac{\Gamma_0}{\langle\Gamma\rangle_t}\frac{\dot{M}_J v_0}{\dot{M}_J t + rS\rho}\hat{e}_z, \tag{2}$$

where $\langle\Gamma\rangle_t$ — time-averaged value of Γ. In the initial state jet consists of a beam of high-energy particles (protons/positrons or electrons) of radius $r \ll R_h = GM/c^2$. Then when interacted with surround medium it could be deformed. For mathematical description lets consider invariant MHD system of equations:

$$\begin{cases} \dfrac{\partial B_\varphi}{\partial t} = 0; \\ \dfrac{\partial B_r}{\partial t} = -\dfrac{\partial}{\partial z}(v_z B_r); \\ \dfrac{\partial B_z}{\partial t} = -v_z \dfrac{\partial B_r}{\partial r}. \end{cases} \tag{3}$$

In it $\vec{B} = (B_r, B_\varphi, B_z)$ are magnetic field of jet current. From the first equation of (3) it follows:

$$B_\varphi = const = B_{\varphi 0}. \tag{4}$$

If $B_r = B_r(r,t)$, then

$$\frac{\partial B_r}{\partial t} = -B_r \frac{\partial v_z}{\partial z} \Rightarrow \left[\frac{dB_r}{B_r} = -\frac{\partial v_z}{\partial z} dt, \quad \frac{\partial v_z}{\partial z} = \frac{\Gamma_0}{\langle \Gamma \rangle_t} \dot{M}_J v_0 t \frac{S\rho}{(\dot{M}_J t + zS\rho)^2} \right] \Rightarrow$$
$$\Rightarrow \ln |B_r| = -\frac{\Gamma_0}{\langle \Gamma \rangle_t} v_0 S\rho \int \frac{\dot{M}_J}{t} dt (\dot{M}_J t + zS\rho)^2 = \tag{5}$$
$$= -\frac{\Gamma_0}{\langle \Gamma \rangle_t} \frac{v_0 S\rho}{\dot{M}_J} \left[\frac{S\rho z}{\dot{M}_J t + Sz\rho} + \ln(\dot{M}_J t + S\rho z) \right],$$

and finally we have:

$$B_r = C(r) \exp\left\{ -\frac{\Gamma_0}{\langle \Gamma \rangle_t} \frac{v_0 S\rho}{\dot{M}_J} \left[\frac{S\rho z}{\dot{M}_J t + Sz\rho} + \ln(\dot{M}_J t + S\rho z) \right] \right\}, \tag{6}$$

where $C(r)$ — arbitrary function of coordinate r. When $B_r \neq B_r(z)$, then

$$\frac{\partial B_r(r,t)}{\partial t} = -\frac{\partial v_z}{\partial z} B_r \Rightarrow \frac{dB_r}{B_r} = -\frac{\partial v_z}{\partial z} dt \Rightarrow \ln |B_r| = -\frac{\partial v_z}{\partial z} t + C_1(r) \Rightarrow$$
$$\Rightarrow B_r = B_{r0} \exp\left\{ -\frac{\partial v_z}{\partial z} t \right\}. \tag{7}$$

From the derived expressions $\partial B_z / \partial t = 0$, and

$$B_z = B_{z0}. \tag{8}$$

Obviously, $B_{z0} = 0$, therefore $B_z = 0$. Component B_φ of magnetic induction vector is equal to magnetic field of straightforward jet current J:

$$B_\varphi = \frac{2J}{cr} = \frac{2}{cr} \frac{e}{m_0} \dot{M}_J. \tag{9}$$

Jet deformation could take place as a result of restructure of its magnetic field via its interaction with interstellar and intergalactic medium plasma. Sufficient condition of field restructure is:

$$m_0 n c^2 \left(\frac{1}{\sqrt{1 - v^2/c^2}} - 1 \right) \geq \frac{B_\varphi^2}{4\pi}, \tag{10}$$

We have from there condition of medium concentration, sufficient for jet structure change

$$n \geq \sqrt{1 - v^2/c^2} \, \frac{e^2}{\pi c^4 m_0^3} \dot{M}_J^2 \frac{1}{r^2}. \tag{11}$$

To solve this inequality it is necessary to derive expression for jet velocity. With effective capture cross section S we have

$$\frac{B_\varphi^2}{4\pi} = \frac{1}{\pi c^2 r^2} \frac{e^2}{m_0^2} \dot{M}_J^2 = n m_0 \Gamma, \tag{12}$$

equation for velocity $v_z \equiv dz/dt$ is:

$$v_0\Gamma_0 t = \frac{dz}{dt}\left[1-\left(\frac{dz}{dt}\right)^2\frac{1}{c^2}\right]^{-1/2} + z\frac{dz}{dt}\frac{e^2}{c^2 m_0^2}\dot{M}_J. \qquad (13)$$

Analyzing differential equation (13), its obvious, that slowing down process of jet is not effective. It is connected to large value of Γ up to $\sim 10^5$ and very low density of surrounding medium.

3. NUMERICAL SIMULATIONS OF JET DESTRUCTION

In the previous section our solutions of MHD equations prove high stability of initial stages of jet propagation. But the observations show strong deformations of jet trajectories in the outer regions of parent galactic halos. As it was shown in previous section, MHD interactions of jet particles with intergalactic medium aren't able to curve jet trajectory. Other mechanism was analyzed in [11]. According to it jets could be curved because of energy loss via Compton and synchrotron mechanisms. This mechanism isn't also effective enough to curve jet. We propose another hypothesis:

- jets are deformed due to the process of frequent inelastic scattering by invisible halo particles.

The only candidate for such a kind of particles could be primordial micro black holes.

Lets consider two dimensional scattering model. Its main parameters are: effective cross section of scattering particles a_s, concentration of scattering particles n_s, scattering $s(\theta)$, and fraction of electron energy after scattering κ. We define another parameter — mean free path l:

$$l = \frac{1}{2\pi a_s^2 n_s}, \quad (a_s \sim 1\,\mathrm{cm}^2). \qquad (14)$$

Numerical simulations was performed in Mathematica 5.0 system using Monte Carlo method. At $t = 0$ jet electron is in zero point of Cartesian plane XY (Y coordinate is directed toward initial jet particle motion) and have its first inelastic collision. Electron moves aside from its initial trajectory on the random angle $\phi = s(random[0,2\pi])$, which is distributed as $s(\theta)$ ($random[0,2\pi]$ — uniformly distributed at $[0,2\pi)$ random value, generated with Mathematica 5.0 random number generator). Electron energy after the first collision is $\Gamma_1 = \kappa\Gamma_0$. There are scheme of numerical algorithm below:

$$\begin{cases} x_0 = y_0 = 0, \\ \phi_0 = \dfrac{\pi}{2}, \\ \phi_k = s\left(random[0, 2\pi]\right), \\ x_k = x_{k-1} + l\sin(\phi_k + \phi_{k-1}), \\ y_k = y_{k-1} - l\cos(\phi_k + \phi_{k-1}), \\ \Gamma_k = \kappa^k \Gamma_0, \\ t_k = t_0 + \sum\limits_{j=1}^{k} \dfrac{l\Gamma_k}{c\sqrt{\Gamma_k - 1}}, \\ k = 1, 2, 3, \ldots \end{cases} \quad (15)$$

For correlation of parameters of the model with experimental data we use data from image catalogue of radio galaxies and quasars [12]. Therefore the main input model parameters are shape of deformed jet part and its linear size. In our model the mean lengthwise size of deformed jet part $\langle D \rangle = 300$ kpc. Other parameters are mean free path of an electron l and number of collisions N. Simulations were performed for one particle with scattering indicatrix of two kinds. When $s(\theta) = s_1(\theta)$,

$$s_1(\theta) = \begin{cases} \theta, & \theta \le \pi \\ 0, & \theta > \pi \end{cases}, \quad (16)$$

region of scattering becomes close to circle with number of collisions N increase. That doesn't fit the experimental data. The second indicatrix $s_2(\theta)$ is chosen according the nature of the process of ultrarelativistic particle deceleration. At high energies of electron it bends at small angles. When it decelerated enough its angular distribution should be close to uniform. There is an example of function with such a constraint is satisfied:

$$s_2(\theta, i) = (-1)^i \frac{\zeta\theta}{N - i + 1} + \frac{\pi}{2}, \quad (17)$$

where i — number of collision, ζ — arbitrary constant. The best fit of the experimental jet shape is satisfied with $\zeta = 0,03N$. According to this model we determine number of collisions before the total slowing down. It is equal to 1130 for $\kappa = 0,95$. The results of our numerical simulations are presented in fig. 1. This plot corresponds to the maximal number of scatters used in simulations — 11 000. When further increased, N leads to very long duration of computer calculations.

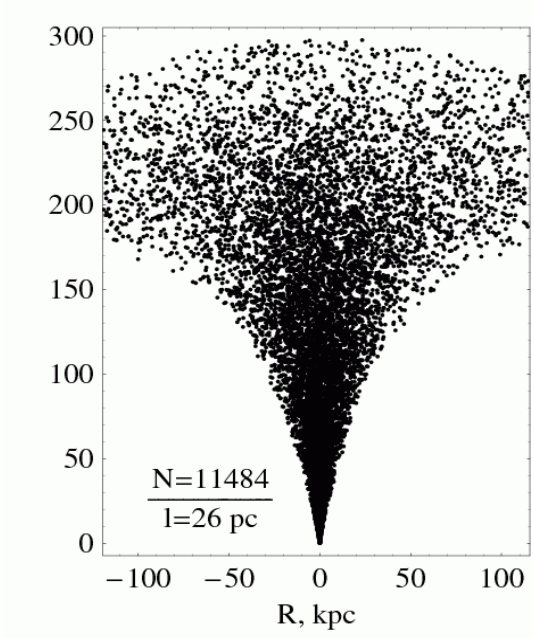

Fig. 1. Deformation of jet in far-halo regions of parent galaxies in consequence of scattering by invisible massive halo particles ($\zeta = 0,03N$).

4. DISCUSSION AND CONCLUSION

Based on relativistic magnetohydrodynamics equations we found that initial jet trajectory is stable and collimated, jet particles don't lose their energy Γ due to interactions with intergalactic medium. In section 4 we propose numerical algorithms and codes for numerical Monte Carlo simulations of scattering of jet electrons by far-halo cold darc matter particles. We simulate final jet evolution stages, their inelastic slowing down and spatial deformation. Simulations are performed with variations of parameters: number of scatters (up to 11000), and mean free path (≥ 25 pc). Its a pity that these results doesn't allow to estimate cold dark matter particle density. That is due to large uncertainties of used parameters and the indicatrix s_2.

According to our simulations we present hypothesis of jet deformation and decelerating in consequence of its particle inelastic scattering by invisible halo particles. Lets consider probable candidates for such a kind of particles. Their properties should be rather unique: comparatively small size (≈1 μ m), absence of

any emission, possibility of transformation of large energy. The first probable candidate for such hypothetic particles is intergalactic dust. But dust particles aren't able to influence the ultrarelativistic electron (positron or even proton) stream because of its large kinetic energy. That is why there is an only candidate among all capable of fitting all experimental and model data. These are primordial microscopic black holes that are about 40 years have been discussed theoretically, but there is no any explicit experimental evidence for them. Probably, an oblique evidence will be found studying AGN jets on at their final evolution stages. Additional investigations are very necessary and important.

REFERENCES

1. N.I. Shakura, R.A. Sunyaev, Astron. Astrophys., 337 (1973).
2. E.J. Guerra, R.A. Daly , in Accretion Phenomena and Related Outflows, IAU Colloquium 163, eds. Wickramasinghe D. T., Bicknell G. V., Ferrario L. (San Francisco: ASP Conf. Series, 695 (1997).
3. K.I. Kellermann, R.C. Vermeulen, J.A. Zensus, M.H. Cohen, Astrophys. J. , 1295 (1998).
4. R.C. Walker, J.M. Benson, S.C. Unwin, Astrophys. J., 546 (1987).
5. C. Hummel et al., Astron. Astrophys., 489 (1992).
6. S.J. Tingay et al., Nature, 141 (1995).
7. R. Mundt, E.W. Brugel, T. Buhrle, Astrophys. J., 275 (1987).
8. M.C. Begelman, R.D. Blandford, M.J. Rees, Rev. Mod. Phys., 255 (1984).
9. G.B. Taylor, R.A. Perely, M. Inoue, T. Kato, H. Tabara, K. Aizu, Astrophys. J. , 41 (1990).
10. C.F. Gammie, J.C. McKinney, Astrophys. J., 444 (2003).
11. A.L. Poplavsky, Dynamics of AGN Jets and Structure of Supermassive Black Hole Magnetospheres. MS Thesis, Belarusian State Uneversity, Minsk, Belarus, (2005), section 3.2.
12. A.H. Bridle A.H., Astron. J., 820 (1994).

VI Serbian-Belarusian Symp. on Phys. and Diagn. of Lab. &
Astrophys. Plasma, Belgrade, Serbia, 22 - 25 August 2006
eds. M. Ćuk, M.S. Dimitrijević, J. Purić, N. Milovanović
Publ. Astron. Obs. Belgrade No. 82 (2007), 285-288 *Contributed paper*

STUDY OF A PULSE ARC DISCHARGE USED FOR DIAMOND-LIKE COATING DEPOSITION

I. P. Smyaglikov[1], E. I. Tochitsky[2], V. G. Tatur[2], N. I. Chubrik[1]
S. V. Goncharik[1], A. I. Zolotovsky[1], M. V. Bel'kov[1]

[1] *Institute of Molecular and Atomic Physics, National Academy of Sciences of Belarus, Independence Av. 70, 220072 Minsk, Belarus, e-mail: ips@imaph.bas-net.by*
[2] *Scientific Engineering Centre "Plasmoteg" Academician Kuprevich Str. 1, Building 3, 220141 Minsk, Belarus*

Abstract. Carbon plasma flows for deposition of diamond-like films are generated with the help of four-electrode system with graphite cathode and self-recovering thin-film conductor of an ignition device in a vacuum chamber with residual pressure down to $5 \cdot 10^{-5}$ Torr. The pulse-periodic carbon arc discharge is considered at discharge current of 4–10 kA, duration of pulses of 100–200 ms and the pulse repetition rate of up to 30 Hz. The form and amplitude of voltage and current of pulses of igniting, supporting and main discharges, and the form of light pulse in various zones of the discharge were measured. The information on reproducibility of the arc discharge of short duration was obtained as well.

1. INTRODUCTION

Diamond-like films find wide application in different fields of engineering and microelectronics. Such films are characterized by a high surface hardness comparable to natural diamond, but have a quasi-amorphous structure consisting of nano-sized areas of different carbon phases. The physicochemical and mechanical properties of diamond-like coatings and films depend strongly on a technique and conditions of their production. Therefore, studying the correlation of coatings' characteristics with parameters of heterogeneous plasma flows used for their depositing is in demand. The present work is aimed at studying high-current arcs of short duration in vacuum to optimise the technology relevant to diamond-like coating deposition.

2. EXPERIMENT

The investigations were carried out on an experimental setup, allowing to get pulsed erosive plasma at a discharge current amplitude of up to 10000 A, the pulse duration of 100–200 μs, and a repetition frequency of pulses of up to 30 Hz as well as to study the plasma by optical and spectroscopic techniques with a time resolution of down to 0.1 μs, spectral resolution of down to 0.01 nm and spatial resolution down to 0.1 mm. The setup incorporates the pulsed plasma accelerator (PPA) [1], the optic-spectral unit for multifunction diagnostics, and the equipment of computer recording of plasma parameters on basis of analog-to-digital converters (ADC). The functional scheme of experimental setup is represented in Fig. 1.

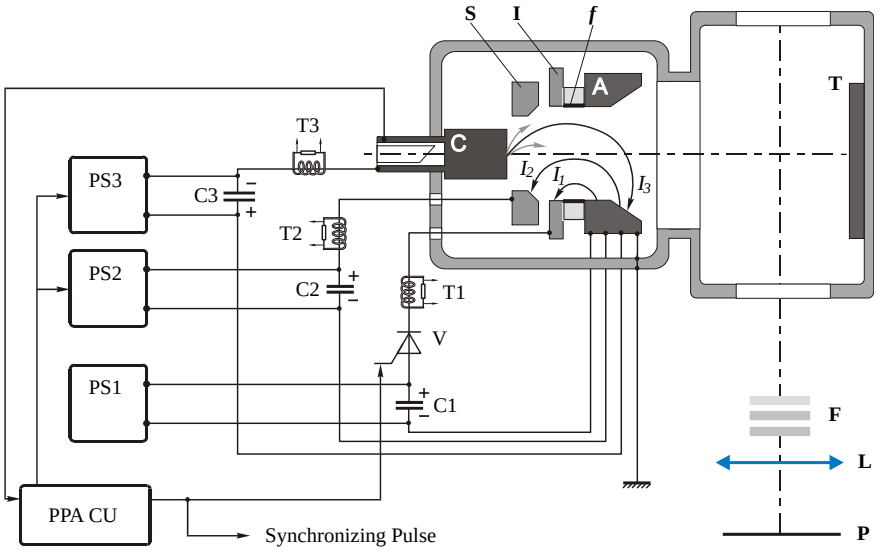

Fig. 1. The functional scheme of experimental setup to study carbon erosive plasma. PPA CU – control unit of PPA; PS1, PS2 and PS3 – power supplies of igniting, supporting and main discharges, respectively; C1, C2 and C3 – capacity storages; V – thyristor; A – anode; C – graphite cathode; S – support electrode; I – ignition electrode; *f* – self-recovering thin-film conductor; T1, T2 and T3 – sensors to measure the amplitude and shape of current pulses; T – target; F –filter set; L – quartz objective; P – image plane of plasma flow. Directions of electron currents of igniting I_1, supporting I_2 and main I_3 discharges are indicated by arrows.

At the beginning of each run of PPA, capacity storages C2 = 200 μF and C3 = 1200 μF are charged up to a voltage level, preset by the control unit PPA CU. Then the capacity storages are disconnected from power supplies PS2 and PS3. The voltage of capacitors C2 and C3 is adjusted in the range of 250÷500 V. Power

supply PS1 maintains the voltage of capacitor C1 = 15 μF on the level of about 800 V.

An electric pulse from the control unit, serving simultaneously as a synchronizing pulse of external peripherals, turns thyristor V on. An igniting current pulse is generated owing to discharging of capacitor C1 through a localized contact of anode A with ignition electrode I, formed by a thin conducting film *f* of the cathode erosion material deposited on a surface of insulator between electrodes I and A. A portion of initiating plasma is produced as a result of flash evaporation of the film. When the above mentioned plasma reaches the interelectrode space between cathode C and support electrode S, the discharge of capacity C2 occurs resulting in strong increase of conductivity of plasma between the cathode and anode, sufficient to initiate the main discharge. Energy of capacity storage C1 is liberated on the cathode by means of a vacuum high-current arc burning in vapour of the cathode eroded in microspots. Under the impact of gas-dynamic and electromagnetic forces the formed plasma flow is accelerated toward the target T. The part of plasma is deposited on interelectrode insulator, thus recovering the thin-film conductor *f* of the ignition system. After that the PPA is ready to the next operation cycle. The repetition frequency of igniting pulses is assigned by the control unit in the range of 0.1 to 35 Hz.

Entrance slits or working sites of peripherals, necessary to carry out the investigations, are arranged in an image plane P of plasma flow. For synchronization the peripherals with the pulsed arc discharge the igniting pulse of control unit PPA CU is used. After completing the registration cycle the software of equipment of computer recording of plasma parameters copies storage contents of ADC boards on a hard disk of the computer during a pause between the igniting pulses.

3. ELECTRICAL CHARACTERISTICS OF PULSED PLASMA FLOWS

Electrical characteristics of pulsed carbon arc were measured with the help of system of recording of currents and voltages of pulsed discharges. The system is realized on the basis of a set of initial transducers (current sensors and compensated voltage dividers) and analog-to-digital converters with the personal computer. The scheme of arrangement of sensors to measure amplitude and shape of current pulses of igniting I_1, supporting I_2 and main I_3 discharges is shown in Fig. 1.

The registered current oscillograms are given in Fig. 2. Current pulses I_1, I_2, I_3 and I_4 were taken from sensors T1, T2, T3 and T4 respectively. According to the results obtained there is a good repeatability of amplitude and shape of all current pulses. For example, maximal change of amplitude of the main discharge current from pulse to pulse does not exceed 10%. The time delay between igniting and supporting pulses and between supporting and main pulses varies in the range of 1÷3 and 5÷20 μs, respectively. The difference of current pulses I_3 and I_4 shows that the considerable part of the main discharge current does not flow to the anode and dissipates on other electrodes.

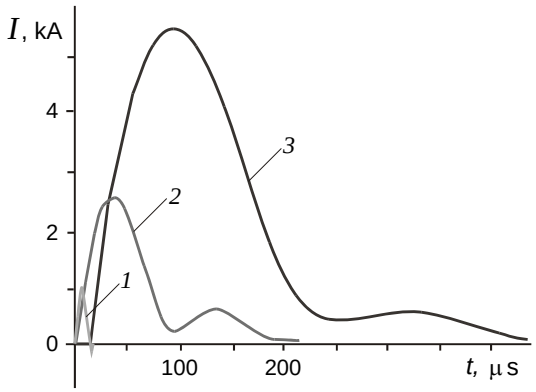

Fig. 2. The current oscillograms taken from sensors T1, T2 and T3.

In spite of steady current characteristics of the discharge in question, radiation intensity in a fixed spatial point of the plasma flow can vary by a factor of ten from impulse to impulse. The light pulse may be bell-shaped or have strong fluctuations of intensity at a frequency of 100–200 kHz. The last is due to formation and decay of cathode spot groups having lifetime of 5–10 μs.

4. CONCLUSION

The studies of carbon erosive plasma in a mode of diamond-like coating deposition have shown a good repeatability in electrical parameters of the used pulsed arc discharge with multi-step process of plasma initiation. The registered voltages and radiation intensities tend to have fluctuations at a frequency of 100–200 kHz. Such behaviour is ordinary for arc discharges with consumable electrodes [2, 3].

REFERENCES

1. E.I. Tochitsky, O.V. Selifanov, V.V. Akulich, I.A. Kapustin, and A.V. Stanishevskii : Surface and Coating Technology **47**, 522–527 (1991).
2. V.D. Shimanovich, I.P. Smyaglikov, A.I. Zolotovsky, S.M. Pankovets, ChubrikN.I. and S.V. Goncharik: Letters to J. Technical Physics **63**, Issue 11, 80–83 (in Russian) (2000)
3. I.P. Smyaglikov, V.D. Shimanovich and A.I. Zolotovsky: High Temperature Material Processes **8**, Issue 2, 221–232 (2004).

AUTHORS INDEX

CONFERENCE PROGRAMME

22. 8. 2006. TUESDAY

09:30 Registration
10:00 Opening ceremony

Chairman: J. Purić

10:30 A. P. Voitovich
INTRINSIC RADIATIVE COLOR CENTERS IN ALKALI HALIDES CRYSTALS AND FILMS: FORMATION AND APPLICATIONS

11:00 M. S. Dimitrijević
COLLISIONS WITH CHARGED PARTICLES AND SPECTRAL LINE SHAPES IN ASTROPHYSICAL PLASMAS – RESEARCH ON BELGRADE ASTRONOMICAL OBSERVATORY 2002-2005

11:30 Coffee break

Chairman: A. P. Voitovich

12:00 V. M. Astashynski, S. I. Ananin, V. V. Askerko, E. A. Kostyukevich, A. M. Kuzmitski, A. A. Mishchuk, M. M. Kuraica, I. P. Dojčinović, J. Purić
STUDIES AND CHARACTERIZATION OF QUASI-STATIONARY COMPRESSION PLASMA FLOWS GENERATED BY GAS-DISCHARGE AND EROSIVE PLASMA ACCELERATORS

12:30 I. P. Dojčinović, M. M. Kuraica, J. Purić
SILICON SINGLE CRYSTAL SURFACE MODIFICATION BY COMPRESSION PLASMA FLOW ACTION

13:00 Lunch break

Chairman: M. S. Dimitrijević

15:00 S. V. Gaponenko
MODIFICATION OF SPECTROSCOPIC TRANSITIONS IN MESOSCOPIC STRUCTURES: CAN IT SHED NEW LIGHT ON ELECTROMAGNETIC VACUUM?

15:30 D. Jevremović, A. Dotter, E. Baron
MODELS OF STELLAR ATMOSPHERES FOR EVOLUTIONARY MODELLING

16:00 Coffee break

Chairman: S. V. Gaponenko

16:30 N. V. Tarasenko, V. S. Burakov, A. V. Butsen, A. A. Nevar, N. A. Savastenko, P. Ya. Misakov
LASER ABLATION AND ELECTRICAL DISCHARGE PLASMAS IN LIQUIDS FOR FABRICATION OFNANOSIZED PARTICLES

17:00 Lj. Hadžievski
DYNAMICS OF WEAKLY RELATIVISTIC ELECTROMAGNETIC SOLITONS IN LASER-PLASMAS

17:30 M. Ivković, S. Jovićević, R. Žikić, N. Konjević
APPLICATIONS OF NON-HYDROGENIC SPECTRAL LINES FOR LOW ELECTRON DENSITY PLASMA DIAGNOSTICS

23. 8. 2006. WEDNESDAY

Chairman: S. Raikov

09:30 A. N. Chumakov, N. A. Bosak, A. M. Kuzmitsky, A. M. Petrenko, V. V. Shkurko, M. Sambuu
EFFECTIVE REGIMES OF LASER PLASMA FORMATION FOR FILMS DEPOSITIONS AND SPECTROCHEMICAL ANALYSIS OF MATERIALS

10:00 N. A. Bosak, A. N. Chumakov, Yu. A. Stankevich
SELECTION OF SOLID PROPELLANT FOR LASER PLASMA ENGINE

10:30 Coffee break

Chairwoman: N. Pejović

11:00 V. V. Mashko, G. I. Ryabtsev, M. V. Bogdanovich, A. S. Drakov, A. I. Enzhyieuski, O. E. Kostik, A. G. Ryabtsev, M. A. Shemelev, L. L. Teplyashin
DIODE-PUMPED SOLID-STATE LASERS WITH CONTROLLED PARAMETERS FOR SPECTROSCOPIC APPLICATIONS

11:30 N. M. Sakan, V. A. Srećković, V. M. Adamyan, I. M. Tkachenko, A. A. Mihajlov
THE METHODS FOR DETERMINATION OF HF CHARACTERISTICS OF NONIDEAL PLASMA

12:00 M. Dačić
CONNECTION OF RADIO-INTERFEROMETRIC WITH OPTICAL OBSERVATIONS AND CREATION OF A NEW REFERENCE FRAME FOR POSITION DETERMINATION OF CELESTIAL OBJECTS

13:00 Lunch break

16:00 Poster session

19:00 Conference dinner

24. 8. 2006. THURSDAY

Chairman: A. Chumakov

10:30 S. Raikov, V. Burakov, E. Dovnar-Zapolskaya, V. Kiris, E. Klyachkovskaya, N. Kozhukh
SPACE-TIME-RESOLVED OPTICAL EMISSION SPECTROSCOPY OF LASER ABLATION PLASMA FOR MICROANALYSIS OF UNIQUE SOLID SAMPLES

11:00 N. M. Šišović, G. Lj. Majstorović, N. Konjević
EXCESSIVE DOPPLER BROADENING OF HYDROGEN AND DEUTERIUM BALMER LINES IN A HOLLOW CATHODE GLOW DISCHARGES

11:30 Coffee break

Chairman: M. Dačić

12:00 F. Krčma, V. Mazánková, I. Soural
SHORT LIVE AFTERGLOW IN PURE NITROGEN AND NITROGEN CONTAINING TRACES OF METHANE AND OXYGEN

12:30 Z. Rašková, F. Krčma
PLASMACHEMICAL REDUCTION FOR THE CONSERVATION OF ARCHAEOLOGICAL ARTIFACTS

13:00 V. I. Arkhipenko, A. A. Kirillov, L. V. Simonchik, S. M. Zgirouski
THE CATHODE LAYER CHARACTERISTICS OF THE NORMAL DC ATMOSPHERIC PRESSURE GLOW DISCHARGE

13:30 Lunch break

Chairman: M. Ćuk

15:30 E. Ershov-Pavlov, K. Catsalap, V. Rozantsev, Yu. Stankevich, K. Stepanov
EMISSION SPECTRA OF LASER-INDUCED PLASMAS AT ELEMENTAL ANALYSIS OF SOLIDS: MEASUREMENT AND MODELING RESULTS

16:00 M. Jelić, S. Kuhn, J. Duhovnik
NOTES ON THE ROLE OF REACTIVE FIELD EFFECTS OF THE PARTICLE ACCELERATION TO THEIR COLLECTIVE MOTION IN PINCHED PLASMAS IN NATURE AND EXPERIMENTS

19:30 Excursion

25. 8. 2006. FRIDAY

Closing ceremony

Fig 1. Conference photo. First row: Sergej V. Gaponenko, N.A. Bosak, Jagoš Purić, Alexandar P. Voitovich, Milivoje Ćuk, Milan S. Dimitrijević. Second row: E. Ershov-Pavlov, N.V. Tarasenko, V.V. Mashko, S. Raikov, Nenad Sakan, A.A. Kirilov, Tomica Nenadović, A.N. Chumakov. Third row: Milorad Kuraica, Nikola Cvetanović, Ivan Dojčinović, Nikola Šišović, Anatolij A. Mihajlov, Goran Poparić, Bratislav Obradović, Milka Nikolić, Nenad Milovanović.

Fig. 2. Opening ceremony. Alexandr P. Voitovich, Milivoje Čuk, Sergej V. Gaponenko, Milan S. Dimitrijević.

Fig. 3. Opening ceremony. Aleksandar Selmak, Vice Minister for Science and Environmental Protection of Serbia.

Fig. 4. Opening ceremony. Aleksandar Lipkovski, Vice Rector of the Belgrade University.

Fig. 5. Opening ceremony. Alexandar P. Voitovich, Milivoje Čuk, Sergej V. Gaponenko, Milan S. Dimitrijević, Vladimir Mackyevich, Ambassador of the Belarus.

Fig. 6. Opening ceremony. Vladimir Mackyevich, Ambassador of the Belarus.

Fig. 7. Conference dinner. Sonja Jovićević, Ivan Dojčinović, Nikola Cvetanović, Nikola Konjević, Milivoje Čuk.

Fig. 8. Conference dinner. Nikola Konjević, Alexandr P. Voitovich, Milivoje Ćuk, Milan S. Dimitrijević, Anatolij A. Mihajlov.

Fig. 9. Conference dinner. Sergej V. Gaponenko. Aleksandar Lipkovski, Jagoš Purić.

Fig. 10. Conference dinner.

Fig. 11. Conference dinner.

CIP - Каталогизација у публикацији
Народна библиотека Србије, Београд

533.9 (082)
52-7 (082)
521-355 (082)
539.18 (082)

SERBIAN - Belarussian Symposium on Physics and Diagnostics of Laboratory and Astrophysical Plasma (6 ; 2006 ; Beograd)
Invited Lectures and Contributed Papers / VI Serbian-Belarussian Symposium on Physics and Diagnostics of Laboratory and Astrophysical Plasma, Belgrade, 22-25 August 2006 ; [organized by Faculty of Physics, University of Belgrade [and] Center for Science and Technology Development [and] Astronomical Observatory] ; edited by Milivoje Ćuk ... [et al.]. - Belgrade : Astronomical Observatory, 2007 (Beograd : Kultura). - 300 str. : ilustr. ; 24 cm. - (Публикације Астрономске опсераторије у Београду = Publications of the Astronomical Observatory of Belgrade, ISSN 0373-3742 ; sv. 82)

Radovi na engl. i belorus. jeziku. - Tekst ćir. i lat. - Tiraž 300. - Bibliografija uz svaki rad. - Registar. - Abstracts.

ISBN 978-86-80019-14-7
1. Ćuk, Milivoje 2. Faculty of Physics (Beograd)
a) Плазма - Зборници b) Астрофизика - Зборници c) Атомска физика - Зборници
COBISS.SR-ID 140643340